UNIVERSITY OF SOUTHAMPTON

FACULTY OF PHYSICAL AND APPLIED SCIENCES

OPTOELECTRONICS RESEARCH CENTRE

Power Scaling of Novel Fibre Sources

Part I: Spectrum-controllable fibre-based amplified spontaneous emission sources

Part II: Efficient intracavity frequency doubling schemes for continuous-wave fibre lasers

by

Rafal Cieslak

Thesis for the degree of Doctor of Philosophy

September 2012

UNIVERSITY OF SOUTHAMPTON

ABSTRACT
FACULTY OF PHYSICAL AND APPLIED SCIENCES
OPTOELECTRONICS RESEARCH CENTRE

Doctor of Philosophy
POWER SCALING OF NOVEL FIBRE SOURCES
By Rafal Cieslak

This thesis explores novel fibre-based coherent light source architectures and strategies for scaling output power. The research focuses on fibre-based amplified spontaneous emission (ASE) sources with broadband output in the ~1 μm spectral region and on internally-frequency-doubled fibre lasers emitting in the visible (green) wavelength range. In *Part I: Spectrum-controllable fibre-based amplified spontaneous emission sources* modelling, development and characterisation of a versatile ASE source based on Yb-doped fibre gain stages, using power-efficient means for spectrum control is presented. Experiments have culminated in a versatile seed source with polarized output and a reasonable degree of spectral control. In its final configuration, the ASE source was capable of producing either a broad spectrum in the 1-1.1 μm band with a full-width at half-maximum of 15-40 nm and output power > 1 W. Alternatively, single/multiple narrow lines with a full-width at half-maximum ranging from several nanometres to < 0.05 nm and output power spectral densities of up to 100 mW/nm could be generated. The output power was temporally stable with fluctuations at the level < 0.3-0.8% of the total output power. Very high spectral stability was obtained, which was limited mostly by the mechanical stability of the external cavity. The output beam was nearly diffraction limited with $M^2 \approx 1.1$. *Part II: Efficient intracavity frequency doubling schemes for continuous-wave fibre lasers* introduces a novel concept for resonant enhancement of the intracavity power in high power continuous-wave fibre lasers that is suitable for a wide range of applications. Using this concept, efficient frequency doubling in continuous-wave Yb-doped fibre lasers has been demonstrated and techniques for using it in devices based on both robustly single-mode and multi-mode fibres have been developed. Finally, this thesis presents wavelength tuning of continuous-wave Yb-doped fibre lasers over ~19 nm in the green spectral region and scaling the generated second harmonic power up to ~19 W with more than 21% pump to second harmonic conversion efficiency.

Table of Contents

List of Tables

List of Figures

List of symbols and abbreviations

AR	anti-reflection
ASE	amplified spontaneous emission
BPP	beam parameter product
CCD	charge-coupled device
CW	continuous-wave
CPM	critical phase matching / critically phase-matched
DFG	difference-frequency generation
ESA	excited-state absorption
ETU	energy transfer up-conversion
FBG	fibre Bragg grating
FPM	Fresnel phase matching
FSR	free spectral range
FWHM	full width at half-maximum
HR	highly reflective
HT	highly transmissive
HTS	high-temperature solution
LMA	large mode area
MEMS	micro electro-mechanical systems
MOPA	master oscillator power amplifier
MPM	Modal phase matching
NCPM	non-critical phase matching
OPA	optical parametric amplification
OPO	optical parametric oscillation / oscillator
PCF	photonic crystal fibre
PER	polarisation extinction ratio
PM	polarisation maintaining
QPM	quasi-phase matching
RE	rare-earth
SBS	stimulated Brillouin scattering
SFG	sum frequency generation

SH	second harmonic
SHG	second harmonic generation
SRS	stimulated Raman scattering
TEM	transverse electromagnetic
YDF	ytterbium doped fibre

Er	erbium
Tm	thulium
Yb	ytterbium
Ho	holmium
Sm	samarium
Pr	praseodymium
Bi	bismuth
Nd	neodymium
LBO	lithium triborate, LiB_3O_5
PZT	Lead Zirconate Titanate, $Pb[Zr_xTi_{1-x}]O_3$, $0 \leq x \leq 1$
YAG	yttrium aluminium garnet, $Y_3Al_5O_{12}$
ZBLAN	fluoride glass family, ZrF_4-BaF_2-LaF_3-AlF_3-NaF

Chapter 2

N_2, N_1	population densities for the lower $^2F_{7/2}$ and upper $^2F_{5/2}$ manifolds of ytterbium
R_{12}, R_{21}	stimulated absorption and stimulation emission rates of the pump
W_{12}, W_{21}	stimulated absorption and stimulation emission rates of the signal
A_{21}	spontaneous emission rate
η_q	quantum efficiency of the pump
$\lambda,\ \lambda_s,\ \lambda_p$	wavelength, signal wavelength, pump wavelength
$\Delta\nu, \Delta\lambda$	frequency bandwidth, wavelength bandwidth
h	Planck constant
c	velocity of light in vacuum
ν, ν_s, ν_p	frequency, signal frequency, pump frequency
σ_a, σ_e	absorption and emission cross-sections for lower and upper level

τ_f	upper laser level lifetime
N	total rare-earth ion concentration
P_p	pump power
$P_s^{\pm}$	signal power propagating in forward (+) or backward (-) direction
A_{core}, A_{clad}	area of the core, area of the inner cladding
P_{psat}	pump saturation power
α_p	pump absorption coefficient
G, $G^{\pm}$	single-pass gain in the fibre, in forward (+) or backward (-) direction
g	gain coefficient
α_s	signal attenuation coefficient
L	length of the fibre section
P_{ASE}^0	noise power at a given point of the single-mode fibre
$P_{ASE}^{\pm}$	ASE power propagating in forward (+) or backward (-) direction
$P_{noise}^{\pm}$	ratio of noise power accumulated after propagation to single-pass gain in forward (+) or backward (-) direction
$\Delta\nu_{ASE}$	effective frequency bandwidth of the ASE spectrum
$\Delta\lambda_{ASE}$	effective wavelength bandwidth of the ASE spectrum
ν_{ASE}, λ_{ASE}	mean frequency, mean wavelength of the ASE spectrum

Chapter 3

R_A, R_B	reflectivity of the facet at the pumped, opposite fibre end
M^2,M_x^2, M_y^2	beam quality factor, beam quality factor in x and y direction
$P_{feedback}$	feedback power returning to the fibre from the external cavity
$P_{background}$	background ASE power built-up in the fibre
ψ, $\psi(\lambda)$	ratio of feedback to background ASE power, at specific wavelength
$\Delta P/P$	power stability (power fluctuations to output power ratio)
Λ_g	diffraction grating constant
w_{0HR}	beam spot size on the surface of the HR mirror
$w_{0grating}$	beam spot size on the surface of the diffraction grating
f	focal length
θ_i, θ_r	incidence angle, beam reflection angle

$\Delta\lambda_r$	spectral resolution of the wavelength selection arrangement
Δx	geometrical distance, between two spectral components separated by the spectral resolution, on the surface of the HR mirror
$\delta\lambda$	FWHM width of the peak formed by the etalon in the external cavity
λ_0	central wavelength of the peak formed by the etalon in the external cavity
d_e	distance between the etalon mirrors
R_e	reflectivity of the mirrors forming the etalon
ψ_l	ratio of the power in a single narrow ASE line to background power

Chapter 4

P_{out}, P	output power from the laser
η_s	slope efficiency of the laser
P_{abs}	pump power absorbed in the laser medium
P_{th}	amount of absorbed pump power required to reach lasing threshold
T_{OC}, γ	output coupler transmission, other losses in the cavity excluding T
A	area of the region where pump light is absorbed
w_p	pumping beam radius
w_l	laser mode radius
I_{sat}	laser signal saturation intensity
w_0	beam waist radius
θ_{NA}	beam divergence half-angle
M^2	beam propagation factor
z_R	Rayleigh range
B	brightness of the laser source
A_e	emitting area
Ω_e	solid angle divergence
M_x^2, M_y^2	beam propagation factors in *x* and *y* directions respectively
Q_d	quantum defect
E_p, E_s	energies for the pump and laser signal photons
n_{clad}, n_{core}	refractive index of the inner cladding, of the core
n_{out}	refractive index of the outer cladding

V	normalized frequency of the fibre
r_{core}	core radius
NA_{core}	numerical aperture of the core
r_{clad}	inner cladding radius
NA_{clad}	numerical aperture (acceptance angle) of the inner cladding
γ_{uf}	factor taking into account the need to underfill the inner-cladding
P_{hmax}	maximum heat deposition per unit length
T_m	softening temperature of silica core
T_s	ambient temperature
K_{clad} , K_{out}	thermal conductivities of silica inner cladding and outer cladding
r_{out}	radius of the polymer coating
H_{out}	heat transfer coefficient for the outer polymer coating
T_d	maximum temperature, that can be tolerated before coating damage
R_t	thermal shock parameter for silica
dn/dT,	temperature gradient of the refractive index for silica
P_{max}	maximum output power extractable from the fibre laser
L	the length of the fibre
γ_h	fractional power converted to heat
λ_{Stokes}	Stokes signal wavelength
λ_{laser}	laser signal wavelength
α_{Stokes}, α_{laser}	absorption coefficients at Stokes and laser signal wavelengths
I_{Stokes}, I_{laser}	optical intensities at Stokes and laser signal wavelengths
g_R	Raman gain coefficient of silica glass for polarised light
P_{th}^{SRS}	threshold for stimulated Raman scattering
A_{eff}	effective area of the laser signal mode field
l_{eff}	effective Raman length
v_A	speed of sound in silica glass
ν_B	frequency shift via Doppler effect
α	loss coefficient for Stokes and laser signal waves
g_B	Brillouin gain coefficient
τ_B	phonon lifetime
p_{12}	longitudinal elasto-optic coefficient
ρ_m	material density

g_{Bmax}	maximum value of Brillouin gain
P_{th}^{SBS}	threshold for stimulated Raman scattering
I_{damage}	surface damage threshold for bulk silica
$\boldsymbol{P_{NL}}$	nonlinear polarisation vector
$\boldsymbol{E}$	electric field vector
ε_0	permittivity of free space
$\chi^{(1)}$	linear component of electric susceptibility
$\chi^{(2)}, \chi^{(3)}$	second and third order nonlinear components of electric susceptibility
i	imaginary unit (square root of negative one)
$E_\omega, E_{2\omega}$	electric field amplitudes for the fundamental and second harmonic waves
$n_\omega, n_{2\omega}$	refractive index values for the fundamental and second harmonic waves
d_{eff}	effective nonlinear coefficient of the medium
Δk	phase velocity mismatch between interacting waves
$\mathbf{k}_\omega, \mathbf{k}_{2\omega}$	wave vectors of the fundamental and second harmonic waves
$\hat{z}$	unit vector in the propagation direction
ω	angular optical frequency
I_0	central intensity in the Gaussian beam profile
I_ω	intensity of the optical wave
A	area of the beam
η_{SHG}	single-pass SHG conversion efficiency
P_ω	optical power at fundamental wavelength
w	the average spot size inside the nonlinear crystal
λ_ω	fundamental wavelength
$T,\ T_{pm}$	temperature, phase matching temperature
n_ω, n'_ω	refractive index values for orthogonal pump polarization components
T_0	room temperature
ΔT_{BW}	temperature bandwidth for phase matching
θ, ϕ	propagation angle (with respect to Z-axis, X-axis)
θ_{pm}	phase matching angle
Ω	angle between optic axis and Z-axis
n_X, n_Y, n_Z	refractive index values along X-, Y-, Z-axis
l_c	coherence length
$\mathrm{n_{eff}}$	effective refractive index

b	confocal parameter
η_c	SHG conversion efficiency in the near field approximation
l_a	walk-off distance
B_ρ	walk-off parameter
ρ	walk-off angle
P_{lost}	power lost in the resonator
P_{gen}	total power generated in the laser medium
α_l	sum of all resonator losses excluding conversion to second harmonic
$\eta_{SHG\,total}$	total SHG conversion efficiency

Chapter 5

L	effective length of the main fibre laser resonator
λ_L, ν_L	resonant wavelengths, frequencies of the the fibre laser resonator
$\Delta\lambda_L$, $\Delta\nu_L$	wavelength spacing, frequency spacing between the fibre resonator modes
$\Delta\Lambda$	spectrum-narrowing element bandwidth
N	number of transmission peaks within the spectrum-narrowing element bandwidth
L_{min}	minimal effective length of the cavity required for stable operation
d	round-trip path length of the enhancement resonator
θ_A, θ_B	angle of incidence on the concave mirror, on crystal (Brewster angle)
R_1,R_2,R_3,R_4	power reflectivity of the enhancement resonator mirrors
r_1,r_2,r_3,r_4	electric field reflectivity of the enhancement resonator mirrors
T_1,T_2,T_3,T_4	power transmittance of the enhancement resonator mirrors
t_1,t_2,t_3,t_4	electric field transmittance of the enhancement resonator mirrors
r_{HR}	electric field reflectivity of the HR concave mirror
R_c	radius of curvature of the concave mirror
L_c	length of the nonlinear crystal
n_ω^Z, n_ω^Y	refractive index at fundamental wavelength along Z, Y axis
$n_{2\omega}^Z$, $n_{2\omega}^Y$	refractive index at second harmonic wavelength along Z, Y axis
E_i, E_t	electric field amplitude incident on the input coupler, transmitted through the output coupler of the enhancement resonator

δ	round-trip phase shift
t_c	round-trip transmission function, excluding input/output coupler loss
α	round-trip loss excluding SHG conversion and mirrors' transmissions
η_{SHG}	single round-trip second harmonic conversion efficiency
P_i	power incident on the input coupler of the enhancement resonator
P_t	power transmitted through the enhancement resonator
P_c	intracavity circulating power near the output coupler surface
P_l	power lost in the enhancement cavity (excluding second harmonic output and input/output coupler transmissions)
P_r	power rejected by the enhancement cavity (via reflection from the input coupler)
$T(\delta)$	transmission function of the enhancement cavity (vs. phase shift)
T_{max}	maximum value of the transmission function
$\delta\lambda$	FWHM width of the peak of the transmission function
$\Delta\lambda$	FSR of the enhancement cavity
F	finesse of the enhancement cavity
ϕ	finesse coefficient of the enhancement cavity
λ_c, ν_c	resonant wavelengths, resonant frequencies of the enhancement cavity
$T_1^{i.m.}$, $R_1^{i.m.}$	power transmittance, reflectivity of impedance-matched input coupler
$P_c^{i.m.}$	power circulating in the impedance-matched enhancement cavity
α'	total round-trip loss excluding the input coupler transmission
Ω_ω, $\Omega_{2\omega}$	fundamental power enhancement, SHG efficiency enhancement factor
ϵ	proportionality constant of SHG efficiency vs. fundamental power
R_ω, $R_{2\omega}$	Fresnel reflection coefficient at fundamental, SH wavelength
d_m	distance between concave mirrors
w_0	resonator mode waist spot size between concave mirrors
δz_0	resonator mode waist position shift (with respect to the initial position half-distance between concave mirrors)
w_1	resonator mode waist spot size between plane mirrors
η_o	overlap integral
E_1, E_2	complex electric fields in a plane, referring to the field of the spatial mode of the main laser mode and the field of the enhancement resonator mode

θ_R	angle of refraction into the substrate of the concave mirror
n_M	index of refraction of the substrate of the concave mirror
x	distance from the centre of the concave mirror to the beam position
δd	maximal displacement distance between etalon mirrors
V_{AC}	driving voltage from the high-voltage supply
ΔV	driving voltage from the high-voltage supply (peak-to-peak value)
δV	driving voltage change corresponding to cavity length increment of one FSR
δt	time corresponding to cavity length increment of one FSR
λ_{HeNe}	wavelength of the He-Ne laser
v_m	velocity of the mirror on the piezoelectric transducer
f, f_c	driving voltage frequency, optical chopper modulation frequency
δd	maximal mirror displacement distance
$\delta\lambda_x$	spectral distance travelled by the transmission peak before the fibre laser completely changes the set of oscillating axial modes
δd_x	distance travelled by the mirror before the fibre laser completely changes the set of oscillating axial modes
δt_x	time needed to completely change the set of oscillating axial modes
t_{rt}	round-trip time of the main fibre laser cavity
$\mathrm{d_B}$	width of the chopper blade
$\Delta\mathrm{t}$	time it takes the chopper blade to fly through the laser beam
P_{peak}	output peak power
P_{CW}	output continuous-wave power
T	period of modulation induced by the optical chopper

Author's Declaration

I, **Rafal Cieslak**, declare that this thesis entitled "**Power Scaling of Novel Fibre Sources"** and the work presented in it are my own. I confirm that:

- this work was done wholly while in candidature for a research degree at the University of Southampton;

- where any part of this thesis has previously been submitted for a degree or any other qualification at this University or any other institution, this has been clearly stated;

- where I have consulted the published work of others, this is always clearly attributed;

- where I have quoted from the work of others, the source is always given. With the exception of such quotations, this thesis is entirely my own work;

- I have acknowledged all main sources of help;

- where the thesis is based on work done by myself jointly with others, I have made clear exactly what was done by others and what I have contributed myself;

- parts of this work have been published (see *List of publications* for details)

Signed:

Date: 24.09.2012

Acknowledgements

It would not have been possible to write this doctoral thesis without the guidance and support of all the kind people around me, to only some of whom it is possible to give particular mention here.

I wish to express my special words of gratitude to the following people: My supervisor, Professor Andy Clarskon for his contagious enthusiasm about lasers, encouragement and patience when nothing worked and I didn't understand why; My senior colleagues: Dr. Ji Won Kim, Dr. Jacob Mackenzie, Dr. Masaki Tokurakawa, Dr. Jessica Ng, Dr. Peter Shardlow and Dr. Pu Wang for their precious advice, and LBO crystal (from Korea); My junior colleagues: Dr. Jaclyn Chan, Dr. Kristian Thaller, Dr Lee Pearson, Mr. Jae Daniel, Mr. Jakub Szela, Mr. Matthew Eckold and Mr. Di Lin for making me feel more at home during my stay in the UK; Laser Quantum Ltd. for their LBO crystals (from England); EPSRC for funding this research project; My parents for always encouraging me to do interesting things in life; My younger sister for always supporting me; And above all, my beloved wife for always being beside me.

To my wife Anna and our daughter Pola, with love

Chapter 1
Introduction

1.1. Motivation

Lasers have contributed to humanity as powerful scientific tools for expanding human knowledge and in many real-life applications. Today, coherent light sources are used in a broad and still increasing range of products. Common application areas include high capacity telecommunication, medicine, manufacturing, construction, surveying, consumer electronics, scientific research and defence. Visionary applications for laser sources and developments in the application areas where lasers have been already adopted constantly ask for higher power and higher brightness. Aside from power and brightness requirements, specific applications place additional demands on the laser sources in terms of mode of operation, polarisation, beam pointing and power stability, beam quality, linewidth and operating wavelength. Some of these applications require both high optical power and well-defined laser output parameters (e.g. specific shape of optical spectrum with high temporal stability), which can be difficult to obtain. In some situations, amplified spontaneous emission (ASE) sources, rather than conventional laser oscillators, can be a better solution. Some applications require high power laser radiation at wavelengths not directly accessible by natural emission from laser materials. In this case, the wavelength of the laser radiation may be changed via nonlinear frequency conversion in an optically nonlinear medium positioned inside or outside of the laser resonator. Rare-earth (RE)-doped solid state lasers, particularly in fibre geometry, are very well suited for applications where high power, high brightness coherent radiation is required. However, it is often challenging to obtain high power laser output in spectral regions outside the natural emission bands of RE-doped fibres. Tailoring the shape of a broad spectrum emitted from a fibre-based ASE source to suit the needs of various applications can also be quite challenging. This body of work presents novel concepts for power scaling of frequency converted fibre lasers, as well as the design

and power scaling strategy for spectrum-controllable fibre-based ASE sources. This thesis will only consider sources operating in continuous-wave (CW) mode of operation and nonlinear frequency conversion schemes while the analysis will focus on second harmonic generation (SHG).

1.2. Research area

The theoretical foundations for lasers and masers, conceptually based upon probability coefficients for the absorption, spontaneous emission, and stimulated emission of electromagnetic radiation, were established by A. Einstein in 1917 [1.1], and detailed calculations on an "optical maser" were published in 1958 by A. L. Schawlow and C. H. Townes [1.2]. The first working laser source, a pulsed solid-state (ruby) laser, was demonstrated by T. H. Maiman in 1960 [1.3], while the first gas (Helium-Neon) laser [1.4], first laser diode [1.5], as well as the first fibre laser [1.6] were demonstrated within the next two years. A diode-pumped solid-state laser was demonstrated in 1964 [1.7], but it was not until 1980's when the laser diodes reached lifetimes and output powers allowing them to replace flash lamps commonly used as pumping sources for early solid-state lasers. The first fibre-based coherent light sources and amplifiers were based on single-clad fibres where pump and signal propagate in a doped core. However, the output power from single-mode diode laser pump sources restricted the fibre laser's output power to a fraction of a watt. The introduction of the double-clad fibre architecture [1.8] allowed pump light to be coupled into a much larger inner-cladding thus relaxing the requirement on the pump source beam quality. Further development of large double-clad fibres, combined with the rapid improvements in diode laser technology, resulted in dramatic progress in scaling output power from RE-doped fibre lasers and amplifiers by a factor of four orders-of -magnitude over the last twenty years (fig. 1.1). Fibre lasers emitting in the ~1 μm wavelength regime were originally based on neodymium (Nd)-doped fibres and reached several tens-of-watts single-mode output power in the late 1990's [1.12]. They were later replaced with ytterbium (Yb)-doped fibre lasers that proved to be more suitable for power scaling for a number of reasons (i.e. smaller quantum defect, wider emission bandwidth, longer upper-state lifetime, as well as a simple energy

level structure free from detrimental quenching processes). Indeed, it was possible to scale the output power from Yb-doped fibre lasers over two orders-of-magnitude in the last decade and currently these devices can yield more than 10 kW in a nearly diffraction-limited beam [1.21].

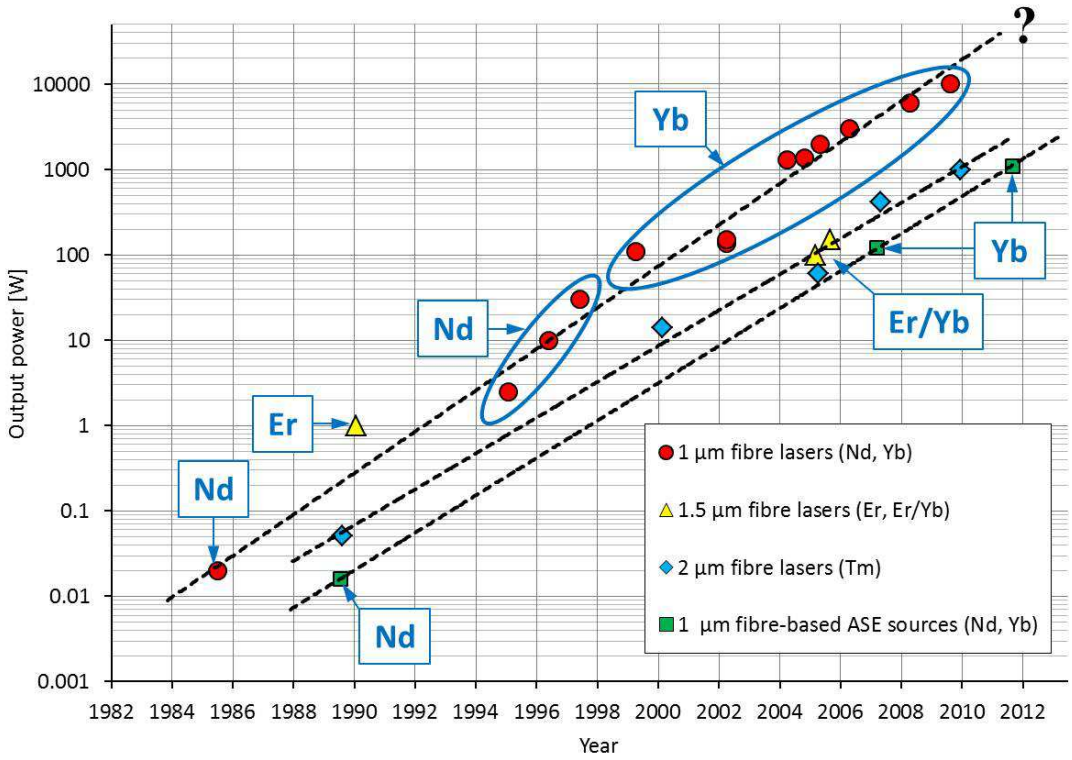

Figure 1.1: Evolution of the output power reached by fibre lasers [1.9-1.29] and fibre-based ASE sources [1.45-1.47] with nearly diffraction limited beam quality emitting in different spectral regions

Fibre lasers with output in the ~1.5 µm wavelength region were based on erbium (Er)-doped and later on Er/Yb-co-doped fibres were employed offering improved pump absorption characteristics. The output power from single-mode fibre lasers emitting in this spectral range increased from watt-level in early 1990's [1.22] to more than a hundred watts of single-mode [1.23, 1.24] and several hundred watts of multimode output [1.33]. However, when compared to Yb-doped fibre lasers emitting at ~1 µm, power scaling of the Er/Yb systems emitting ~1.5 µm is more challenging for a number of reasons, including larger quantum defect, imperfect energy transfer from Yb to Er ions and spurious Yb emission at ~1 µm in the Er/Yb-doped fibre core.

Fibre lasers emitting in the ~2 μm spectral region, based on thulium (Tm)-doped fibres typically yield output power of an order-of-magnitude lower than current Yb-doped fibre devices. Nevertheless, Tm-doped fibre lasers have been developed as rapidly increasing in terms of output power from several milliwatts in the late 1980's [1.25] to kilowatt-class lasers with a nearly diffraction limited beam [1.29]. Development of silica fibres doped with Bismuth (Bi) enabled access to 1.15-1.5 μm band complementing the spectral range available from RE-doped fibers. Although the output power from Bi-doped fibre lasers is still relatively low [1.36] the prospects for scaling to higher power levels, using in-band pumping schemes with Yb-doped fibre lasers, look very promising.

Power scaling work has been also done with fibre lasers at longer wavelengths including the mid-infrared (mid-IR) spectral region. These devices, typically using different laser transitions in holmium- (Ho-), dysprosium- (Dy-), and Er-doped fluoride glasses, can be tuned over relatively broad ranges to access wavelengths required for specific applications. Although RE-doped fibre lasers emitting in the in the 3-4 μm delivered only several milliwatts [1.34, 1.35], more recent experiments using novel glass compositions with improved transmission characteristics demonstrated watt-class Ho fibre lasers around ~3 μm [1.30], a ten-watt-class Er fibre laser at 2.78 μm [1.31] and more than hundred watts from a Ho-doped silica fibre laser emitting at 2.13 μm [1.32]. Output at shorter wavelengths in the visible and ultraviolet (UV) spectral region has been also demonstrated with fibre lasers. Laser emission in the red, green and blue-green regions was observed in praseodymium (Pr)-doped fibres. These devices delivered ~250 mW in the red band and several milliwatts in the blue-green region [1.37-38]. Output power of ~30 mW in the red spectral range was also obtained with samarium (Sm)-doped fibre laser [1.39]. Power scaling in these wavelength bands is particularly challenging due to the very limited power of available pump sources, such as semiconductor and solid-state lasers emitting in the UV and blue spectral regions, required for efficient pumping of Pr- and Sm-doped fibre lasers. One solution to this problem is to use pump sources emitting at longer wavelengths, tailored for multi-stage pumping of RE-doped fibre lasers. This approach allowed generating over a watt output in the red band [1.40], ~150 mW in the blue-green [1.41] and ~100 mW in the green spectral range [1.42] from Pr-doped fibre lasers. In the blue-green band emission was obtained in Ho-, Er-

and Tm-doped fibres with a maximum output power of ~375 mW [1.44]. Emission in the violet and UV spectral regions (with sub-milliwatt output power) was also demonstrated using Nd-doped fibres [1.43]. However, these upconversion fibre lasers are typically based on fluoride glass fibres such as the ZBLAN (ZrF_4-BaF_2-LaF_3-AlF_3-NaF) family and their output power is limited by thermal and optical damage effects occurring at relatively modest power in these fragile and low melting temperature materials.

Overall fibre lasers have experienced stable exponential growth in output power over the last three decades in ~1 μm [1.9-1.21] and ~2 μm [1.25-1.29] wavelength regimes, where the output power has increased by more than 2dB per year (fig. 1.1). Studies by various independent research groups suggest that scaling the output power from a single fibre cannot go on forever. At some point the maximum power that can be extracted from fibre laser will be fundamentally limited by optical damage, thermal and nonlinear effects. Nevertheless, every year still brings new fibre designs aiming to mitigate the nonlinear effects, and new materials with lower losses and higher damage thresholds are being developed. It is not clear when the upper limit on the power extractable from a single aperture will be reached, but we can certainly expect continuous increase in brightness of the fibre lasers over the years to come.

Although fibre-based lasers and amplifiers deliver output with impressive power and brightness in the near-IR spectral band, increase in available output power has not been so dramatic in other wavelength regimes. The output power from fibre lasers emitting in the visible spectral region is currently limited to a fraction of a watt, and further power scaling of these architectures looks very challenging. On the other hand, impressive power levels available in the near IR wavelength regime offer the prospect of much higher powers in visible band via nonlinear frequency conversion. Efficient frequency doubling by second harmonic generation (SHG) in “bulk” solid-state lasers has its limitations and in fibre lasers it is not particularly easy. These issues will be discussed in more detail in next chapters of this thesis. Nevertheless, the highest power available from a laser source with decent beam quality was obtained from a fibre laser using an external resonant enhancement cavity scheme for efficient frequency doubling [1.51]. Although very efficient and capable of delivering multi-hundred watts visible output, this approach involves complex cavity

stabilisation systems and has certain limitations on fundamental power level. This thesis will discuss the challenges of power scaling of the current technology and propose an alternative scheme for efficient frequency doubling of high power fibre lasers. The proposed scheme will potentially alleviate the limitations of external resonant SHG while maintaining its exceptional efficiency and offering the potential of scaling to much higher power levels in the visible spectral range.

ASE sources (sometimes called superluminescent or, erroneously, superfluorescent sources) belong to another group of coherent light sources, similar to lasers, but typically not utilising an optical resonator. In many cases some form of a resonator helps to build up the ASE signal and an ASE source can become a laser when the population inversion and thus round-trip gain are sufficiently large to reach the lasing threshold. The first fibre-based ASE sources were demonstrated in late 1980's and like their laser counterparts were based on Nd-doped fibres. These sources delivered only several milliwatts of optical output in their early days [1.45], but their output power increased greatly over the years following the development of high power fibre laser technology. Advanced techniques for fibre end termination aiming to lower the feedback combined with multi-stage amplification allowed scaling output power from Yb-doped fibre-based ASE sources to over the 100 W level in 2007 [1.46]. More recent papers report development of kilowatt-class narrowband, fibre-based ASE sources [1.47] emitting in the ~1 µm spectral range. Development of ASE sources emitting in the ~1.5 µm has been mainly driven by applications in the relatively low-power optical communication market, therefore progress in power scaling was somewhat slower. Nevertheless, several watt-class ASE source in this spectral region were demonstrated in 2008 [1.48] and recent work resulted in a source generating ~16 W of broadband output at 1.55 µm [1.49]. In the ~2 µm spectral region, output powers as high as ~11 W have been demonstrated with Tm-doped fibre-based ASE sources [1.50]. High power fibre-based ASE sources remain relatively underexplored when compared to high power fibre lasers. So far only spectrally narrow ASE signals were successfully amplified to very high power levels. Little is known about properties of high power broadband sources with different spectral characteristics. Part of this thesis will discuss the design strategy and development of a versatile, fibre-based ASE source that can be used either independently or incorporated as a seed source in a high power amplifier chain.

1.3. Thesis structure

This PhD thesis entitled “Power Scaling of Novel Fibre Sources” concentrates on two main themes and, as such, has been divided into two sections: *Part I: Spectrum-controllable fibre-based ASE sources,* discusses design and power-scaling strategies for ASE sources based on diode-pumped fibre architectures and forms the second and third chapter of this thesis. *Part II: Efficient intracavity frequency doubling schemes for CW fibre lasers,* discusses a novel concept for efficient nonlinear frequency doubling in high-power CW fibre lasers and forms the third, fourth, and fifth chapter of this thesis.

Chapter 1 briefly introduces the motivation for this work and reviews the most important results in the area of scaling the output power from fibre-based lasers and ASE sources. It describes the rapid technological developments leading to dramatic increase in maximum output power obtained from fibre-based sources emitting in the ~1, ~1.5 and ~2 µm spectral regions over the last 30 years. We discuss progress in power scaling of mid-IR fibre lasers presenting recent results in the 2-4 µm spectral range. Conventional and upconversion fibre lasers emitting in the visible and UV wavelength regions are reviewed. Finally, we present the progress in scaling the output power from fibre-based ASE sources emitting in the ~1, ~1.5 and ~2 µm spectral regions. Finally we discuss the thesis structure.

In chapter 2 we introduce the background information on fibre-based ASE sources. It begins with an extended motivation for carrying research in this area, reviews the prior art not only in terms of scaling the output power but also with respect to specific applications and various approaches to control the spectral characteristics of fibre-based ASE sources. This introduction is followed by brief discussion on the spectroscopic properties of Yb and fibre geometries used in the experiments. Finally, this chapter introduces a semi-analytical theoretical model that is later applied to various ASE source configurations presented and discussed in the next chapter.

All experimental work relating to spectrum-controllable ASE sources is presented in chapter 3. Various types of ASE sources with increasing complexity illustrating the

development of the final, most versatile configuration were examined. The semi-analytical model was extended to allow modelling the performance of the laser in terms of output power, polarisation extinction ratio or controllable signal-to-background noise ratio. Experimental results are presented, discussed and used to verify the applicability of the theoretical model for all ASE source configurations.

Chapter 4 provides background information on the strategy and challenges of power scaling in solid-state lasers with particular emphasis on the fibre laser geometry. The second part of this chapter focuses on nonlinear frequency doubling of solid-state lasers. Chapter 4 begins with an introduction of laser performance metrics. The following sections discuss the impact of pump beam parameters, sources of heat generation in the active medium and thermal effects affecting the laser's performance. Most popular laser geometries aiming to mitigate thermal effects in the laser medium are reviewed in the next section. The fibre laser geometry is studied in more detail; firstly, core- and cladding-pumping schemes are demonstrated. Physical mechanisms ultimately limiting the output power extractable from a fibre laser are reviewed. The first part of chapter 4 is concluded with a discussion on the general power scaling strategy for future fibre laser systems. The second part of this chapter begins with a general overview of nonlinear effects and basic theory on second harmonic generation. Different phase matching techniques for SHG are reviewed, followed by a brief discussion on the effects of tight beam focusing. The next section presents the important parameters of nonlinear crystals and introduces the lithium borate material used in the experiments described in following chapters of this thesis. In the next section, chapter 4 discusses the most popular approach to generating visible laser radiation via intracavity SHG in solid-state lasers and fundamental limitations of this technique. Finally, the most common approaches to frequency doubling of high power fibre lasers, including external resonantly-enhanced SHG, are presented and evaluated.

Chapter 5 introduces a novel concept for efficient frequency doubling of high power fibre lasers. A theoretical model of a resonant enhancement cavity with two partially transmitting mirrors is constructed. Following sections discuss the impact of the enhancement cavity design, mode-matching and level of optical feedback on the output power and SHG conversion efficiency. The next section presents experimental

results on temporal characteristics on the fibre laser with the resonant enhancement cavity integrated within the main resonator. Finally, the concept of using modal interference to aid efficient coupling of the output beam from a multimode fibre to the fundamental mode of the free-space enhancement resonator is proposed and experimentally verified.

All experimental work related to the novel concept of efficient SHG in a high power fibre laser is presented in chapter 6 of this thesis. After a short introduction design considerations for two different phase matching configurations are discussed. The next section presents preliminary results obtained with a travelling-wave resonator, followed by three sections focusing on three optimised standing-wave resonator configurations. Alignment procedures and performance characteristics of the three laser configurations are discussed in detail.

Finally, Chapter 7 concludes the thesis by summarising the main achievements of the work. It also offers suggestions for future research directions and a few potential solutions to the problems identified in the previous chapters of this thesis.

References

[1.1] A. Einstein, “Zur Quantentheorie der Strahlung”, Physikalische Zeitschrift, vol. 18, pp. 121-128, 1917. English translation: “On the Quantum Theory of Radiation”, by D. ter Haar, The Old Quantum Theory, Pergamon Press, New York, 1967

[1.2] A. L. Schawlow and C. H. Townes, “Infrared and optical masers”, Phys. Rev. 112, vol. 6, pp. 1940-1939, 1958

[1.3] T. H. Maiman, “Stimulated optical radiation in ruby”, Nature, vol. 187, p. 493, 1960

[1.4] A. Javan, W. R. Bennett Jr. and D. R. Herriott, “Population inversion and continuous optical maser oscillation in a gas discharge containing a He–Ne mixture”, Phys. Rev. Lett., vol. 6, no. 3, p. 106, 1961

[1.5] R. N. Hall, G. E. Fenner, J. D. Kingsley, T. J. Soltys, and R. O. Carlson, “Coherent light emission from GaAs junctions”, Phys. Rev. Lett., vol. 9, no. 9, p. 366, 1962

[1.6] E. Snitzer, “Optical Maser Action of Nd+3 in a Barium Crown Glass”, Phys. Rev. Lett., vol. 7, no. 13, 1961

[1.7] R. J. Keyes, R. J., “Injection luminescent pumping of CaF2:U3+ with GaAs diode lasers”, Appl. Phys. Lett., Vol. 4, No. 3, pp. 50–52, 1964

[1.8] E. Snitzer, H. Po, F. Hakimi, R. Tumminelli and B.C. McCollum, "Double clad, offset core Nd fibre laser", in Optical Fibre Sensors, page PD5, Optical Society of America, 1988

[1.9] L. Reekie, S. B. Poole and D. N. Payne, “Neodymium-doped silica single-mode fibre lasers”, Electron. Lett., vol. 21, no. 17, pp. 738-740, 1985

[1.10] H. Zellmer, U. Willamowski, A. Tunnermann, H. Welling, S. Unger, V. Reichel, H.-R. Muller, J. Kirchhof and P. Albers, “High-power cw neodymium-doped fibre laser operating at 9.2 W with high beam quality”, Opt. Lett., vol. 20, no. 6, pp. 578-580, 1995

[1.11] A. Tünnermann, “High-power Nd double-clad fibre lasers”, at Conference on Lasers and Electro-Optics, 2-7 June 1996

[1.12] H. Zellmer, A. Tünnermann, H. Welling and V. Reichel, “Double-Clad Fibre Laser with 30 W Output Power”, at Optical Amplifiers and Their Applications, Victoria, B. C., Canada, 21 July 1997

[1.13] V. Dominic, S. MacCormack, R. Waarts, S. Sanders, S. Bicknese, R. Dohle, E. Wolak, P.S. Yeh and E. Zucker, “110 W fibre laser”, at Conference on Lasers and Electro-Optics, 23-28 May 1999, paper CPD11–1

[1.14] N.S. Platonov, D. V Gapontsev, V.P. Gapontsev and V. Shumilin, “135W CW fibre laser with perfect single mode output”, at Conference on Lasers and Electro-Optics, 19-24 May 2002, paper CPDC3–1

[1.15] J. Limpert, A. Liem, S. Hoffer, H. Zellmer, A. Tünnermann, S. Unger, S. Jetschke and H. R. Müller, “150W Nd/Yb co-doped fibre laser at 1.1µm”, at Conference on Lasers and Electro-Optics, 19-24 May 2002, paper CThx1

[1.16] A. Liem, T. Limpert, H. Zellmer, A. Tunnermann, V. Reichel, K. Morl, S. Jetschke, S. Unger, H.P. Muller, J. Kirchhof, T. Sandrock and A. Harschak, “1.3 kW Yb-doped fibre laser with excellent beam quality", at Conference on Lasers and Electro-Optics, San Francisco, California, 16 May 2004, paper CPDD2

[1.17] Y. Jeong, J. Sahu, D. Payne and J. Nilsson, “Ytterbium-doped large-core fibre laser with 1.36 kW continuous-wave output power”, Opt. Express, vol. 12, no. 25, pp. 6088–6092, 2004

[1.18] V. Gapontsev, D. Gapontsev, N. Platonov, O. Shkurikhin, V. Fomin, A. Mashkin, M. Abramov and S. Ferin, “2 kW CW ytterbium fibre laser with record diffraction-limited brightness”, Conference on Lasers and Electro-Optics Europe, 12-17 June 2005, paper CJ1-1-THU

[1.19] F. Fomin, A. Mashkin, M. Abramov, A. Ferin, and V. Gapontsev, “3 kW Yb fibre lasers with a single mode output”, at International Symposium on High-Power Fibre Lasers and their Applications, St. Petersburg, June 2006, paper HPFL-3

[1.20] D. Gapontsev, “6kW CW Single mode Ytterbium fibre laser in all-fibre format”, 21st Annual Solid State and Diode Laser Technology review, 2-5 June 2008

[1.21] E. Stiles, “New developments in IPG fiber laser technology”, in Proceedings of the 5th International Workshop on Fibre Lasers, 30 September - 1 October, 2009

[1.22] V. P. Gapontsev and L. E. Samartsev, “High-Power Fibre Laser”, Advanced Solid State Lasers, Salt Lake City, Utah, 5 march 1990

[1.23] A.Yusim, J.Barsalou, D.Gapontsev, N.Platonov, O.Shkurikhin, V.Gapontsev, Y.Barannikov and F.Shcherbina, “100 Watt single-mode CW linearly polarized all-fibre format 1.56-µm laser with suppression of parasitic lasing effect”, Proc. of SPIE, vol. 5709, pp.69-77, 2005

[1.24] Y. Jeong, J. K. Sahu, D. B. Soh, C. A. Codemard and J. Nilsson, “High-power tunable single-frequency single-mode erbium:ytterbium codoped large-core fibre master-oscillator power amplifier source”, Opt Lett., vol. 30, no. 22, pp. 2997-2999, 2005

[1.25] D. C. Hanna, M. J. McCarthy, I. R. Perry and P. J. Suni, "Efficient high-power continuous-wave operation of monomode Tm-doped fibre laser at 2um pumped by Nd:YAG laser at 1.064um", Electron. letters, vol. 25 no. 20, 1989

[1.26] A. Hayward, W.A. Clarkson, P.W. Turner, J. Nilsson, A.B. Grudinin, and D.C. Hanna, "Efficient cladding-pumped Tm-doped silica fibre laser with high power singlemode output at 2µm", Electron. Lett., vol. 36, no. 8, pp. 711–712, 2000

[1.27] Y. A. Barannikov, F. V. Shcherbina, V. P. Gapontsev, M. Meleshkevich and N. S. Platonov, "Linear-polarization, CW generation of 60 W power in a

single-mode, Tm fibre laser", at Conference on Lasers and Electro-Optics, 2005

[1.28] M. Meleshkevich, N. Platonov, D. Gapontsev, A. Drozhzhin, V. Sergeev and V. Gapontsev, "415W Single-Mode CW Thulium Fibre Laser in all-fibre format", at Conference on Lasers and Electro-Optics, 2007

[1.29] Thomas Ehrenreich, Ryan Leveille, Imtiaz Majid, Kanishka Tankala, Glen Rines and Peter Moulton, "1-kW, All-Glass Tm:fibre Laser", SPIE Photonics West, 28 January 2010

[1.30] J. Li, D. D. Hudson and S. D. Jackson, "High-power diode-pumped fibre laser operating at 3 μm", Opt. Lett., vol. 36, no. 18., pp. 3642–3644, 2011

[1.31] X. Zhu and R. Jain, “10-W-level diode-pumped compact 2.78 μm ZBLAN fibre laser,” Opt. Lett., vol. 32, no. 1, pp. 26–28, 2007

[1.32] Alexander Hemming, Shayne Bennetts, Nikita Simakov, John Haub and Adrian Carter, "Development of resonantly cladding-pumped holmium-doped fibre lasers", Proc. of SPIE, vol. 8237, pp. 82371J-1-8, 2012

[1.33] Y. Jeong, S. Yoo, C. A. Codemard, J. Nilsson, J. K. Sahu, D. N. Payne, R. Horley, P. W. Turner, L. M. B. Hickey, A. Harker, M. Lovelady and A. Piper, “Erbium:ytterbium codoped large-core fibre laser with 297 W continuous-wave output power”, IEEE J. Sel. Top. Quant. Electron. vol. 13, pp. 573–579, 2007

[1.34] J. Schneider, C. Carbonnier and U.B. Unrau, “Characterization of a Ho3+-doped fluoride fibre laser with a 3.9 μm emission wavelength”, Appl. Opt., vol. 36, pp. 8595–8600, 1997

[1.35] C. Carbonnier, H. Többen and U. B. Unrau, “Room temperature CW fibre laser at 3.22 μm”, Electron. Lett., vol. 34, no. 9, pp. 893–894, 1998

[1.36] M. Dianov, “Bi-doped glass optical fibres: Is it a new breakthrough in laser materials?”, J. Non-Cryst. Solids, vol. 355, pp. 1861–1864, 2009

[1.37] J. Y. Allain, M. Monerie and H. Poignant, “Tunable CW lasing around 610, 635, 695, 715, 885 and 910 nm in praseodymium-doped fluorozirconate fibre”, Electron. Lett., vol. 27, no. 2., pp. 189-191, 1991

[1.38] R. G. Smart, J. N. Carter, A. C. Tropper, D. C.Hanna, S. T. Davey, S. F. Carter and D.Szebesta, “CW Room temperature operation of praseodymium-doped fluorozirconate glass fibre lasers in the blue-green, green and red spectral regions”, Opt. Commun., vol. 86, no. 3-4, pp. 333-340, 1991

[1.39] M. C. Farries, P. R. Morkel and J. E. Townsend, “Samarium(3+)-doped glass laser operating at 651 nm”, Electron. Lett., vol. 24, pp. 709-711, 1988

[1.40] T. Sandrock, H. Scheife, E. Heumann and G. Huber, „High-power continuous-wave upconversion fiber laser at room temperature” Opt. Lett., vol. 22, pp. 808–810, 1997

[1.41] H.Zellmer, P. Riedel and A.Tünnermann, “Visible upconversion lasers in praseodymium-ytterbium-doped fibers”, Appl. Phys. B, vol. 69, pp. 417–421, 1999

[1.42] H. Zellmer, K. Plamann, G. Huber, H. Scheife, and A. Tunnermann, „Visible double-clad upconversion fibre laser”, Electron. Lett., vol. 34, pp. 565–567, 1998

[1.43] D. S. Funk, J. G. Eden, “Glass fiber lasers in the ultraviolet and visible”, IEEE J. Select. Top. Quant. Electron., vol. 1, pp. 784–791, 1995

[1.44] W. H. Loh, B. N. Samson, Z. E. Harutjunian and R. I. Laming, “Intracavity pumping for increased output power from a distributed feedback erbium fibre laser”, Electron. Lett., vol. 32, p. 1204, 1996

[1. 45] M. J. F. Digonnet and K. Liu, “Analysis of a 1060-nm Nd:SiO2 superfluorescent fiber laser”, J. Lightwave Technol, vol. 7, pp. 1009–1015, 1989

[1.46] P. Wang, J. K. Sahu, W. A. Clarkson, “Power Scaling of Ytterbium-doped Fiber Superfluorescent Sources”, IEEE J. Sel. Top. Quant., vol. 13, pp. 580-587, 2007

[1.47] Oliver Schmidt, Andrea Kliner, Miroslaw Rekas, Christian Wirth, Stephan Rhein, Thomas Schreiber, Ramona Eberhardt, and Andreas Tuennermann, “Relative intensity noise characterization of a linear polarized 1.1 kW fiber-amplified narrow-band ASE source”, at Frontiers in Optics, San Jose, California, October 16, 2011, paper FTuW

[1.48] S. P. Chen, Z.-J. Liu, Y. G. Li, K. C. Lu and S. H. Zhou, “Resonantly pumped high power flat L-band erbium doped superfluorescent fiber source”, Opt. Express, vol. 16, no. 1, 2008

[1.49] Wenting Chen, Deyuan Shen, Ting Zhao and Xiaofang Yang, “High power Er,Yb-doped superfluorescent fiber source with over 16 W output near 1.55 μm”, Opt. express, vol. 20, no. 13, 2012

[1.50] Broadband Tm-doped superfluorescent fiber source with 11 W single-ended output power”, Opt. Express, vol.16, no.15, pp.11021-11026, 2008

[1.51] Y. Grapov, V. Gapontsev and A. Avdokhin, “New generation of high power green fiber laser”, 6th International Symposium on High-Power Fiber Lasers and Their Applications”, St. Petersburg, Russia, 26-28 Junes 2012

Chapter 2
Fibre-based ASE sources

2.1. Introduction

This chapter introduces background information on fibre-based ASE sources with particular emphasis on power scaling. Section 2.2 explains the motivation for this research subject, and section 2.3 reviews the prior art in the topic area. Next sections describe the gain medium used in the experiments, including information on ytterbium spectroscopy (section 2.4) and fibre architectures used in the project (section 2.5). A theoretical model, developed for ASE sources is expounded in section 2.6. The chapter ends with a conclusions section (2.7).

2.2. The motivation

Fibre based light sources have seen a dramatic evolution over recent years. Improvements in high power and high brightness diode pump sources, combined with double-clad fibre architectures have resulted in dramatic progress in scaling output power from RE-doped fibre lasers and amplifiers. Ytterbium (Yb)-doped fibre lasers currently yield more than 10 kW of output power in 1 μm wavelength regime [2.1], while erbium-ytterbium (Er-Yb) and thulium (Tm)-doped fibre oscillators deliver more than 100 W at ~1.5 μm [2.2] and more than 1kW in ~2.0 μm regime [2.3] respectively. Fibre sources are heavily researched due to their many advantages, such as superior output beam quality and thermal handling compared to conventional crystal-based laser systems. Additionally, high gain values are easily achievable in fibres, thanks to the high inversion density obtainable in the doped core and the flexibility of selecting relatively long lengths of the gain medium. Fibre based ASE sources, in particular, deliver uniquely good temporal stability, and smooth intensity profile compared to their laser counterparts. They are also

distinguished by their broadband spectrum, making fibre ASE sources particularly interesting for various applications. One approach for power scaling of an ASE source is to use a low power seed source and a chain of power amplifiers, with the seed ASE source employing sophisticated methods of spectrum tailoring by the use of Micro Electro-Mechanical Systems (MEMS) within its external feedback arrangement. This architecture was chosen because it would be easier to first tailor spectral and temporal characteristics of a seed source then scale the output power to higher levels [2.4, 2.5, 2.6]. Our initial step was to investigate various seed source configurations to develop an understanding of the basic physics behind ASE sources. These experiments will be designed for Yb-doped fibre systems operating in the ~1.0 μm wavelength regime. However, it is hoped that these architectures will be easily transferable to Er-Yb- and Tm-doped fibres to access the ~1.5 and ~2.0 μm wavelength regions. The use of multiple amplification stages can be later used to scale output powers above the 100 W level, both in continuous-wave (CW) and pulsed modes of operation. ASE sources with such brightness and versatility would enable access to new, promising applications such as precision material processing, metrology or gas sensing.

2.3. Background work

Historically, amplified spontaneous emission (ASE) was considered an undesirable process in high-gain laser systems. It was found, however, by harnessing ASE, significant, stable output power in a broad wavelength spectrum could be extracted from a gain medium without the need for a cavity. Thus, ASE-based sources (known in those early days as “superradiant lasers” or “mirrorless lasers” [2.7, 2.8, 2.9]) became established as an attractive and viable light source.

Fibre-based ASE sources, benefiting from high gain values easily achievable in rare-earth doped cores, have found use in a wide range of applications such as medical imaging [2.10], sensing [2.11], low coherence interferometry [2.12] and optical communication [2.13]. However, power scaling of these devices remains a relatively unexplored area. Erbium-doped fibre ASE sources used in telecommunication

systems yield relatively low output power levels of ~16 W [2.14]. Higher output powers of ~30 W have been reported in a solid state amplifier configuration based on a Nd-doped laser crystal [2.15]. The highest ASE power levels in single-ended operation have been obtained with ytterbium-doped fibres: 62 W of output power by using a twisted end termination from a single stage ASE source, 122 W of output power from a two-stage (seed and amplifier) ASE source [2.16] and ~1 kW from a complex narrowband ASE source (complex seed source and multiple amplification stages [2.17]). In terms of spectrum shaping, sophisticated methods including Micro Electro-Mechanical Systems (MEMS) have been applied successfully to modify the output from ASE sources [2.18, 2.19]. The concept of implementing a spectrum shaping element in an external feedback arrangement has been presented for both narrowband [2.20] and broadband feedback [2.21], but in spite of its potential this has seen little development.

2.4. Yb spectroscopy

Ytterbium is a rare earth element (lanthanide) with the electronic structure $(Xe)4f^{14}5d^{0}6s^{2}$. When introduced into a host material such as silica glass, Yb atoms (dopant delivered in the form of Yb_2O_3) become triply ionized (3+). The performance of Yb^{3+} in silica fibres was first investigated by H. Pask, et. al. [2.22].

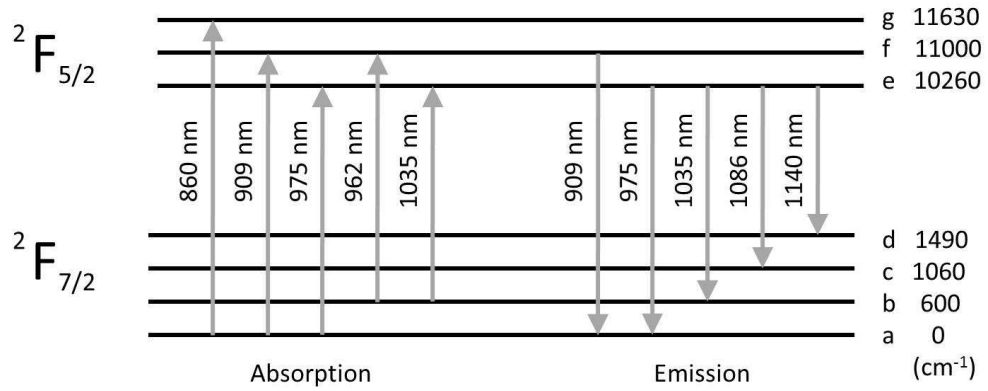

Figure 2.1: The Yb^{3+} energy level structure with indicated absorption and emission transitions [2.22]

The Yb^{3+} energy level structure (fig. 2.1) is relatively simple compared to other rare-earth ions. Only two manifolds (separated by spin-orbital interactions) are relevant for optical wavelengths: the $^2F_{7/2}$ ground state and $^2F_{5/2}$ excited state. These manifolds split into Stark sublevels (a-d) and (e-g) respectively via crystal field (Stark) interaction, but the transitions between sublevels are not fully resolved for Yb-doped silica fibres at room temperature, due to strong homogeneous and some inhomogeneous broadening [2.22]. It has been found [2.23, 2.24] that the bandwidth and peak wavelengths of the absorption and emission spectra vary with the host glass composition. The fluorescence decay time also varies with the host material and ranges between 0.8-1.5 ms [2.23]. Variations in host glass composition are usually the result of additional dopants used to increase the Yb_2O_3 solubility in silica and the refractive index of the core relative to the inner cladding. Typical cross-sections for an Yb-doped germanosilicate glass [2.22] are presented in fig. 2.2.

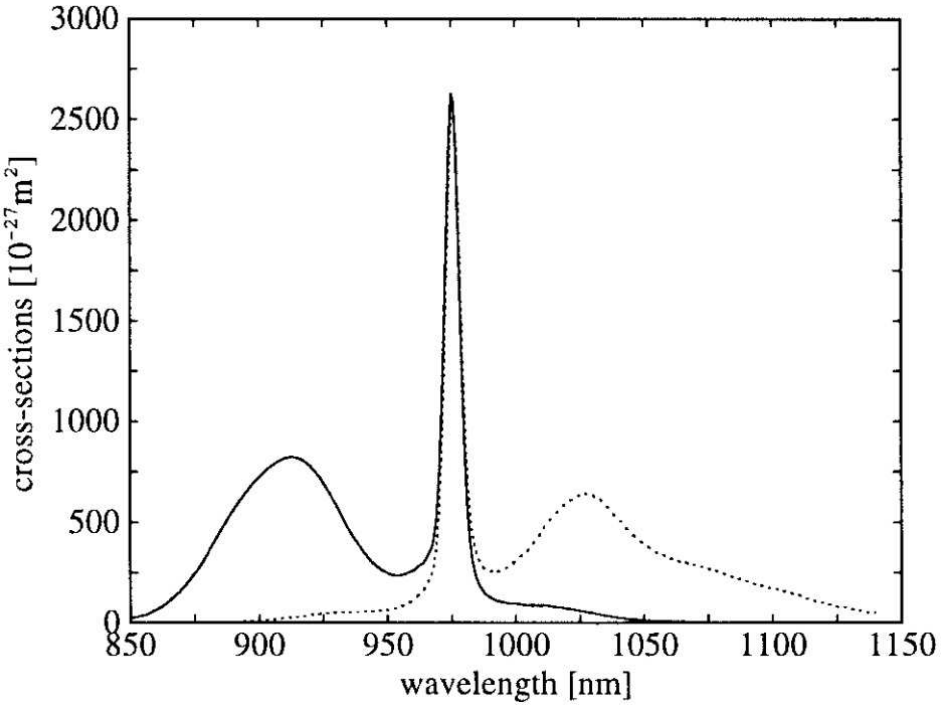

Figure 2.2: Yb-doped fibre absorption (solid) and emission (dotted line) cross-sections [2.22]

2.5. Fibre architectures

As the experiments are oriented towards the high-power operation regime, we chose to cladding-pump our ASE seed source. This relaxes the requirements on the pump beam quality and alignment, and allows the use of a high power, low-brightness diode bar with maximum output power of 40 W at 975 nm as a pump source. A typical design of a double-clad fibre for cladding pumping consists of a circular RE-doped core, which is the primary waveguide for light emitted by the active ions. This region is surrounded by a pure silica inner cladding with a much larger area and lower refractive index relative to the core, which forms a multimode waveguide for a high-power multimode pump beam. The inner cladding is typically surrounded by a polymer outer cladding with a lower refractive index value. A circular inner cladding geometry is not optimal for efficient pump light absorption inside the doped region of the core, due to possible helical ray trajectories that do not overlap with the core. Various inner cladding shapes and core offsets can improve pump absorption significantly by breaking the cladding-core symmetry [2.26, 2.27]. Two inner cladding geometries were used in this experimental work: D-shaped and polarisation maintaining (PM) “Panda” (both shown in fig. 2.3). The inner cladding of the “Panda” fibre incorporates two circular stress rods which both induce stress birefringence in the fibre and break the core-cladding symmetry by virtue of their lower refractive index than pure silica.

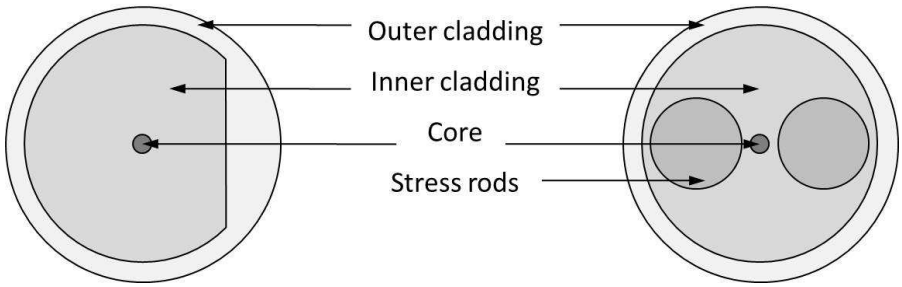

Figure 2.3: D-shaped and PM “Panda” double-clad fibre cross-sections

2.6. Theoretical model of ASE sources

N_1 and N_2 (the population densities for the lower $^2F_{7/2}$ and upper $^2F_{5/2}$ manifolds in Yb system respectively) under steady-state conditions are determined by the following rate equations [2.23]:

$$\frac{dN_2}{dt} = (R_{12} + W_{12})N_1 - (R_{21} + W_{21} + A_{21})N_2 = 0 \tag{2.1}$$

$$\frac{dN_1}{dt} = -(R_{12} + W_{12})N_1 + (R_{21} + W_{21} + A_{21})N_2 = 0 \tag{2.2}$$

where the transition rates (i.e. pump absorption rate R_{12}, stimulated emission rate at pump wavelength R_{21}, signal reabsorption rate W_{12}, stimulated emission rate at signal wavelength W_{21}, and spontaneous emission rate A_{21}) are given by:

$$R_{12} = \eta_q \frac{\sigma_a(\lambda_p)I_p}{h\nu_p},\ R_{21} = \eta_q \frac{\sigma_e(\lambda_p)I_p}{h\nu_p},\ W_{12} = \frac{\sigma_a(\lambda_s)I_s}{h\nu_s},\ W_{21} = \frac{\sigma_e(\lambda_s)I_s}{h\nu_s},\ A_{21} = \frac{1}{\tau_f}$$

η_q is the pumping quantum efficiency, $\lambda_s = c/\nu_s$ and $\lambda_p = c/\nu_p$ are signal and pump wavelengths respectively (c is velocity of light in vacuum, ν_s and ν_p are signal and pump frequencies respectively), σ_a and σ_e are the absorption and emission cross-sections for lower and upper level respectively, h is the Planck constant and τ_f is the upper level lifetime.

$N = N_1 + N_2$ is the total rare-earth ion concentration, therefore:

$$N_2 = \frac{N(R_{12} + W_{12})}{R_{12} + R_{21} + W_{12} + W_{21} + A_{21}} \tag{2.3}$$

The pump power P_p depletion and the signal power (P_s^+ - co-propagating with the pump, P_s^- - counter-propagating with respect to the pump) growth along a double-clad fibre (in z direction) can be expressed as:

$$\frac{dP_p}{dz} = \frac{A_{core}}{A_{clad}}\left[\sigma_e(\lambda_p)N_2 - \sigma_a(\lambda_p)N_1\right]P_p \tag{2.4}$$

$$\frac{dP_s^+}{dz} = [\sigma_e(\lambda_s)N_2 - \sigma_a(\lambda_s)N_1]P_s^+ \tag{2.5}$$

$$\frac{dP_s^-}{dz} = [\sigma_e(\lambda_s)N_2 - \sigma_a(\lambda_s)N_1]P_s^- \tag{2.6}$$

where A_{core} and A_{clad} are the core and inner-cladding areas respectively.

In general, equations (2.4-2.6) have to be solved numerically to calculate fibre gain and signal output power. However, by making simplifying assumptions, the small signal gain and pump power depletion rate can be obtained [2.22]:

If we consider negligible ASE and no signal power, then by substituting (2.3) into (2.4):

$$\frac{dP_p}{dz} = -\frac{A_{core}h\nu_p N_2(z)}{\eta_q \tau_f} \tag{2.7}$$

By extracting $N_2(z)$ from (2.7) and substituting into (2.4):

$$\ln\left[\frac{P_p(z)}{P_p(0)}\right] + \frac{P_p(z) - P_p(0)}{P_{psat}} = -\frac{A_{core}}{A_{clad}}\sigma_a(\lambda_p)Nz \tag{2.8}$$

where

$$P_{psat} = \frac{A_{clad}h\nu_p}{\eta_q\tau_f\left[\sigma_a(\lambda_p) + \sigma_e(\lambda_p)\right]}$$

is the pump saturation power.

For low pumping powers, i.e. $P_p(0) \ll P_{psat}$ (2.8) can be solved analytically to give:

$$P_p(z) = P_p(0)\exp(-\alpha_p z) \tag{2.9}$$

where

$$\alpha_p = \frac{A_{core}}{A_{clad}} \sigma_a(\lambda_p) N$$

is the pump absorption coefficient.

The single-pass gain for the fibre of length *l* is given by the following expression:

$$G = exp\left[\int_0^l g(z)dz - \alpha_s l\right] \tag{2.10}$$

where

$$g(z) = \sigma_e(\lambda_s)N_2(z) - \sigma_a(\lambda_s)N_1(z)$$

and α_s is the signal attenuation coefficient.

Extracting $N_2(z)$ from (2.7) and substituting into (2.10) produces a simplified expression for the small signal gain:

$$G = exp\left(\frac{\eta_q \tau_f [\sigma_a(\lambda_s) + \sigma_e(\lambda_s)] P_{abs}}{A_{core} h\nu_p} - \sigma_a(\lambda_s) N l - \alpha_s l\right) \tag{2.11}$$

where P_{abs} is the absorbed pump power.

The outlined treatment so far has neglected the amplified spontaneous emission process. Every excited ion can spontaneously relax from the upper state to the ground state by emitting a photon, which is uncorrelated to any other photon present in the medium. This noise power can be amplified as it travels along the fibre via stimulated emission of more photons within the same electromagnetic field mode. This process can eventually result in significant ASE power at the fibre output.

To compute the output ASE power, the spontaneous emission power at a given point in the fibre has to be calculated. The total noise power in bandwidth $\Delta\nu$ is defined as the noise power of one photon per mode of the electromagnetic field multiplied by

number of modes in bandwidth $\Delta\nu$ (including both orthogonal polarizations) [2.28]. The noise power at a given point in a single transverse mode fibre (in a given direction) is therefore:

$$P_{ASE}^{0} = 2h\nu\Delta\nu \approx 2hc^{3}\Delta\lambda/\lambda^{2} \tag{2.12}$$

Expression (2.12) that will be used in our model can be derived from simple considerations on the noise power of a single photon in a given mode and the number of modes present in the optical bandwidth in one dimension [2.28]. More accurate expression for the equivalent noise power, however, should take into account the waveguiding effect and geometry of the fibre so that the noise power is proportional to the solid angle in which light can be captured and guided by the fibre core [2.29, 2.30].

The total ASE power at a certain point *z* in the fibre is given by the sum of the ASE power in previous section and local noise power given by (2.12). The expression for ASE power growth in a given direction is thus similar to the equation for signal amplification (2.5-2.6), except for the addition of an extra factor describing the stimulated emission of photons by the local noise power which is proportional to the product $\sigma_e(\nu)N_2(z)$ [2.29]:

$$\frac{dP_{ASE}^{+}(\nu)}{dz} = [\sigma_e(\nu)N_2(z) - \sigma_a(\nu)N_1(z)]P_{ASE}^{+} + P_{ASE}^{0}(\nu)\sigma_e(\nu)N_2(z) \tag{2.13}$$

$$\frac{dP_{ASE}^{-}(\nu)}{dz} = [\sigma_e(\nu)N_2(z) - \sigma_a(\nu)N_1(z)]P_{ASE}^{-} - P_{ASE}^{0}(\nu)\sigma_e(\nu)N_2(z) \tag{2.14}$$

A simplified model for ASE growth along the fibre building can be formulated either by treating it as a signal with effective bandwidth $\Delta\nu_{ASE}$ or by splitting the broad spectrum into *m* strips and treating each as an independent signal with narrow bandwidth of $\Delta\nu_{ASE}/m$. The population equation (2.3) also needs to be modified to include depletion of the upper level by each of these signals.

In general, equations (2.13-2.14) have to be solved numerically for a wide range of wavelengths to calculate total ASE output power. However, by making simplifying assumptions, we can obtain expressions for ASE signal growth and ASE output power in the low-power regime. Following the reasoning (2.1-2.8), the population density of the upper level N_2 can be considered as not being depleted by ASE growth as long as its power remains at low levels, i.e.

$$P_{ASE} \ll P_{ASEsat} = \frac{A_{core} h\nu_{ASE}}{\eta_q \tau_f [\sigma_a(\lambda_{ASE}) + \sigma_e(\lambda_{ASE})]} \tag{2.15}$$

where $\lambda_{ASE} = c/\nu_{ASE}$ can be treated as the mean wavelength (ν_{ASE} – the mean frequency) of the broad ASE spectrum with total power P_{ASE} or as the central wavelength of each spectrum strip consisting of fractional power $P_{ASE}(\lambda)$. In this regime equation (2.19) can be used, assuming that $P_p(0) \ll P_{sat}$.

Extracting $N_2(z)$ from (2.7) and using (2.9) produces:

$$N_2(z) = N_2(0) \exp(-\alpha_p z) \tag{2.16}$$

where

$$N_2(0) = \frac{\alpha_p P_p(0) \eta_q \tau_f}{A_{core} h\nu_p} \tag{2.17}$$

is the population of the upper level in z = 0 point in the fibre.

Solving equations (2.16) and (2.13-2.14) results in expressions for ASE power at given point in the fibre in both directions. The forward ASE power can be expressed by:

$$P_{ASE}^{+}(z) = [P_{ASE}^{+}(0) + P_{noise}^{+}(z)] G^{+}(z) \tag{2.18}$$

where $P_{ASE}^{+}(0)$ is the ASE input power (at point z = 0),

$$G^{+}(z) = \exp\left\{\frac{N_2(0)}{\alpha_p}[\sigma_a(\lambda_{ASE}) + \sigma_e(\lambda_{ASE})]\left[1 - \exp\left(-\alpha_p z\right)\right] - N\sigma_a(\lambda_{ASE})z\right\} \quad (2.19)$$

is the single-pass gain (after propagation distance z) and

$$G^{+}(z)P^{+}_{noise}(z) = G^{+}(z)P^{0}_{ASE}(\lambda_{ASE})\int_0^z \left[\frac{N_2(z)\sigma_e(\lambda_{ASE})}{G^{+}(z)}\right]dz \quad (2.20)$$

is the noise power accumulated after propagation distance z, with $N_2(z)$ given by (2.16). Similar equations can be derived for the backward propagating ASE.

Solving equations (2.13-2.14) and (2.16) shows that $G^{+}(L) = G^{-}(0) = G$, where L is the fibre length and G is the small signal single-pass gain with the same total value for ASE propagation in both directions.

2.7. Conclusions

This chapter explained the motivation for research in the area of fibre-based ASE sources and discussed some aspects relevant to power scaling of such sources. Yb-doped fibre was presented as a gain medium best suited for the experiments that will be discussed in the next chapter of this thesis. Finally, this chapter introduced a theoretical model for fibre-based ASE sources. It is based on rate equations in the steady state condition for the two manifolds of an Yb system, and takes into account pump absorption and re-emission, stimulated absorption of the ASE signal and its reabsorption, as well as spontaneous broadband emission along the length of the Yb-doped fibre. Simplifying assumptions valid in the low-power regime were introduced, and expressions for the generation and power build-up of ASE signal in the core of the cladding-pumped RE-doped fibre were derived. This proposed semi-analytical model can be used to predict output powers of ASE sources and ASE power distribution along the fibre, taking into account the reflectivities of the fibre ends. Various ASE source configurations and the applicability of the simplified model in those cases will be discussed in the next chapter.

References

[2.1] V. Fomin, M. Abramov, A. Ferin, A. Abramov, D. Mochalov, N. Platonov and V. Gapontsev, “10 kW single-mode fiber laser,” presented at 5th International Symposium on High-Power Fiber Lasers and Their Applications, St. Petersburg, 28 June - 1 July, 2010

[2.2] Y. Jeong, J. K. Sahu, D. B. Soh, C. A. Codemard and J. Nilsson, “High-power tunable single-frequency single-mode erbium:ytterbium codoped large-core fibre master-oscillator power amplifier source”, Opt Lett., vol. 30, no. 22, pp. 2997-9299, 2005

[2.3] Thomas Ehrenreich, Ryan Leveille, Imtiaz Majid, Kanishka Tankala, Glen Rines and Peter Moulton, "1-kW, All-Glass Tm:fibre Laser", SPIE Photonics West, 28 January 2010

[2.4] Y. Jeong, J. Nilsson, J. K. Sahu, D. B. S. Soh, C. Alegria, P. Dupriez, C. A. Codemard, D. N. Payne, R. Horley, L. M. B. Hickey, L. Wanzcyk, C. E. Chryssou, J. A. Alvarez-Chavez, and P. W. Turner, “Single-frequency single-mode plane-polarized ytterbium-doped fiber master-oscillator power amplifier source with 264 W output power”, Opt. Lett., vol. 30, pp. 459–451, 2005

[2.5] P. Dupriez, A. Piper, A. Malinowski, J. K. Sahu, M. Ibsen, Y. Jeong, L. M. B. Hickey, M. N. Zervas, J. Nilsson, and D. J. Richardson, “321 W average power 1 GHz 20 ps 1060 nm pulsed fiber MOPA source”, Proc. Opt. Fiber Commun. Conf., Anaheim, CA, 2005, Paper PDP3.

[2.6] J. Limpert , F. Roser, T. Schreiber, and A. Tuennermann, “High-power ultrafast fiber laser systems”, IEEE J. Sel. Top. Quant., vol. 12, no. 2, pp. 233–244, 2006

[2.7] A. E. Siegman, “Lasers”, University Science Books, Mill Valey, California, 1986

[2.8] L. W. Casperson, “Threshold characteristics of mirrorless lasers”, J. Appl. Phys. vol. 48, p. 256, 1977

[2.9] O. Svelto, “Principles of Lasers”, Plenum, 1998

[2.10] E. A. Swanson, S. R. Chinn, C.W. Hodgson, A. M. Vengsarkar, S. Grubb, B. Bouma, G. Tearney, and J. G. Fujimoto, “Spectrally shaped rare-earth doped fiber ASE sources for use in optical coherence tomography”, Proc. Conf. Lasers Electro-Opt., pp. 211-211, 1996

[2.11] S. Martin-Lopes, M. Gonzalez-Herraez, A. Carrasco-Sanz, F. Vanholsbeeck, S. Coen, H. Fernandez, J. Solis, P. Corredera, and M. L. Hernanz, “Broadband spectrally flat and high power density flight source for fibre sensing purposes”, Meas. Sci. Technol., vol. 17, pp. 1014–1019, 2006

[2.12] R. C. Youngquist, S. Cm, and D. E. N. Davies, “Optical coherence-domain reflectometry: A new optical evaluation technique”, Opt. Lett., vol. 12, pp. 158–60, 1987

[2.13] J. S. Lee, Y. C. Chung, and D. J. DiGiovanni, “Spectrum-sliced fiber amplifier light source for multichannel WDM application”, IEEE Photon. Technol. Lett., vol. 5, pp. 1458-1461, 2002

[2.14] Wenting Chen, Deyuan Shen, Ting Zhao and Xiaofang Yang, “High power Er,Yb-doped superfluorescent fiber source with over 16 W output near 1.55 μm”, Opt. express, vol. 20, no. 13, 2012

[2.15] G. Smith, P. C. Shardlow and M. J. Damzen, “High-power near-diffraction-limited solid-state amplified spontaneous emission laser devices”, Opt. Lett., vol. 32, no. 13, 2007.

[2.16] P. Wang, J. K. Sahu, W. A. Clarkson, “Power Scaling of Ytterbium-doped Fiber Superfluorescent Sources”, IEEE J. Sel. Top. Quant., vol. 13, pp. 580-587, 2007

[2.17] Oliver Schmidt, Andrea Kliner, Miroslaw Rekas, Christian Wirth, Stephan Rhein, Thomas Schreiber, Ramona Eberhardt, and Andreas Tuennermann, “Relative intensity noise characterization of a linear polarized 1.1 kW fiber-amplified narrow-band ASE source”, at Frontiers in Optics, San Jose, California, October 16, 2011, paper FTuW

[2.18] J. J. Russell, J. Moon, J. Sirkis, A. D. Kersey, and H. Lara, “Programmable Broadband Light Source for Fiber Sensor Applications”, Proc. of 16th International Conference on Optical Fiber Sensors, Nara, Japan, 2003

[2.19] W. Duncan, B. Lee, P. Rancuret, B. Sawyers, W. Stalcup, L. Endsley and D. Powell, “DLP Switched Blaze Grating; the Heart of Optical Signal Processing”, Proc. of SPIE, vol. 4983, 2003

[2.20] A. Bouchier , G. Lucas-Leclin, F. Balembois, and P. Georges, “Spectrally Narrowed Amplified Spontaneous Emission Source at 977 nm Based on a Single-Mode Ytterbium-Doped Fiber”, IEEE Photon. Technol. Lett., vol. 16, no. 9, pp. 2021-2023, 2004

[2.21] R. Paschotta, J. Nilsson, A. C. Tropper, and D. C. Hanna, “Efficient Superfluorescent Light Sources with Broad Bandwidth”, IEEE J. Sel. Top. Quant., vol. 3, no. 4, pp. 1097-1099, 1997

[2.22] H. Pask, R. J. Carman, D. C. Hanna, A. C. Tropper, C. J. Mackechnie, P. R. Barber and J. M. Dawes, “Ytterbium-doped silica fiber lasers: Versatile sources for the 1-1.2 μm region”, IEEE J. Sel. Top. Quant., vol. 1, pp. 2-12, 1995

[2.23] R.Paschotta , J. Nilsson, A. C. Tropper and D. C. Hanna, “Ytterbium doped fiber amplifiers”, IEEE J. Sel. Top. Quant., vol. 44, pp. 1049-1056, 1997

[2.24] M. J. Weber, J. E. Lynch, D. H. Blackburn and D. J. Cronin, “Dependence Of The Stimulated-Emission Cross-Section Of Yb-3+ On Host Glass Composition”, IEEE J. Quantum Electron. vol. 19, pp. 1600-1608, 1983

[2.25] M. J. F. Digonnet, “Rare-Earth- Doped Fiber Lasers and Amplifiers”, 2nd edition, Marcel Dekker, Inc. New York, 2001

[2.26] D. Kousnetsov , J. V. Moloney, “Efficiency of pump absorption in double-clad fiber amplifiers. II. Broken circular symmetry”, J. Opt. Soc. Am. B, vol. 19, pp. 1259-63, 2002

[2.27] J. Xu, J. Lu, L. Lu and K. I. Ueda, “Influence of cross-sectional shape on absorption characteristics of double clad fiber lasers”, Proc. Conf. Lasers and Electro-Opt., Long Beach, USA, vol. 1, pp. 520-521, 2002

[2.28] P. C. Becker, N. A. Olsson, J. R. Simpson, “Erbium-Doped Fiber Amplifiers”, Academic Press, London, 1999

[2.29] D. C. Jones and A. M. Scott, “A model of a fibre amplifier incorporating amplified spontaneous emission”, Proc. of SPIE, vol. 5335, pp. 73-80, 2004

[2.30] A. Laliotis and E. M. Yeatman, “Modeling Signal and ASE Evolution in Erbium-Doped Amplifiers With the Method of Lines”, J. Lightwave Technol., vol. 24, no. 3, pp. 1589-1600, 2006

Chapter 3

Spectrum-controllable fibre-based ASE seed source

3.1. Introduction

This chapter describes the development of a fibre-based ASE seed source with spectrum shaping elements in an external feedback arrangement of the system. Several architectures of the ASE source with increasing degree of complexity were studied, and their performance was compared to the theoretical model described in the previous chapter of the thesis. Section 3.2 introduces a simple fibre-based ASE source with double-ended output and explains how the theoretical model can be applied to account for multiple reflections from the fibre facets. Section 3.3 demonstrates a single-ended ASE source and discusses the validity of the model with respect to the pump and ASE output power levels. A polarised ASE source and theoretical expressions for polarisation extinction ratio are introduced in section 3.4. Section 3.5 demonstrates a 'narrow' line ASE source and discusses the impact of ASE light guided in the inner cladding on the overall performance of the system. The final configuration, which allows shaping of the spectrum in the external feedback arrangement, is described in section 3.6 and the performance of this system for different lengths of the fibre and spectral bandwidths is presented. The advantages of this approach over external spectrum-shaping and the minimal spectral resolution available for this system are also discussed. Section 3.7 introduces a way of decreasing the minimum resolution limit using an etalon in the external feedback arrangement.

3.2. ASE source with double-ended output

The initial experiment involved constructing an ASE source with a double-ended output, based on L = 8.4 m of ytterbium-doped double-clad fibre (*Nufern*) with a core and D-shaped inner cladding diameter of 28 μm and 380 μm respectively. Both ends of the fibre were polished at an angle of approximately 12°. Pump light was provided by a diode bar at 975 nm (fig. 3.1). In this section we compare the measured output power of this configuration with the model constructed from the theory outlined in chapter 2, and discuss the applicability of the model.

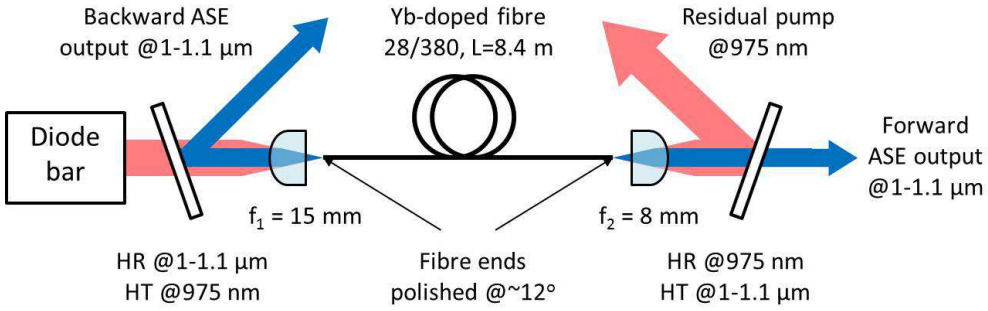

Figure 3.1: ASE source, double-ended operation – experimental set-up

Internal reflectivity of the fibre facet can be defined as a fraction of power in the fibre prior to exiting the fiber end that is launched back to the fibre's core via Fresnel reflection from silica-air interface. If the pumped fibre end (End A) has reflectivity R_A and the opposite fibre end (End B) reflectivity is R_B, ASE power building up in the active medium can be enhanced via multiple reflections between fibre facets. According to (2.18) backward ASE power starting from noise near the End B is amplified to the value of $P^-_{noise}G$ after a single pass in the fibre. Part of this power $P^-_{noise}GR_A$ is reflected back and adds to the noise power co-propagating with the pump. Forward ASE near the End B after a single pass is amplified to the $(P^-_{noise}GR_A + P^+_{noise})G$ (see fig. 3.2).

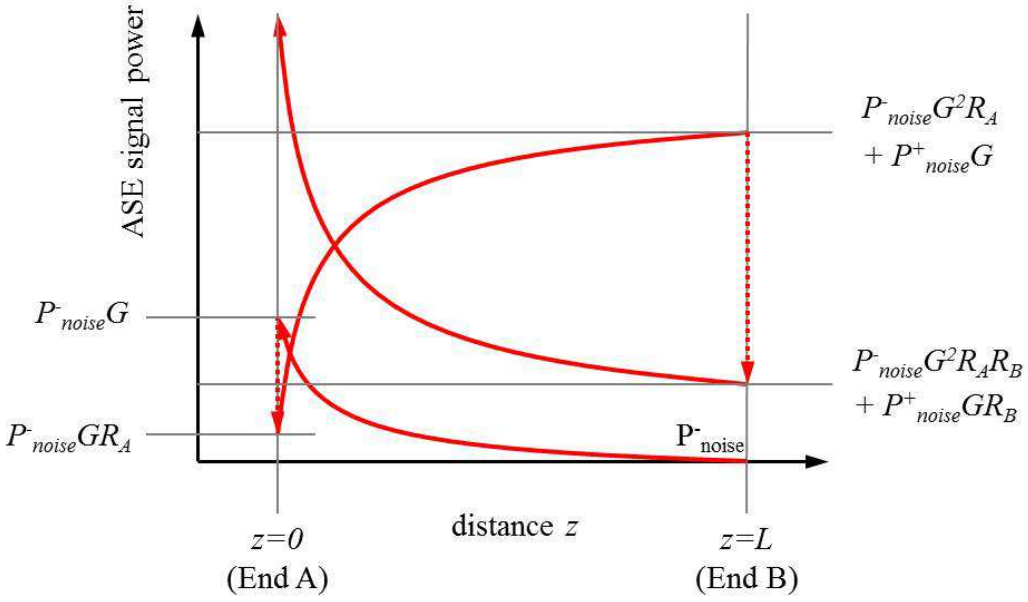

Figure 3.2: ASE signal power build-up via multiple reflections between the fibre facets

ASE photons can experience multiple round-trips inside the fibre, with overall round-trip gain of: $R_B G R_A G$ (assuming negligible core propagation loss). Therefore to include all possible multiple reflections, the ASE power near End B has to be multiplied by a factor $\sum_{n=0}^{\infty}(G^2R_AR_B)^n$. This geometric series is convergent for $G^2R_AR_B < 1$ and therefore the total forward ASE output power (including output coupler transmission) is given by expression:

$$P^+_{ASE}(l) = \frac{(P^-_{noise}GR_A + P^+_{noise})G}{1 - G^2R_AR_B}(1 - R_B) \tag{3.1}$$

A similar analysis can be done for backward ASE output power:

$$P^-_{ASE}(0) = \frac{(P^+_{noise}GR_B + P^-_{noise})G}{1 - G^2R_AR_B}(1 - R_A) \tag{3.2}$$

For $G^2R_AR_B \geq 1$ the roundtrip gain exceeds the round-trip loss and lasing threshold is reached.

Assuming that the polished fibre ends were of similar finish and quality (i.e. $R_A \approx R_B = R_f$), the reflectivity of the fibre ends can be calculated from the round-trip gain at the lasing threshold condition, $G^2 R_f^2 = 1$. We know the dependence of single pass gain on launched pump power from (2.19) and (2.17), and can therefore estimate the reflectivities as: $R_f = (1 \pm 0.5) \times 10^{-5}$. Here we have treated the ASE as a single signal with effective bandwidth of $\Delta\lambda_{ASE} = 30$ nm according to the measured output spectra (fig. 3.3b). According to (2.19), (2.20) and (2.16), G, P_{noise}^{+} and P_{noise}^{-} are in general functions of launched pump power, therefore the output ASE power versus pump can be calculated (fig. 3.3a).

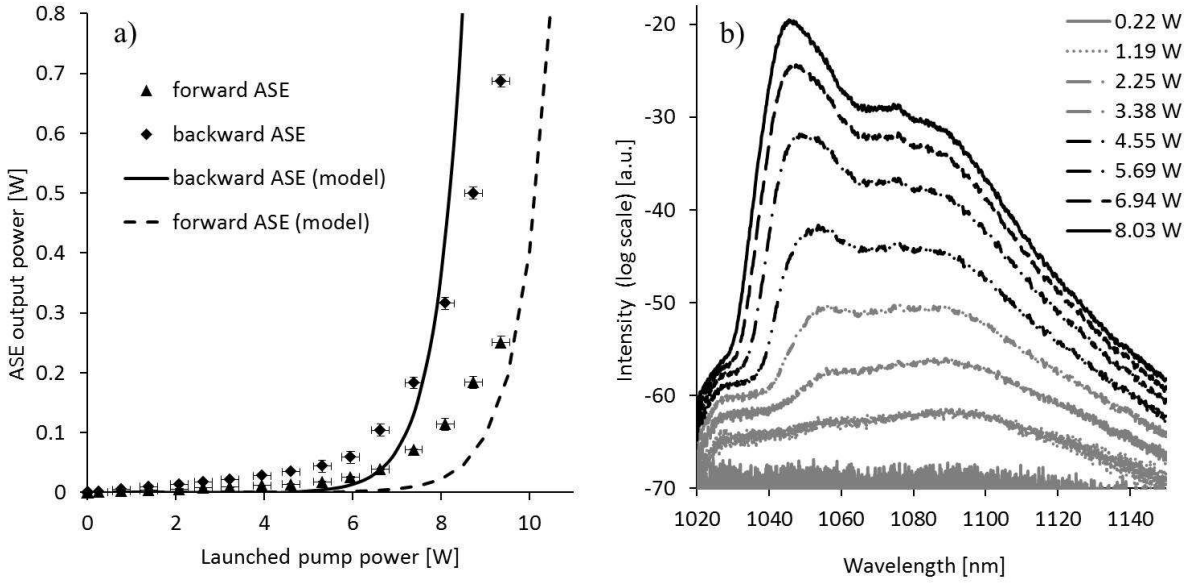

Figure 3.3: a) Output power from both ends of the ASE source b) Forward ASE spectra for different launched pump powers

The discrepancies between model predictions and experimental results are mainly due to limitations in the model. Theoretical analysis breaks down for high ASE powers (2.15), i.e. $(P_{ASE}^{+} + P_{ASE}^{-}) \geq P_{ASEsat} \approx 1$ W, where upper level population depletion can be no longer neglected, and at high pumping powers $P_p > P_{psat} \approx 7$ W. Besides the theoretical limitations of the model, many other factors could greatly affect the source performance. The fibre core is not truly single mode which may give higher spontaneous noise power than expected in a model derived for a single-transverse-mode fibre. A fraction of the measured output power was coming from

noise spontaneously emitted at angles guided in the inner cladding rather than a fibre core (this issue will be discussed in more detail in section 3.5). Moreover, bend losses for pump and ASE power have not been included in the theoretical model. In spite of the simplified analytical treatment, the proposed model proved helpful in estimating the amount of pump power required for significant (i.e. with >1% pump to ASE signal conversion) ASE power build-up. It also illustrates the difference between forward and backward ASE output powers arising from re-absorption loss in the fibre.

3.3. ASE source with single-ended output

The next stage in experiments involved characterizing the ASE source with a single-ended output. A HR mirror was used to provide feedback into the active fibre. Due to the much higher reflectivity at one end of the feedback arrangement the source became vulnerable to reflections from the diagnostic equipment that caused unwanted parasitic lasing which, in turn triggered self-pulsing, eventually destroying the fibre facets. In order to suppress feedback a Faraday isolator (consisting of a Faraday rotator between polarisers crossed by 45 degrees) had to be employed at the output (fig. 3.4).

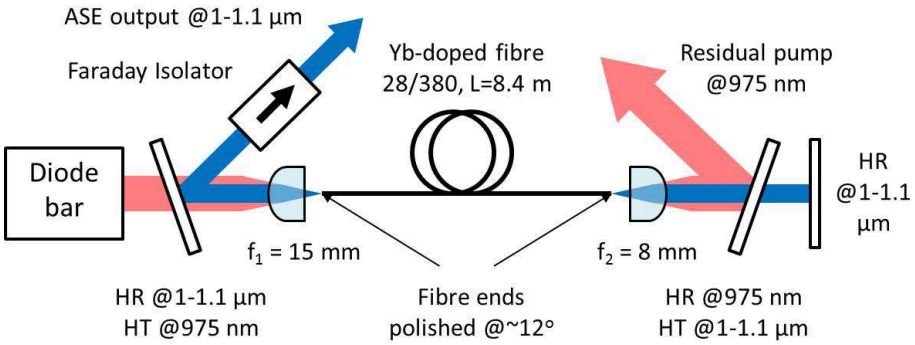

Figure 3.4: ASE source configuration for single-ended operation

The same analytical treatment as in section 3.2 was applied to single end operation. Equations (3.1) and (3.2) were used with $R_B = 1$ (fig. 3.5a). Due to the much higher measured output powers, the model's predictions deviate from the experiment above $P_{ASE} \geq P_{ASEsat} \approx 1$ W (where the ASE power significantly depletes upper level population and saturates the gain) and for saturating pump powers $P_p \geq P_{psat} \approx 7$ W (where the pump power significantly depletes the ground level population). Nevertheless, the expected trends of a lower pump required for significant ASE build-up and higher slope efficiency for single end operation were observed. We also observed slight changes in the output spectrum, even at low pumping powers (fig. 3.5b). This is because using a HR mirror at one of the feedback arrangement ends forces double-pass amplification of the ASE signal, resulting in a higher re-absorption loss, which is more significant for shorter wavelengths. Moreover, re-absorbed ASE at shorter wavelengths act as a pump for ASE emitted at longer wavelengths. As a result of this processes, some fraction of the ASE power (originating from noise co-propagating with the pump power) creates a second peak in the spectrum with a local maximum around 1075 nm. Beam quality factors for both double- and single-end output ASE sources were measured to be $M_x^2 \approx M_y^2 = 2 \pm 0.5$.

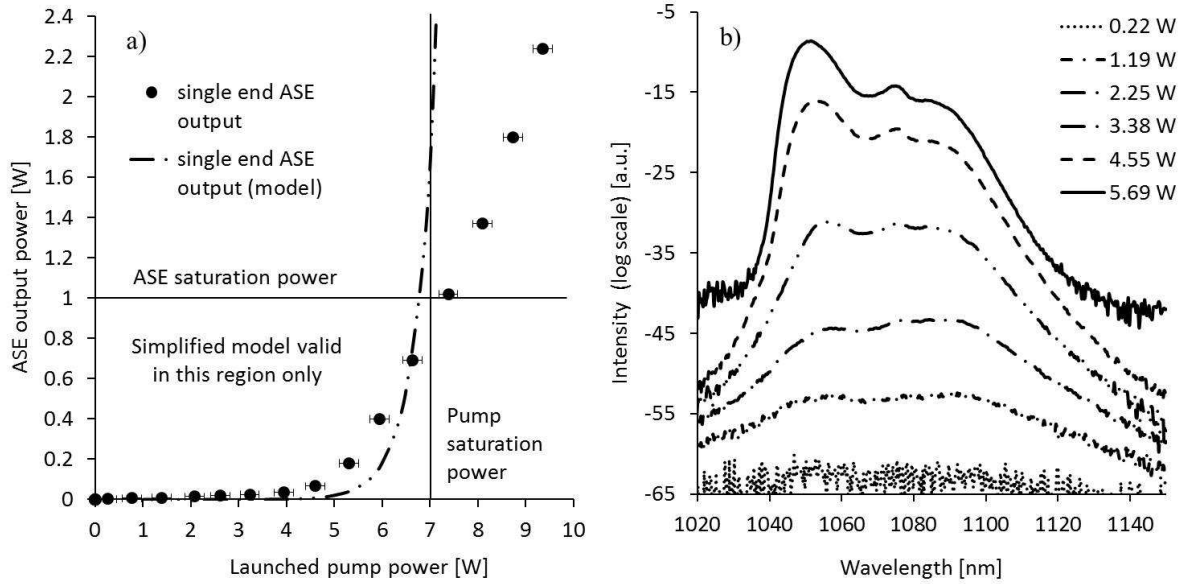

Figure 3.5: a) Output power from single-ended ASE source b) Output spectra for different launched pump powers

3.4. Polarised operation with broadband feedback

In order to efficiently produce polarised output, an ASE source was constructed with an ytterbium-doped double-clad polarisation maintaining (PM) panda fibre. The fibre was 14.1 m in length, with a core and cladding diameter of 30 μm and 400 μm respectively. The fibre ends were polished at an angle of approximately 15 degrees. A half-wave plate and a polariser (prism polarising beam splitter) were placed inside an external feedback arrangement terminated with a HR mirror. The polarised output was optimized by rotating the half-wave plate and monitoring the output polarisation extinction ratio (PER). When the polarisation plane constrained by the external feedback arrangement matched one of the birefringence axes of the PM fibre, the output polarisation extinction ratio (PER), measured with a rotating analyser (fig. 3.6), reached a maximum value.

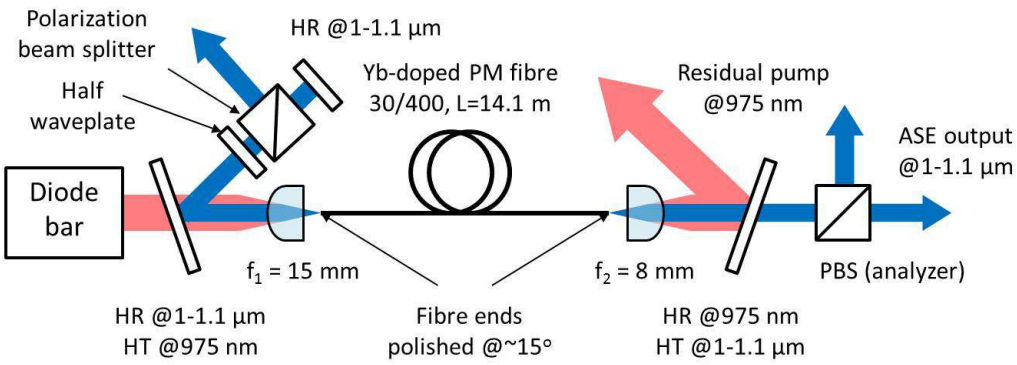

Figure 3.6: ASE source with polarised, broadband feedback - experimental set-up

Again, the model presented in section 3.2 can be used to analyse each polarisation state independently. Both polarisation components originate from half of the total noise power $P_{noise}^{+/-}/2$. The ASE power polarised along the axis constrained by the polarising element builds up in a feedback arrangement with effective reflectivities $R_A = 1$, and $R_B \approx R_f = 10^{-5}$, while the ASE power polarised orthogonally builds up in a feedback arrangement with effective reflectivities $R_A \approx R_B = R_f$. Assuming that $P_{noise}^{+} = P_{noise}^{-}$ it can be shown with appropriate equations in the form of (3.1)

that the expected feedback to background power ratio (where feedback power $P_{feedback}$ builds in external feedback arrangement and background power $P_{background}$ builds in internal feedback arrangement between fibre ends) is given by the equation:

$$\frac{P_{feedback}}{P_{background}} = \psi = \frac{(1 - G^2 R_A R_B)(1 + G)}{(1 - G^2 R_B)(1 + G R_A)} \tag{3.3}$$

while the theoretical limit for maximum PER (assuming that the background is unpolarised) can be given by:

$$\mathrm{PER}_{max} = \frac{P_{feedback} + P_{background}/2}{P_{background}/2} = 2\psi + 1 \tag{3.4}$$

The M^2 parameter for the ASE output from Panda fibre was $M_x^2 \approx M_y^2 = 1.6 \pm 0.4$. The output power efficiency was similar to the measured values in section 3.3. The temporal power stability (defined as power fluctuations to total output power ratio) was measured to be in the range of: $0.3\% < \Delta P/P < 0.8\%$ (over time ~1 minute) depending on the pumping power. Values of output PER for an ASE source with broadband, polarised feedback were measured to be much lower than expected (PER < 3), and the reasons for this will be discussed in the next section.

3.5. Polarised operation with narrowband feedback

In the next phase of the experiments, we introduced a tuning element in the external feedback arrangement by replacing the HR mirror with a diffraction grating (grating constant $\Lambda_g \approx 1.67$ µm or 600 lines per mm) in Littrow configuration (fig. 3.7). An isolator in conjunction with a half-wave plate was employed at the output in order to suppress back-reflections from the diagnostic equipment leading to unwanted lasing.

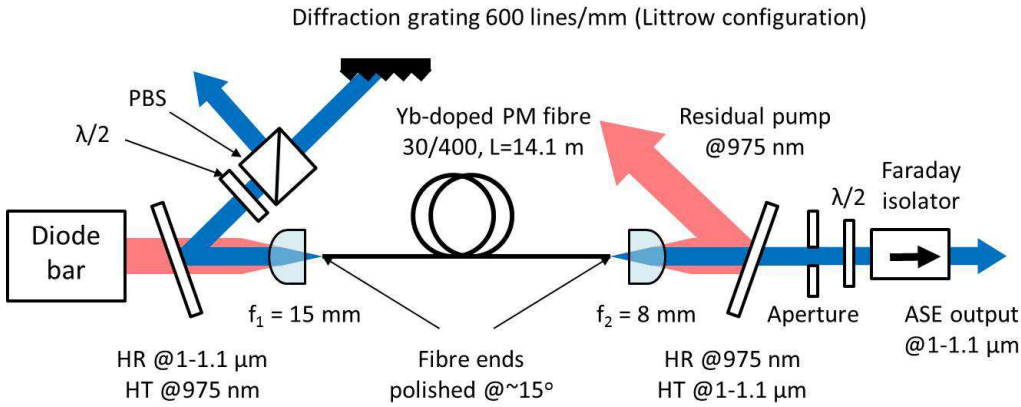

Figure 3.7: ASE source with polarised, narrowband feedback - experimental set-up

Strong modulation of the output spectrum was observed which we attributed to modal interference from the higher order modes operating in the fibre. This issue was resolved by introducing bend loss to suppress these higher order modes. Optimal performance was achieved by coiling 6 m of the fibre to a bend radius of 50 mm. Effective higher order mode suppression was confirmed by the reduction of the M^2 parameter to nearly diffraction-limited beam quality: $M_x^2 \approx M_y^2 = 1.1 \pm 0.2$. Due to the tuneable feedback into the fibre, the output spectrum consisted of a very low, broad, ASE background and a narrowline peak of effective bandwidth $\Delta\lambda_{FWHM} = 1.4 \pm 0.1$ nm. The bandwidth value was measured by fitting a Gaussian function to the spectrum after higher order mode suppression (fig. 3.8).

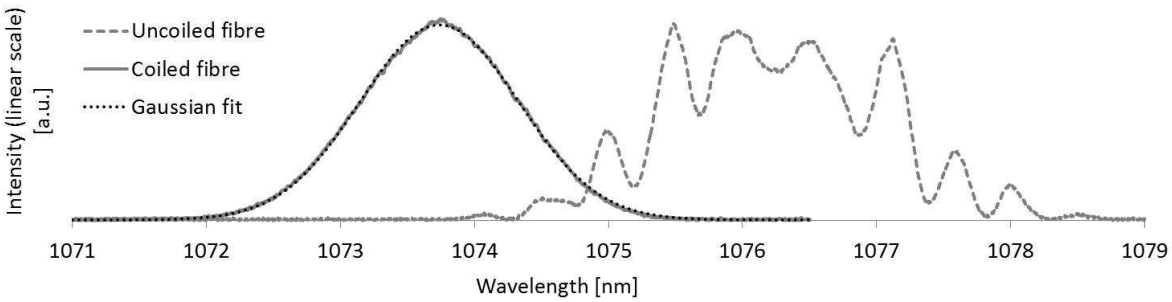

Figure 3.8: ASE source with narrowband feedback spectrum before and after multimode interference suppression (central wavelength changed after grating rotation)

Placing a variable diameter aperture in the output beam just after the dichroic mirror proved helpful in explaining the unexpectedly low PER values obtained in the previous section. Changing the diameter of the aperture resulted in significant variations in both the output power and PER values. When we set the diameter of the aperture to be roughly similar in size to the beam exiting the fibre core, the PER was maximized at a value of 14 ± 2, compared to the low value of 2.5 ± 0.5 measured with a fully opened aperture. The output power changed correspondingly, increasing to roughly twice its initial value when the aperture was opened.

More detailed investigations were made by rotating the diffraction grating to tune the central wavelength of the feedback signal. The tuning curves differ significantly for a fully opened and "closed" (diameter of ~1 mm) aperture (fig. 3.9a). The tuning curve for an open aperture showed a constant background power of approximately 13 mW, independent of the grating angle. For a closed aperture this background power dropped to approximately 1 mW. This indicated significant amounts of unpolarised broadband background ASE power propagating in the inner cladding rather than in the fibre core. Spectral measurements of the cladding light confirmed this hypothesis; the spectrum showed an emission peak close to 1030 nm, which corresponds to the Yb:glass emission spectrum without the re-absorption loss (fig. 3.9b). These observations can be accounted for in the following manner; due to the long length of fibre used, significant reabsorption of the ASE signal would occur at the non-inverted sections of the fibre. The ions in these sections (now excited) would then undergo spontaneous emission, adding to the light spontaneously emitted along the fibre in random directions. A small fraction of this power is emitted at angles larger than the NA of the core and thus is not guided by the core but propagates within the undoped cladding. In addition, light reflected from the angled facets can be coupled into the inner cladding of the fibre. These mecahnisms result in a measurable amount of light at the output. When the aperture is open, therefore, spectral and power measurements would be affected by this cladding light. This can be resolved by closing the aperture such that it clips a significant portion of the cladding light while transmitting light from the core (fig. 3.9).

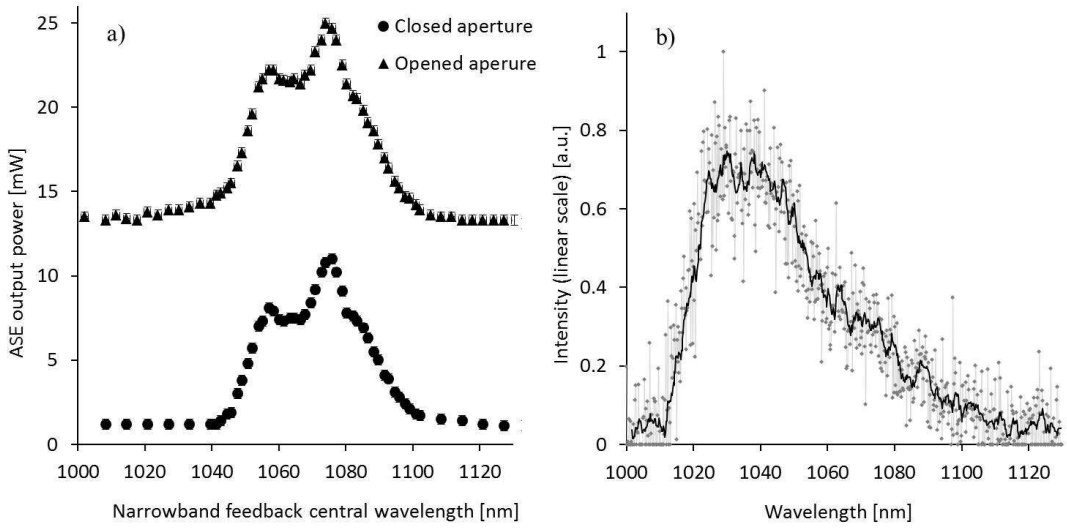

Figure 3.9: a) ASE source with narrowband feedback tuning curve b) Cladding-guided light spectrum

Our theoretical model predicts that light propagating in the core has a feedback to background spectral power density ratio described by

$$\frac{P_{feedback}(\lambda)}{P_{background}\,(\lambda)} = \psi(\lambda) = \frac{[1 - G^2(\lambda)R_A R_B][1 + G(\lambda)S(\lambda)]}{[1 - G^2(\lambda)S(\lambda)R_B][1 + G(\lambda)R_A]} \tag{3.5}$$

where $S(\lambda)$ is the function describing spectral reflectivity of the external feedback arrangement. Measured values of ψ, defined as (3.3) range from 6 to 10, depending on the fed back central wavelength. The measured PER was roughly twice this value, which corresponds to the simplified analysis (3.4). From these results we concluded that, the fibre length needed to be reduced (to 6.5 m) for future experiments to prevent high re-absorption losses in the non-inverted section of the active medium. A shorter length is also expected to yield a higher feedback to background power ratio ψ and a reduction of power guided in the cladding due to higher single pass gain values $G(\lambda)$ of a shorter fibre. These expectations have been met in the next experiment described in the following section.

3.6. Wavelength selection in external feedback arrangement

The set-up thus far with a diffraction grating has provided tuneable feedback with a constant linewidth and shape. In order to achieve more flexibility in spectrum control further modifications to the experimental set-up were necessary. Firstly, we magnified the output beam (after the half-wave plate and the polariser) with a telescope (f_3 = 4.5 mm and f_4 = 160 mm) to create a beam waist of $w_0 \approx 10$ mm upon the grating surface. A large spot size on the grating would yield high spectral resolution of the tuning element in the external feedback arrangement. Next, light from the first diffraction order reflected from the grating was focused onto a retro-reflecting HR mirror with a lens of focal length f_5 = 300 mm. The lens and the mirror separation was designed to be the same as the lens-grating distance, f_5. This grating-lens arrangement transforms the beam consisting of a broad spectrum into a single horizontal line on the mirror surface. Wavelength selection in this configuration is then done by placing a narrow vertical slit on a translation stage directly in front of the HR mirror. The slit selects a range of spectral components to be fed back. Adjusting the slit width changes the effective bandwidth, while translating the slit selects the feedback central wavelength (fig. 3.10). Monochromatic light reflected from the diffraction grating surface as a beam of spot size $w_{0\,grating}$ is focused on a HR mirror plane to the spot size of [3.1]:

$$w_{0HR} \approx \frac{M^2 \lambda f_5}{\pi w_{0grating}} \tag{3.6}$$

From differentiating the grating equation in normal incidence approximation: $\lambda = \Lambda_g \sin\theta_r$ (incidence angle $\theta_i \approx 0$, beam is reflected at angle $\theta_r = 2\delta$ to grating normal, δ - groove angle) and geometry of the system ($\theta_r \approx \Delta x/f$), two spectral components differing by $\Delta\lambda_r$ are spatially separated on the HR mirror plane by:

$$\Delta x \approx \frac{f_5}{\Lambda_g \cos\theta_r} \Delta\lambda \tag{3.7}$$

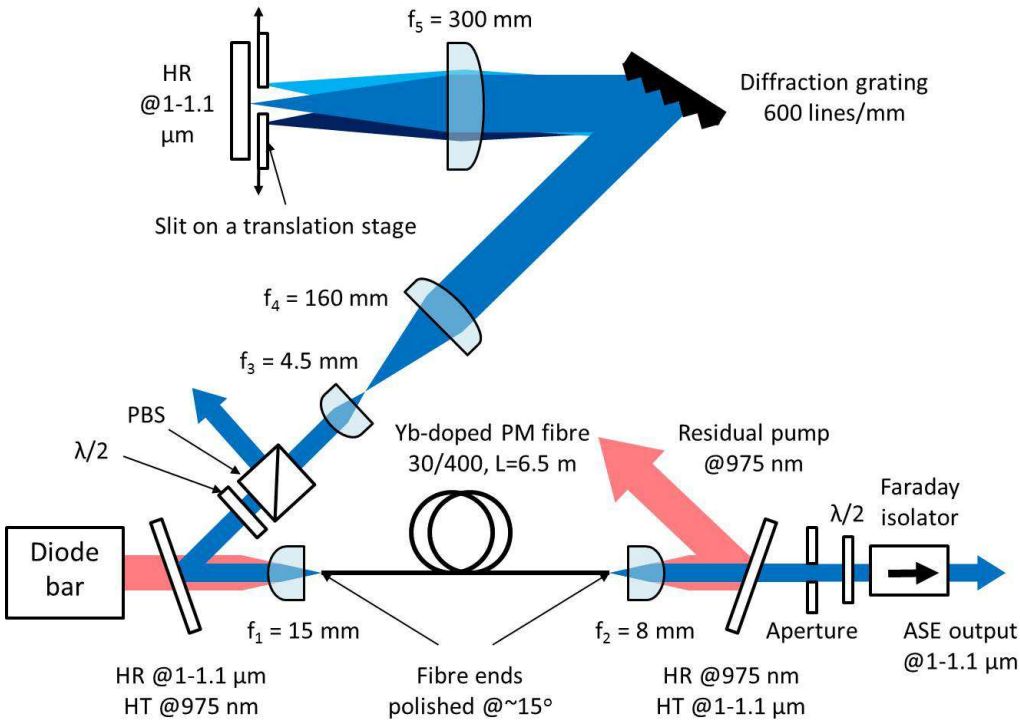

Figure 3.10: ASE source with wavelength selection in the external feedback arrangement

If we consider two adjacent, not overlapping light spots on the HR mirror separated by $\Delta x = 2w_{0HR}$, comparing (3.6) and (3.7) leads to the minimum spectral resolution for this wavelength selection system:

$$\Delta\lambda_r \approx \frac{2M^2\lambda\Lambda_g \cos\theta_r}{\pi w_{0grating}} \tag{3.8}$$

$\Delta\lambda_r \approx$ 0.1-0.3 nm, depending on the incident angle.

This expression describes an ideal situation where the slit positioned very close to the HR mirror, whereas in the set-up it was placed at a few mm away from the mirror, which reduced the resolution slightly. In this configuration, we managed to obtained narrow lines in the output spectrum with effective bandwidth down to 0.5 nm. Further reduction of the bandwidth was not feasible as it would cause corresponding losses in the feedback spectral power density.

The tuning curves for narrowband feedback depend highly on the ASE spectrum shape entering the external feedback arrangement. Longer fibres provide broader spectra but lower power densities, giving a broad tuning range but low feedback to background power ratios. Shorter fibres provide much higher values of ψ >200 due to higher values of single-pass gain (and weaker re-absorption loss) but give a narrower tuning range (fig. 3.11).

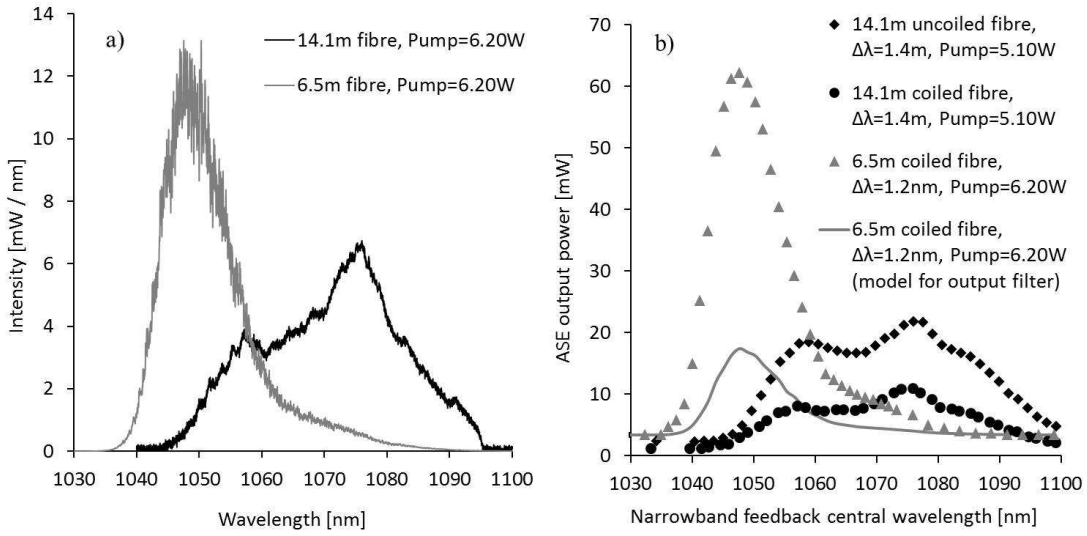

Figure 3.11: a) ASE spectra for different fibre lengths b) ASE source with narrowband feedback tuning curves at different pump powers and fibre lengths

To highlight the advantages of this approach for wavelength selection, we compared it to an alternative method of obtaining a narrowband ASE spectrum, namely the use of a narrowband filter at the output of a conventional ASE source. We developed a simple model, involving integrating power in the broadband feedback ASE source output spectrum over the narrow section of wavelengths, and compared the calculated power levels available from the use of an output filter with the experimental output powers obtained with our current approach. Our computations showed that wavelength selection in an external feedback arrangement provides much higher output power in narrow linewidths than the output filter. Experimental to modeled power ratio increased with narrower feedback bandwidth up to the value of 7 at the resolution limit of ~0.5 nm. For broader feedback bandwidths the performance of the external feedback arrangement scheme was comparable to the levels expected from the output filter (fig. 3.12a). It should be noted that output

spectral power densities depend on the overlap of the feedback spectrum with the gain spectrum and the feedback bandwidth. For broader feedback, the larger total power inside the fibre depletes the upper level population causing gain saturation and reducing output spectral power density. These mechanisms are illustrated in the figure showing the evolution of the output spectra as the slit inside the external feedback arrangement is being opened (fig. 3.12b). For a very narrow slit, the source is operating in the regime below minimum spectral resolution (3.8), the power is clamped due to losses in the external feedback arrangement, and 0.5 nm narrowline with low spectral density is observed. Maximum power density is observed for bandwidth 0.5-0.8 nm with round trip gain reaching lasing threshold. Widening the slit further feeds more power into the fibre significantly depopulating upper level, saturating gain and returning the system below lasing threshold. For increasing slit widths the total output power is rising, but the spectral power densities drop along with the saturated gain value.

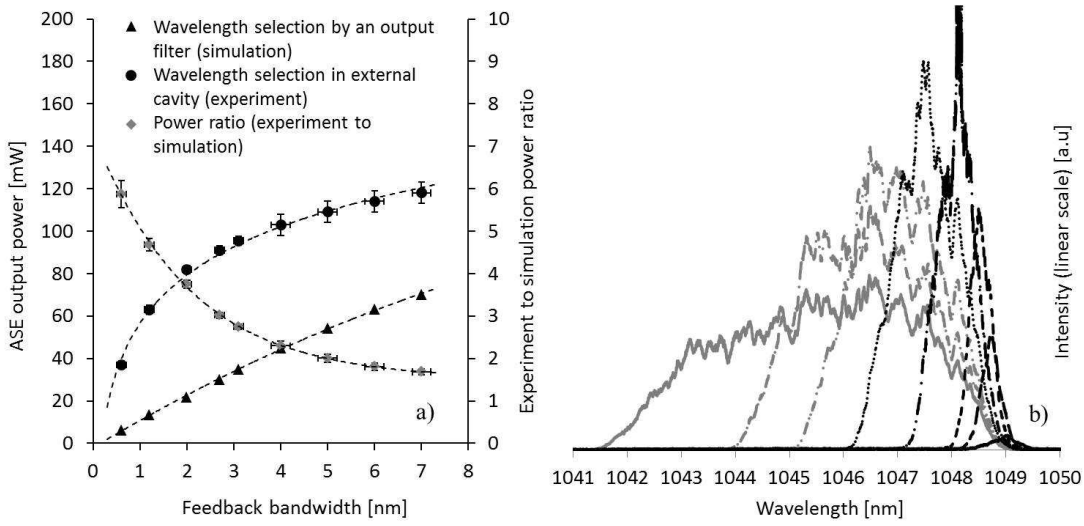

Figure 3.12: a) Comparison between measured output power values (wavelength selected in external feedback arrangement) and theoretical power values expected with an ideal filter at the source output b) ASE spectra for different widths of the slit in the external feedback arrangement

To investigate an additional method of spectrum control by applying uniform attenuation for all spectral components, a neutral density filter was placed in the external feedback arrangement between the lens and the HR mirror (in the setup from fig. 3.10). Increased feedback arrangement losses raised the lasing threshold, enabling more pumping power being launched into the active fibre before the onset of lasing. There is a significant difference between the broad spectrum without additional losses (fig. 3.13a) and with neutral density filter inside the external feedback arrangement (fig.3.13b). In the first case gain peak around 1070 nm consisting of ASE power after double pass inside the fibre (shifted towards longer wavelengths due to re-absorption) dominates over the emission peak around 1050 nm (mostly single-pass ASE power). In the second case both peaks are comparable and the spectrum is effectively broadened.

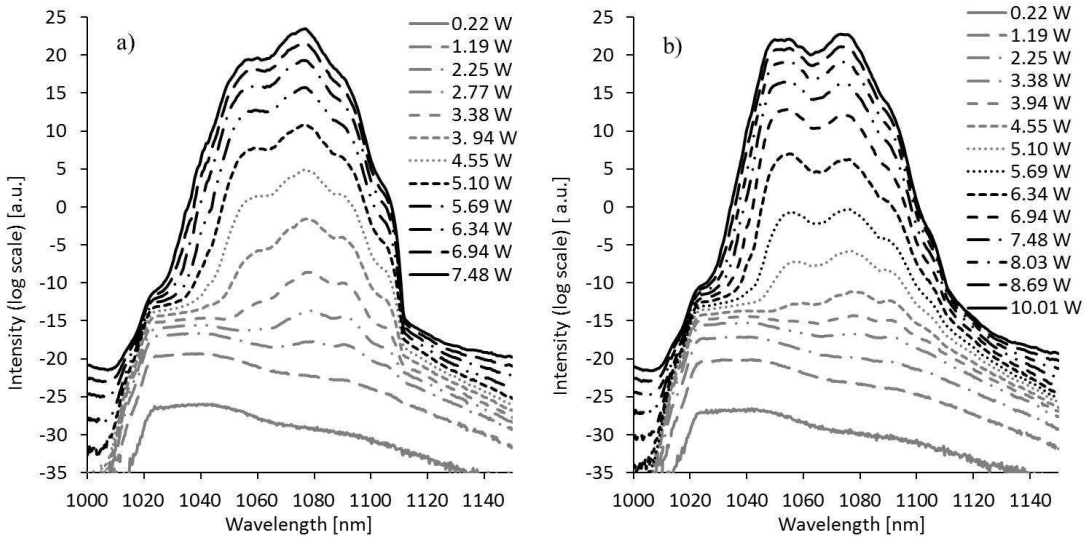

Figure 3.13: a) ASE source with external feedback arrangement for wavelength selection spectra (slit fully open) at different pump powers b) Spectra produced with the same set-up with additional attenuation (uniform over all spectral components) in the external feedback arrangement

In this section we have described how the use of a slit inside the external feedback arrangement enabled narrowband output with a minimum achievable bandwidth of 0.5 nm. The next section of this chapter describes further modifications to the experimental setup, which enabled us to achieve even better resolution (3.8).

3.7. Narrow linewidth operation using an etalon

Certain applications (e.g. optical sensing of gases, wavelength division multiplexing in optical communication) require temporally and spectrally stable narrow linewidth output with a single line, or multiple lines evenly spaced in a spectral domain. Spectral resolution of the ASE source described in the previous section was only ~0.5 nm and thus the obtainable linewidth was not narrow enough for such applications. However, a simple modification of the external feedback arrangement facilitated truly narrowline operation of the ASE source. Two parallel mirrors with identical reflectivity $R_e \approx 0.95$ creating a Fabry-Pérot cavity were placed in the external feedback arrangement between the telescope and the diffraction grating (fig. 3.14).

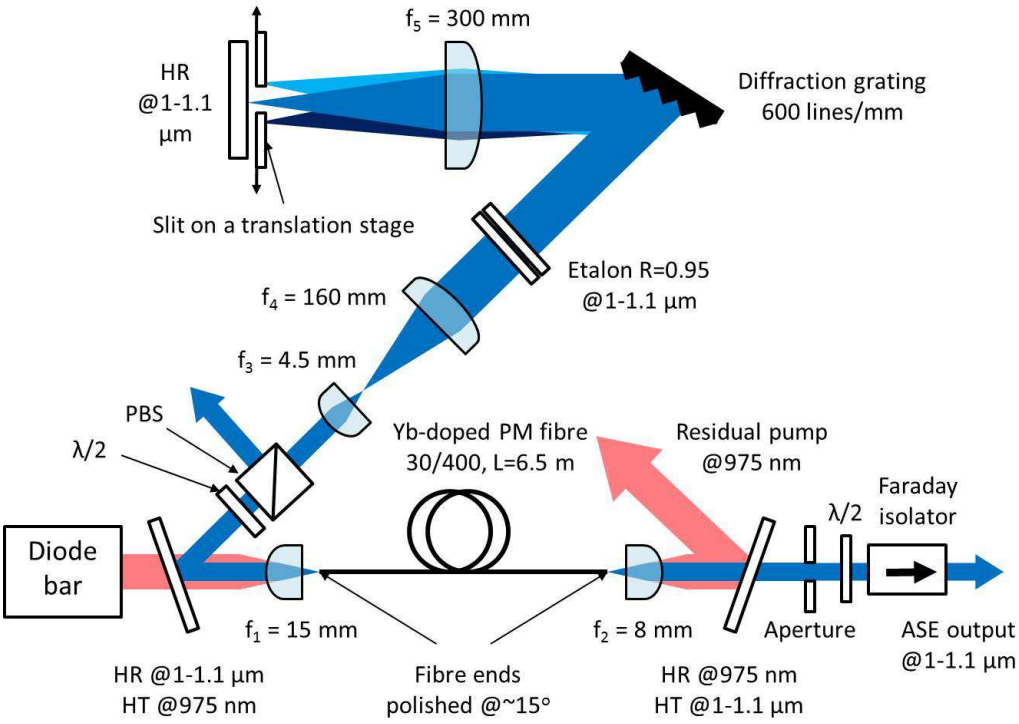

Figure 3.14: ASE source with narrow linewidth output using an etalon positioned in the external feedback arrangement

The etalon's mirrors were aligned by monitoring the spectrum transmitted by the mirrors and optimizing for narrow peaks and a low background. The peak width (FWHM) is theoretically limited by (see Appendix A):

$$\delta\lambda \geq \frac{\lambda_0^2}{2\pi d_e} \frac{(1-R_e)}{\sqrt{R_e}} \tag{3.9}$$

where λ_0 is the peak central wavelength, and d_e is the mirrors separation. It is certainly possible to reach spectral resolution comparable to the (3.9) limit with confocal Fabry-Perot interferometers. However, the finesse of a plane-plane etalon is typically limited by the surface flatness to ~40, and so the minimum peak width $\delta\lambda$ would be ~1/40 of the spacing between the narrow lines in the output spectrum (FSR), i.e. $\delta\lambda \geq \lambda_0^2/(80 d_e)$.

This shows that multiple, very narrow spectral lines can be fed back from the external feedback arrangement to the active fibre. The linewidth can easily be changed and significantly narrowed by adjusting the mirror separation of the etalon d_e. Any number of lines (in special cases a single line) can be chosen by changing the width of the slit near the HR mirror. Lines to be fed back can be also selected by translating the slit along the mirror surface. If we calculate the feedback to background spectral density ratio from the simplified model (3.5), the ratio of power in the narrow line component of the spectrum, to the power in the broad background can be estimated with:

$$\frac{P_{narrowline}}{P_{background}} = \psi_l \approx \frac{\psi(\lambda_0)\delta\lambda}{\Delta\lambda_{ASE} - \delta\lambda} \tag{3.10}$$

where $\Delta\lambda_{ASE}$ is the effective bandwidth of broad ASE background and λ_0 is the central wavelength of the narrow line spectral component.

ASE operation below lasing threshold was achieved, producing a single narrow line with FWHM of $\delta\lambda$ < 0.05 nm (limit of the optical spectrum analyser resolution), $P_{ASE}(\lambda_0) \approx$ 65 mW / nm and $\psi(\lambda_0) > 60$ (fig. 3.15b). The latter value could be most

probably improved by further optimization of the etalon mirrors. For multiple line operation, higher power spectral densities were observed compared to the broadband feedback regime, due to much weaker gain saturation (fig. 3.15a).

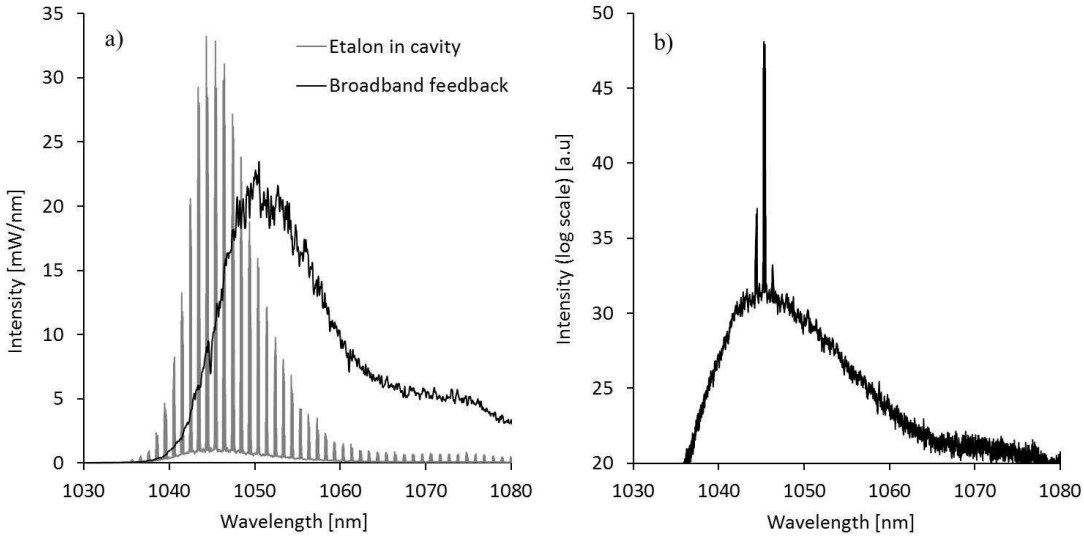

Figure 3.15: a) ASE spectra with and without etalon in the external feedback arrangement b) ASE spectrum with etalon and slit in the external feedback arrangement

3.8. Conclusions

Thus far we have studied several different configurations of a fibre-based ASE seed source. Experimental set-ups of increasing complexity have been built and characterised to explore the capabilities and limitations of these devices. To gain an understanding of the basic physical mechanisms present in ASE sources a simplified theoretical model has been constructed which has proved useful in predicting system performance in the low power (unsaturated gain) regime. We also looked into the influence of various parameters (pump power, fibre architecture, length, doping levels, external feedback arrangement loss, spectral reflectivity, fibre facet quality, etc.) on the system performance. Novel concepts for wavelength selection and narrowing the linewidth in the external feedback arrangement have been applied, and the advantages of these approaches over the conventional method of wavelength selection after the source output have been discussed. This series of experiments

have culminated in a versatile seed source with polarized output and a reasonable degree of spectral control. In its current configuration, the source is capable of producing either a broad spectrum in the 1-1.1 μm spectral region with a FWHM of 15-40 nm and output power > 1W, or single/multiple narrow lines with a FWHM ranging from several nanometres to < 0.05 nm and output power spectral densities of up to 100 mW / nm. The output power is temporally stable with fluctuations at the level < 0.3-0.8% of the total output power. Very high spectral stability (including line width fluctuations and central peak position) was obtained, which is limited mostly by the mechanical stability of the external feedback arrangement. The output beam is nearly diffraction limited with $M^2 \approx 1.1$. These performance parameters make the final device a very reliable light source that can outperform various laser sources at many potential applications. However, the main drawback, observed when it is operating in narrowband regime, is the low broad (spectral) background (see fig. 3.14a) which can account for a significant portion of the total output power. This would become an issue when launched into an amplifier chain because the background light will be amplified along with the signal, ultimately reducing effective output power in the narrow line.

References

[3.1] A. E. Siegman, “Lasers”, University Science Books, Mill Valey, California, 1986

Chapter 4

Power scaling of solid-state lasers and nonlinear frequency conversion

4.1. Introduction

Scaling the output power from laser sources has been an activity preoccupying many in the scientific community ever since the invention of the laser. This process is constantly driven by a huge range of applications and the prospect of many more for high-power laser sources in various areas, such as scientific research, medicine, materials processing, defence, remote detection, free-space communication and others. Most applications place additional demands on the laser source (e.g. in terms of beam quality, linewidth, mode of operation, stability, etc.) that can be difficult to achieve under high power operation. Some applications require operating wavelengths that are not directly accessible by existing high-power laser architectures and require efficient nonlinear frequency conversion schemes. For a long time the high-power laser area has been dominated by gas lasers and conventional 'bulk' solid-state lasers. Fibre lasers are a relatively new and rapidly developing technology in this area.

This chapter discusses scaling the output power of solid-state lasers and their nonlinear frequency conversion. Section 4.2 reviews the challenges of power scaling of solid-state lasers in general, discusses the sources and consequences of heat deposition in the laser medium. It concludes with a review of the most popular laser geometries aiming for very high output power levels. Power scaling of the fibre laser architecture is discussed in detail in section 4.3. Section 4.4 covers the background on nonlinear frequency doubling of lasers and discusses most popular frequency doubling schemes for 'bulk' solid-state lasers as well as for fibre laser architecture.

4.2. Power scaling of solid-state lasers

4.2.1. Performance of solid-state lasers

Raw output power alone should not be used as an indicator of the laser's performance. For most applications it is desirable to maximise the efficiency of the laser (i.e. the output power to pump power ratio), while maintaining other laser beam characteristics such as beam propagation factor, output power and beam pointing stability, laser linewidth and central wavelength, at the desired level.

The output power from a solid-state laser can be approximated with a simple expression [4.1]:

$$P_{out} \approx \eta_s (P_{abs} - P_{th}) \tag{4.1}$$

where η_s is the slope efficiency of the laser with respect to the absorbed pump power, P_{abs} is the pump power absorbed in the laser medium, and P_{th} is the amount of absorbed pump power required to reach the threshold for lasing.

Following the simplified rate equation approach introduced for ASE sources in section 2.6 we can derive general expression for lasing threshold. This condition is met when amount of pump power absorbed is enough to generate round-trip gain (including resonator losses) reaching unity. For a standing-wave laser resonator with an active medium of single-pass gain G, output coupler of transmission T_{OC}, and round-trip loss of other optical elements in the cavity γ, the condition for threshold to be reached can be expressed as: $G^2(1 - T_{OC})(1 - \gamma) = 1$. Assuming rapid decay of energy from the pump excitation level into the upper laser level so that pump level population is negligible, we can follow equations (2.1-2.11) to obtain the amount of absorbed pump power required to reach threshold:

$$P_{th} = \frac{Ah\nu_p}{2\tau_f \eta_q [\sigma_a(\lambda_s) + \sigma_e(\lambda_s)]} [-\ln(1 - T_{OC}) - \ln(1 - \gamma) + 2\sigma_a(\lambda_s) N l + 2\alpha_s l] \tag{4.2}$$

A is the area of the region where pump light is absorbed: for a top-hat pump intensity profile $A = \pi w_p^2$ ($A = \pi r_{core}^2$ for fibres of core radius r_{core}), and for pump beam with Gaussian intensity distribution $A = \pi\left(w_p^2 + w_l^2\right)/2$, where w_p is the pumping beam radius and w_l is the laser mode radius (assuming negligible beam divergence across the active medium length). The other symbols have been defined in section 2.6.

When operating the laser many times above threshold, i.e. when signal intensity is large compared to laser signal saturation intensity $I_{sat} = h\nu_s/\tau_f[\sigma_a(\lambda_s) + \sigma_e(\lambda_s)]$ and when the background losses (due to reabsorption and signal attenuation) are significantly lower than T_{OC} and γ, the slope efficiency can be calculated using Rigrod analysis [4.2] and approximated with [4.3]:

$$\eta_s = \frac{P_{out}}{P_{abs}} \approx \frac{T_{OC}\sqrt{1-\gamma}}{T_{OC}\sqrt{1-\gamma} + \gamma\sqrt{1-T_{OC}}}\left(\frac{\nu_s}{\nu_p}\right)\eta_q \approx \frac{T_{OC}}{T_{OC}+\gamma}\left(\frac{\nu_s}{\nu_p}\right)\eta_q \qquad (4.3)$$

where the last approximation is valid for low values of useful and non-useful losses, i.e. $T_{OC}, \gamma \ll 1$. It is clear from (4.3) that the output power is a linear function of absorbed pump power with the slope directly proportional to the ratio of its laser signal to pump frequency. This explains the advantage of in-band pumping, where the pump photon energy bridges the manifolds used in the laser transition, leading to small quantum defect. On the other hand, if the pump frequency is too close to the laser signal frequency, significant reabsorption from the lower laser level can limit the extractable output power, because it acts as a saturable loss leading to increase of the lasing threshold. Also, the achievable laser gain can be limited by stimulated emission caused by the pump light. Unlike the lasing threshold (4.2), the slope generally depends only on spectral properties of the laser transition and cavity losses. However, for larger areas of the pumped region A, higher level of background losses, as well as for shorter upper laser level lifetimes τ_f the lasing threshold has a higher value leaving less output power for a given amount of available pump power, even for lasers with high slope efficiency. For these reasons a good balance of all mentioned parameters is required to maximise the laser's output power.

Most popular ways to quantify laser beam quality include so-called beam parameter product (BPP) and beam propagation factor (often called “M squared factor”, “beam quality factor” or "beam propagation ratio" as per the ISO 11146 standard [4.4]) denoted M^2. The BPP of a laser beam is defined as the product of beam radius w_0 (measured at the beam waist) and the beam divergence half-angle θ (measured in the far field) - the higher the BPP, the lower the beam quality. The BPP can also be defined for non-Gaussian beams. In that case, second moments should be used for the definitions of beam radius and divergence. The smallest possible BPP of λ/π is achieved with a diffraction-limited Gaussian beam, where λ is the mean wavelength of the laser beam. The beam propagation factor (M^2) can be defined as the ratio of the BPP of an actual beam to that of an ideal Gaussian beam at the same wavelength, i.e.

$$M^2 = \theta \pi w_0 / \lambda \tag{4.4}$$

Beam quality defines a minimum waist radius (and hence maximum intensity) that can be obtained at a given distance from a focusing lens. It also determines the Rayleigh range z_R defined as the distance along the propagation direction of a beam from the waist to the place where the area of the beam’s cross-section is doubled (i.e. for circular beams where radius increases by a factor of $\sqrt{2}$) and for a Gaussian beam it is given by $z_R = \pi w_0^2 / M^2 \lambda$. Laser beams of high quality enable strong focusing at long working distance between focusing optics and the laser target. Long Rayleigh range implies large depth of focus (i.e. tolerance of placement of the image plane, e.g. laser beam target) and large depth of field (the range of distances in object space for which object points are imaged with acceptable sharpness with a fixed position of the image plane) allowing more flexibility and tolerances on mechanical stability in an optical system. For these reasons laser beams with M^2 factor close to 1 are preferred in many applications, and maintaining good laser beam quality at high output power is one of the main challenges in power scaling of modern laser sources.

4.2.2. Pump sources

Raw high output power of the pump source is not enough for efficient pumping of solid-state laser sources. According to (4.2) a low value of lasing threshold can only be obtained if the pump beam can be focused onto a small region with low divergence to maintain reasonably good overlap with the laser mode in the active laser medium. In case of diode-pumped fibre lasers the pump beam has to be delivered with the divergence within the acceptance angle and the waist size matched (or smaller) to the size of the inner cladding. For those reasons both high power and high beam quality of the pumping beam are required to scale the output power from solid-state lasers. Radiance (sometimes also called brightness) of a laser source is a quantity combining the output power and beam quality and can be defined as a ratio of emitted power P to the product of the emitting area A_e and solid angle divergence of the beam Ω_e, i.e.

$$B = \frac{P}{A_e \Omega_e} = \frac{P}{\pi w_0^2 \pi \theta^2} = \frac{P}{M_x^2 M_y^2 \lambda^2} \tag{4.5}$$

where M_x^2 and M_y^2 are beam propagation factors in *x* and *y* directions respectively.

Although the first diode-pumped solid-state laser was demonstrated in 1964 by Keyes [4.5], solid-state lasers were mainly pumped with flash-lamps until the 1980s due to limited lifetime and low output power from diode laser sources. Since then, development of fabrication techniques has allowed scaling the output power from laser diode systems to the multi-kilowatt regime [4.6]. While it is possible to scale the output power of a diode source by constructing linear and two-dimensional arrays of emitters to form bars and stacks, the maximum brightness of diode laser system cannot be greater than that of a single emitter. Commercially available diode laser systems are currently capable of delivering ~2kW output with beam propagation factor in the order of $M^2 \approx 150$ and radiance of $B \approx 50$ MW/cm^{2}sr [4.6]. Nevertheless, the brightness of the state-of-the-art diode laser systems still remains more than two orders-of-magnitude lower than that of the modern fibre lasers [4.7]. Despite their poor beam quality high power diode arrays are excellent sources for

pumping solid-state lasers. Compared to flash-lamps, diode sources have relatively narrow bandwidth so nearly all the pump light can be concentrated into the absorption band of a solid-state laser material. This results in an improved optical efficiency of the solid-state laser and reduced amount of unwanted heat generated in the active laser medium. Compared to laser diodes, solid-state laser materials have relatively high damage thresholds, so diffraction limited beams with high efficiency can be produced by pumping the solid-state laser with one or multiple diode laser sources emitting output with poor beam quality. For this reason solid-state lasers (and fibre lasers in particular) are often called “brightness converters” as they deliver high brightness laser output while the pump energy is delivered with poor beam quality laser diode sources.

4.2.3. Heat deposition in the laser medium

Even when using high quality crystals with low background loss and state-of-the-art pump sources, the efficiency of solid-state lasers is generally limited by the quantum defect of the laser transition resulting from the energy difference between the pump and laser signal photons. This portion of pump energy is converted to heat in the active laser medium. Other sources of heat include fluorescence quenching processes such as excited-state absorption (ESA) at pump and signal wavelengths, energy transfer up-conversion (ETU), energy transfer to impurities and defects, as well as absorption of the fluorescence and stray pump light in the mount (and polymer coating in case of fibre lasers).

a) Quantum defect

For most laser transitions, relaxation from the pump level to the upper laser level as well as from the lower laser level to the ground level is thermal in nature and involves phonon emission. A fraction of pump photon energy that is converted to heat during conversion to a laser signal photon is called the quantum defect of the laser transition. It can be defined as the fractional energy difference between the pump photon and the laser signal photon, i.e.:

$$\mathrm{Q_d} = \frac{E_p - E_s}{E_p} = 1 - \frac{\lambda_p}{\lambda_s} \tag{4.6}$$

where E_p and E_s are the energies for the pump and laser signal photons respectively, while λ_p and λ_s are the pump and laser signal wavelengths respectively. The quantum defect places an upper limit on the laser efficiency and lower limit on the fraction of pump power that is inevitably converted to heat degrading the beam quality and limiting the maximum output power from the laser. For these reasons a pump wavelength close to the laser signal wavelength is preferred. Lasers with quantum defect less than one percent have been reported [4.8].

b) Fluorescence quenching

The behaviour of solid-state lasers at population inversion densities typical for low pump powers can be understood by simple rate equation analysis (2.1-2.11). As the population inversion density becomes large with increasing pump power, several different processes collectively known as lifetime quenching processes become significant resulting in degradation of the solid-state laser performance. Lifetime quenching processes decrease the number of excited ions in the upper laser level for a given pump power and hence reduce the effective lifetime and overall fluorescence intensity from the quenched electronic states. This in turn reduces the gain in the laser medium thus raising the threshold for lasing. The net result is degradation in laser efficiency (especially in a pulsed mode) as well as additional heat loading in the active laser material via non-radiative decay (emission of phonons in the host material). Lifetime quenching can have different origins. Energy transfer processes between laser-active ions can be significant in materials with high active ion concentrations (particularly when ion clustering occurs), for this reason they are often called concentration quenching processes. Two examples of concentration quenching process that can lead to significant decrease in efficiency and extra heat loading in the gain medium are energy-transfer up-conversion (often called Auger up-conversion or cooperative up-conversion) and cross-relaxation of ions, schematically presented in Fig. 4.1a and 4.1b respectively.

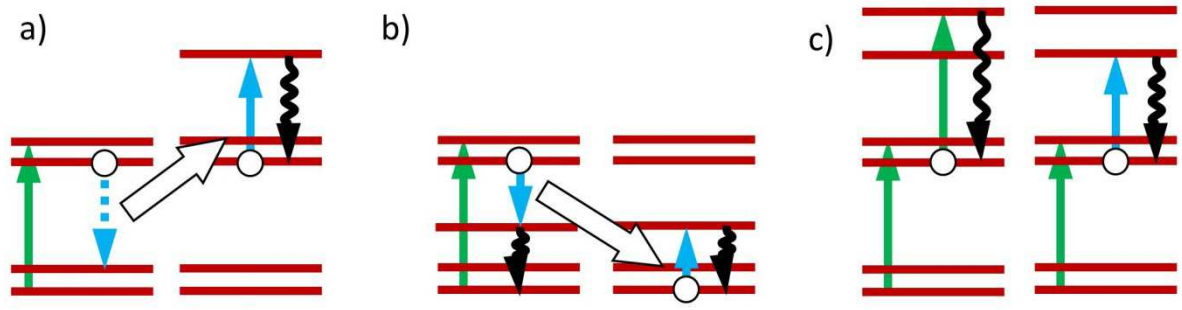

Figure 4.1: Schematic representation of lifetime quenching processes; a) energy transfer up-conversion, b) cross-relaxation of ions c) excited state absorption at pump and signal wavelengths

ETU occurs when two neighbouring ions (in this case both in the upper laser energy level) exchange energy. The donor ends up in the lower energy level, while the acceptor is transferred to a higher energy level, where the energies depend on the allowed transitions in the laser material. The acceptor eventually decays back to the upper laser level and the donor decays to the ground state, while these transitions can be radiative, non-radiative or a combination of both. Essentially, the ETU process converts two ions in the upper laser level into one ion in the upper level and one in the ground state plus the difference in energy contributing to thermal loading of the active medium and/or fluorescence at other wavelengths. Depopulation of the upper level due to ETU process increases for higher doping concentrations and higher population densities of the upper laser level [4.9].

Energy transfer can also lead to cross relaxation of ions (fig. 4.1b). The donor in the upper laser level state transfers its energy to the acceptor in the ground state and both ions end up in some intermediate energy level from where they both decay to the ground state via multi-phonon emission or in some cases via a radiative process. Essentially, cross relaxation process converts one ion in the excited state and one ion in the ground state to two ions in the ground state with the remaining energy contributing to thermal loading and/or fluorescence at different wavelengths.

Another mechanism that can quench the effective lifetime of the upper laser level, called excited-state absorption is schematically illustrated in fig. 4.1c. The ion in the excited state can be transferred to a higher energy state via absorption of a photon at pump or laser signal wavelength, before eventually decaying back to the upper laser level via non-radiative processes contributing to the thermal load. While ESA is a common problem in broadband gain media such as transition-metal-doped crystals with complicated energy levels structure, it is not present in laser materials with a simple electronic structure, such as Yb-doped crystals. Other mechanisms leading to lifetime quenching and heat generation in the active medium include direct multi-phonon emissions from the upper laser level to the lower electronic states, energy transfer to ions of different type (e.g. impurities in the laser material) or colour centres (i.e. defects in the crystal structure).

4.2.4. Thermal effects in the laser medium

All of the mechanisms reviewed above can deposit significant amount heat in the active laser material under strong optical pumping, which leads to increase in temperature in the laser medium. Without means for efficient heat removal this thermal load can lead to change in spectroscopy, change in thermo-optical and thermo-mechanical properties of the active laser medium, and ultimately to physical damage of the material via burning or melting. Active cooling is thus essential in most high power laser systems to remove the unwanted heat. All heat removal methods, however, induce a temperature gradient between the centre of the pumped region and the heat sink. For example, this temperature gradient leads to aberrated thermal lensing in case of a “bulk” end-pumped, edge-cooled solid-state laser or thermal guiding/anti-guiding in case of a fibre laser leading to laser mode distortion or loss. It also leads to thermally-induced stress that can result in added birefringence and lensing effects as well as physical damage by fracture. Thermal effects originating from both high temperature and strong temperatue gradient become more pronounced at high pump powers leading to reduced efficiency of the laser, beam quality degradation and ultimately to material damage.

a) Thermally induced stress

High pump power levels and the associated thermal loading in laser media cause differential expansion and thus induce stress in the active laser material. In general the refractive index value in the region under compression is different from that in the region under tension. In end-pump lasers compression occurs in radial, and tension in the tangential direction. Resulting birefringence causes retardation of tangential component with respect to the radial component of the electric field in the beam and thus significant depolarisation of the laser signal beam passing through the laser material. Consequently, this effect can lead to high loss in polarising elements in the laser resonator. Thermally induced depolarization is particularly problematic in gain media with low natural birefringence. Thermally-induced stress also sets the ultimate limit of how much power can be absorbed in the laser material under intense optical pumping. When the tension reaches the breaking stress of the material, the laser medium experiences a stress-induced fracture. The fracture limit depends mainly on heat deposition density per unit length, material properties and geometry [4.10].

b) Aberrated thermal lens

Aside from induced birefringence, thermally induced stress also affects the distribution of refractive index in the laser material. As the refractive index value is temperature dependent, the index of refraction is further affected by the temperature gradient. These two effects contribute to the effect known as thermal lensing - the laser signal beam passing through a radially symmetric laser material under intense pumping behaves as if it was transmitted through a highly abberated spherical lens. Another effect that degrades the beam quality even further is related to thermal-expansion-induced distortion of the end faces, known as end-face bulging. The relative contribution of the thermally induced birefringence, temperature gradient and end-face bulging to the overall thermal lens depends on the thermo-optical and thermo mechanical properties of the material. For many typical “bulk” solid-state laser materials the refractive index variation with temperature dominates, (it accounts for >80% of the thermal lens contribution in the case of Nd:YAG [4.10]).

4.2.5. Impact of laser medium geometry

Many laser architectures with different geometries of the laser medium, aiming for output power and brightness scaling have been developed up to date. The most popular approach to reduce thermal effects in the laser medium is to increase the ratio of the cooled surface area to the pumped volume. This can be achieved in various ways, and solid-state laser technology development took several courses, concentrating around different types of the laser medium geometry. Some of the more popular architectures with their strengths and limitations in the pursuit of scaling the output to very high power levels are discussed as follows.

a) Side-pumped slab lasers

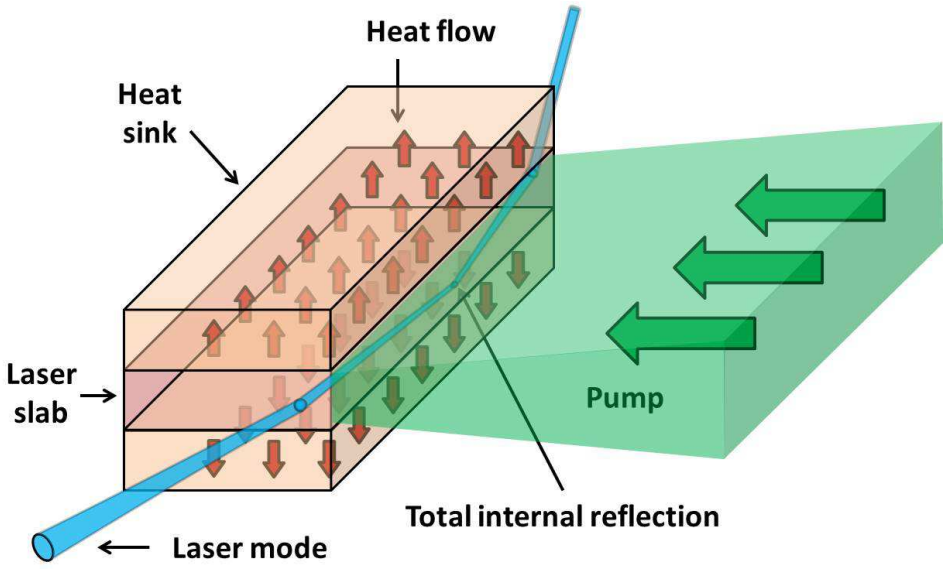

Figure 4.2: Side-pumped slab laser configuration

Diode pumped slab lasers benefit from side-pumped geometry schematically illustrated in fig. 4.2. In this scheme, heat is extracted through the two largest areas - top and bottom faces of the active medium, which remain in thermal contact with water-cooled heat sinks. Pump light is generally delivered through one or two remaining side surfaces, while the laser radiation is orthogonal to the pump beams. This configuration benefits from high aspect ratio of the side surfaces which allows

matching them to the high-aspect-ratio pump beam as emitted directly from a laser diode bar. This eliminates the need for sophisticated beam shaping systems, places low demand on the quality of the pumping beam and results in high pump coupling efficiency. The limitation of the slab approach, however, is a poor overlap between the laser mode and the pumped volume which means the stored energy is difficult to extract from the laser material. For media with high absorption at pump wavelength, the region of highest inversion density is located close to the pumped face. For this reason it is often beneficial to transmit the laser mode through the laser medium in such a manner that it undergoes a total internal reflection from the pumped surface. The overlap between the population-inverted volume and the laser mode is then larger than in a single-pass scheme and the overall efficiency of the laser increases. Another attraction to this approach is that the laser beam is being horizontally inverted upon reflection. Hence, the effects caused by the horizontal gradients in refractive index and gain acquired during the pass through the first half of the active medium are compensated for during the pass through the second half of the laser material. This results in an improved beam quality with little degradation in the horizontal direction. Multiple total internal reflections are often used in the so-called “zig-zag” laser geometry. Another way to increase the extraction efficiency is to allow for multiple passes through the active medium, each one directed for different part of the pumped volume, by using external mirrors folding the laser cavity. From a thermal perspective, slab lasers benefit from lower temperature difference and higher fracture limit. However, due to lack of radial symmetry, thermal lensing in slab lasers can be slightly more problematic to handle due to strong astigmatism of the thermal lens (the temperature profile is relatively flat in the two long dimensions, but a strong gradient exists in the vertical direction). Thermally-induced stress associated which the temperature gradient is also significant in slab lasers. It is typically strongest at the sides and may cause fracture of the crystal at high powers. For this reason the slab needs to be made as thin as possible with the width and length increased. Side-pumped slab lasers can be scaled to very high output power levels, potentially hundreds of kilowatts [4.11] but they typically offer much worse beam quality than thin-disk and fibre laser architectures.

b) End-pumped rod lasers

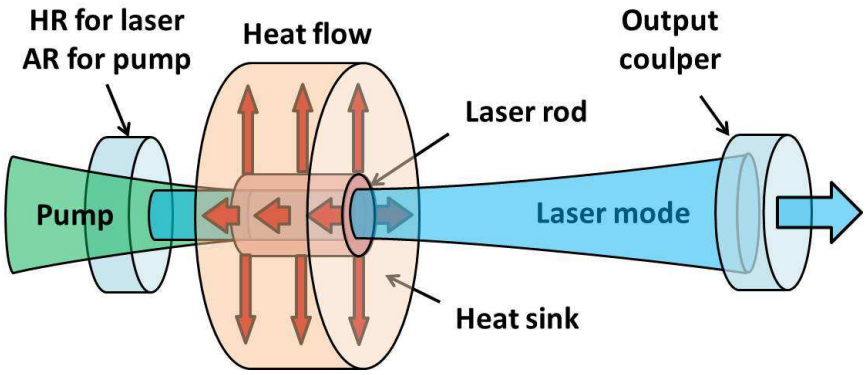

Figure 4.3: Typical arrangement of an end-pumped rod laser

In the end-pumped rod laser configuration (fig. 4.3) heat is extracted through the side surface of the rod, while the pump is delivered through the circular face and is collinear with the laser signal. Unlike side-pumped schemes, this approach enables good spatial overlap between the fundamental mode of the laser resonator and the pumped volume allowing for high extraction of the stored pump energy. The cylindrical symmetry of the end-pumped laser rod implies that the thermal lensing effects are radially symmetric and can be compensated for with relatively simple optical arrangements. On the other hand, thermal lensing effect is particularly strong in laser rods and leads to strong aberrations in the wings of the pumping beam. The most popular way to deal with this effect is to use longer rods and lower the active ion concentration in the laser material so the thermal load is distributed over the larger volume, temperature gradient is lower and the heat can be extracted more efficiently. This requires a pump source delivering a high quality beam that can maintain small size across the crystal of increased length. Other techniques aiming to mitigate thermal effects include using composite laser crystals terminated with undoped caps, or multi-segmented rods comprising sections with different doping levels for more uniform distribution of the thermal load. An extreme case of an end-pumped laser rod is that of a “single-crystal fibre”. Such fibres can be pulled directly from a melt, with no subsequent polishing except for the input and output faces. They contain a waveguide structure for the pump light, which is reflected at the crystal-air (or crystal-coating) interface, while the laser mode is propagated free-

space in the volume of the crystal medium. Rod lasers compete with slab, fibre and thin-disk laser architectures up to the range of several hundred watts, possibly even a few kilowatts [6], but scaling to higher power levels is rather challenging.

c) Face-pumped thin-disc lasers

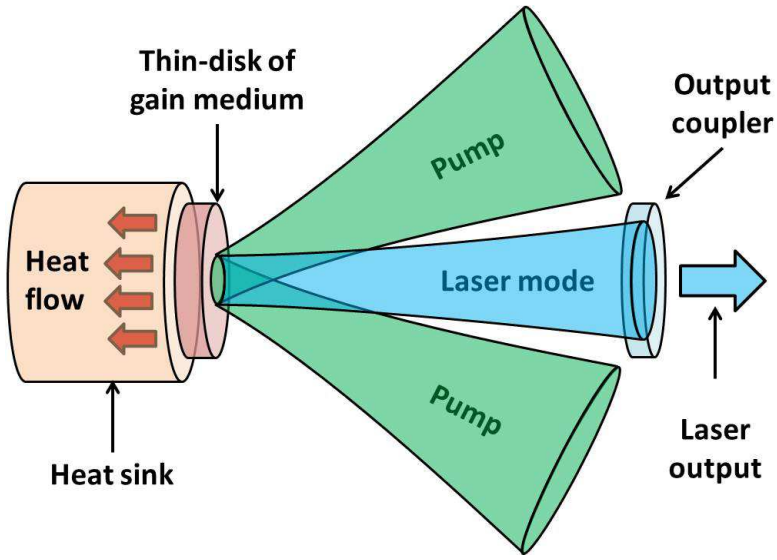

Figure 4.4: Typical thin-disk laser configuration

Fig. 4.4 illustrates a typical thin-disk laser configuration. This architecture is based on a thin-disk (typically few hundred microns in thickness) of laser gain medium with the back surface bonded to a water-cooled heat sink. The back surface is generally HR-coated and the front surface AR-coated for both laser and pump wavelengths. The pump beam is delivered at an angle to the resonator mode. The laser resonator can be formed between the back, HR-coated surface of the gain medium and an output coupler, but the thin-disk can also act as a cavity folding mirror so the round-trip gain in the resonator is doubled and threshold for lasing reduced. For this reason more complex designs using multiple reflections from the thin-disk per round-trip are typically used. Due to low absorption resulting from the limited thickness of the gain medium, the pump beam is often recycled after first reflection and directed back onto the pumped region in a multi-pass pump configuration. For a thin-disk scheme, the cooling surface to the pumped volume ratio is large, and the feat flow is collinear with the laser beam axis, which

dramatically reduces thermal effects. Furthermore, power scaling can be aided by simply increasing the pumping beam radius, thus increasing the cooling area as well as the area of the pumped volume, and adjusting the resonator design for increased laser mode radius. In this way, peak intensity and peak temperature can remain unchanged even for higher pump and output power levels. Consequently, the main source of thermal lensing is from mechanical stress in the disk leading to bending of the crystal due to the difference in expansion of its front and back surface, rather than aberrations via thermal dependence of the refractive index. Both effects, however, can be reduced by keeping the disk thickness small. Another limitation in thin-disk laser architectures arises from the amplified spontaneous emission (ASE) in the transverse direction, which limits the gain for the laser signal in the longitudinal direction. This effect can be supressed by using composite crystals with undoped layer bonded over a thin active layer and absorbing coatings on the sides of the thin-disk to prevent Fresnel reflection from the air-crystal boundaries. A 5 kilowatt single disk laser based on Yb:YAG capable of fundamental mode operation up to 300 W has been demonstrated [4.13]. Thin-disk lasers are currently in fierce competition with high-power fibre lasers. Within the next years, both technologies are expected to show significant further progress, and it is not entirely clear which one will acquire the larger market share.

d) Cladding-pumped fibre lasers

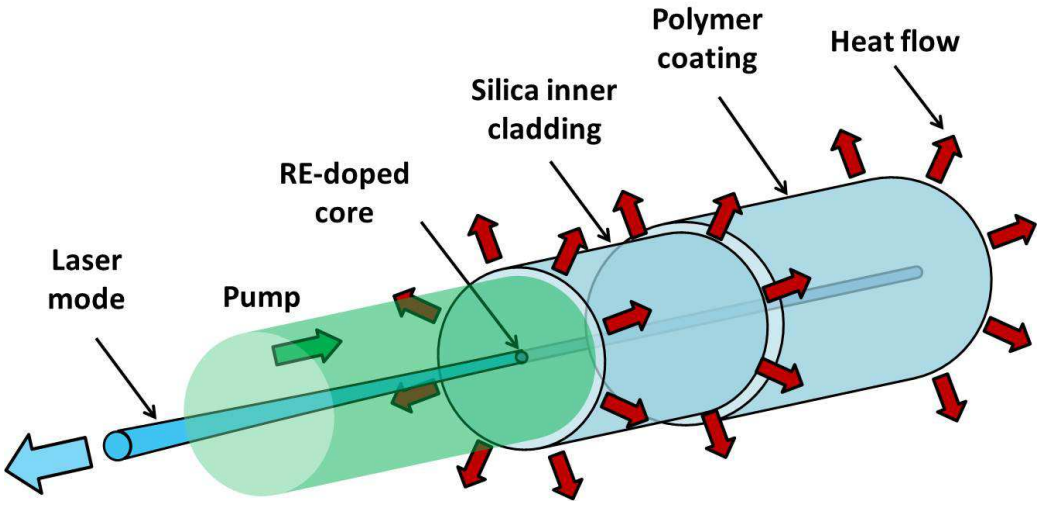

Figure 4.5: Cladding-pumped fibre end in a high-power fibre laser

While the first fibre lasers delivered output power in the order of few milliwatts, modern high power lasers are capable of several kilowatts of output power from a single fibre. This power scaling potential arises from a very high surface-to-volume ratio allowing for efficient removal of the thermal load and the waveguiding geometry, which dominates over thermo-optical problems under conditions of significant heating. High power fibre lasers are nearly always based on double-cladd fibres with a silica glass inner cladding and a rare-earth-doped core. These architectures are cladding-pumped with high power diode lasers, typically fibre-coupled diode bars. Light can be launched into the inner cladding through the glass-air interface of the front face of the fibre (fig. 4.5) using free-space optics or alternatively, using an all-fibre pump delivery scheme (see section 4.3.1). The laser resonator can be formed with free space mirrors in external cavities or internally between fibre Bragg gratings (FBG) written into the core. In many configurations even the Fresnel reflections from cleaved faces of the fibre provide sufficient feedback for lasing. If the core of the fibre supports only the fundamental mode the output from the fibre laser has a diffraction-limited beam quality. For very high output power levels, the core needs to be fairly large to avoid too large optical intensities, which also helps to improve the pump absorption dependent on the cladding to core area ratio. For such larger mode areas, the beam quality can be degraded due to the presence of higher order modes, but can be still fairly good compared to other laser architectures operating at similar power levels.

High-power fibre laser systems often use laser-amplifier combinations where a low power master oscillator is followed by a chain of fibre amplifiers, typically with increasing mode areas. In this way it is easier to control the properties of the seed laser to obtain high power output with desired properties at the end of an amplifier chain. Heat management is typically easy in fibre lasers when compared with other laser architectures. Air cooling is sufficient in many cases. For more demanding applications water cooling and increased length of the fibre with lower doping concentration can be applied. The output power from fibre lasers is limited by large optical intensities in the core area and the onset of damage. High optical intensities also lead to nonlinear effects in the fibre core, significant even for continuous-wave operation and potentially reducing the maximum output power that can be obtained from the fibre laser. Despite these limitations, an output power of 10 kilowatts has

been recently demonstrated from a single-mode fibre [4.7] and further increase in output power should be possible. The fibre laser architecture is also well suited for various beam combination techniques - once the limit of the power obtainable from a single fibre has been reached, this approach will be an option towards further power scaling. It is expected that laser systems using beam-combination techniques will reach output power levels in the range of hundreds of kilowatts in the near future. Possible applications for such systems include directed energy weapons [4.14], long distance optical communication [4.15] and materials processing [4.16]. Novel fibre-based laser systems aiming for power scaling and efficient nonlinear frequency conversion are the main subject of this thesis, hence the limitations and general power scaling strategy for fibre laser architectures will be discussed in more detail later in section 4.3.

4.3. Power scaling of cladding-pumped fibre lasers

4.3.1. Core- and cladding-pumping

Most common rare-earth elements used in high power fibre lasers and amplifiers are: Ytterbium (Yb^{3+}) emitting in the region of 1-1.1 µm, Erbium (Er^{3+}) emitting around 1.55 µm, Thulium (Tm^{3+}) emitting at 1.8-2.0 µm and Holmium (Ho^{3+}) emitting around 2.0-2.1 µm. Other, lower power fibre architectures sometimes use different wavelengths emitted by rare-earth elements such as Praseodymium (Pr^{3+}) at 1.3 µm and Samarium (Sm^{3+}) at 0.65 µm as well as Bismuth (Bi^{3+}) in the 1.3-1.5 µm region.

a) Core-pumping

Pump light can be launched into the fibre core or into the inner cladding, depending on the pump beam quality. In a core pumping arrangement the refractive index profile across the fibre is generally chosen such that $n_{clad} < n_{core} < n_{out}$, so that only the modes propagating in the doped core are supported (where n_{clad}, n_{core} and

n_{out} stand for the index of refraction in the inner cladding, RE-doped core and outer cladding regions respectively). This scheme offers a high absorption coefficient due to the high overlap factor between the pump field and the RE-doped region, which allows for using shorter device lengths. On the other hand, core-pumping requires a pump beam of high quality that can be coupled into a relatively small core area. For a core of the step-index fibre to be robustly single mode at wavelength λ its normalised frequency, defined as:

$$V = \frac{2\pi r_{core}}{\lambda} NA_{core} \tag{4.7}$$

(where r_{core} is the core radius and $NA_{core} = \sqrt{n_{core}^2 - n_{clad}^2}$ is its numerical aperture), must be in the range of $0 < V < 2.405$. By comparing definitions (4.4) and (4.7) it is clear that beam propagation factor of the pump beam must satisfy at least $M^2 \leq V/2$ in order to be able to couple efficiently into the fibre core.

b) Cladding-pumping

In order to scale the output from fibre lasers to very high power levels, high power diode sources with poor beam quality must be used. Core coupling is not possible in such cases and the fibre design has to be changed so it allows for propagation of the pump light in the inner cladding, i.e. $n_{core} < n_{clad} < n_{out}$. The requirement for pump beam quality in this cladding-pumping scheme is relaxed due to the increased spot size and acceptance angle of the inner cladding so that $M^2 \leq \pi r_{clad} NA_{clad} \gamma_{uf} / \lambda$, where r_{clad} is the inner cladding radius, $NA_{clad} = \sqrt{n_{clad}^2 - n_{out}^2}$ is its numerical aperture (acceptance angle) and γ_{uf} is a factor which takes into account the need to underfill the inner-cladding and inner-cladding's NA to avoid pump-induced damage to the outer-coating. The value for γ_{uf}, typically in the 0.7-1 range, depends on the situation, and the pump power in particular.

Pump light propagating in the inner cladding only partially overlaps with the core area with the result that much longer device lengths are required for efficient pump absorption compared with core-pumped architectures. A conventional inner-cladding with radial symmetry allows for helical ray trajectories around the core region (fig. 4.6a), and as such is not preferred. Although pump absorption can be increased by bending the fibre, this approach is not very effective for larger fibres and higher NA's. Other structures, breaking the circular symmetry, thus allowing for increased absorption have been developed [4.17-4.19], with some examples schematically illustrated in fig. 4.6.

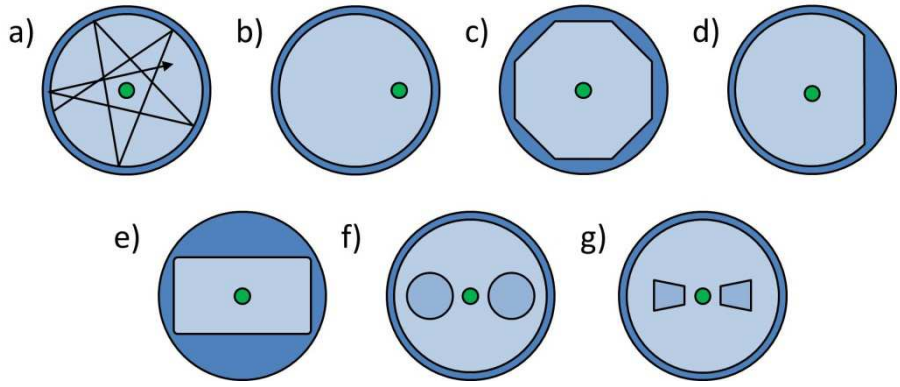

Figure 4.6: Typical inner-cladding structures for cladding-pumped fibre lasers:
a) conventional radially symmetric with indicated helical ray trajectories b) with an offset core c) octagonal d) D-shaped e) rectangular f) "Panda" g) "Bow-tie"

One method to increase pump light absorption is to break the radial symmetry by offsetting the fibre core (fig. 4.6b). Since a large offset is required for significant increase in absorption, fabrication and splicing of such a fibre is quite difficult. Fabrication of the polygon-shaped inner-claddings (octagonal cladding in fig. 4.6c) can be somewhat challenging, but they offer very effective pump absorption and, being axially symmetric, are relatively easy to splice. Fibres with D-shaped inner cladding (fig. 4.6d) are relatively easy to fabricate and offer very effective way to increase the pump absorption. Hence, they are popular with laser systems pumped with a circular free-space beam where splicing is not required. For lasers pumped with asymmetric beams the rectangular cladding (fig. 4.6e) can be more suitable. The inner cladding design can be also altered to induce strong birefringence in the fibre core. If polarised light is then launched into such a core, its polarisation state is

maintained over the entire length of the fibre. Such fibres are desired in both fibre oscillators and amplifiers. The most common “Panda” (fig. 4.6f) and “Bow-tie” (fig. 4.6e) inner cladding geometries incorporate stress rods to induce strong stress birefringence in the core and break the radial symmetry by introducing a refractive index change in two regions of the cladding’s cross section, thus increasing the pump absorption.

Another way to increase the pump absorption coefficient is to increase the core size to the inner-cladding area ratio. Apart from increased pump absorption, larger cores offer lower optical intensity for a given level of output power, thus higher threshold for nonlinear effects and optical damage. According to (4.7) for the larger fibre core to remain robustly single-mode at given wavelength, its numerical aperture has to be lower. Current fabrication techniques can achieve numerical apertures as low as 0.04-0.05 for step index fibres, which places an upper limit for the size of a single-mode core. For a fibre operating at 1 um, this means the largest core radius that supports only the fundamental mode is $r_{core} \approx 10$ um.

c) Host material

Silica glass is generally the material of choice for high-power fibre lasers and amplifiers for a number of reasons. Two of the most important factors are a high melting temperature and mechanical strength of silica, allowing for relatively easy power handling at high pump and laser output power levels. Another important feature is its very low loss in the near-infrared spectral region which minimises background losses and heat loading in fibre lasers and amplifiers. Silica based systems are also compatible with existing telecom components, and relatively simple and well-established telecom fibre fabrication techniques. Splicing and cleaving silica glass is also relatively easy compared to other host materials. Finally RE doping offers access to broad range of laser wavelengths desired in high-power laser applications. Other glasses (e.g. fluoride glass) can offer an extended range of operating wavelengths in visible and mid-infrared regimes, but these fibres have a relatively poor power handling capability and are not compatible with silica-based components.

d) Pump delivery schemes

In case of cladding-pumped fibre lasers the simplest way is to launch the pump light directly into the inner cladding at one or both fibre ends of the active fibre. This technique does not require special fibre components; however, high-power pump radiation propagates through air, free-space optics and an air–glass interface, which is very sensitive to dust and misalignment. A common approach to make the pump delivery more robust is the use of tapered fibre bundle pump combiners [4.20] that transfer the pump power from multiple fibre-coupled laser diode sources into one large-core multimode fibre that can be spliced directly to the inner cladding of the RE-doped fibre. Several alternative pump injection techniques have been developed as well. One of the most powerful single-mode fibre lasers to date used a “tandem pumping” scheme, where the main active fibre was in-band pumped with other fibre lasers [4.7]. Other kilowatt class fibre lasers use “GT-wave fibre” technology where the pump light is launched into two undoped fibres wound around the active fibre so that the light is gradually transferred into the RE-doped fibre [4.21]. One of the first kilowatt class fibre laser systems used three multimode fibres tightly coiled in a form of disks for easier thermal management, side-pumped directly with diode bars [4.22]. Other simple side-pumping scheme uses v-grooves and substrates to deliver pump light in multiple injection points [4.23].

In general, there are many types of diode pump sources and many different coupling schemes for launching pump light into double-clad fibres. In all cases, however, brightness of the single pump emitter is the ultimate limiting factor on how much pump power can be launched into a given fibre. Both end-pumping and side-pumping have their strengths and limitations. End-pumping techniques offer relatively higher brightness of the pump light launched into the fibre, shorter device lengths and more flexibility in fibre design. Side-pumping configurations, On the other hand, allow for distributed pumping (and distributed heat loading), offering robust and alignment free architectures with easy access to the ends of the active fibre. The final choice of pumping scheme is thus dependent on the specific application.

4.3.2. Thermal effects in fibres

Fibre lasers benefit from a geometry with large surface to core volume ratio facilitating efficient heat removal. Thermal loading can be spread over a long length of the active medium, and waveguide properties of the core usually dominate over thermally-induced changes in the refractive index. Although thermal management in fibres is much easier than in other laser architectures, fibre lasers are not completely immune to the effects of heat generation. Various sources of heat discussed in section 4.2.4 contribute to heat deposition in the fibre core. Quantum defect heating, excited state absorption, energy-transfer up-conversion and transfer to non-radiative sites in the core are the most common sources of thermal loading in high-power fibre lasers. Yet another mechanism that can add up to detrimental thermal effects arises from the absorption of fluorescence and stray pump light in the outer cladding and fibre-holding mounts.

a) Melting of the core and polymer coating damage

A fibre laser with its outer cladding heat sunk or convection cooled can be considered as a medium of cylindrical geometry with periphery at a fixed temperature. The heat deposition per unit length required to soften or melt the material can be calculated from steady-state heat transfer equation [4.24]. For a double-clad fibre, maximum heat deposition per unit length before onset of softening or melting can be expressed as:

$$P_{hmax} = 4\pi(T_m - T_s)\left[\frac{1}{K_{clad}} + \frac{2}{K_{clad}}\ln\left(\frac{r_{clad}}{r_{core}}\right) + \frac{2}{K_{out}}\ln\left(\frac{r_{out}}{r_{clad}}\right) + \frac{2}{r_{out}H_{out}}\right]^{-1} \quad (4.8)$$

where $T_m \approx 2000$ K is the softening temperature of the silica core, T_s is the ambient temperature, $K_{clad} \approx 1$ $Wm^{-1}K^{-1}$ and $K_{out} \approx 0.1$ $Wm^{-1}K^{-1}$ are the thermal conductivities of the silica inner cladding and polymer outer cladding respectively, r_{core}, r_{clad} and r_{out} are the radii of the fibre core, inner cladding and polymer coating respectively, while H_{out} is the heat transfer coefficient for the outer polymer coating. This suggests that in a typical fibre laser configuration convection cooling

(i.e. H_{out} in the order of ~10 $Wm^{-2}K^{-1}$) is generally sufficient for keeping a fibre core below its melting point. However, the threshold for thermal damage in the polymer coating is generally reached first. For a typical polymer outer-coating the maximum temperature that can be tolerated before the coating begins to degrade $T_d \approx 150°C$. This leads to the following upper-limit on the heat deposition density:

$$P_{hmax} = 4\pi(T_d - T_s)\left[\frac{2}{K_{out}}\ln\left(\frac{r_{out}}{r_{clad}}\right) + \frac{2}{r_{out}H_{out}}\right]^{-1} \quad (4.9)$$

which is roughly one order of magnitude lower than the heat deposition required for melting the fibre core. Therefore, the strategy required for scaling to higher power levels is to increase the inner cladding diameter whilst reducing the outer polymer coating thickness and applying more aggressive cooling (i.e. conduction cooling with H_{out} in the order of ~1000 $Wm^{-2}K^{-1}$). Low-index glass outer cladding is also an alternative for kilowatt class fibre lasers.

b) Thermally-induced stress

Thermal stresses in a fibre can be calculated from the temperature distribution [4.24]. Thermally-induced fracture in fibre occurs when those stresses exceed the tensile strength of silica. The maximum allowed heat deposition density before the onset of fracture is given by:

$$P_{hmax} = \frac{4\pi R_t}{1 - (r_{core}^2/2r_{clad}^2)} \approx 4\pi R_t \quad (4.10)$$

where $R_t \approx 4300$ W/m is a thermal shock parameter for silica, and the approximation is valid for small core to inner cladding radius ratio. This suggests that thermally-induced fracture is not likely to be a problem in fibre lasers with heat deposition density < 50 kW/m. This is beyond current capacity of pump sources and well above the damage thresholds arising from other thermal effects.

c) Thermal lens

Thermally-induced temperature gradients in the fibre core can produce a modified refractive index profile and hence thermal guiding. This thermal lens becomes competitive with the index guiding from the fibre core when at the heat deposition density approximately equal to [4.25]:

$$P_{hmax} \approx \frac{\pi K_{clad} \lambda_s^2}{2 \frac{dn}{dT} r_{core}^2} \tag{4.11}$$

where λ_s is the wavelength of the laser signal and dn/dT is the temperature gradient of the refractive index. For silica glass $\mathrm{dn/dT} \approx 11.8\times 10^{-6}\ \mathrm{K}^{-1}$ [4.26]. Thermal guiding has significant effect on guiding properties and hence performance in large-core fibres. For materials with positive dn/dT such as silica glass thermal guiding leads to tighter mode confinement in the fibre core, degradation in beam quality and reduced efficiency of the laser. In materials with negative dn/dT such as phosphate glasses, the same effect is responsible for mode-distortion and increased propagation loss due to less confinement in the core which also leads to reduced efficiency. Thermal guiding is not a serious problem for conventional fibres with relatively small cores, but will impact on performance in large core devices.

d) Change in spectroscopy

According to (2.11) and (4.2), threshold and gain are functions of emission and absorption cross sections which are in general temperature dependent. As population of sub-levels is proportional to the Boltzmann factor, an increase in temperature due to heat generation in the fibre increases threshold and reduces gain. This effect will be most pronounced at shorter wavelengths for transitions with more three-level character. As a result, efficient operation of the fibre laser may be limited to longer wavelengths.

Assuming all pump power is absorbed in the fibre core, the maximum power that can be extracted from a fibre laser can be expressed as a function of fractional power converted to heat γ_h and written as:

$$P_{max} \approx P_{hmax} L(1-\gamma_h)/\gamma_h, \tag{4.12}$$

where L is the length of the fibre laser. If we consider the quantum defect a main source of generated heat, i.e. $\gamma_h \approx Q_d$ a free-running Yb-doped fibre laser pumped at maximum absorption wavelength will yield $P_{max} \approx 10 P_{hmax} L$, whereas Er-Yb-codoped system, pumped at the same wavelength - only $P_{max} \approx 1.7 P_{hmax} L$. In any case, however, the maximum power that can be extracted is directly proportional to the maximum heat deposition density limited by various thermal effects. The lowest value of P_{hmax} calculated from (4.8-4.11) will limit the maximum output power that can be obtained from the fibre laser.

4.3.3. Nonlinear effects in fibres

The response of a dielectric medium to light becomes increasingly nonlinear with growing laser signal intensity. This plays particularly important role in fibre laser architectures where tight optical confinement in the core area is combined with low material losses and long interaction lengths. When considering continuous-wave high power fibre lasers and amplifiers there is an interest in broad bandwidth sources as well as in single-frequency lasers that operate with very narrow spectral lines. These two types of systems have different, but functionally similar limitations arising from non-linear effects. In the broadband case, the relevant limiting effect is stimulated Raman scattering (SRS). In the narrowband case, output power can be limited by stimulated Brillouin scattering (SBS). For pulsed operation, other nonlinear effects can limit the output power. These include self-focusing occurring at relatively high peak powers (> 4 MW in silica optical fibres [4.27]), self- and cross-phase modulation as well four-wave mixing in multi-mode and birefringent fibres. As this thesis targets CW fibre lasers, only stimulated inelastic scattering processes that play significant role in such systems will be discussed:

a) Stimulated Raman scattering

In stimulated Raman scattering, a laser signal photon excites vibration in the glass lattice and scatters into a photon with a lower frequency. The energy difference is absorbed by the host material in form of an optical phonon (heat), as the lattice makes the transition between two vibrational states. Photons resulting from Raman scattering form a Stokes wave (at wavelength λ_{Stokes} longer than the main laser signal wavelength λ_{laser}) that can be guided in the fibre core in both directions and experience amplification by stimulated emission at this new wavelength if the latter is within Stokes gain bandwidth. This Raman amplification process along propagation direction *z* can be described with a simple set of differential equations:

$$\begin{aligned} \frac{dI_{Stokes}}{dz} &= I_{Stokes}(g_R I_{laser} - \alpha_{Stokes}), \\ \frac{dI_{laser}}{dz} &= -I_{laser}(g_R I_{Stokes}\frac{\lambda_{Stokes}}{\lambda_{laser}} + \alpha_{laser}), \end{aligned} \tag{4.13}$$

where α_{Stokes} and α_{laser} are absorption coefficients at Stokes and laser signal wavelengths respectively, I_{Stokes} and I_{laser} are optical intensities at Stokes and laser signal wavelengths respectively and $g_R \approx 1 \times 10^{-13}$ m/W is the Raman gain coefficient of silica glass for polarised light (the value is a factor-of-two lower for unpolarised signal). The Raman gain spectrum in silica optical fibres spans from 0 to ~40 THz with the gain maximum corresponding to ~13 THz frequency shift (~50 nm shift towards longer wavelengths for a laser signal ~1.1µm).

Although SRS has a number of important applications, such as Raman lasers [4.28] and amplifiers [4.29], it mainly plays a detrimental role in high-power fibre lasers as it acts as a loss mechanism. Assuming that Raman gain spectrum has a Lorentzian line shape and that polarisations of laser signal and Stokes wave are maintained, "threshold" for stimulated Raman scattering is given by [4.30]:

$$P_{th}^{SRS} \approx \frac{16A_{eff}}{g_R l_{eff}} \tag{4.14}$$

where A_{eff} is the effective area of the laser signal mode field, and $l_{eff} = [1\text{-}\exp(-\alpha_{laser}L)]/\alpha_{laser}$ is the effective Raman length at the end of the fibre of length L. Once the threshold for SRS is reached, the energy from the laser signal power is transferred to the Stokes wave very efficiently. The latter can then act as the pump for a second-order Stokes wave and so on. SRS is one of the main effects limiting maximum power obtainable from cladding pumped fibre lasers and amplifiers. Possible solutions to mitigate the effects of SRS include increasing the core size, shortening length of the fibre and introducing distributed loss at Stokes wavelength.

b) Stimulated Brillouin scattering

Stimulated Brillouin scattering is another inelastic scattering process which also involves scattering a laser signal photon to a lower frequency photon. The energy difference is absorbed by the host material in a form of an acoustic phonon. High-intensity laser signal in the fibre core can create, via electrostriction process, a travelling acoustic wave propagating with a speed of sound v_A. The laser signal wave is scattered backwards via Bragg diffraction at this acoustic wave and undergoes frequency shift $\nu_B = \nu_{laser} - \nu_{Stokes} = 2nv_A/\lambda_{laser}$ via Doppler effect. In silica glass v_A ≈6 km/s, so the frequency shift ν_B is 17.5 GHz (or ~0.06 nm wavelength shift) at $\lambda_{laser} \approx 1$ µm. Amplification of the Stokes Brillouin wave can be described by the following equations:

$$\begin{aligned} \frac{dI_{Stokes}}{dz} &= -I_{Stokes}(g_B I_{laser} - \alpha), \\ \frac{dI_{laser}}{dz} &= -I_{laser}(g_B I_{Stokes} + \alpha), \end{aligned} \tag{4.15}$$

where α is a common loss coefficient for Stokes and laser signal waves (due to the very small frequency shift), and g_B is a Brillouin gain coefficient. If we assume exponential temporal decay of the acoustic wave with phonon lifetime τ_B, the Brillouin gain spectrum $g_B(\nu)$ has a Lorentzian shape with FWHM bandwidth $\Delta\nu_B = 1/(\pi\tau_B)$ [4.31] according to:

$$g_B(\nu) = \frac{\Delta\nu_B^2 g_B(\nu_B)}{4(\nu - \nu_B)^2 + \Delta\nu_B^2} \tag{4.16}$$

where

$$g_B(\nu_B) = \frac{2\pi n^7 p_{12}^2}{c\lambda_{laser}^2 \rho_m v_A \Delta\nu_B}$$

n is the refractive index, p_{12} is longitudinal elasto-optic coefficient and ρ_m is material density. In pure silica $g_B \approx 1 \times 10^{-10}$ m/W and $\Delta\nu_B \approx$ 10MHz but in silica fibres the Brillouin linewidth is generally broader (~50-100 MHz) [4.25] and Brillouin gain is lower, due to the presence of RE dopants and inhomogeneities. For a laser linewidth $\Delta\nu_{laser}$ comparable or broader than the Brillouin gain spectrum bandwidth $\Delta\nu_B$, the maximum value of Brillouin gain decreases according to:

$$g_{Bmax} = \frac{\Delta\nu_B}{\Delta\nu_B + \Delta\nu_{laser}} g_B(\nu_B)\,, \tag{4.17}$$

It is clear from (4.17) that SBS is mainly an issue for very narrow linewidth sources, such as single-frequency lasers. The "threshold" for SBS is given by [4.30]:

$$P_{th}^{SBS} \approx \frac{21 A_{eff}}{g_B l_{eff}} \tag{4.18}$$

In practice threshold can be still somewhat higher than calculated from (4.18) due to dopants and inhomogenities, but this rough guide indicates that SBS can be particularly challenging to overcome when scaling the output power of single frequency fibre lasers. SBS acts as a distributed loss limiting the maximum output power that can be extracted from narrow line fibre lasers. Possible solutions mitigating the effects of SBS include increasing the core size, shortening length of the fibre and introducing a temperature gradient over the length of the fibre [4.32].

4.3.4. Optical damage in fibres

Optical damage in optical fibres caused by electron avalanche driven by high intensity laser beams has been studied extensively [4.33-4.35], yet an accurate optical damage threshold value for silica glass has not been established. There are optical damage mechanisms that are unique to the fibre architecture, such as the "fibre fuse effect" [4.36], that should also be taken into consideration. Fibre damage is typically observed at the end facets, so end-caps allowing the fibre mode to expand in bulk silica prior to striking an air-glass interface can increase the surface damage limit. Without end-caps the surface damage limit is in the order of I_{damage} ~10 W/μm^2 for silica glass [4.37]. For fibres with spliced end-caps the surface damage threshold for bulk silica is I_{damage} ~20 W/μm^2 [4.38]. Clearly, the maximum output power, P_{max} that can be extracted from the fibre is limited by these optical damage thresholds according to:

$$P_{max} = I_{damage} A_{eff} \tag{4.19}$$

4.3.5. Power scaling strategy

J. W. Dawson *et al.* [4.25] constructed a relatively simple theory combining all effects limiting the output power obtainable from a single fibre laser, as discussed in sections 4.2.3-4.2.5. After adding one "soft" constraint due to limited available brightness of pump sources and possible doping concentrations, they concluded that a "hard" limit on the output power from a 'broadband' fibre laser is around 36 kW and from a narrowband fibre laser is around 2 kW. Main results of this analysis are shown in fig. 4.7.

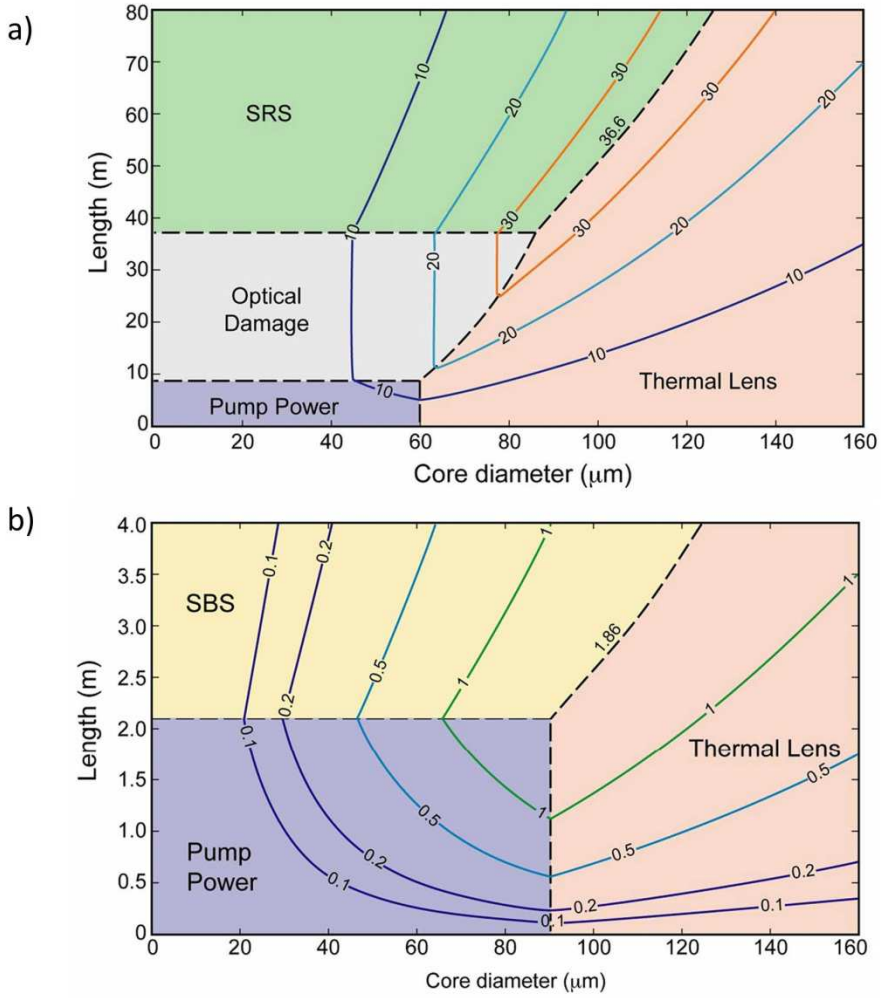

Figure 4.7: Contour plot presenting the limit of maximum output power (in kilowatts) extractable from a typical single fibre laser due to thermal, nonlinear and optical damage effects as well as limited brightness of the pump source as a function of fibre length and core diameter. a) Broadband fibre laser case (SBS effects neglected) b) Narrowband fibre laser case (SRS effects ignored) [after 4.25]

Fig. 4.7a presents the maximum output power that can be extracted from a typical Yb-doped silica fibre laser cladding pumped with a diode source of maximum brightness $B \approx 10\ \mathrm{MW/cm^2 \cdot sr}$. Although the brightness of diode pump sources increased since 2008, and the pump power limited region area would be smaller for modern laser systems, the output power is still ultimately limited by SRS and thermal lensing to the level of ~36.6 kW for a ~38 m long fibre with 85µm core. For shorter fibres with the same core size the maximum output power is likely to be reduced by thermal lensing effects, while for smaller core sizes the output power will be limited

by surface optical damage (or SRS in case of longer fibres). Narrowband fibre lasers suffer from the same limitations with an additional constraint of SBS strongly limiting the output power even for relatively short devices (fig.4.7b – pump power limited region calculated for diode lasers of maximum brightness $B \approx 2$ MW/cm^2·sr.). The SBS threshold combined with thermal lensing ultimately limit the output power of these sources to ~1.8 kW. These numbers can be improved by using special waveguide designs to supress detrimental SRS and SBS effects [4.39], applying more aggressive cooling techniques as well as modifying material composition to obtain higher thermal and optical damage thresholds. Nevertheless, physical mechanisms described in sections 4.2.3-4.2.5 are most likely to remain the main factors limiting power scaling of fibre lasers and amplifiers.

It is clear from fig. 4.7 that within certain constraints, scaling the core diameter and the fibre length allows further power scaling. While it is generally straightforward to increase the fibre length up to 40-50 metres without affecting the laser's performance, scaling the core radius typically leads to a number of problems. The number of modes supported by the fibre core is greater for larger core diameters. This has a dramatic impact on the output beam quality as well as beam pointing stability, and many applications require single-spatial mode or very few modes operation. Although the maximum core diameter supporting only fundamental mode is around 20 µm, as explained in section 4.2.2, relatively good beam quality has been demonstrated from few-mode double-clad fibre lasers with cores as big as 30 µm [4.40]. Fibres of larger diameter are generally strongly multi-mode with the number of guided modes $\sim V^2/2$. As a rough guide, in the worst case scenario, the beam quality (M^2) $is \approx V/2$ when all modes are excited.

One way to obtain single-mode operation is to selectively excite one (fundamental or higher order mode) in the fibre. This condition is quite difficult to obtain in a conventional step-index fibre as large modes are likely to scatter into their neighbouring mode due to perturbations of the waveguide and finite manufacturing tolerance [4.41]. Another approach for obtaining single-mode operation in a multi-mode fibre that was proven more successful relies on introducing selective loss for higher order modes (or selective gain for the fundamental mode) in the fibre core.

This can be done by bending the fibre, which induces higher loss for higher-order modes relative to the fundamental mode [4.42] (or by using a core design with the RE dopant confined to the central region, thus providing more gain to the fundamental mode). Tapered multimode fibres can be also used to locally reduce the diameter of the fibre core so that only the fundamental mode propagates with low loss [4.43].

Scaling mode area is also possible with special, strictly single mode fibre designs. One possibility is to use a fibre with complex, ring-structured refractive index profile [4.44]. Such architectures benefit from expanded fundamental mode area, but are more challenging to fabricate. Another popular approach is to use a microstructured ("holey") fibre, sometimes called photonic crystal fibre (PCF), with a solid core surrounded by the cladding with strategically positioned air holes. Guiding properties of such fibre are defined purely by its geometry. The relative size and positions of the air holes can be designed in such a way that only fundamental mode is supported in the solid core of the fibre. Yb-doped PCF fibre with intrinsically single-mode 40 µm core has been demonstrated [4.45]. Properties of the inner-cladding in PCF fibres can be also tailored in a similar way, in order to obtain a high NA pump guide [4.46]. Other PCF designs allow for increased leakage loss for higher order modes of the solid core [4.47] or supporting only one polarisation state [4.46]. Microstructured fibres show great potential in the area of power scaling and >1.5 kW output from Yb-doped fibre with a nearly diffraction limited beam has already been demonstrated [4.48].

Scaling the core area further is challenging as the long fibre required for very high power operation must be bent to be packaged. In Yb-doped fibre lasers it is difficult to maintain single-mode operation with effective mode diameter above 50 µm even for loosely coiled large core fibres (e.g. 100 µm core, 0.5 m bending radius) [4.25]. This suggests that the power scaling limit due to optical damage is reached at ~10 kW for a single aperture coiled fibre laser. Further power scaling can be performed in long and straight waveguide structures with a large core, called rod-type fibres [4.48], but the physical dimensions required for obtaining very high power levels (> 40 m long devices) make them somewhat impractical for most applications.

4.4. Nonlinear frequency conversion

4.4.1. Overview

Many applications require high power laser beams in spectral regions (e.g. UV, visible, mid-IR) that are not directly accessible with conventional laser sources. The most common approach to generate light at these desired wavelengths is via nonlinear frequency conversion processes. Various nonlinear processes can be employed for this purpose. Second harmonic generation (SHG) and sum frequency generation (SFG) can be used to convert light to shorter wavelengths in materials with non-zero second order nonlinearity, while difference-frequency generation (DFG) optical parametric oscillation (OPO) and amplification (OPA) can be used for light conversion to longer wavelengths in similar materials (OPA in media with third order nonlinearity is also possible). Other techniques for frequency conversion rely on Raman conversion and amplification in a bulk material or an optical fibre with third order nonlinearity. Optical rectification is often used for generating terahertz radiation and high harmonic generation in gases can be used to convert laser light to radiation at extremely short wavelengths. In supercontinuum generation processes, various nonlinearities contribute to the generation of high-brightness broadband light in a highly nonlinear optical fibre. Nonlinear frequency conversion often requires single polarisation state light and fulfilling a phase matching condition. In addition, nonlinear processes can be efficient only at sufficiently high optical intensities. Such peak intensities are relatively easy to obtain in lasers emitting short pulses, however special techniques of intensity enhancement have to be applied in case of CW lasers. One way to facilitate high optical intensity is to perform intracavity nonlinear frequency conversion inside a high finesse laser resonator. This approach with its strengths and limitations will be discussed in detail in section 4.4.6. Another technique, which can be applied to single-frequency (as well as mode-locked) laser sources, is based on the use of a low-loss, actively stabilised resonant enhancement cavity. Applicability of this approach as well as other methods for frequency doubling the output of CW fibre lasers will be discussed in section 4.4.7. This chapter will focus mainly on the process of second harmonic generation, with

relevant theory and background information on SHG reviewed in sections 4.4.2-4.4.5. However, similar approaches can be applied to other nonlinear processes aiming for efficient nonlinear conversion of "bulk" and fibre based CW laser sources to access different wavelength regimes.

4.4.2. Second harmonic generation

When light of high intensity is incident on a dielectric medium, a separation of bound charges is induced and results in a collection of dipole moments rapidly oscillating with the incident electric field. The resulting nonlinear polarisation $\boldsymbol{P_{NL}}$ induced by the total electric field $\boldsymbol{E}$, defined as the net average dipole moment per unit volume, can be expressed as [4.49]:

$$\boldsymbol{P_{NL}} = \underbrace{\varepsilon_0 \chi^{(1)} \boldsymbol{E}}_{\substack{\text{linear} \\ \text{response}}} + \underbrace{\varepsilon_0 \chi^{(2)} \boldsymbol{EE}}_{\substack{2^{\text{nd}}\text{order} \\ \text{NL response}}} + \underbrace{\varepsilon_0 \chi^{(3)} \boldsymbol{EEE}}_{\substack{3^{\text{rd}}\text{ order} \\ \text{NL response}}} + \underbrace{\cdots}_{\substack{\text{higher order} \\ \text{NL response}}} \tag{4.20}$$

where ε_0 is the permittivity of free space, $\chi^{(1)}$ is the linear component of electric susceptibility, while $\chi^{(2)}$ and $\chi^{(3)}$ are second and third order nonlinear components of electric susceptibility respectively. $\chi^{(2)}$ disappears for materials with inversion symmetry such as amorphous silica, but can be significant in some families of crystals, while $\chi^{(3)}$ is non-zero for all materials.

If the total electric field is expanded in terms of its Fourier components, then the nonlinear polarisation will consist of several terms oscillating at various combination frequencies, resulting in generation of light at new frequencies, dependent on the frequencies of incident fields. Second harmonic generation (SHG) is a second order ($\chi^{(2)}$) nonlinear process in which a single pump wave at fundamental frequency ω generates a wave at second harmonic frequency 2ω as it propagates through a nonlinear medium (in this case, a crystal). These waves are coupled through the nonlinear polarisation of the medium, and their amplitude changes along the interaction length (z - propagation direction) can be described with coupled-wave equations, first solved by Armstrong et al. [4.50]:

$$\frac{dE_{2\omega}}{dz} = \frac{i\omega}{n_{2\omega}} d_{eff} E_{\omega}^2 \exp(i\Delta kz) \tag{4.21}$$

$$\frac{dE_{\omega}}{dz} = \frac{i2\omega}{n_{\omega}} d_{eff} E_{\omega}^* E_{2\omega} \exp(-i\Delta kz) \tag{4.22}$$

where $i = \sqrt{-1}$, E_ω and $E_{2\omega}$ are the amplitudes of the fundamental and second harmonic waves respectively, n_ω and $n_{2\omega}$ are the refractive index values of the medium in the direction of respective wave polarizations, d_{eff} is the effective nonlinear coefficient of the medium, and Δk represents the phase velocity mismatch between interacting waves:

$$\Delta k = (2\mathbf{k}_\omega - \mathbf{k}_{2\omega}) \cdot \hat{z} \tag{4.23}$$

where $\mathbf{k}_\omega$ and $\mathbf{k}_{2\omega}$ are the wavevectors of the fundamental and second harmonic waves respectively, and $\hat{z}$ is the unit vector in the propagation direction. The intensity of the optical wave at the frequency ω is given by:

$$\mathrm{I}_\omega = 2\varepsilon_0 n_\omega c |E_\omega|^2 \tag{4.24}$$

where c is the velocity of light in vacuum. The total optical power within a Gaussian beam of spot size w_0 and central intensity I_0 can be calculated by integrating the intensity over the beam area A:

$$P = \int_A I \, dA = \frac{1}{2} \pi w_0^2 I_0 \tag{4.25}$$

The frequency conversion efficiency (in the infinite plane wave approximation, including fundamental wave depletion along the interaction length) is given by [4.49]:

$$\eta_{SHG} = \frac{P_{2\omega}}{P_\omega} = \tanh^2\left(\sqrt{\epsilon P_\omega}\right) \mathrm{sinc}^2(\Delta kL/2) \tag{4.26}$$

where P_ω is the optical power incident on the crystal of the length L, and

$$\epsilon = \frac{16\pi d_{eff}^2 L^2}{w^2 \varepsilon_0 n_\omega^2 n_{2\omega} c \lambda_\omega^2} \tag{4.27}$$

where $w = L^{-1} \int_L w(z)dz$ is the average spot size inside the nonlinear crystal and λ_ω is the fundamental wavelength. Although this approach neglects the effects of tight focusing and absorption in the crystal (a more detailed analysis was presented by Boyd and Kleinman in [4.51]), it provides an adequate description for the experimental configurations described in the next chapters of this thesis. Due to the $\mathrm{sinc}^2(\Delta kL/2)$ factor, the conversion efficiency (4.26) is severely reduced even for small values of Δk. If the fundamental wave power is not significantly depleted along the interaction length (i.e. we operate in the small conversion regime) and the phase matching condition $\Delta k = 0$ is met, equation (4.26) simplifies to:

$$\eta_{SHG} = \epsilon P_\omega \tag{4.28}$$

4.4.3. Phase matching techniques

There are various techniques for achieving the phase matching condition ($\Delta k = 0$), including angular phase matching of $\mathbf{k}_\omega$ and $\mathbf{k}_{2\omega}$ vectors, temperature tuning of refractive index values, quasi-phase matching in periodic media, or obtaining phase matching with an aid of wave-guiding effects.

a) Non-critical phase matching

The configuration where the fundamental and second harmonic waves propagate along one of the crystal's principal axes with refractive indices satisfying the phase matching condition at a certain phase matching temperature T_{pm} is known as non-critical phase matching (NCPM). Specifically, Type I NCPM phase matching in SHG process refers to a configuration when the pump wave is polarized along one of the crystal's principal axes and the second harmonic wave is polarized in the

orthogonal directions, while Type II refers to the pump having two orthogonal components along the crystal principal axes. The general condition for collinear non-critical phase matching (NCPM) can be expressed as:

$$n_{2\omega}(T_{pm}) = \frac{1}{2}\left[n_{\omega}(T_{pm}) + n'_{\omega}(T_{pm})\right] \tag{4.29}$$

which for Type I SHG (ooe) simplifies to:

$$n^{e}_{2\omega}(T_{pm}) = n^{o}_{\omega}(T_{pm}) \tag{4.30}$$

where the refractive index values at fundamental frequency n_{ω}, n'_{ω} for orthogonal pump polarization components are generally different and o,e refer to the refractive index values along the ordinary and extraordinary axes respectively. If we expand the refractive index into a Taylor series around room temperature T_0:

$$n^{k}_{j}(T_{pm}) = n^{k}_{j}(T_0) + \left.\frac{\partial n^{k}_{j}}{\partial T}\right|_{T=T_0}(T_{pm} - T_0) \tag{4.31}$$

the phase matching temperature can be obtained from (4.30):

$$T_{pm} = T_0 + \frac{n^{e}_{2\omega}(T_0) - n^{o}_{\omega}(T_0)}{\left[\frac{\partial n^{o}_{\omega}}{\partial T} - \frac{\partial n^{e}_{2\omega}}{\partial T}\right]_{T=T_0}} \tag{4.32}$$

The temperature bandwidth can be determined by expanding the phase velocity mismatch in a Taylor series around the phase matching temperature:

$$\Delta k(T) = \left.\frac{\partial(\Delta k)}{\partial T}\right|_{T=T_{pm}} \Delta T \equiv \gamma_T \Delta T \tag{4.33}$$

The $\mathrm{sinc}^2(\Delta kL/2)$ factor in (4.26) drops to 0.5 when:

$$\Delta kL \approx 2.784 \tag{4.34}$$

It follows that the temperature bandwidth is then:

$$\Delta T_{BW} = |2.784/(\gamma_T L)| \tag{4.35}$$

where, for Type I SHG (ooe):

$$\gamma_T = \frac{4\pi}{\lambda_\omega}\left[\frac{\partial n_\omega^o}{\partial T} - \frac{\partial n_{2\omega}^e}{\partial T}\right]_{T=T_{pm}}$$

b) Critical phase matching

Another technique of obtaining phase matching condition, called critical phase matching, refers to a configuration where the interacting beams are aligned to some angle (or angles) to the principal axes of the nonlinear crystal. A major advantage of critical phase matching is that the crystal temperature can often be close to room temperature.

In uniaxial crystals, there is a single axis of symmetry, often designated the Z-axis, coinciding with the principal optic axis. Hence, the principal refractive indices are $n_X = n_Y = n^o$ and $n_Z = n^e$. For propagation at an angle θ with respect to the Z-axis, the extraordinary wave has a refractive index given by:

$$\frac{1}{[n^e(\theta)]^2} = \frac{\cos^2(\theta)}{[n^o]^2} + \frac{\sin^2(\theta)}{[n^e]^2} \tag{4.36}$$

This relation can be used to calculate the phase matching angle for the SHG process.

In biaxial crystals there are two optic axes that lie in in the XZ plane (it is conventional to take $n_Z > n_Y > n_X$). Those optic axes make an angle Ω with respect to the Z-axis, which is given by:

$$\sin\Omega = \frac{n_Z}{n_Y}\left(\frac{n_Y^2 - n_X^2}{n_Z^2 - n_X^2}\right)^{1/2} \tag{4.37}$$

and are situated symmetrically about the Z-axis. In general the beam can propagate at an angle θ with respect to the Z-axis, and at an angle ϕ with respect to the X-axis. The refractive indices of the two allowed modes of propagation can be calculated from the Fresnel equation [4.49]:

$$\frac{\sin^2\theta\cos^2\phi}{(n)^{-2} - (n_X)^2} + \frac{\sin^2\theta\sin^2\phi}{(n)^{-2} - (n_Y)^2} + \frac{\cos^2\theta}{(n)^{-2} - (n_Z)^2} = 0 \tag{4.38}$$

This relation can be used to calculate the phase matching angles for the SHG process. For type I (ooe) SHG the phase matching direction is given by angles ϕ_{pm} and θ_{pm} in planes XY and XZ respectively:

$$\tan^2\phi_{pm} = \frac{1 - (n_\omega^Z/n_{2\omega}^Y)^2}{(n_\omega^Z/n_{2\omega}^X)^2 - 1} \tag{4.39}$$

$$\tan^2\theta_{pm} = \frac{1 - (n_\omega^Y/n_{2\omega}^X)^2}{(n_\omega^Y/n_{2\omega}^Z)^2 - 1} \tag{4.40}$$

These attribute “critical” comes from the fact that this phase matching technique is much more sensitive to angular misalignment of the interacting beams than non-critical phase matching. The angular bandwidth for the SHG process can be determined by expanding the phase velocity mismatch due to angular deviation $\Delta\theta = \theta - \theta_{pm}$ from the phase matching direction (θ_{pm} angle) into a Taylor series:

$$\begin{aligned}\Delta k(\theta - \theta_{pm}) &= \left.\frac{\partial(\Delta k)}{\partial\theta}\right|_{\theta=\theta_{pm}} \Delta\theta + \frac{1}{2}\left.\frac{\partial^2(\Delta k)}{\partial\theta^2}\right|_{\theta=\theta_{pm}} (\Delta\theta)^2 \\ &\equiv \gamma_{CPM}\Delta\theta + \gamma_{NCPM}(\Delta\theta)^2\end{aligned} \tag{4.41}$$

where CPM and NCPM stand for critical phase matching and non-critical phase matching respectively.

Since $\gamma_{CPM}(\theta_{pm} = 90^{\circ}) = 0$, the second term of (4.41) is included for the NCPM process. For the CPM process only the first term should be retained. Substituting (4.41) to (ΔkL = 2.784) produces the following expressions for angular phase matching bandwidths [4.49]; for Type I NCPM SHG (ooe):

$$\Delta\theta_{BW} = |2.784/(\gamma_{NCPM}L)|^{1/2} \tag{4.42}$$

where

$$\gamma_{\text{NCPM}} = \frac{2\pi}{\lambda_\omega} n_{2\omega}^e \left[\frac{(n_{2\omega}^e)^2}{(n_{2\omega}^o)^2} - 1\right] \approx \frac{4\pi}{\lambda_\omega}(n_{2\omega}^e - n_\omega^o)$$

and for Type I CPM SHG (ooe):

$$\Delta\theta_{BW} = |2.784/(\gamma_{NCPM}L)| \tag{4.43}$$

Where

$$\gamma_{\text{CPM}} = \frac{2\pi}{\lambda_\omega}(n_\omega^o)^3 \left[\frac{(n_{2\omega}^o)^2 - (n_{2\omega}^e)^2}{(n_{2\omega}^o)^2(n_{2\omega}^e)^2}\right] \sin 2\theta_{pm} \approx \frac{4\pi}{\lambda_\omega}(n_{2\omega}^e - n_\omega^o) \sin 2\theta_{pm}$$

The small range of beam angles where critical phase matching works also implies that the beam divergence must be limited. This implies that a larger beam must be used hence limiting SHG efficiency compared to the case of NCPM.

c) Quasi-phase matching (QPM)

In the quasi-phase matched SHG process, a plane wave field of amplitude E_1 at frequency ω_1 and wavevector $k_1 = n_1\omega_1/c$, where n_1 is the refractive index, passes through a medium with quadratic nonlinear susceptibility *d*, generating a nonlinear polarization wave proportional to dE_1^2 at frequency $\omega_2 = 2\omega_1$ and wavevector $2k_1$. The polarization wave radiates a free second harmonic wave with wavevector $k_2 = n_2\omega_2/c$. The forced and free waves accumulate a phase shift of π over a distance known as the coherence length [4.52],

$$l_c = \frac{\pi}{(k_2 - 2k_1)} = \frac{\lambda_\omega}{4(n_2 - n_1)} \tag{4.44}$$

where λ_ω is the wavelength of the fundamental wave in vacuum.

The direction in which the power is flowing between the fundamental and harmonic wave depends on their relative phases, and hence changes its sign every coherence length. By applying change in the sign of the nonlinear susceptibility every coherence length, a phase shift of π is induced for the polarization wave, which effectively re-phases the interaction and leads to monotonic power flow into the harmonic wave, as illustrated in fig. 4.8 [4.52].

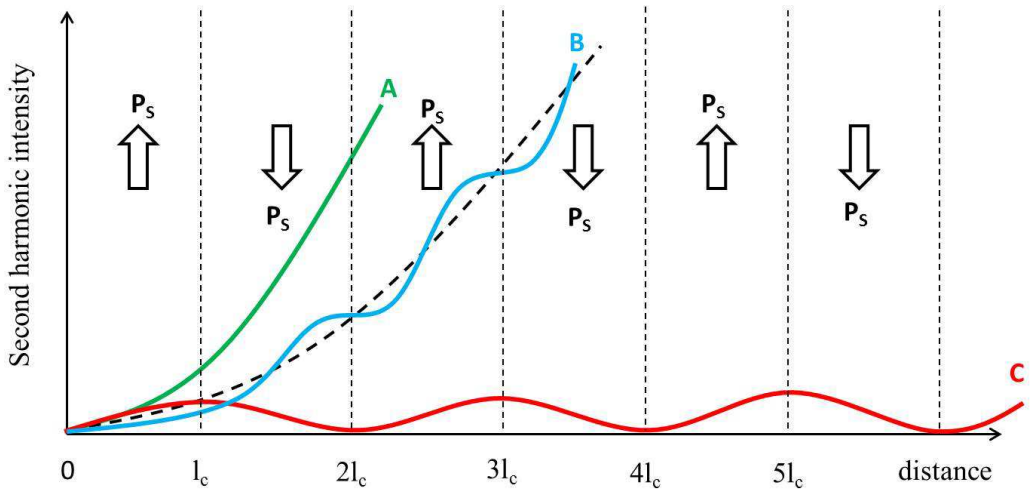

Figure 4.8: Effect of phase-matching on the growth of second harmonic intensity with distance in a nonlinear crystal. A: perfect phase-matching in a uniformly poled crystal; C: non-phase-matched interaction; B: first-order QPM by flipping the sign of the spontaneous polarization (P_S) every coherence length (l_c) of the interaction curve C

As QPM processes do not rely on birefringence, any choice of polarizations can be used. This means that all waves can be polarised in parallel allowing the largest nonlinear susceptibility tensor component to be exploited. It is possible to use QPM in isotropic media (such as e.g. GaAs) where birefringent phase matching is not possible. For the same reason, it is always possible to use QPM with waves propagating along a crystal axis, eliminating the problem of Poynting-vector walk-off. Nonlinear conversion processes using QPM can be made very efficient as

periodic poling can be applied to crystals with particularly high nonlinearity, thus utilizing larger nonlinear coefficients than those accessible with birefringent phase matching. The QPM technique, however, has a number of limitations. Parasitic higher-order nonlinear processes can generate light at wavelengths other than desired output from the first-order process. The fabrication of periodically poled crystals with high quality is challenging, and is possible only with certain crystal materials. The success rates of the required procedures depend strongly on material details, including its type, density, stoichiometry, surface treatment and other properties. For different nonlinear processes, many different poling periods are required, and each new value may require an expensive new lithographic mask. Small aperture periodically-poled crystal-based devices suffer from thermally-induced de-phasing significantly reducing conversion efficiency, and for high intensities the output power is limited by nonlinear absorption and ultimately by crystal damage [4.53]. Periodic poling can be applied only to crystals with fairly limited thickness, which excludes large aperture devices suitable for very high power levels.

d) phase-matching in waveguide structures

One method to increase the efficiency of the nonlinear process is to increase the interaction length by using a waveguide or optical fibre. While channel and planar waveguides can be made of birefringent material such as $LiNbO_3$, most fibres can be used for $\chi^{(3)}$ processes only (one exception is electric field poling that can be used to break the inversion symmetry in the core area [4.54]). If the fibre is sufficiently long and light can be confined in a small effective mode area, efficient nonlinear frequency conversion is possible even at low powers.

Modal phase matching (MPM) is a simple solution to the problem of phase velocity synchronism for nonlinear frequency conversion in waveguides, but is challenging to achieve in practice due to poor spatial overlap between the interacting modes. Waveguides generally support several modes, each with different propagation constants (i.e. effective refractive index n_{eff}). For higher-order modes this value is lower and therefore phase matching in the SHG process ($n_{eff}^{\omega} = n_{eff}^{2\omega}$) can occur if the fundamental mode propagates in a lower order mode than the second harmonic.

The expected normalized conversion in optimized semiconductor-based structures is a factor of 20 lower than in birefringently phase-matched waveguides. However, the structure can be combined with a laser diode on a single chip to provide an integrated semiconductor source of tuneable light based on nonlinear frequency conversion [4.55].

Cerenkov phase matching is another type of phase matching technique that has also been considered for efficient SHG in waveguides. In this process, the fundamental wave is a waveguide mode, while the second harmonic is a radiation mode, i.e., it propagates out into the cladding or substrate of the waveguide at a certain angle. This angle is determined by the condition that the phase velocity of the fundamental guided mode is matched to the phase velocity of the second harmonic radiation mode. The theory of Cerenkov phase matching has been developed for crystal-cored fibres and channel waveguides [4.56] as well as for planar waveguides [4.57].

Fresnel phase matching (FPM) is a technique that allows accessing efficient nonlinear three-wave-mixing processes in isotropic, semiconductor-based waveguides. The three waves can be introduced from the side and trapped by total internal reflection in the semiconductor wafer in a “zig-zag” configuration. The thickness of the wafer is chosen such that the distance travelled between two reflections is close but not exactly equal to the coherence length for difference frequency generation (DFG) process. Upon the total internal reflection at the wafer surfaces, the three waves experience a Fresnel phase shift that can be tuned by adjusting the angle, the polarization, and frequency of the interacting waves. When properly tuned, the DFG power constructively builds up at each total internal reflection. Such a device is simple to construct and tune in the mid-IR spectral region that is not accessible by QPM in ferroelectric periodically poled crystals [4.58].

4.4.4. Focusing

Frequency conversion with strongly focused Gaussian beams has been discussed in detail in [4.51]. This section will only briefly discuss how material parameters influence the conversion efficiency in this regime. The essential properties of the Gaussian beam are its waist radius, w_0, and the distance over which its radius remains essentially collimated (the confocal length) $b = 2\pi n w_0^2/\lambda$.

Let us first consider the case of noncritical phase-matching. For near-field focusing ($L < b$), the conversion efficiency is the same as given by (4.28). However, the increase in the efficiency predicted for small spot sizes breaks down for w_0 sufficiently small that b < L. This is caused by the shortened interaction length as the rapid diffraction becomes more significant than the increased peak intensity. In the near field approximation, the conversion efficiency for confocal focusing (b = L) is obtained by taking $w_0 = \sqrt{L\lambda/2\pi n}$:

$$\eta_c = \gamma_{nc} L P_\omega \tag{4.45}$$

where $\gamma_{nc} = 16\pi^2 d_{eff}^2/\epsilon_0 c n^2 \lambda^3$.

Numerical calculations show that the exact efficiency for confocal focusing is 0.81 η_c and that the actual optimum that can be reached at b = L/2.84, is 1.07 η_c [4.59], but this tighter focusing is rarely used in practice. For a typical nonlinear coefficient of 5 pm/V, a wavelength of 1 μm, and a refractive index of 2, γ_{nc} = 0.4% $W^{-1}cm^{-1}$.

For critical phase-matching, the efficiency of the nonlinear interaction can be further reduced by the Poynting vector walk off effect, that causes the SH beam to walk away from the fundamental after a distance $l_a = \sqrt{\pi} w_0/\rho$. The optimum focusing is close to confocal in the presence of walk-off, but the efficiency depends on the walk-off parameter $B_\rho = \rho\sqrt{\pi n L/2\lambda}$. The optimum efficiency for B_ρ = 1 is approximately 0.58 η_c and, for B_ρ > 1.5, can be well approximated $\eta_c/\sqrt{2}B_\rho$. In this latter limit the efficiency is given by [4.59]:

$$\eta_{cr} = \gamma_{cr}\sqrt{L}P_{\omega} \tag{4.46}$$

where $\gamma_{nc} = 16\pi^{3/2}d_{eff}^2/\epsilon_0 cn^{5/2}\lambda^{5/2}\rho$.

In this case the efficiency scales only with $\sqrt{L}$ and is inversely proportional to the walk-off angle ρ. Consequently for a material with the same properties as the example in the noncritical case, but having a walk-off angle ρ = 2°, the efficiency is reduced to γ_{cr} = 0.04% $W^{-1}cm^{-1/2}$.

4.4.5. Nonlinear crystals

The physics of the frequency conversion process place severe demands on potential nonlinear crystals; therefore relatively very few materials find application in nonlinear optics. Only a few percent of surveyed crystalline phases offer a non-zero nonlinear coefficient, sufficient birefringence for phase-matching and transparency at relevant wavelengths. Additional demands for many applications include mechanical and chemical stability as well as the possibility for production in the form of adequately-sized and uniform single crystals. As a result, only a few tens of different crystalline phases have ever been applied to practical nonlinear frequency conversion.

a) Optical transmission and loss

The material must possess reasonable transmission at wavelengths involved in the nonlinear interaction to yield sufficient conversion efficiency. The nominal transmission range is determined by the identity of the crystalline phase. The high-frequency cut-off is caused by inter-band electronic transitions and the low-frequency cut-off occurs due to phonon absorption. Within this nominal transmission range, even relatively small amounts of optical loss can be critical. This is particularly true for nonlinear configurations involving high average power, where low absorption can lead to heat generation and material damage, as well as in high finesse resonators, where both absorption and scattering adversely affect the device's

performance. Such small losses originating from chemical impurities, colour centres, inclusions, and free carriers can be extremely process and wavelength dependent. Scattering in nonlinear crystals can be caused by mechanical strain, grain boundaries, compositional inhomogeneity, or inclusions. Surface losses often dominate volume losses within the nominal transmission range, and in general depend on the cutting, polishing, and coating processes performed in preparing the crystal surface.

b) Nonlinear susceptibility

The optical response of the nonlinear material is determined by the atomic arrangement. For nonlinear coefficients of the medium to be non-zero, its point group must lack a centre of inversion symmetry - the relationship between chemical bonding and nonlinear susceptibility has been discussed in detail in [4.60]. The nonlinear coefficients are elements of a third-rank tensor, as they relate the optical response to two optical fields. The effective nonlinear coefficient d_{eff} is obtained by projecting the polarization of the input and output fields onto the d tensor and can be highly directionally-dependent. It can also vary among different nonlinear interactions requiring different phase-matching directions and polarizations - the procedures for calculating specific d_{eff} values have been discussed in [4.61]. In general, nonlinear coefficients within the nominal transmission range of the medium do not depend strongly on wavelength or fabrication process.

c) Birefringence and phase-matching

Birefringent phase-matching in nonlinear optics depends on a relatively small difference in refractive index values for different polarizations. For this reason small variations of refractive index within a crystal can result in large differences in birefringence and hence phase-matching characteristics. These variations often originate from variations in composition and internal strain within a crystal. Some nonlinear processes place strong demands on process-dependent material quality as the required birefringence uniformity can be less than $\pm 10^{-6}$/cm. However, phase-matching bandwidths are dependent on thermal and angular derivatives of the birefringence and as such can be relatively insensitive to the fabrication process. On

the other hand, these properties can be highly direction-dependent and thus may vary between different nonlinear interactions. Another mechanism affecting phase-matching characteristics relates to thermally induced change in birefringence originating from absorption in high average power applications.

d) Laser damage resistance

Numerous undesirable effects can occur when a high-intensity laser beam is incident on the nonlinear crystal. Catastrophic failure of the crystal can be initiated in its volume or on the surfaces. Alternatively, the laser beam can induce uncontrollable change in the material's properties without destroying the crystal. Damage resistance to laser radiation is difficult to quantify, as the processes leading to damage tend to be highly probabilistic and strongly depend on surface cleanliness, history of the sample as well as laser beam parameters such as, wavelength, mode structure, pulse length and energy, waist size and location. In many applications, catastrophic laser damage is most likely to be initiated on a surface of the nonlinear crystal. This process involves complex physical mechanisms occurring in the presence of imperfections on the crystal’s surface, such as residual scratches, polishing-induced inclusions and foreign particulates that can locally intensify the electric field. Surface damage resistance is thus strongly dependent on surface processing (i.e. cutting, polishing, coating, and cleaning). The damage threshold in terms of laser fluence (energy per unit area) for a given surface scales approximately with the square root of the pulse length and inversely with the square root of the spot size. Intensity at the exit surface is slightly higher due to internal Fresnel reflection, thus catastrophic surface damage is typically observed to be initiated on the exit face of the crystal. Bulk damage in most cases is caused by a thermally-induced fracture mechanism. Absorption and scattering effects increase the thermal load in the crystal, while mechanical strain lowers its resistance to fracture. Bulk catastrophic damage resistance thus strongly depends on the crystal fabrication process. Incoming and generated high intensity optical radiation can also induce changes in the refractive indices (known as the photorefractive effect), or the optical absorption (the photochromic effect). Although these optically-induced changes are generally not catastrophic, they can affect phase-matching stability or output beam quality and can lead to other catastrophic phenomena. Optically induced changes are typically more

severe at high average powers, strongly depend on wavelength, crystal temperature and composition. In most cases, photorefractive and photochromic effects are reversible upon removal of the incoming radiation.

e) Lithium triborate (LBO) crystal

In this thesis we will focus only on devices using one material from the borate family of the nonlinear crystas: Lithium triborate (LiB_3O_5) or LBO. This biaxial material chosen for the experimental work combines wide transparency window (0.16 - 2 μm), high damage threshold (18.9 GW/cm^2 for a 1.3 ns laser pulse at 1053 nm), and adequate birefringence for phase-matching a broad range of visible and UV interactions with wide acceptance angle and small walk-off. LBO has a peritectic melting point near 834°C, which precludes the possibility of preparing crystals by standard melt-growth techniques. Most of the LBO crystals reported to date have been grown by a top-seeded high-temperature solution (HTS) growth method [4.59]. Growth temperatures range between 750 and 830 °C. Growth runs of four to six weeks yield lens-shaped or cylindrical boules, depending on whether the seed is slowly withdrawn during growth. Crystals as large as 35 mm in diameter by 20 mm in length have been grown. A core of rather common spherical inclusions is typical at the centre of a crystal running along its axis of growth. Oriented and fabricated crystals are usually restricted to linear dimensions less than few centimetres. Thermal expansion characteristics can somewhat complicate coating processes. The properties and applications LBO have been reviewed in [4.62].

LBO crystals have been demonstrated as an efficient nonlinear material suitable for a broad range of applications. They can be used to generate the second and third harmonics of 1.06 μm radiation and can be temperature-tuned for noncritical phase-matching [4.63]. LBO has also been successfully applied to SHG of dye [4.64] and Ti:sapphire lasers [4.65]. Wavelengths as short as 188 nm have been generated by SFG in LBO crystals. OPOs pumped by the second through fourth harmonics of 1.06. Excimer and Nd:YAG harmonic pumped OPOs in LBO have been described in [4.66].

4.4.6. Intracavity SHG in conventional ‘bulk’ solid-state lasers

There is increasing demand for high power continuous-wave laser sources emitting in the visible spectral region, that is not directly accessible for high power ‘bulk’ solid-state lasers and fibre lasers. High power lasers emitting in the visible are required in a broad range of applications such as laser processing of materials, projection displays, medicine, sensing and defence. The standard method of accessing the visible wavelength region is via nonlinear frequency conversion of near-infrared solid-state and fibre lasers. For high-peak-power pulsed lasers sources, simple single-pass nonlinear conversion schemes generally suffice. However, in the CW regime more sophisticated schemes are usually needed to obtain high intensities required for efficient nonlinear frequency conversion. Frequency doubling in high power solid-state lasers must employ a nonlinear medium that can handle very high average powers. Materials with good thermo-optical and thermo-mechanical properties that can be used in such applications generally have relatively modest nonlinear coefficients. Such relatively weak nonlinearity combined with an increased mode size area typically allows for frequency conversion with efficiency in the order of few percent per kilowatt per centimetre of nonlinear medium. Clearly this is not enough even for the state-of-the-art multi-kilowatt-class CW solid-state lasers.

The most popular method for generating high power visible output is via intracavity second harmonic generation in a diode-pumped ‘bulk’ solid-state laser. Fig. 4.9 presents a typical high-finesse resonator configuration suitable for efficient intracavity frequency doubling. The laser cavity comprises a bulk active medium (in this case a laser rod) in thermal contact with an actively cooled heat sink, and a nonlinear crystal typically housed in an oven for maintaining the phase matching temperature. Feedback for lasing is provided by a couple of high reflectors at the laser wavelength - in this case one reflector is highly transmissive at the pump wavelength and is also used for pump in-coupling. The resonator is designed so that the laser mode size in the active medium is optimized for a good overlap with the pump beam while the mode size in the nonlinear crystal is optimal for maximum

conversion efficiency. This approach exploits the relatively low resonator losses to achieve high intracavity power circulating in the resonator and hence high second harmonic conversion efficiency.

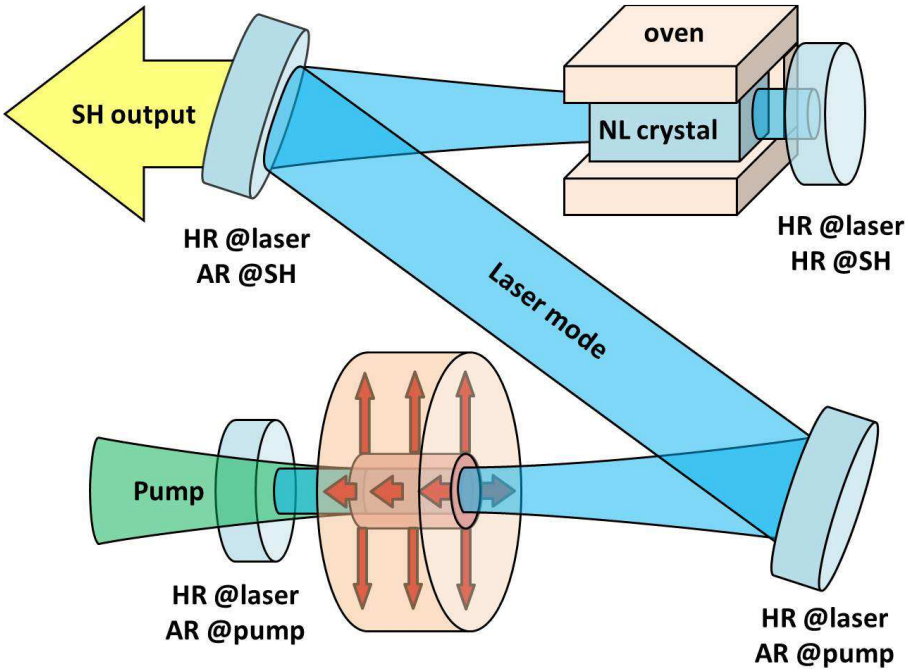

Figure 4.9: Typical configuration for intracavity-frequency-doubled 'bulk' solid-state laser

In the small conversion regime (4.28) the second harmonic output power $P_{2\omega}$ as well as the power lost in the resonator P_{lost} increases with an increasing circulating fundamental power P_{ω}:

$$P_{2\omega} = \eta_{SHG} P_{\omega}, \qquad P_{lost} = \alpha_l P_{\omega} \tag{4.47}$$

where η_{SHG} is the single-pass conversion efficiency given by (4.28) and α_l is the sum of all other resonator losses.

Intracavity fundamental power is thus inversely proportional to resonator losses:

$$P_{\omega} = \frac{P_{gen}}{\eta_{SHG} + \alpha_l} \tag{4.48}$$

where $P_{gen} = P_{2\omega} + P_{lost}$ is the total fundamental power generated in the laser medium.

The total conversion efficiency of the intracavity-frequency-doubled laser $\eta_{SHG\,total}$ can be defined as a ratio of the output second harmonic power to the total power generated in the active medium, so that:

$$\eta_{SHG\,total} = \frac{P_{2\omega}}{P_{gen}} = \frac{\eta_{SHG}}{\eta_{SHG} + \alpha_l} \tag{4.49}$$

Consequently, if the single-pass second harmonic conversion efficiency is a dominating loss in the resonator, most of the infrared power generated in the active medium can be converted to the second harmonic output and extracted through one of the resonator mirrors.

Intracavity second harmonic generation has allowed nearly diffraction-limited visible output with power in the order of ~60 W and >50% of total SHG conversion efficiency [4.67]. However, scaling to higher powers is challenging due to heat generation effects in the laser crystal, as discussed in sections 4.2.3-4.2.5. Thermal effects in the laser medium lead to degradation of the laser mode quality and thus cause increased resonator losses. This in turn results in reduction of the intracavity power (4.48) and the total SHG conversion efficiency (4.49). Thermal effects in the nonlinear crystal are usually less of a problem, as they tend to be weaker than in the laser medium. Another disturbing problem, typical for intracavity-frequency-doubled solid-state lasers, manifests itself in a very strong intensity noise (what is sometimes called the “green problem”). This complex effect arises from nonlinear dynamics of the resonator modes and can be affected by spatial hole burning, oscillation of higher order modes as well as nonlinear frequency conversion itself. These instabilities can be alleviated by increasing the number of longitudinal modes or enforcing single-frequency operation. However, it is often difficult to maintain control over all thermal effects and instabilities in the intracavity-frequency-doubled ‘bulk’ solid-state laser, and so most commercially available CW visible lasers emitting a single spatial mode output have been limited to output powers of ~20 W.

4.4.7. Nonlinear frequency doubling schemes for CW fibre lasers

Another approach for generating high power visible laser radiation is via frequency doubling of a high power fibre laser. As discussed in section 4.3 of this chapter, the fibre laser geometry is relatively immune to the effects of heat generation and offers a route to very high power levels in the near-infrared wavelength regime via the use of a cladding-pumped architecture. For these reasons, fibre laser architectures offer the prospect of much higher power levels in the visible regime via nonlinear frequency conversion than in the case of 'bulk' solid-state laser. Most common approaches to frequency doubling of cladding-pumped fibre lasers are schematically presented in fig. 4.10.

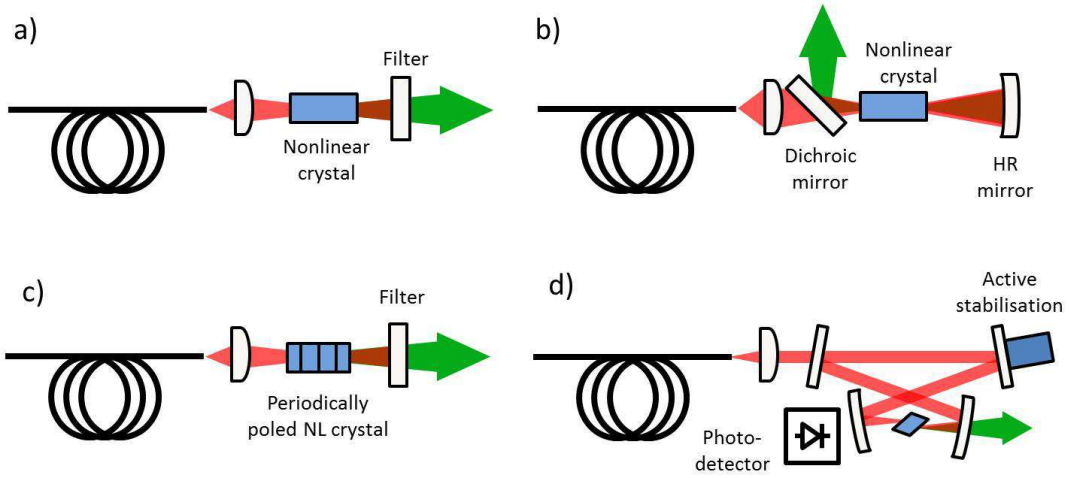

Figure 4.10: Schematic arrangements for most common approaches to frequency doubling of high power double-clad fibre lasers: a) single-pass external SHG b) intracavity SHG c) single-pass external SHG using periodically poled nonlinear crystal d) external resonantly-enhanced SHG

Simple external frequency conversion scheme using a birefringently phase matched nonlinear crystal (fig. 4.10a) can only be efficient if the fibre laser is producing high peak power pulses. In a CW regime even multi-kilowatt systems using external conversion schemes do not achieve significant conversion efficiency and only a small fraction of their output power can be converted to second harmonic wavelength.

Unfortunately, the technique of intracavity second harmonic generation (fig. 4.10b), commonly used with ‘bulk’ solid-state lasers is not well-suited to cladding-pumped fibre lasers [4.68]. The main obstacle is their high resonator loss, both in terms of core propagation loss and losses associated with coupling into the fibre’s core. These losses are compensated for with very high gain obtainable in fibres, which allows for generating very high fundamental power in the near infrared regime. High gain - high loss resonators typically employ output couplers with high transmission to maximise the output power and minimise the effect of cavity loss. Consequently, the intracavity power in most fibre lasers is not much higher, and often comparable to the output power of the fibre laser. For this reason it is not possible to benefit from significant intensity enhancement, which is often the most important factor in case of intracavity-frequency-doubled ‘bulk’ solid-state lasers.

Single-pass frequency doubling of the laser output in a quasi-phase-matched periodically-poled nonlinear crystal is an alternative route for efficient frequency doubling (4.10c). Relatively high conversion efficiency can be achieved using this approach but the output power is limited by thermal effects in the periodically poled crystal – even small absorption leads to thermal dephasing and ultimately to crystal damage [4.69].

Another solution to the problem of efficient frequency conversion is to employ a technique of external resonant cavity second harmonic generation (4.10d) in conjunction with a high-damage-threshold nonlinear crystal (e.g. lithium triborate). This approach has been successfully applied to CW fibre sources, delivering nearly diffraction limited second harmonic output with impressive output power of ~170 W [4.70] which is currently not achievable in any other laser configuration. The operation principle of externally-frequency-doubled fibre laser system can be explained with an aid of fig. 4.11.

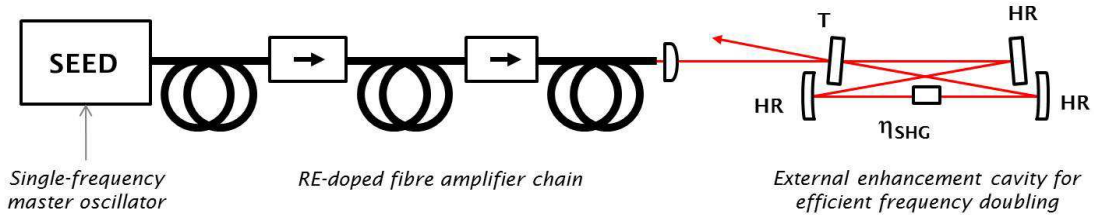

Figure 4.11: Typical arrangement of an externally-frequency-doubled laser system.

Fig. 4.11 schematically illustrates a typical configuration for a fibre laser system employing external resonant enhancement cavity for efficient nonlinear frequency conversion. Such arrangement comprises a low-power single frequency master oscillator, a fibre amplifier chain, shaping optics and an external resonant enhancement cavity for frequency doubling. The master oscillator can be fibre-based, 'bulk' solid-state laser or any other type of laser in general. A fibre amplifier chain consists of one or more stages based on rare-earth doped fibre with Faraday isolators in between, typically with increasing fibre core size from one amplifying stage to another. External resonant enhancement cavity is a free-space ring resonator with one partially transmitting mirror (an input coupler) and a nonlinear crystal configured for efficient nonlinear frequency conversion process.

Output from the fibre MOPA can be efficiently coupled into external enhancement cavity when certain conditions are met: The MOPA output is spatially-matched to the TEM_{00} mode of the external resonator, the frequency of the MOPA is matched to a resonant frequency of the external resonator, and the transmission of the input coupler T is approximately equal to round-trip loss γ (excluding T) of the cavity. For an ideal low-loss resonator, single-pass second harmonic conversion η_{SHG} dominates other losses so that: $T \approx \gamma \approx \eta_{SHG}$. Such a system is capable of very efficient conversion and can deliver very high second harmonic output power, but suffers from a number of limitations. One drawback is an added complexity of the system since a fibre based single-frequency fibre master-oscillator power-amplifier is required. As explained in sections 4.3.3 and 4.3.5, power scaling of single-frequency sources is challenging and their output power is ultimately limited by stimulated Brillouin scattering. Another disadvantage of external resonant frequency doubling comes from the fact that the master-oscillator and resonant cavity lengths must be

actively stabilized to ensure that the resonance condition is maintained at all times. This is normally done with a power detector and actuators in a feedback loop, which adds cost and complexity to the laser system.

This thesis introduces and discusses a novel scheme for efficient nonlinear frequency conversion of high power fibre lasers, alternative to external frequency doubling. This new approach benefits from all the strengths of the external resonator approach, but at the same time is free from the limitations of the external doubling discussed above. The principle of operation and design consideration for a ring enhancement cavity integrated *within* the fibre laser resonator will be discussed in detail in the next chapter of this thesis.

4.5. Conclusions

This chapter reviewed the principles and challenges of power scaling in solid-state laser sources. The most important metrics of laser performance such as lasing threshold, slope efficiency or beam quality factor have been introduced and discussed. Various mechanisms leading to heat deposition in the laser medium (e.g. quantum defect, fluorescence quenching processes), as well as detrimental thermal effects (thermal lensing, thermally-induced stress) originating from heat generation and thermal gradients have been examined. Different approaches to mitigating thermal effects with the emphasis on certain laser medium geometries (end-pumped rods, side-pumped slabs, thin-disk and fibre lasers) have been presented.

The next section of this chapter examined the cladding-pumped fibre laser architecture with its strengths and limitations. The effects of heat generation, nonlinearities and optical damage in fibre geometry have been studied in more detail. The fundamental limit on the maximum power in a diffraction-limited beam extractable from a single aperture fibre laser has been examined and estimated to lie in the range of ~30-40 kW. The current power scaling strategy towards this limit (mainly focusing on scaling the effective mode area) has been discussed.

The final section of this chapter reviewed relevant background theory on second harmonic generation, introducing expressions for frequency conversion efficiency, phase matching temperature, phase matching angles, and bandwidths for two phase matching techniques used in experiments discussed in the next chapters of this thesis. The most important properties of nonlinear crystals have been examined, with an emphasis on the lithium triborate that was used in our experiments. Finally, the most popular approaches for generating high power visible radiation have been discussed. These included intracavity frequency doubling in ‘bulk’ solid-state lasers as well as various methods used for efficient frequency conversion in fibre lasers. Although this chapter only reviewed the methods and challenges of efficient second harmonic generation in solid-state laser sources, the conclusions that have been drawn from this discussion can be typically extrapolated to other nonlinear processes used for frequency conversion to other useful wavelengths.

References

[4.1] E. C. Honea, R. J. Beach, S. B. Sutton, J. A. Speth, S. C. Mitchell, J. A. Skidmore, M. A. Emanuel and S. A. Payne, “115W Tm:YAG Diode-pumped solid-state laser”, IEEE J. Quantum Electron., vol. 33, no. 9, pp. 1592–1600, 1997

[4.2] W. W. Rigrod, “Saturation Effects in High-Gain Lasers”, J. Appl. Phys., vol. 38, no. 8, pp. 2487-2490, 1965

[4.3] W. A. Clarkson, “CLEO 2008 short course: High Power Fiber Lasers and Amplifiers”, in Conference on Lasers and Electro-Optics, San Jose, May 4-9, 2008

[4.4] ISO 11146:2005(E), "Lasers and laser-related equipment — Test methods for laser beam widths, divergence angles and beam propagation ratios”

[4.5] R. J. Keyes, “Injection luminescent pumping of CaF2:U3+ with GaAs diode lasers, Appl. Phys. Lett., vol. 4, no. 3, pp. 50–52, 1964

[4.6] kW-class Direct Diode Lasers with Comparable Brightness to Fiber, Disk, and Carbon Dioxide Lasers, at Advanced Solid-State Photonics (ASSP), San Diego, January 29, 2012, paper AW3A

[4.7] V. Fomin, M. Abramov, A. Ferin, A. Abramov, D. Mochalov, N. Platonov, and V. Gapontsev, “10 kW single mode fiber laser,” in Proc. of 5th International Symposium on High-Power Fiber Lasers and Their Applications, St. Petersburg, Russia, Jun. 28- Jul. 1, 2010, Session HPFL-1.3

[4.8] S. Ricaud, D. N. Papadopoulos, A. Pellegrina, F. Balembois, P. Georges, A. Courjaud, P. Camy, J. L. Doualan, R. Moncorgé and F. Druon, "High-power diode-pumped cryogenically cooled Yb:CaF2 laser with extremely low quantum defect", Opt. Lett. vol. 36, pp. 1602-1604, 2011

[4.9] Z. Xiong, Z. G. Li, W. L. Huang, and G. C. Lim, “Detailed Investigation of Thermal Effects in Longitudinally Diode-Pumped Nd:YVO4 Lasers”, IEEE J. Quantum Electron., vol. 39, no. 8, pp. 979–986, 2003

[4.10] W. Koechner, "Solid-State Laser Engineering", Springer Series in Optical Sciences, Vol. 1, 6th, rev. and updated ed., 2006

[4.11] T. S. Rutherford, W. M. Tulloch, E. K. Gustafson, R. L. Byer, “Edge-pumped quasi-three-level slab lasers: design and power scaling”, IEEE J. Quantum Electron. vol. 36 no. 2, pp. 205-219, 2000

[4.12] H. Bruesselbach and D. S. Sumida, “A 2.65-kW Yb:YAG single-rod laser”, IEEE J. Sel. Top. Quantum Electron. vol. 11, no. 3, pp. 600-603, 2005

[4.13] A. Killi, I. Zawischa, D. Sutter, J. Kleinbauer, S. Schad, J. Neuhaus and C. Schmitz, “Current status and development trends of disk laser technology”, in “Solid-state Lasers XVII: Technology and Devices”, Proc. SPIE, vol. 6871, 2008

[4.14] J. Marmo, H. Injeyan, H. Komine, S. McNaught, J. Machan and J. Sollee, “Joint High Power Solid-state Laser program advancements at Northrop Grumman” in “Fiber Lasers VI: Technology, Systems, and Applications”, Proc. SPIE, vol. 7195, 2009

[4.15] G. S. Mecherle, “Laser diode combining for free space optical communication”, Proc. SPIE, vol. 616, p. 281, 1986

[4.16] J. D. Majumdar and I. Manna, “Laser material processing”, Int. Mater. Rev., vol. 56, no. 5/6, 2011

[4.17] W. A. Clarkson, N. P. Barnes, P. W. Turner, J. Nilsson and D. C. Hanna, “High-power cladding-pumped Tm-doped silica fiber laser with wavelength tuning from 1860 to 2090nm”, Opt. Lett., vol. 27, no. 22, pp. 1989–1991, 2002

[4.18] A. Liu, and K. Ueda, “The absorption characteristics of circular, offset, and rectangular double-clad fibers”, Opt. Commun., vol. 132, pp. 511–518, 1996

[4.19] S. D. Jackson .and T. A. King, “High-power diode-cladding-pumped Tm-doped silica fiber laser”, Opt. Lett., vol. 23, no. 18, pp. 1462–1464, 1998

[4.20] A. Kosterin, V. Temyanko, M. Fallahi, and M. Mansuripur, “Tapered Fiber Bundles for Combining High-power Diode Lasers”, Applied Optics, vol. 43, no. 19, pp. 3893-3900, 2004

[4.21] A.B. Grudinin, D.N. Payne, P.W. Turner, J. Nilsson, M.N. Zervas, M. Ibsen, and M.K. Durki, “Multi-fibre arrangements for high power fibre lasers and amplifiers”, US patent no. 6826335, 2004.

[4.22] K. Ueda, H. Sekiguchi, and H. Kan, “1 kW CW output from fiber-embedded disk lasers”, in Proc. of the Conf. on Lasers and Electro-Optics 2002, Long Beach, USA, May 19–24, 2002, post-deadline paper CPDC4

[4.23] R. J. Ripin and L. Goldberg, “High efficiency side-coupling of light into optical fibres using imbedded v-grooves,” Electron. Lett., vol.31, pp. 2204-2205, 1995

[4.24] D. C. Brown and H. J. Hoffman, “Thermal, stress, and thermo-optic effects in high average power double-clad silica fiber lasers”, IEEE J. Quantum Electron., vol. 37, no. 2, pp. 207–217, 2001

[4.25] J. W. Dawson, M. J. Messerly, R. J. Beach, M. Y. Shverdin, E. A. Stappaerts, A. K. Sridharan, P. H. Pax, J. E. Heebner, C. W. Siders and C.P.J. Barty, “Analysis of the scalability of diffraction-limited fiber lasers and amplifiers to high average power”, Opt. Express, vol. 16, no. 17, pp. 13240-13266, 2008

[4.26] D. E. Gray, “American Institute of Physics Handbook“, Third Edition, McGraw-Hill, 1972

[4.27] M. Y. Cheng, Y. C. Chang, and A. Galvanauskas, “High-energy and high peak-power nanosecond pulse generation with beam quality control in 200-µm core highly multimode Yb-doped fiber amplifiers”, Opt. Lett., 30, pp. 358-360, 2005

[4.28] S. A. Skubchenko, A. Y. Vyatkin and D. V. Gapontsev, “High-power CW linearly polarized all-fiber Raman laser IEEE Photonics Tech. Lett., vol. 16, pp.1014-1016, 2004

[4.29] J. Stone, “CW Raman fiber amplifier,” Appl. Phys. Lett., vol. 26, pp.163-165, 1975

[4.30] R. G. Smith, “Optical Power Handling Capacity of Low Loss Optical Fibers as Determined by Stimulated Raman and Brillouin Scattering”, Applied Optics, vol. 11, no. 11, pp. 2489-2494, 1972

[4.31] A. Kobyakov, S. Kumar, D. Q. Chowdhury, A. B. Ruffin, M. Sauer and S. R. Bickham, “Design concept for optical fibers with enhanced SBS threshold”, Opt. Express, vol. 13, no. 14, 2005

[4.32] V. I. Kovalev and R. G. Harrison, “Suppression of stimulated Brillouin scattering in high-power single-frequency fiber amplifiers”, Opt. Lett., vol. 31, pp. 161-163, 2006

[4.33] B. C. Stuart, M. D. Feit, A. M. Rubenchik, B. W. Shore and M. D. Perry, “Laser-induced damage in dielectrics with nanosecond to subpicosecond pulses”, Phys. Rev. Lett. Vol. 74, pp. 2248-2251, 1995

[4.34] A. V. Smith, B. T. Do and M. Soderlund, “Deterministic nanosecond laser-induced breakdown thresholds in pure and Yb3+ doped fused silica”, Proc. SPIE, vol. 6453, 2007

[4. 35] A. A. Said, T. Xia, A. Dogarlu, D. J. Hagan, M. J. Soileau, E. W. Van Stryland and M. Mohebi, “Measurement of the optical damage threshold in fused quartz”, Appl. Opt. vol. 36, pp. 3374-3376, 1995

[4.36] R. Kashyap and K. J. Blow, “Observation of catastrophic self-propelled self-focusing in optical fibres”, Electron. Lett., vol. 24, pp. 47-49, 1988

[4.37] V. Gapontsev, D. Gapontsev, N. Platonov, O. Shkurkhin, V. Fomin, A. Mashkin, M. Abramov and S. Ferin, “2 kW CW ytterbium fiber laser with record diffraction limited brightness,” in Proceedings of the Conference on Lasers and Electro-Optics Europe, 2005

[4.38] A. V. Smith, B. T. Do, G. R. Hadley, and R.L. Farrow, “Optical damage limits to pulse energy from fibers” J. Quantum Electron, vol. 15, no. 1, pp. 153–158, 2009

[4.39] M. Li, X. Chen, J. Wang, A. Liu, S. Gray, D. T. Walton, A. B. Ruffin, J. Demeritt and L. A. Zenteno, “Fiber designs for higher power lasers”, Proc. SPIE, vol. 6469, pp. 64690H1-64690H9, 2007

[4.40] J. Limpert, A. Liem, H. Zellmer and A. Tunnermann, “500 W continuous-wave fibre laser with excellent beam quality”, Electron. Lett., vol. 39, no. 8, pp. 645–647, 2003

[4.41] S. Ramachandran, J. W. Nicholson, S. Ghalmi, M. F. Yan, P. Wisk, E. Monberg and F. V. Dimarcello, “Light propagation with ultralarge modal areas in optical fibers”, Opt. Lett. 31, pp. 1797-1799, 2006

[4.42] J. P. Koplow, D. A. Kliner and L. Goldberg. “Single-mode operation of a coiled multimode fiber amplifier”, Opt. Lett., vol. 25, no. 7, pp. 442–444, 2000

[4.43] J. Alvarez-Chavez, A. B. Grudinin, J. Nilsson, P. W. Turner and W. A. Clarkson, “Mode selection in high power cladding pumped fibre lasers with tapered section”, Conference on Lasers and Electro-Optics, Washington D.C., paper CWE7, p.247-248, 1999

[4.44] H. L. Offerhaus, J. Alvarez-Chavez, J. Nilsson, W. A. Clarkson, P. W. Turner, D. J. Richardson and A. B. Grudinin, “Characteristics of Q-

switched cladding-pumped ytterbium-doped fibre laser with different high energy fibre designs", J. Quantum Electron., vol.37, pp.199-206, 2001

[4.45] J. Limpert, A. Liem, M. Reich, T. Schreiber, S. Nolte, H. Zellmer, A. Tunnermann, J. Broeng, A. Petersson and C. Jakobsen, "Low-nonlinearity single-transverse-mode ytterbium-doped photonic crystal fiber amplifier", Opt. Express, vol. 12, no. 7, pp. 1313–1319, 2004

[4.46] K. P. Hansen, C. B. Olausson, J. Broeng, K. Mattsson, M. D. Nielsen, T. Nikolajsen, P. M.W. Skovgaard, M. H. Sø rensen, M. Denninger, C. Jakobsen, and H. R. Simonsen, "Airclad fiber laser technology", Proc. SPIE, vol. 6873, pp. 687307–687307–12, 2008

[4.47] L. Dong, J. Li, and X. Peng, "Bend-resistant fundamental mode operation in ytterbium-doped leakage channel fibers with effective areas up to 3160 μm2", Opt.Express, vol. 14, no. 24 , pp. 11512, 2006

[4.48] J. Limpert, N. Deguil-Robin, I. Manek-Hönninger, F. Salin, F. Röser, A. Liem, T. Schreiber, S. Nolte, H. Zellmer, A. Tünnermann, J. Broeng, A. Petersson, and C. Jakobsen, "High-power rod-type photonic crystal fiber laser," Optics Express, vol. 13, p. 1055, 2005

[4.49] R. L. Sutherland, "Handbook of nonlinear optics", Marcel Dekker, New York, 1996

[4.50] J. Armstrong, N. Bloembergen, J. Ducuing, and P. S. Pershan, "Interactions between light waves in a nonlinear dielectric", Phys. Rev. 127, p. 1918, 1962

[4.51] G. D. Boyd and D. A. Kleinman, "Parametric interactions of focused Gaussian light beams", J. Appl. Phys. 39, pp. 3597-3639, 1968

[4.52] D. S. Hum, M. M. Fejer, "Quasi-phasematching", C. R. Physique, vol. 8, no.11, pp. 180-198, 2007

[4.53] Z. M. Liao, S. A. Payne, J. W, Dawson, A. D. Drobshoff, C. A. Ebbers, D. M. Pennington, I. Jovanovic and L. R. Taylor, “Thermally induced dephasing in periodically poled KTiOPO4 nonlinear crystals” at Nonlinear Optics: Materials, Fundamentals, and Applications, Waikoloa, HI, United States, 2-6 August, 2004

[4.54] P. G. Kazansky, L. Dong and P. St. J. Russell, “High second-order nonlinearities in poled silicate fibers”, Opt. Lett., vol. 19, no. 10, pp. 701-703, 1994

[4.55] S.Venugopal Rao, K. Moutzouris and M Ebrahimzadeh, “Nonlinear frequency conversion in semiconductor optical waveguides using birefringent, modal and quasi-phase-matching techniques”

[4.56] K. Chikuma and S. Umegaki, “Characteristics of optical second harmonic generation due to Cerenkov-radiation-type phase matching”, J. Opt. Soc. Am. B, vol. 7, p. 768, 1990

[4.57] M. J. Li, M. de Micheli, Q. He and D. B. Ostrowsky, “Cerenkov configuration second harmonic generation in proton-exchanged lithium niobate guides”, IEEE J. Quantum Electron., vol. 26, p.1384, 1990

[4.58] R. Haıdar, N. Forget, P. Kupecek, and E. Rosencher,” Fresnel phase matching for three-wave mixing in isotropic semiconductors”, J. Opt. Soc. Am. B, vol. 21, no. 8, pp. 1522-1534, 2004

[4.59] P. F. Bordui, M. M. Fejer, “Inorganic crystals for nonlinear optical frequency conversion”, Annu. Rev. Mater. Sci. vol..23, pp. 321-79, 1993

[4.60] C. T. Chen, “A localized quantum theoretical treatment, based on an anionic coordination polyhedron model, for the EO and SHG effects in crystals of the mixed-oxide types”. Sci. Sin., vol. 22, p. 756, 1979

[4.61] D. A. Roberts, “Simplified characterization of uniaxial and biaxial nonlinear optical crystals: a plea for standardization of nomenclature and conventions” IEEE J. Quantum Electron. vol. 28, pp. 2057-74, 1992

[4.62] C. Chen, Y. Wu, A. Jiang, B. Wu, G. You, R. Li and S. Lin, “New nonlinear-optical crystal: LiB_3O_5”, J. Opt. Soc. Am. B, vol. 6, no. 4, pp. 616–621, 1989

[4.63] S. P. Velsko, M. Webb, L. Davis, C. Huang, “Phase-matched harmonic generation in lithium triborate (LBO)”, IEEE J. Quantum Electron. vol., no. 9, p. 2182, 1991

[4.64] K. Kato, “Tunable UV generation to 0.2325 μm in LiB_3O_5”, vol. 26, no. 7, pp. 1173-1175, 1990

[4.65] A. Nebel and R. Beigang, “External frequency conversion of cw mode-locked Ti:Al2O3 laser radiation”, Opt. Lett., vol. 16, no. 22, pp. 1729–1731, 1991

[4.66] C. L. Tang, W. R. Bosenberg, T. Ukachi, R. J. Lane, and L. K. Cheng, "Optical parametric oscillators", Proc. IEEE, vol. 80, pp. 365–374, 1992

[4.67] L. McDonagh and R. Wallenstein, “Low-noise 62 W CW intracavity-doubled TEM00 Nd:YVO4 green laser pumped at 888 nm”, Opt. Lett., vol. 32, no. 7, pp. 802–804 2007

[4.68] V. A. Akulov, D. M. Afanasiev, S. A. Babin, D. V. Churkin, S. I. Kablukov, M. A. Rybakov and A. A. Vlasov., “Frequency Tuning and Doubling in Yb-Doped Fiber Lasers,” Laser physics, vol. 17, pp. 124–129, 2007

[4.69] G. K. Samanta, S. Chaitanya Kumar, Kavita Devi and M. Ebrahim-Zadeh, “Multicrystal, continuous-wave, single-pass second-harmonic generation with 56% efficiency “, Opt. Lett., vol. 35, no. 20, pp. 3513-3515, 2010

[4.70] Y. Grapov, V. Gapontsev, A. Avdokhin, “New generation of high power green fiber laser”, 6th International Symposium on High-Power Fiber Lasers and Their Applications, St. Petersburg, Russian Federation, June 26-28, 2012

Chapter 5

Intracavity power enhancement via use of an internal resonator

5.1. Introduction

The previous chapter discussed the challenges of scaling the output power of solid-state lasers with particular emphasis on cladding-pumped fibre lasers and efficient nonlinear frequency conversion of these devices. It explained how existing techniques are either limited in second harmonic output power and conversion efficiency or require complex opto-mechanical components and electronics for active cavity length stabilisation. This chapter introduces a novel approach for intracavity power enhancement in continuous-wave fibre lasers to enable efficient nonlinear frequency conversion that is free from the main limitations of the conventional technologies. This concept is based on the use of a low-roundtrip-loss free-space internal enhancement cavity integrated within a main fibre laser cavity, which does not require any active length stabilisation. A detailed concept overview and discussion on the laser behaviour in the spectral domain are presented in section 5.2. The principles of power build-up and fundamental features of the resonant enhancement cavity with two partially transmitting mirrors are discussed in section 5.3, while section 5.4 describes the main cavity design criteria. Section 5.5 focuses on spatial mode-matching between the fundamental enhancement resonator mode and the laser mode in the external fibre laser cavity arrangement and presents experimental results on spatial mode-matching of a ring “bow-tie” cavity’s fundamental mode to the spatial mode of a fibre laser based on a single-mode fibre. Feedback of the external cavity arrangement and its impact on the fibre laser’s performance is discussed in section 5.6 of this chapter. Experiments characterising temporal performance of the fibre laser with an internal enhancement resonator are

described in section 5.7. Section 5.8 introduces a modal interference approach to allow efficient coupling between a fundamental mode of the enhancement resonator and the output from a multi-mode fibre.

5.2. Concept overview

The internal resonant enhancement cavity, containing the nonlinear crystal is used to avoid the problems associated with the high fibre resonator loss and enables efficient second harmonic generation. The underlying principle of operation of this novel intracavity power enhancement scheme can be explained with reference to fig. 5.1, which is a conceptual diagram of the internally-frequency-doubled cladding-pumped fibre laser, with the main laser cavity in a ring configuration. This concept is based on three main elements of the fibre oscillator: a diode-pumped fibre-based gain stage, a resonant enhancement cavity, and a spectrum narrowing element.

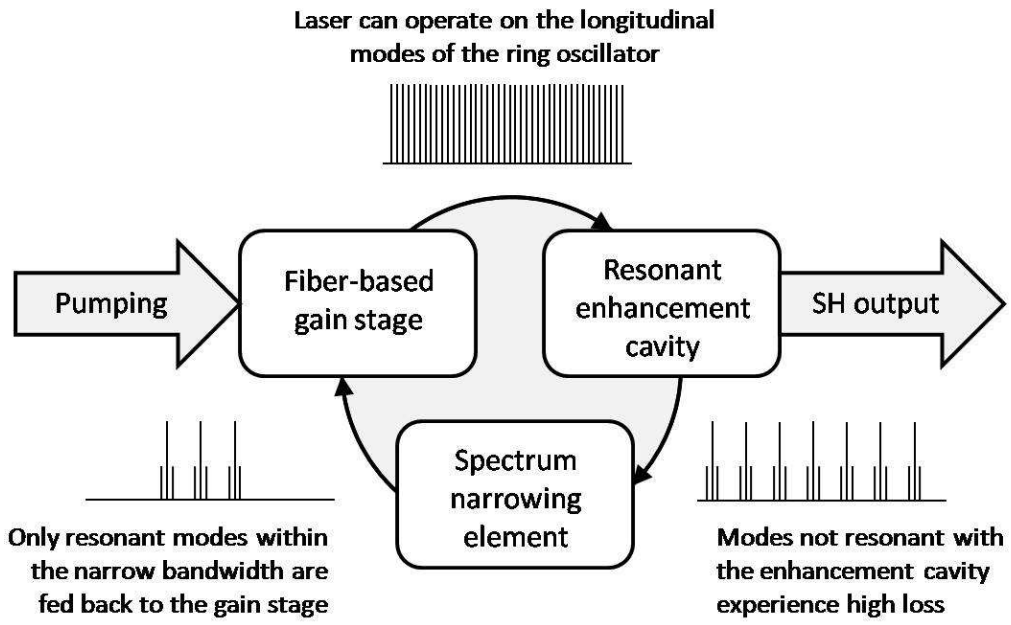

Figure 5.1: Internally-frequency-doubled fibre laser – concept (ring configuration)

The fibre laser can oscillate on the longitudinal modes of its main ring cavity, with the mode frequencies (wavelengths) defined by the effective round-trip path length of the main resonator L_{eff}:

$$\lambda_L = \frac{L_{eff}}{m} \quad \text{or} \quad \nu_L = m\frac{c}{L_{eff}} \tag{5.1}$$

evenly spaced by:

$$\Delta\lambda_L = \frac{\lambda_L^2}{L_{eff}} \quad \text{or} \quad \Delta\nu_L = \frac{c}{L_{eff}} \tag{5.2}$$

Fig. 5.2 illustrates this principle in the spectral domain:

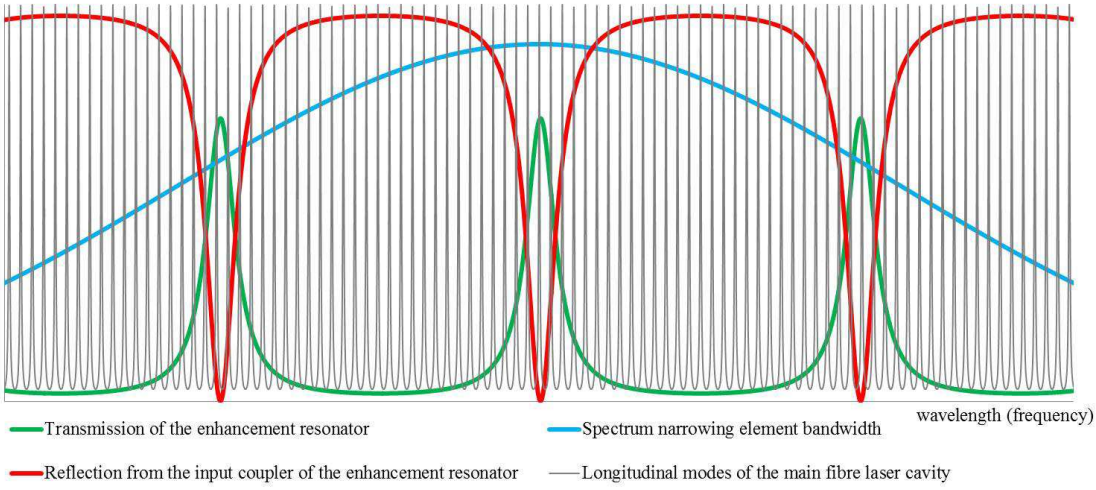

Figure 5.2: Intracavity enhancement resonator – concept overview in the spectral domain

Only those axial modes, represented by the grey lines in fig. 5.2, that are resonant in the enhancement cavity can be transmitted through the resonant enhancement cavity without significant loss. All other modes experience high loss via reflection from the input coupler of the enhancement resonator. The spectrum narrowing feedback element (e.g. diffraction grating) is used to select the lasing wavelength and to reduce the emission bandwidth so that it is smaller than the phase-matching bandwidth for second harmonic generation in the nonlinear crystal. The laser can then oscillate on the axial modes that lie both within the transmission peaks of the enhancement cavity and within the spectrum-narrowing element bandwidth – the blue line in fig. 5.2. This leads to high intracavity power in the enhancement cavity at the fundamental

wavelength and, hence, high second harmonic conversion efficiency. The intracavity powers attainable via this approach can be much higher than for a conventional intracavity-frequency-doubled fibre laser with the same pump power if the round-trip loss of the enhancement cavity is small compared to the round-trip loss for the fibre laser. This condition is usually quite straightforward to achieve. A major attraction of this approach compared to external cavity resonant second harmonic generation is that the fibre laser does not have to lase on a single-axial mode.

The laser can be designed to operate on a large number of axial modes that are simultaneously resonant in the enhancement cavity. This is generally easy to achieve in a fibre laser because of the long round-trip path length and hence small axial mode separation. In practical configurations there is always a large number (typically10^2-10^3) of transmission peaks N within the spectrum-narrowing element bandwidth $\Delta\Lambda$:

$$N \approx d\Delta\Lambda/\lambda^2 \tag{5.3}$$

(where d is the round-trip path length of the enhancement resonator), and multiple longitudinal modes within each transmission peak. To ensure stable operation on multiple axial modes of the fibre laser, the length of the fibre and the enhancement cavity design should be carefully chosen so there is at least one axial mode within each transmission peak of the enhancement cavity. This condition is achieved when axial mode separation (5.2) is smaller than the width of the transmission peak (5.9). This relation leads to the minimal effective length for the main laser cavity:

$$L_{min} \approx dF \tag{5.4}$$

This means that the main cavity round-trip length must be F times longer than the round-trip length of the enhancement cavity, where F is the enhancement resonator finesse. In cases where L_{min} is substantially longer than a typical active fibre length needed for pump light absorption, a section of a matched passive fibre can be spliced to the active RE-doped fibre to extend the total cavity length. For the main cavity round-trip lengths greater than (5.4) there are always many axial modes that satisfy the resonance condition and active stabilization of the cavity length is not needed.

Hence, this approach is immune to thermally-induced and mechanically-induced path length variations. An important feature of the resonant enhancement cavity is that it transmits light in both directions. The transmission of the enhancement cavity for resonant wavelengths depends on the transmission of its input and output couplers as well as its power-dependent round-trip loss. In the ring fibre laser configuration, oscillation in forward direction (indicated by arrows in fig. 5.1) is not favoured. For the same incident power levels, the round-trip loss of the enhancement cavity, associated with the power-dependent second harmonic loss, is greater in the forward direction when compared to reverse direction. Hence, in order to yield efficient second harmonic output, a non-reciprocal device (e.g. a Faraday isolator) is needed to enforce unidirectional oscillation in the forward direction. The non-reciprocal device should be positioned after the enhancement cavity, to minimise the loss in the fundamental power entering the cavity.

An alternative arrangement to the ring configuration is presented in fig. 5.3. The linear oscillator configuration is based on the same principle, but the resonant enhancement cavity is now integrated within a standing-wave fibre laser's cavity.

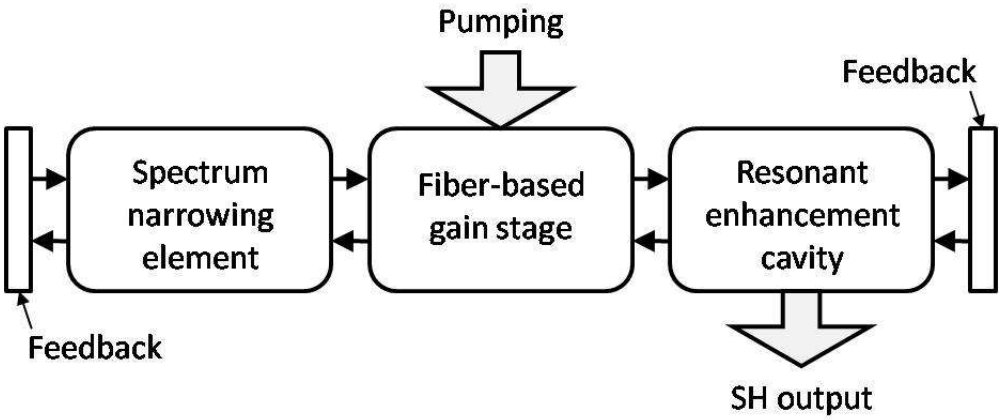

Figure 5.3: Internally-frequency-doubled fibre laser – concept (linear configuration)

The main difference from the ring configuration is that the fundamental light needs to pass the resonant enhancement cavity twice per round-trip (in opposite directions). The standing-wave cavity configuration allows for removal of the non-reciprocal device and its practical implementation is more straightforward than the ring cavity

configuration. The disadvantage of using this approach is the fundamental power loss in the feedback path. After first transmission through the enhancement resonator in forward direction and reflection from the feedback element laser signal experiences high loss due to the impedance mismatch (see next section 5.3).

5.3. Resonant enhancement cavity

As it has been explained in Chapter 4 the second harmonic generation efficiency is proportional to the incident fundamental power (eq. 4.28). To obtain high second harmonic power, the nonlinear crystal can be placed inside a low-roundtrip-loss free-space resonator to benefit from the high intracavity power. An example of such cavity configuration, a ring resonator in a "bow-tie" scheme, is illustrated in fig. 5.4.

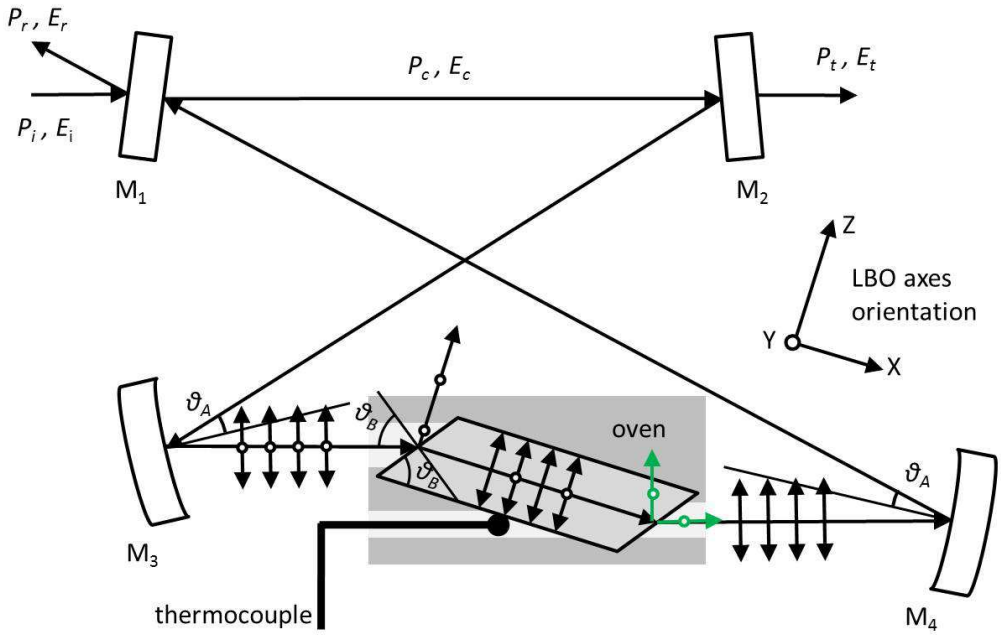

Figure 5.4: Enhancement cavity in a "bow-tie" configuration with a Brewster-cut LBO

The ring resonator comprises two plane-plane mirrors: an input coupler M_1 and an output coupler M_2 with reflectivities $R_1 = r_1^2$ and $R_2 = r_2^2$ at the fundamental wavelength respectively, two concave mirrors M_3 and M_4 (radius of curvature R_c) with high reflectivity $R_3 = R_4 = r_{HR}^2$ at the fundamental wavelength and high

transmission at the second harmonic wavelength, and a Brewster-angled LBO crystal of length L_c housed in an oven and cut for type I non-critical phase-matching (i.e. the beam is incident on the crystal surface at Brewster angle ϑ_B). r_1, r_2 and r_{HR} are the electric field reflection coefficients at fundamental wavelengths for mirror M1, M2 and M3 respectively. The oven is driven by a temperature controller connected to a thermocouple in thermal contact with the surface of the crystal. To minimize losses the incident beam has to be polarized in the XZ plane, which means the generated second harmonic will be polarized along the Y axis (Z axis corresponds to an optical axis of the crystal with the highest refractive index value at the fundamental wavelength, n_ω^Z).

If the incident electrical field amplitude is E_i, the amplitude transmitted by the cavity E_t, will be:

$$E_t = \sum_{n=0}^{\infty} E_i t_1 t_2 \left(t_1 t_2 t_c e^{i\delta}\right)^n = \frac{E_i t_1 t_2}{1 - r_1 r_2 t_c e^{i\delta}} \tag{5.5}$$

where $\delta = \frac{2\pi}{\lambda} d$ is the round-trip phase shift (d - round-trip path length), $t_1 = \sqrt{1 - r_1^2}$, $t_2 = \sqrt{1 - r_2^2}$ are the amplitude transmittances of the mirrors M_1 and M_2 respectively, and the round-trip transmission function (excluding input and output coupler losses) t_c is given by:

$$t_c = r_{HR}^2 \sqrt{(1 - \alpha)(1 - \eta_{SHG})} \tag{5.6}$$

where α is the sum of all losses excluding conversion to second harmonic output and mirrors' transmissions (i.e. residual reflections and scattering from crystal surfaces, scattering from mirror surfaces, scattering and absorption in the crystal, aperture transmission losses) and η_{SHG} is the single round-trip second harmonic conversion efficiency, defined as the ratio of second harmonic output power to fundamental circulating power incident on the crystal.

The power transmission function, defined as the ratio of power transmitted P_t by the mirror M_2 to the power P_i incident on the mirror M_1, is given by:

$$T(\delta) = \frac{E_t E_t^*}{E_i E_i^*} = \frac{(t_1 t_2)^2}{(1 - r_1 r_2 t_c)^2 + 4 r_1 r_2 t_c \sin^2(\delta/2)} \tag{5.7}$$

This function is plotted in fig. 5.5. We can see that it is similar to the transmission function of an etalon (appendix A), and only resonant wavelengths (frequencies) close to the resonance condition i.e. $\sin^2(\delta/2) = 0$ are transmitted.

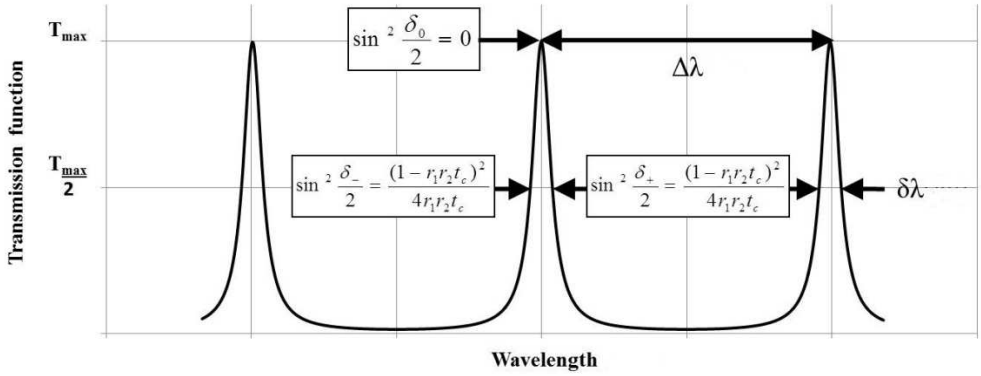

Figure 5.5: Power transmission function of the "bow-tie" resonant enhancement cavity

The transmission function $T(\delta)$ reaches its maximum value $T = T_{max}$ when the phase-shift $\delta = 2\pi m$ (i.e. $\lambda = d/m$), where $m = 1, 2, 3$ ...

$$T_{max} = \left(\frac{t_1 t_2}{1 - r_1 r_2 t_c}\right)^2 \tag{5.8}$$

and half of that value $T = T_{max}/2$ for $\delta = 2\pi m \mp \delta_{\mp}$, where $\delta_{\mp} = \mp 2 \sin^{-1}\left(\frac{1 - r_1 r_2 t_c}{2\sqrt{r_1 r_2 t_c}}\right)$.

Hence, the width of the enhancement cavity resonant mode is:

$$\delta\lambda = \frac{\lambda^2}{2\pi d}(\delta_+ - \delta_-) = \frac{2\lambda^2}{\pi d} \sin^{-1}\left(\frac{1 - r_1 r_2 t_c}{2\sqrt{r_1 r_2 t_c}}\right) \tag{5.9}$$

or $\delta\nu = c\delta\lambda/\lambda^2$ in the frequency domain.

Meanwhile, the free spectral range (FSR), i.e. the spectral distance between the transmission peaks of the enhancement cavity, is given by:

$$\Delta\lambda = \frac{\lambda^2}{2\pi d}[2\pi(m+1) - 2\pi m] = \frac{\lambda^2}{d} \tag{5.10}$$

or $\Delta\nu = c\Delta\lambda/\lambda^2 = c/d$ in the frequency domain.

The finesse of the cavity is defined as a ratio of the FSR and the cavity mode width and can be expressed as:

$$\mathrm{F} = \frac{\Delta\lambda}{\delta\lambda} = \frac{\pi}{2\sin^{-1}\left(1/\sqrt{\phi}\right)} \tag{5.11}$$

where the finesse coefficient:

$$\phi = \frac{4r_1 r_2 t_c}{(1 - r_1 r_2 t_c)^2}$$

A set of expressions as a function of power P_i incident on the input mirror of the enhancement cavity (M_1) can be written; including expressions for the power transmitted by the ring resonator P_t that is extracted through the output coupler mirror (M_2), the intracavity power circulating inside the resonator P_c before hitting the output coupler M_2, the power lost in the cavity (excluding second harmonic output and input/output coupler transmissions) P_l and the power rejected from the cavity via reflection from the input coupler M_1 surface P_r (equations 5.12-5.15):

$$P_t = P_i T = \frac{P_i (t_1 t_2)^2}{(1 - r_1 r_2 t_c)^2 + 4r_1 r_2 t_c \sin^2(\delta/2)} \tag{5.12}$$

$$P_c = P_i T/t_2^2 = \frac{P_i t_1^2}{(1 - r_1 r_2 t_c)^2 + 4r_1 r_2 t_c \sin^2(\delta/2)} \tag{5.13}$$

$$P_l = P_c r_2^2 (1 - t_c^2) = \frac{P_i t_1^2 r_2^2 (1 - t_c^2)}{(1 - r_1 r_2 t_c)^2 + 4 r_1 r_2 t_c \sin^2(\delta/2)} \tag{5.14}$$

$$P_r = P_i - P_t - P_l = P_i \frac{(r_1 - r_2 t_c)^2 + 4 r_1 r_2 t_c \sin^2(\delta/2)}{(1 - r_1 r_2 t_c)^2 + 4 r_1 r_2 t_c \sin^2(\delta/2)} \tag{5.15}$$

Factors containing $\sin^2(\delta/2)$ term in equations (5.12-5.15) disappear for resonant wavelengths (frequencies) satisfying the condition:

$$\lambda_c = \frac{d}{m} \quad \text{or} \quad \nu_c = m \frac{c}{d} \tag{5.16}$$

Optimum performance of the resonant enhancement cavity can be achieved when the input coupler transmission is equal to the sum of all other losses in the resonator, that is, when the cavity meets the impedance matching condition:

$$r_1 = r_2 t_c \tag{5.17}$$

Assuming a small conversion regime (4.28), with circulating power given by (5.13) and using (5.6), impedance matching condition (5.17) can be rewritten as a function of power P_i incident on the input coupler M_1 and proportionality constant ϵ defined by (4.27).

$$r_1^2 = r_2^2 r_{HR}^4 (1 - \alpha) \left(1 - \frac{\epsilon P_i r_2^2 r_{HR}^2}{1 - r_1^2}\right) \tag{5.18}$$

Solving (5.18) for r_1 leads to an expression for the optimal (impedance-matched) input coupler transmission:

$$T_1^{i.m.} = 1 - r_1^2 = \frac{\alpha'}{2} + \sqrt{\frac{\alpha'^2}{4} + \epsilon P_i \frac{1 - \alpha'}{1 - \alpha}} \tag{5.19}$$

where $\alpha' = 1 - r_2^2 r_{HR}^4 + \alpha$ is a total round-trip loss (excluding the input coupler transmission), accounting for losses in the crystal α and leakage losses through the

output coupler M_2 and concave mirrors M_3 and M_4. Equation (5.19) can be found in a simplified form ($r_2 = r_{HR} = 1$ i.e. $\alpha' = \alpha$) in many papers regarding SHG in external resonant cavities [5.1].

If we consider only resonant wavelengths (5.16) no power is reflected from the input coupler of the impedance-matched resonator $P_r = 0$, according to (5.15), and thus the resonated power (5.13) reaches its maximum value:

$$P_c^{i.m.} = \frac{P_i}{1 - R_1} \tag{5.20}$$

The transmission function (5.8) of the impedance matched resonator no longer depends on the loss α and is then equal to:

$$T^{i.m.} = \frac{T_2}{T_1^{i.m.}} \tag{5.21}$$

If we compare the SHG process in the small conversion regime using an impedance-matched resonator and the SHG using the laser beam directly incident on the nonlinear crystal (i.e. single-pass configuration), we can see that the fundamental power enhancement factor Ω_ω in the resonant cavity can be expressed as:

$$\Omega_\omega = \frac{P_c r_2^2 r_{HR}^2}{P_i} = \frac{R_2 R_3}{1 - R_1^{i.m.}} \tag{5.22}$$

This number also describes the SHG efficiency enhancement factor (defined as a ratio of the resonantly-enhanced SHG conversion efficiency $\eta_{SHG}^{r.e.}$ to the single pass SHG conversion efficiency $\eta_{SHG}^{s.p.}$:

$$\Omega_\omega = \frac{\eta_{SHG}^{r.e.}}{\eta_{SHG}^{s.p.}} = \frac{\epsilon P_c r_2^2 r_{HR}^2}{\epsilon P_i} = \frac{R_2 R_3}{1 - R_1^{i.m.}}$$

Second harmonic output enhancement factor $\Omega_{2\omega}$ will be then given by:

$$\Omega_{2\omega} = \frac{\epsilon(P_c r_2^2 r_{HR}^2)^2}{\epsilon P_i^2} = \Omega_\omega^2 = \left(\frac{R_2 R_3}{1 - R_1^{i.m.}}\right)^2 \tag{5.23}$$

If we make the M_2 and M_3 mirrors transmission losses small, the enhancement factors will be approximately:

$$\Omega_\omega \approx \left(1/T_1^{i.m.}\right) \quad \text{and} \quad \Omega_{2\omega} \approx \left(1/T_1^{i.m.}\right)^2 \tag{5.24}$$
$$\tag{5.25}$$

where the transmission of the impedance-matched input coupler should be chosen to be approximately equal to the sum of round-trip losses in the enhancement cavity:

$$T_1^{i.m.} \approx \eta_{SHG} + \alpha' \tag{5.26}$$

In the scheme illustrated in the fig. 5.4, the fundamental beam is incident on the LBO crystal's surface at an angle (to the surface's normal, in the plane of incidence) close to $\theta_B \approx \tan^{-1}(n_\omega^Z)$, thus minimising losses from the Fresnel reflection R_ω from each of the crystal surfaces for the fundamental wavelength:

$$R_\omega \approx \frac{\tan^2\left[\theta_B - \left(\pi/2 - \theta_B\right)\right]}{\tan^2\left[\theta_B + \left(\pi/2 - \theta_B\right)\right]} = 0 \tag{5.27}$$

On the other hand second harmonic output experiences loss by Fresnel reflection R_ω of:

$$R_{2\omega} \approx \frac{\sin^2\left[\theta_B - \left(\pi/2 - \theta_B\right)\right]}{\sin^2\left[\theta_B + \left(\pi/2 - \theta_B\right)\right]} = \cos^2\left[2\tan^{-1}(n_\omega^Z)\right] \approx 19.4\% \tag{5.28}$$

Hence, only 80.6% of the second harmonic power generated in the LBO crystal can be extracted in the main output beam.

5.4. Enhancement cavity design optimization

The simplified ray transfer (ABCD) matrix [5.2] for the round-trip in the empty "bow-tie" resonator (i.e. without the nonlinear crystal), with the starting point at the waist between the concave mirrors, can be expressed in the form:

$$\begin{bmatrix} A & B \\ C & D \end{bmatrix} = \begin{bmatrix} 1 & \frac{d_m}{2} \\ 0 & 1 \end{bmatrix} \begin{bmatrix} 1 & 0 \\ -\frac{2}{R_c} & 1 \end{bmatrix} \begin{bmatrix} 1 & d - d_m \\ 0 & 1 \end{bmatrix} \begin{bmatrix} 1 & 0 \\ -\frac{2}{R_c} & 1 \end{bmatrix} \begin{bmatrix} 1 & \frac{d_m}{2} \\ 0 & 1 \end{bmatrix} \quad (5.29)$$

Where d_m is the distance the light travels between the concave mirrors' surfaces. Waist spot size (radius) w_0 and its position δz_0 (with respect to point at half-distance between the plane mirrors) can be calculated from [5.3]:

$$w_0 = \sqrt{\frac{\lambda}{2\pi} \sqrt{\frac{4 - (A + D)^2}{C^2}}} \quad (5.30)$$

$$\delta z_0 = \frac{A - D}{2C} \quad (5.31)$$

Likewise the waist in the upper arm of the resonator (i.e. between M_1 and M_2 mirrors) spot size and position shift can be calculated from (5.30) and (5.31) respectively, with elements of the ray transfer matrix of a round-trip starting at the upper arm waist position amended to:

$$\begin{bmatrix} A & B \\ C & D \end{bmatrix} = \begin{bmatrix} 1 & \frac{d - d_m}{2} \\ 0 & 1 \end{bmatrix} \begin{bmatrix} 1 & 0 \\ -\frac{2}{R_c} & 1 \end{bmatrix} \begin{bmatrix} 1 & d_m \\ 0 & 1 \end{bmatrix} \begin{bmatrix} 1 & 0 \\ -\frac{2}{R_c} & 1 \end{bmatrix} \begin{bmatrix} 1 & \frac{d - d_m}{2} \\ 0 & 1 \end{bmatrix} \quad (5.32)$$

It should be noted that (5.30) and (5.31) are approximate values of waist spot size and position which are slightly different in a practical configuration with a nonlinear crystal for the Y and Z crystal axis directions, due to astigmatism caused by non-normal incidence on the concave mirrors and crystal surfaces. For the Brewster-angled crystal configuration it is possible to compensate the astigmatism arising from

refraction at Brewster-angled surfaces by setting a certain incidence angle on the concave mirrors. Such angle of incidence should result in a difference between focal lengths of the concave mirrors in the XZ plane and the XY plane respectively. Geometrical analysis [5.4] deliver stable mode size solutions at incident angles close to θ_A satisfying:

$$R_c \tan(\theta_A) \sin(\theta_A) = L_c[(n_\omega^Z)^2 - 1]/(n_\omega^Z)^3 \tag{5.33}$$

Wave analysis [5.5], however, shows that the beam waist inside the crystal remains non-circular in the centre of the stability range. For a critically-phase matched crystal with perpendicular surfaces, astigmatism cannot be fully compensated, so the incidence angle on the concave mirrors must be kept small (e.g. $\theta_A < 5^\circ$, where astigmatic effects are negligible).

5.5. Mode matching

In addition to the impedance matching condition (5.13) and optimal waist spot size in the nonlinear crystal for efficient nonlinear frequency conversion, another important design aspect is a good geometrical overlap between the fundamental mode of the enhancement resonator and the beam (essentially also a spatial mode of the main laser cavity) incident on its input coupler. Mathematically, the quality of mode matching can be quantified with an overlap integral:

$$\eta_o = \frac{|\int E_1^* E_2 dA|}{\sqrt{\int |E_1|^2 \, dA \int |E_2|^2 \, dA}} \tag{5.34}$$

where E_1 and E_2 are the complex electric fields in a plane, referring to the field of the spatial mode of the main laser mode and the field of the enhancement resonator mode, and the integration spans the whole beam cross-section. If we consider only fundamental resonator modes overlapping, the mode matching will depend on the relative waist positions, spots sizes, and the angular relationship between propagation directions.

In practice the overlap integral depends on many factors including the quality of the beam exiting the core of the fibre laser. For this reason mode matching was examined experimentally in an oscillator configuration - a fibre laser with an empty (i.e. without a nonlinear crystal) “bow-tie” enhancement resonator, as shown in fig. 5.6.

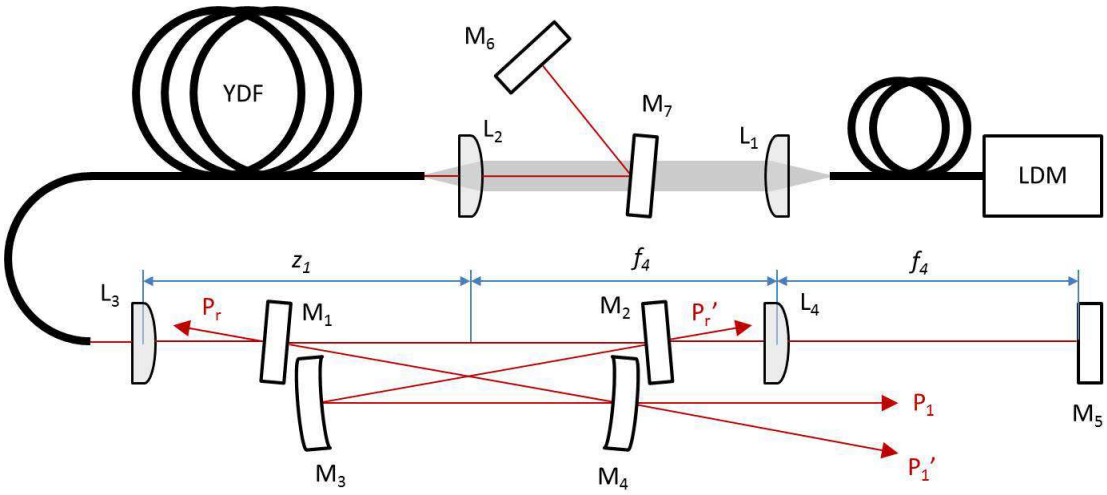

Figure 5.6: Fibre laser with an internal enhancement resonator – experimental set-up

The experimental set-up was based on a section (5 metres in length) of a relatively standard ytterbium-doped fibre (YDF) with a single-mode core, 0.075 in NA, 9.6 µm in diameter, and pure silica D-shaped inner-cladding, 0.4 in NA, 150 µm in diameter. Feedback for lasing from one end of the fibre was provided by an external cavity terminated with a simple broadband reflector M_6, with high reflection ($R_6 > 99.9\%$) at the central wavelength of the emission bandwidth ~1080 nm. From the other side of the fibre, the feedback was provided by another external cavity containing a ring enhancement cavity and terminated with another broadband reflector M_5 with high reflection ($R_5 > 99.9\%$). Pump light from a fibre-coupled (220 µm core, NA of 0.22) laser diode-bar module (LDM) at 975 nm was launched into the fibre end adjacent to the reflector M_6 with the aid of a dichroic mirror M_7 and two lenses L_1 and L_2 (with focal lengths of f_1 = 15 mm and f_2 = 8 mm respectively) in a telescopic configuration. The enhancement resonator with a “bow-tie” geometry consisted of a plane input (M_1) and output coupler (M_2) partially transmitting (T_1 = 6.0% and

T_2 = 1.2% respectively), a concave mirror M_3 with high reflectivity ($R_3 > 99.5\%$) and a concave output coupler mirror M_4 with transmission simulating the single-pass SHG conversion efficiency (T_4 = 5.5%) at central laser wavelength. Transmissions of the four mirrors forming the resonant enhancement cavity where chosen to be close to the impedance matching condition (5.17). Despite a small deviation from the ideal impedance matching, it should be possible to launch ~99% of the light incident on the input coupler according to (5.15) for a perfect spatial overlap ($\eta_o = 1$) with this set of mirrors. The concave mirrors were chosen with curvature radius R_c = 200 mm, and distances between the mirrors were respectively: $|M_1M_2|$ = 252 mm, $|M_2M_3|$ = 257 mm, $|M_4M_1|$ = 254 mm, and $|M_3M_4|$ = 252 mm. The incidence angle was made as small as the geometry of the cavity allowed, i.e. $\theta_A \approx 4.8^\circ$ in order to minimise the astigmatism effects. Such a cavity supported a fundamental mode with a waist spot size of ~77 μm between the concave mirrors and another waist of ~310 μm between the planar mirrors. The beam leaking through the planar output coupler (M_2) was being re-collimated with a lens L_4 (of focal length f_4 = 250 mm) to form a waist on the surface of the broadband reflector M_5. In this way, beam incident on the output coupler (M_2) after reflection from M_5 could be mode-matched (not impedance-matched, though) to the enhancement resonator in the reverse direction of propagation. Fine tuning of the resonator mode size could be performed by changing the resonant enhancement cavity length (e.g. changing the distance between the concave mirrors). In order to yield good spatial overlap between the enhancement resonator mode and the spatial mode of the fibre laser external cavity, the beam exiting the fibre core was tailored to match the waist spot size (~310 μm) and position (half-distance between the planar mirrors) with the waist in the upper arm of the enhancement resonator. Fine tuning of the waist spot size and position was performed by varying the distance z_1 between the waist and the focusing lens L_3 (with focal length of f_3 = 8 mm) and later fine adjustment of the position of the fibre end with respect to the lens L_3. Figure 5.7 shows the far-field images of the reflected beam taken with a CCD camera, after sufficient attenuation, during the alignment procedure (i.e. fine tuning of the waist spot size and position).

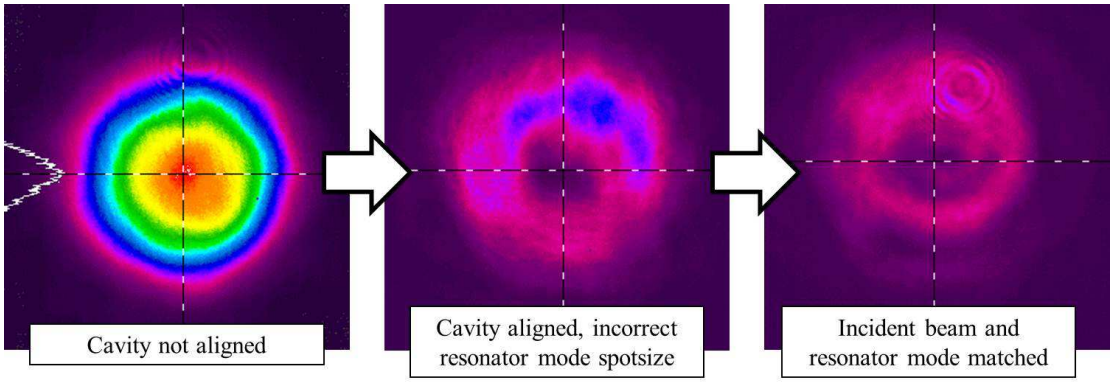

Figure 5.7: Beam profiles of the beam rejected from the enhancement resonator (CCD camera images after sufficient attenuation of the beam)

Best coupling was obtained for the distance z_1 = 326 mm. For the arbitrarily chosen incident power of 2.24 W (where the incidence power was monitored with an aid of a reflection from a small angle wedge) only P_r = 100 mW was reflected from the input coupler, corresponding to ~96% of incident power effectively launched into the fundamental mode of the enhancement resonator ($\eta_o \approx 96\%$). Power extracted through the concave output coupler (M_4) was P_1 = 1.65 W which corresponds to ~76% of the total incident power. The remaining power was distributed as follows: ~2.2% was fed back to the fibre, ~12% was lost via reflection from the non-impedance-matched coupling into the enhancement resonator in the reverse propagation direction and ~6% was lost via M_3 and M_4 mirror leakage losses. The intracavity power was 30 W which corresponds to the enhancement factor $\Omega_\omega \approx$ 14.5. This experiment confirmed that it is possible to integrate the enhancement cavity within the main cavity of the fibre laser without suffering significant loss on coupling between the main cavity mode and the enhancement resonator mode. It also proved that the circulating power in the enhancement resonator can be more than order of magnitude higher than the intracavity power in the main fibre laser cavity, and that most of the power launched into enhancement resonator can be efficiently extracted with an output coupling mechanism (e.g. a partially transmitting mirror or SHG process in a nonlinear crystal) with only few percent single pass efficiency/transmission.

5.6. Optical feedback

The feedback for lasing in the external cavity containing the enhancement resonator was provided by the broadband reflector M_5. The enhancement cavity was designed in such a way so that only ~16% of the total power incident on the input coupler M_1 was leaking through the output coupler M_2 to be used in a feedback path. If we consider the transmission through the enhancement cavity in the reverse direction (i.e. in the feedback path) the beam incident on the input coupler M_2 suffers significant loss due to impedance mismatch. The power transmitted through the cavity in the reverse direction was measured (with and aid of a reflection from a small-angle wedge) to be 49 mW out of 360 mW (~14%) incident on the output coupler mirror M_2 in the feedback path. The biggest loss in the feedback path was the reflection due to impedance mismatch (~70%), the rest was lost via leakage of the M_3 and M_4 mirrors (2% and 14% respectively). Total feedback efficiency (i.e. power returning to the fibre after double transmission through the enhancement cavity) was thus < 2.2%, which was more than sufficient for efficient locking of the longitudinal modes of the fibre laser to the resonant modes of the enhancement cavity. The fibre laser in the described configuration can operate efficiently with very small amount of feedback (sub-percent reflection into the fibre is generally sufficient to lock the longitudinal modes of the main cavity). For some configurations it is possible to observe efficient locking of the laser modes to the enhancement cavity resonant frequencies even without the mirror M_5 that usually provides the feedback for lasing. Researchers using enhancement cavities for resonantly enhanced nonlinear frequency conversion observed this kind of optical locking of solid state lasers [5.6] and diode lasers [5.7, 5.8, 5.9] and attributed it to the scattering from the imperfections in the nonlinear crystal surfaces. In the laser configuration described in the previous section there is no nonlinear crystal in the enhancement cavity (fig. 5.6), thus optical feedback must have a different origin. The optical feedback locking effect can occur, when the beam incident on the surface of the mirror at a given incidence angle θ_A is refracted in the direction close to the normal to the back (planar) surface of the mirror (fig. 5.8). The refracted ray can then reflect from the back surface of the mirror (via Fresnel reflection mechanism, as this side of the mirror is not typically

coated for efficient reflection at fundamental wavelength) and launch power efficiently into the counter-propagating resonator mode of the enhancement cavity.

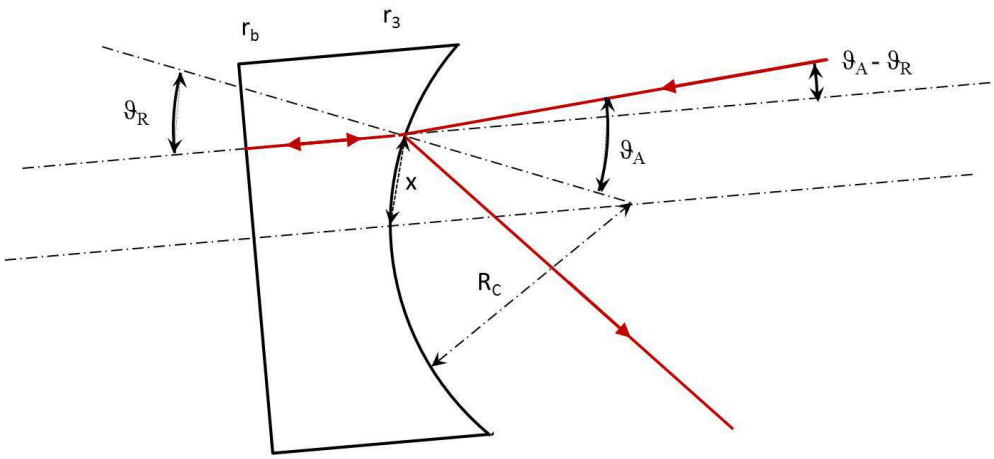

Figure 5.8: Geometry with the feedback for lasing arising from the Fresnel reflection from the back surface of the concave mirror (radius of curvature and incidence angle not to scale)

The ray refracts at an angle

$$\theta_R = \sin^{-1}(\sin\theta_A / n_M) \tag{5.35}$$

where n_M is the refractive index of the glass substrate. This effect is the strongest when the beam is incident not at the centre of the mirror but off-set by a certain distance (in the plane of incidence) from the centre

$$x \approx R_c \sin(\theta_A)/n_M \tag{5.36}$$

and the mirror is rotated by θ_R (in the plane of incidence) to compensate for the translation of the mirror (i.e. the beam reflected from the tilted mirror with an off-set incidence point has the same direction as the beam reflected from a centrally positioned mirror). This hypothesis was confirmed by blocking the feedback path (i.e. removing the mirror M_5 from the system), placing the highly reflective mirror on the 2D-translation stage and monitoring the output power for different positions of the incident beam on the mirror surface. Efficient locking was observed only when

the beam was incident on the mirror close to a point off-set from the centre of the mirror by ~1cm (in the plane of incidence), which stays in perfect agreement with (5.36). The power returning to the fibre was measured to carry ~0.55% of the total power incident on the enhancement cavity and the coupling efficiency dropped to 56% after removing the broadband reflector M_5 (from 96% with the M_5 mirror providing ~2.2% feedback).

It should be noted that for both scenarios, i.e. with and without the broadband reflector M_5, overall feedback efficiency was significantly lower than the Fresnel reflection of the perpendicularly cleaved fibre end (~4.0%). This means that the fibre laser in this configuration is operating on the common modes of the cavity formed by the mirror M_6 and the fibre end, and the cavity formed by mirror M_6 and one of the mirrors providing feedback from the external cavity (M_5 or M_3). At the same time those common modes have to be resonant in the enhancement cavity. This condition can be difficult to achieve when the emission spectrum is narrowed to be within the phase matching bandwidth of the nonlinear process. In addition, mechanically and thermally induced cavity length variations greatly influence the frequencies of the common modes and their spectral position relative to the transmission peaks of the enhancement cavity, which in turn affects the laser stability. This constraint on the operating frequencies can be alleviated by reducing the reflection from the fibre end so it is significantly lower than the overall feedback efficiency from the external cavity arrangement.

Splicing a coreless end-cap to the active fibre is a technique that is commonly used for increasing the spot size at the silica-air interface in high-power fibre amplifiers to reduce the intensity at the silica-air interface [5.10]. This can also greatly suppress unwanted feedback, especially when the surface at the silica-air interface is cleaved or polished at a small angle with respect to the fibre cross section plane. A section of a solid silica glass fibre (the cladding is formed by surrounding air) without a doped core is fusion-spliced to the output end of an active fibre (fig. 5.9).

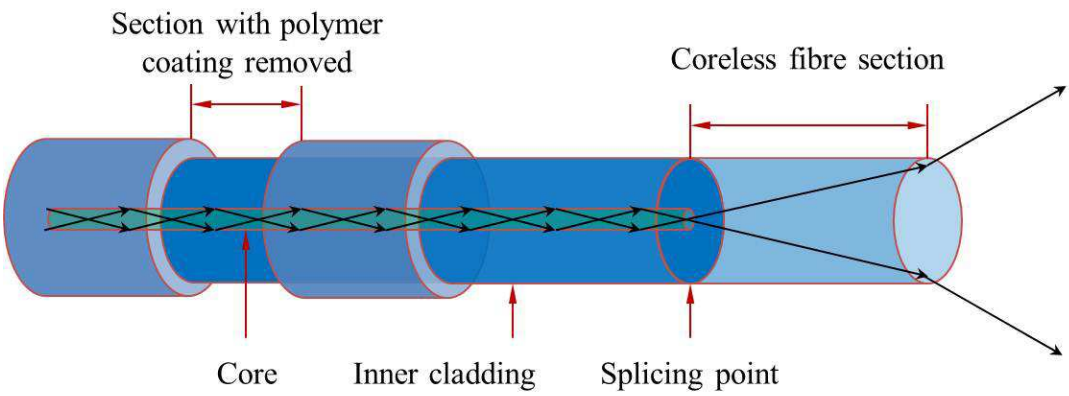

Figure 5.9: Fibre end termination scheme for feedback suppression (fibre sections lengths not to scale)

The mode propagating in the fibre core expands after entering the coreless end-cap and cannot be efficiently launched into the core after Fresnel reflection from the silica-air interface. A small fraction of this light can be, however, launched into the inner cladding of the fibre, thus it is important to supress the propagation of the cladding modes. The latter can be done by removing one or more sections of the polymer coating forming an outer cladding and replacing it with a medium of refractive index matching the refractive index of the inner cladding. It should be also noted that suppression of the cladding modes via this technique significantly improves mode matching between the beam exiting the fibre and the fundamental mode of the resonant enhancement cavity. The use of coreless end-caps in the experiments on internally-frequency-doubled fibre lasers generally improved the output power stability and enabled reaching higher output powers. The downside of using the end-caps is the lack of feedback that would be desired in some situations. If the external cavity becomes misaligned or blocked, the laser would generally switch to lase on modes of the cavity formed by the Fresnel reflection at the output end of the fibre. For the laser having the end-cap spliced on the end of the fibre, in case of cavity misalignment (e.g. due to thermal expansion under high-power operation) there is no alternative feedback for lasing and the gain in the fibre builds to a level where the laser can lase in a cavity formed by impurities in the core or stray reflections from objects outside the fibre. This mode of operation is generally very unstable, with self-pulsing behaviour leading quickly to fibre facet damage.

5.7. Temporal characteristics

Temporal characteristics such as axial mode forming timescales and sensitivity to vibrations of the fibre laser with an enhancement resonator integrated within the main laser cavity were investigated with an aid of a mechanical modulator (optical chopper) and a mirror attached to a transducer made of piezoelectric ceramic material (Lead Zirconate Titanate – PZT). The ring-shaped piezoelectric transducer was attached to the planar output coupler of the enhancement cavity (M_2) in a way so that it wasn't blocking the beam double-passing through the enhancement cavity (fig. 5.10). Its purpose was to scan the cavity length by a distance corresponding to a few (1-15) free spectral ranges with scanning frequencies in the range of 10 Hz - 2.4 kHz. At the same time the output power (P_1) and rejected power (P_r) were monitored with an aid of photo-detectors.

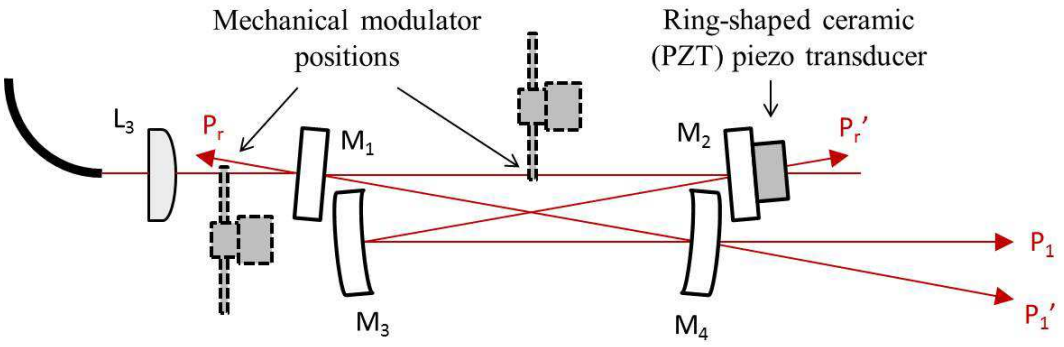

Figure 5.10: The position of mechanical modulating elements in the enhancement cavity

He-Ne laser and a simple scanning Fabry-Perot interferometer, configured as in figure 5.11 were used for the calibration of the PZT transducer and measurements of the maximum mirror displacement and velocities obtainable with this device. The beam from the laser was passing through the first stationary mirror and second scanning mirror attached to the ring-shaped piezoelectric element, both partially transmitting (T=2.2%) at He-Ne laser wavelength, and eventually incident on a photodetector (PD) connected to the oscilloscope (OSC). Piezoelectric transducer was connected to the triangle driving voltage V_{AC} with the frequency f and peak-to-

peak amplitude ΔV. The mirror glued to the transducer was being displaced by a distance proportional to the applied voltage.

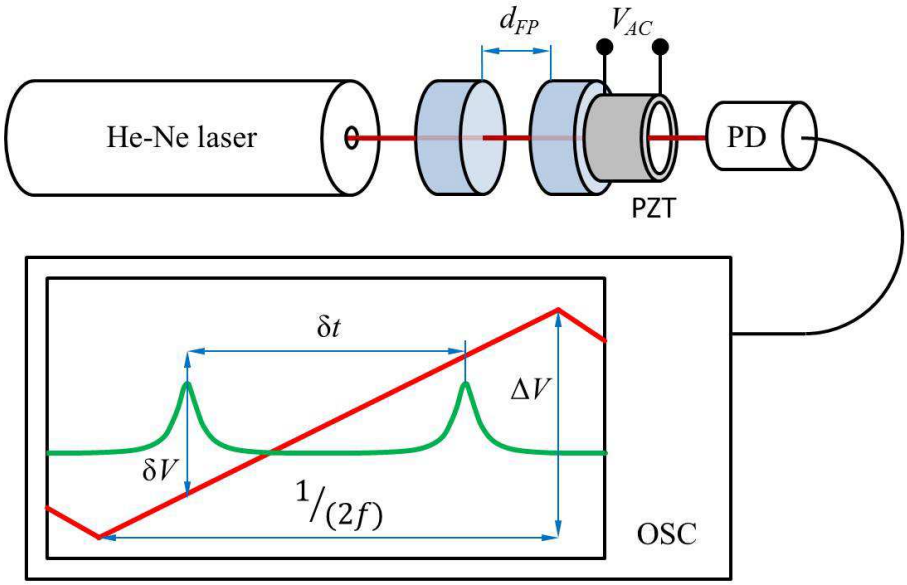

Figure 5.11: Experimental set-up for the piezoelectric ceramic (PZT) transducer calibration

Subsequent transmission peaks, separated in time by δt correspond to the mirror traveling the half of the He-Ne laser wavelength distance ($\lambda_{HeNe}/2$), during the driving voltage change of $\delta V = p\ \lambda_{HeNe}/2$ (where p is the voltage-to-displacement proportionality constant). During half of the scanning cycle the mirror travels the maximal displacement distance δd proportional to the driving voltage ΔV:

$$\delta d = \Delta V \frac{\lambda_{\mathrm{HeNe}}}{2\delta V} \tag{5.37}$$

with the velocity given by

$$v_m = 2f\delta d \tag{5.38}$$

or

$$v_m = \frac{\lambda_{HeNe}}{2\delta t} \tag{5.39}$$

Figure 5.12 shows the values of a) maximal mirror displacement calculated from the direct readings of the voltage across the PZT transducer (5.37), and b) maximal

mirror velocity; black circles are calculated from (5.37 and 5.38), red squares are calculated from the readings of the temporal separation of transmission peaks from the oscilloscope (5.39) plotted against scanning frequency *f*.

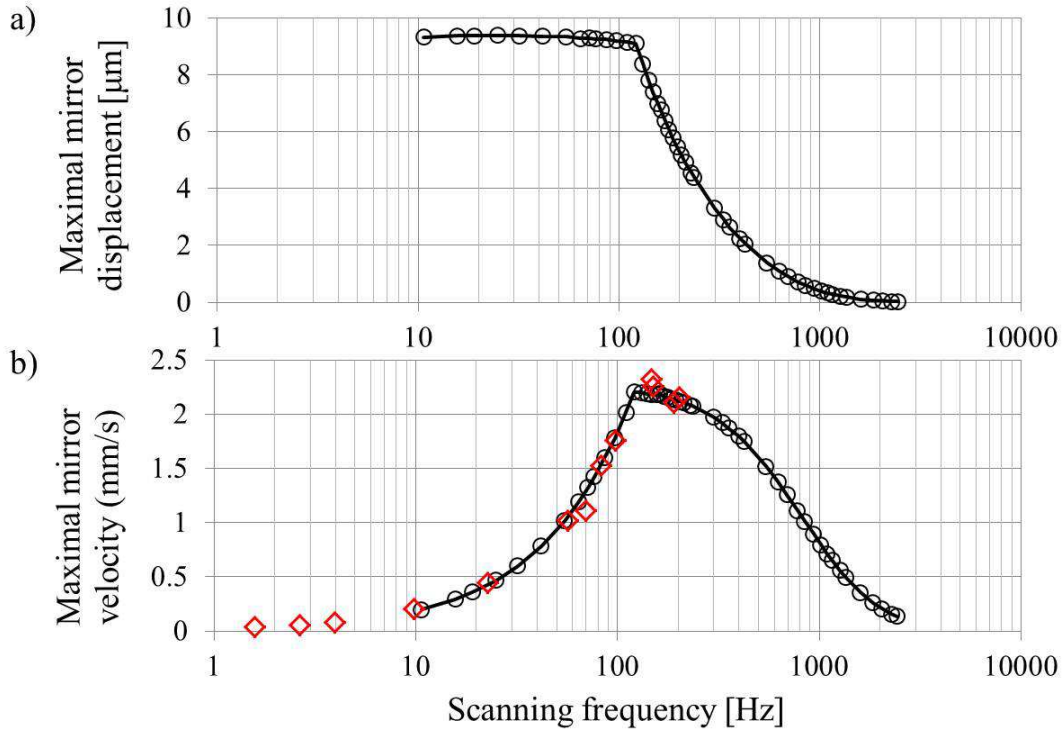

Figure 5.12: Piezoelectric ceramic (PZT) transducer calibration: a) maximal mirror displacement b) maximal mirror velocity plotted against scanning frequency

The piezoelectric transducer was then attached to the output coupler M_2 of similar weight and size to the mirror used in the calibration experiment and the mirror was scanned over the full range of frequencies (0-2.4kHz) while the output power of the fibre laser (P_1) was monitored with an aid of a photo-detector. The cavity length was being changed by the maximum distance of $2\delta d \cos\theta_A$ =18.53 µm (1.83×10^{-5} relative change in cavity round-trip length) and with maximum rate of change in cavity length $v_d = 4f\delta d \cos\theta_A = 4.42$ mm/s (for the scanning frequency ~120Hz).

This corresponds to ~0.02 nm (5.14 GHz) change in the spectral position resonant frequency of the cavity per half of the scanning period with the maximum frequency sweeping speed of ~4.78 nm/s. The fibre laser in this configuration completely changes the set of oscillating longitudinal modes of its main fibre laser cavity, when

the transmission peak moves by the spectral distance $\delta\lambda_x$ given by (5.9). Using (5.10) and (5.11) leads to:

$$\delta\lambda_x = \lambda^2/(dF) \tag{5.40}$$

Finesse (5.11) for this set of cavity mirrors is $F \approx 48$, so $\delta\lambda_x \approx 2.4\times10^{-5}$ nm. The spectral position of the transmission peak is proportionally dependent on the cavity length, so the transmission peak travels the spectral distance (5.40) while the cavity length changes by $\delta d_x = \lambda/F \approx 22.5$ nm. In other words, the laser completely changes the set of oscillating longitudinal modes, every $\delta t_x = \delta d_x/v_d \approx 5.1$ µs, ~810 times during each half of the scanning cycle ($f \approx 120$ Hz). Power stability measurements showed no evidence of breaking the resonance condition throughout the whole scanning frequency range and the output power remained stable with the stability better than 1.3% (standard deviation to main value ratio) for timescales 100ns-10ms, despite the constant change in the cavity length. The conclusion we can draw from this experiment is that the longitudinal modes of the main fibre laser cavity (with the round-trip time $t_{rt} \approx 60$ ns) form relatively quickly and it takes less than $N = \delta t_x/t_{rt} \approx 80$ round-trips to establish stable axial modes that can be efficiently launched to the enhancement resonator.

Another experiment investigating the temporal characteristics of the fibre laser with the enhancement resonator integrated in the main cavity used the optical chopper. These experiments were carried out with the chopper positioned between the fibre gain stage and the enhancement cavity as well as inside the enhancement resonator (fig. 5.10). Its purpose was to switch the laser between the cavity formed by mirror M_6 and the fibre end adjacent to the lens L_3, and the main cavity of the fibre laser formed by the mirror M_5 and mirror M_6 (including double pass through the enhancement cavity). At the same time power in the reflected beam (P_r) and the power in the output beam (P_1) where monitored (after sufficient attenuation) with photo-detectors. The chopper had 20 evenly spaced blades of width $d_B \approx 1.05$ cm at the beam position separated with open slits of the same width. The blades were flying through the beam of spot size $w_1 \approx 310$ µm with the modulation frequency in the range of 0-1 kHz. Figure 5.13 shows an exemplary experimental result for the

modulation speed $f_c \approx 430$ Hz taken with the set-up comprising the optical chopper modulating the beam inside the enhancement cavity in the waist position between the planar mirrors; a) the oscilloscope trace with the voltage proportional to the output optical power (P_1) extracted through the concave output coupler M_4, and b) the oscilloscope trace with the voltage proportional to the optical power reflected from the input coupler of the enhancement cavity (M_1). For $f_c = 430$ Hz chopping frequency the time it takes the blade to fly through the beam (gradually unfolding the beam) is $\Delta t = w_0/(d_B f_c) = 70$ µs and leaves the cavity fully open for the next ~1025 µs, before the next blade start covering the beam (for the next 70 µs) leaving the cavity fully blocked for the next ~1025 µs.

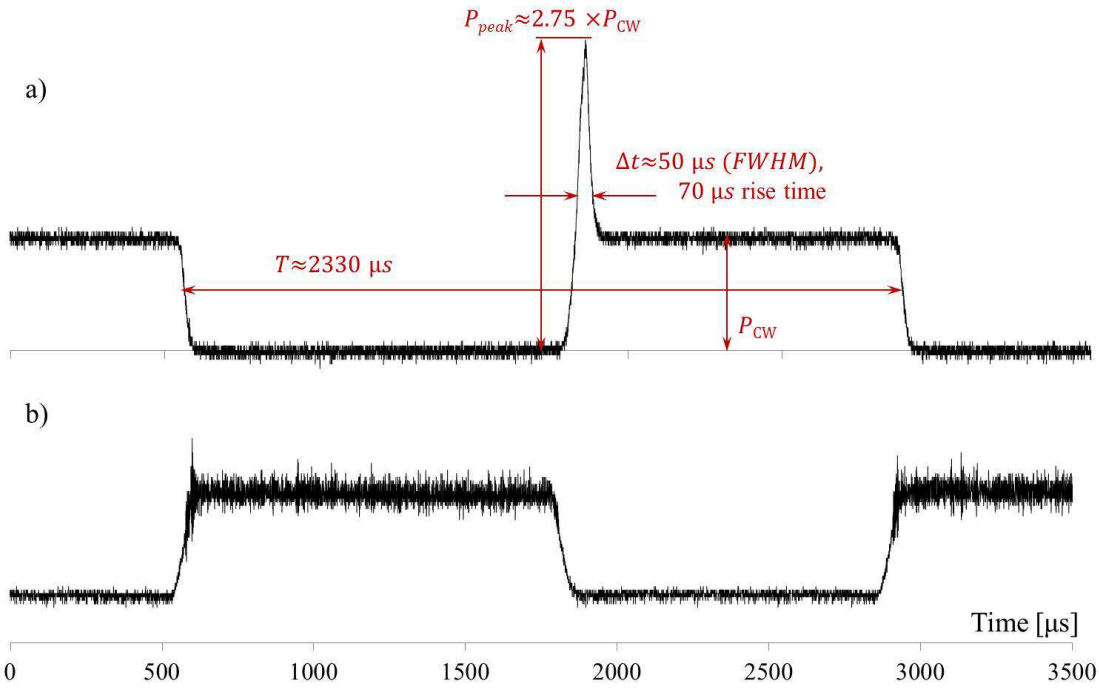

Figure 5.13: The fibre laser modulated with a chopper inside the enhancement cavity: a) output power extracted through the concave output coupler b) power of the beam reflected from the input coupler (traces not to scale in the vertical axis with respect to each other)

When the blades are not blocking the beam inside the enhancement resonator the fibre laser oscillates inside its main cavity, the output extracted through the concave output coupler remains at the constant level P_{CW} (fig. 5.13a, time 0-500 µs) and a small fraction of power, depending on the mode-matching factor, is rejected from the cavity (fig. 5.13b, time 0-500 µs). As one of the chopper blades starts to fly through

the beam, the mode-matching factor (5.34) gradually decreases so the fraction rejected from the cavity gradually increases to the value of input coupler mirror reflectivity R_1. (fig. 5.13b, time 530-600 µs). The rest is blocked by the chopper blade so the output power gradually decreases from the value P_{CW} to 0 (fig. 5.13a, time 530-600 µs). While the blade is blocking the beam there is no output from the enhancement cavity (fig. 5.13a, time 600-1750 µs) and the fibre laser reaches the steady state in the cavity of a lower Q-factor (and higher population inversion) starting with relaxation oscillations (fig. 5.13b, time 580-610 µs) and eventually stabilising at constant output power (fig. 5.13b, time 620-1750 µs), R_1 of which is reflected from the input coupler. As the chopper blade starts gradually unblocking the fundamental mode of the enhancement resonator, the overlap factor increases again enabling gradually increasing fraction of the power to be launched into the resonator. Once enough power is circulating in the enhancement resonator, the external cavity arrangement provide more feedback for the modes resonant in the main laser cavity which has now a higher Q-factor compared to an "off" state, when the beam is blocked with a chopper blade. The oscillating modes extract the inversion built-up during the "off" state and form a ~50 µs (FWHM) long pulse (fig. 5.13a, time 1800-1900 µs) with peak power ~2.75 times the power extracted in the steady state, and the rejected power gradually returns to a lower level defined by the mode matching factor in the "on" state (fig. 5.13a, time 1800-1900 µs). Although the switching times measured between the "off" and "on state depend on the modulation frequency, the pulse width remained constant for a given feedback level and cavity length across the tested frequency range. After all extra inversion is extracted, the laser returns to the steady state of the higher Q-factor cavity and the whole cycle continues. Very similar results were obtained with the optical chopper positioned between lens L_3 and the enhancement cavity. The only difference was the limited access to the power not launched to the ring resonator, as it was blocked by the chopper blade in the "off" state (oscillations in the low Q-factor cavity). All other features in the oscilloscope traces remained the same.

This experiment confirmed that the longitudinal modes of the fibre laser with a resonant enhancement resonator integrated within the main laser cavity form relatively quickly - no delays or power rise times longer than the modulation speed were observed. A simple example of a "Q-switched" operation was demonstrated

with a 0-1 kHz repetition rate, which leaves the door open to using fibre laser architectures with intracavity enhancement resonators in pulsed regime of operation.

Overall it was demonstrated that it was not possible to break the optical frequency lock between the resonant enhancement cavity and the main fibre laser cavity with sub-kHz modulation of the cavity Q-factor or cavity vibrations up to 18.5 µm in amplitude and 4.4 mm/s in cavity length rate of change in a similar frequency range. We conclude that the laser's longitudinal modes form relatively quickly within a small number of roundtrips (most probably well below 80 which is the upper limit - higher numbers were ruled out by the described experiment).

5.8. Modal interference

All experiments described previously were based on fibre with a robustly single-mode core. As it has been explained in chapter 4 of this thesis, the ability of the design to accommodate the use of a gain medium with a larger core area than the limit for robustly single-mode behaviour is an important advantage. Using a larger core increases the catastrophic facet damage threshold and the threshold for unwanted nonlinear loss processes and thus facilitates further power scaling. In this section we describe an approach that allows efficient coupling of multiple transverse modes in the fibre core to the fundamental spatial mode of the enhancement resonator. The fibre laser can oscillate on multiple transverse modes inside the fibre's core which, on exiting the fibre end adjacent to the internal enhancement cavity, have relative phases and powers such that they interfere to yield a combined (resultant) beam that can be substantially spatially-matched to the fundamental transverse (TEM_{00}) mode of the internal enhancement cavity by using an appropriate arrangement of lenses.

The underlying physical principle for this approach can be explained as follows: In a multi-mode fibre core, the number of allowed transverse modes depends on the refractive index of the core (n_{core}), the refractive index of the surrounding cladding material (n_{clad}) and the core diameter, where $n_{core} > n_{clad}$ for guidance. Each

transverse mode is characterized by an effective propagation constant and related effective refractive index (n_{eff}), where $n_{core} > n_{eff} > n_{clad}$. The exact value for n_{eff} for a particular mode depends on the details of the fibre design and the mode, but as a rough guide low order modes have a smaller mode size than higher order modes and hence have a higher value for n_{eff}. Each allowed transverse mode of the fibre has a range of allowed frequencies (5.1), which define the axial modes associated with a particular transverse mode. The effective length of the fibre laser resonator depends, amongst other things, on the length of the optical fibre and the effective refractive index, n_{eff} of a particular transverse mode. Since the values for n_{eff} are, in general, different for different transverse modes, the associated axial mode frequencies are also different. However, at certain frequencies the axial modes of two or more transverse modes share the same frequency and there is a well-defined phase relationship between these modes. The internal enhancement cavity acts as a spatial filter and a frequency filter, since only the transverse modes of the fibre core which interfere to yield a combined beam that is substantially spatially-matched to the fundamental mode of the enhancement cavity and with axial mode frequencies that are resonant in the internal enhancement cavity are fed back to the fibre gain element and hence can lase. Other transverse modes with different axial mode frequencies experience a high reflection loss at the input coupler to the enhancement cavity and hence are suppressed. Preferential lasing on the fundamental (TEM_{00}) mode of the enhancement cavity may be aided by the use of one or more apertures in the enhancement cavity to help suppress higher order transverse modes.

This effect of modal interference was investigated in an experimental set-up very similar to the one from figure 5.5, but with the single-mode fibre replaced by an Yb-doped fibre (*Nufern PLMA-YDF-25/345*) with a slightly multimode, 25 µm diameter core, NA ≈ 0.055, and a pure silica inner-cladding, NA=0.4, 345 µm in diameter. The normalised frequency parameter for operating wavelength $\lambda = 1080$ nm was $V \approx 4.0$. The modal structure for this fibre (where the refractive index profile was approximated with a parabolic function) was found with an aid of commercially available software (*Optiwave, Optifiber software package*). Figure 5.13 shows the calculated values of effective refractive index plotted against the diameter of the fibre core.

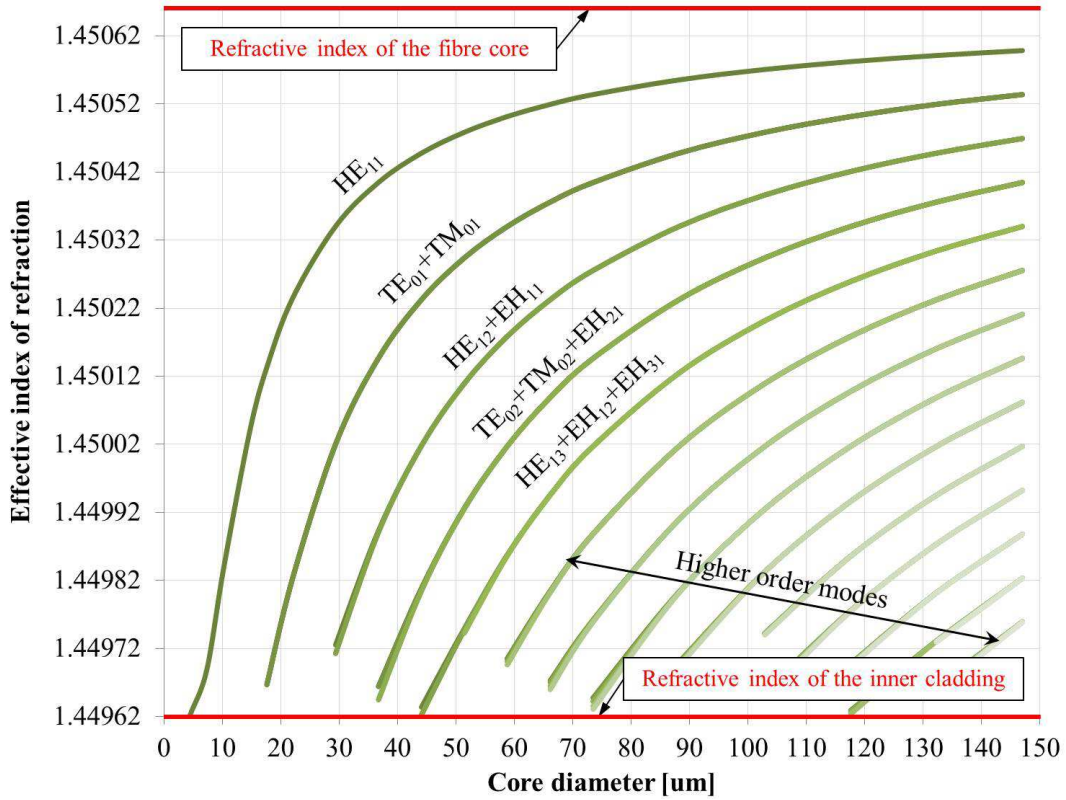

Figure 5.14: Simulation of the effective refractive index values for different spatial modes propagating in the fibre as a function of the fibre core diameter

Certain modes form groups of modes with similar effective refractive index values. Although the modes within a group propagate with the same velocity in the fibre core, they can have substantially different spatial electric filed distributions (profiles). Mode profiles grouped in the first five sets of modes with similar effective refractive indices (as calculated with *Optifiber*) are shown in figure 5.14:

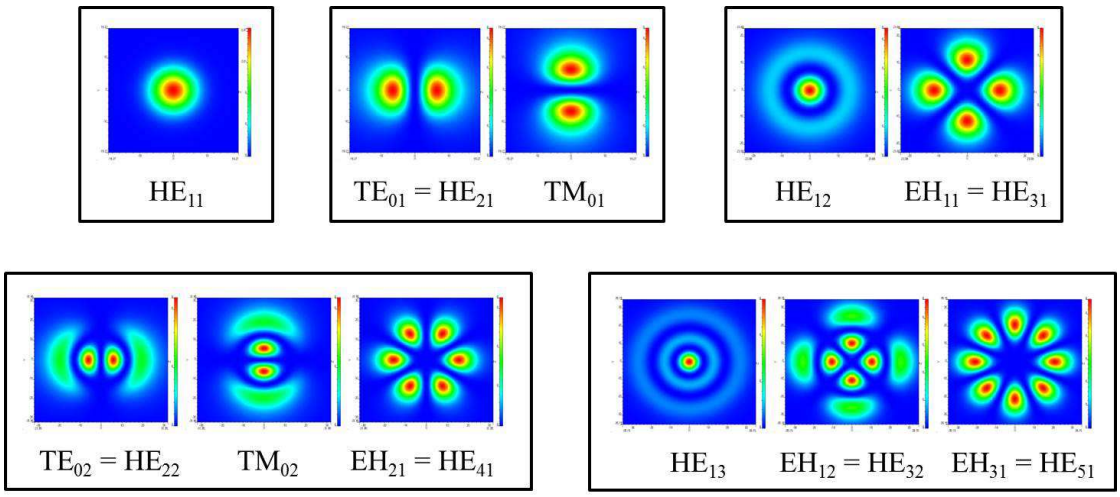

Figure 5.14: Simulation of the mode profiles for the five groups of spatial modes with the highest values of the effective refractive index propagating in the fibre (spatial modes with a similar effective refractive index value are grouped together)

According to the simulation results the Yb-doped fibre with a 25 µm core, which was used in the experiment, supported only 5 modes from the first three groups shown in fig. 5.14. These modes can add up constructively to form a spatial distribution close to the fundamental mode profile, only for a fixed phase relationship occurring at certain frequencies (wavelengths). The mode field at the facet of the fibre is then close to Gaussian beam profile. Figure 5.15a shows the simulated total output power after double-pass propagation through a 5 m section of a fibre used in the experiment, as a function of wavelength, assuming that all three groups of modes were launched into the fibre with equal amplitudes. The beating pattern corresponds to the separation between the wavelengths, for which the groups of modes interfere constructively. The smaller spacing of ~0.2 nm corresponds to beating between the individual modes, and the wider spacing of ~1.0 nm corresponds to the separation between the wavelengths for which all three groups of modes add-up in phase. For different ratios of power in the individual modes the relative height of the peaks would be different but the spectral separation would remain the same as it depends only on the effective refractive index values and the effective length of the fibre laser resonator. Figure 5.15 b) is a part of the measured laser output's spectrum. Well defined peaks can be observed, with a spectral separation of ~1 nm. We can conclude that the peaks correspond to the wavelengths, for which all three groups of modes interfere constructively and form a superposition of modes with a transverse profile

having a high mode-matching factor with the fundamental mode of the resonant enhancement cavity. The spectrum of the fibre laser is affected by many factors including spatial hole burning and the spectral overlap between the resonant frequencies of the enhancement resonator and the frequencies of the constructive super-positions of the supported mode groups (Vernier effect), but the characteristic feature arising from the mode super-positions exiting the fibre all in-phase every ~1nm is clearly visible. The best mode-matching factor in this fibre laser configuration was measured to be ~81%.

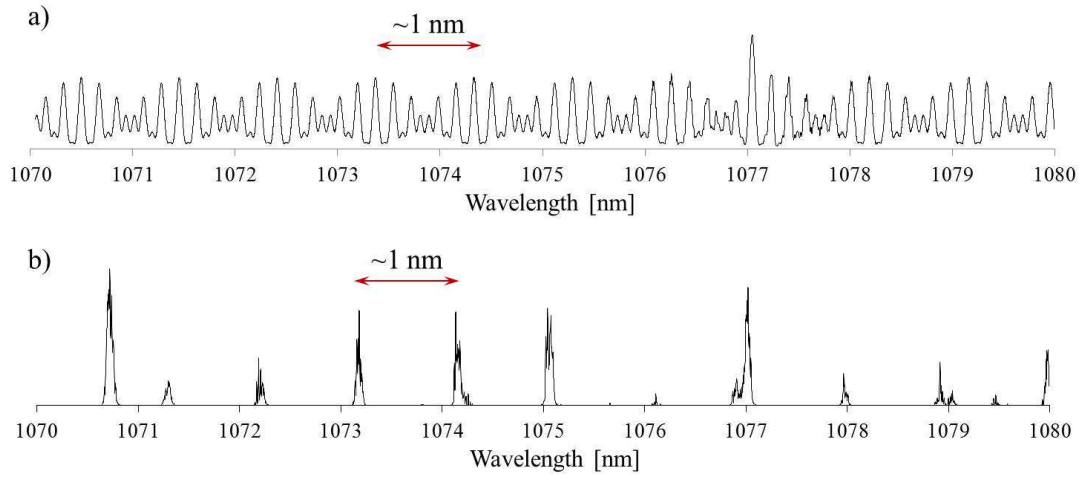

Figure 5.15: a) Simulation of the beating pattern between three groups of modes after a double pass through the multimode fibre section b) The output spectrum of the fibre laser using modal interference to couple light into the internal enhancement cavity's fundamental mode

5.9. Conclusions

This chapter introduced the concept of the power enhancement via use of an internal free-space enhancement resonator integrated within a main fibre laser cavity. The theory and design criteria for the enhancement cavity with two partially transmitting mirrors have been presented. The importance of spatial mode-matching between the fundamental mode of the enhancement resonator and the fibre laser's mode as well as the optical feedback from the external cavity arrangement has been discussed. These were illustrated with the experiments, where the empty "bow-tie"

enhancement cavity was integrated within the main cavity of a fibre laser based on an Yb-doped fibre with a single-mode core. The best spatial mode-matching between the fibre laser's mode and the fundamental mode of the enhancement resonator was measured to be ~96% and the feedback level sufficient for efficient frequency locking was very low (typically <3%). The optical locking was proven to be very tolerant to vibrations, as the output power laser remained stable (< 1.3%) under resonant enhancement cavity vibrations greater than 18 μm in amplitude and 4.4 mm/s in cavity length's rate of change. The axial modes needed for maintaining the frequency lock formed quickly in < 5 μs (< 80 round trips) timescale. Simple mechanical modulation of the external cavity arrangement's Q factor induced optical pulse formation rather before breaking the resonance condition and proved a route to a pulsed regime of operation using this kind of resonator architectures feasible. Modal interference approach for efficient coupling between the fundamental mode of the resonant enhancement resonator and the multi-spatial-mode content of the external cavity arrangement was introduced and experimentally confirmed with a fibre laser set-up based on an Yb-doped fibre with a multi-mode core. The best mode-matching factor between an empty "bow-tie" cavity and a multi-spatial-mode fibre laser's mode was measured to be ~81%.

References

[5.1] E. S. Polzik and H. J. Kimble, "Frequency doubling with KNbO3 in an external cavity", Opt. Lett., vol. 16, no. 18, 1991

[5.2] H. Kogelnik, T. Li,"Laser Beams and Resonators", Appl. Opt. vol. 5, no. 9, pp. 1550-1567, 1966

[5.3] A. Yariv, "Optical Electronics", 4th edition (Philadelphia, PA: Saunders), 1991

[5.4] M. H. Dunn and A. I. Ferguson, "Coma compensation in off-axis laser resonators", Opt. Commun., vol. 20, pp. 214-219, 1977

[5.5] J. Hald, “Second harmonic generation in an external ring cavity with a Brewster-cut nonlinear crystal: theoretical considerations”, Opt. Commun., vol. 197, pp. 169-173, 2001.

[5.6] C.S. Adams and A. I. Ferguson “Tunable narrow linewidth ultra-violet light generation by frequency doubling of a ring Ti:sapphire laser using lithium tri-borate in an external enhancement cavity”, Opt. Commun., vol. 90, pp. 89-94, 1992

[5.7] A. Hemmerich, D. H. McIntyre, C. Zimmermann and T. W. Hansch, “Second-harmonic generation and optical stabilization of a diode laser in an external ring resonator”, Opt. Lett., vol. 15, no. 7, pp. 372-374, 1990

[5.8] C. Tamm, “A Tunable Light Source in the 370 nm Range Based on an Optically Stabilized, Frequency-Doubled Semiconductor Laser”, Appl. Phys. B, vol. 56, pp. 295-300, 1993

[5.9] D. Skoczowsky, A. Jechow, H. Stürmer, T. Poßner, J. Sacher, R. Menzel “Quasi-monolithic ring resonator for efficient frequency doubling of an external cavity diode laser”, Appl. Phys. B, vol 98, pp. 751–757, 2010

[5.10] J. Limpert, S. Höfer, A. Liem, H. Zellmer, A. Tünnermann, S. Knoke and H. Voelckel, “100-W average-power, high-energy nanosecond fiber amplifier”, Appl. Phys. B, vol. 75, no. 4-5, pp. 477-479, 2002

Chapter 6

Internal resonantly enhanced frequency doubling in CW fibre lasers

6.1. Introduction

This chapter describes the development and power scaling of a frequency-doubled continuous-wave Yb-doped fibre laser employing an internal resonant enhancement cavity, which has been introduced in the previous chapter. Design considerations for the enhancement cavity and nonlinear crystal orientations corresponding to two different phase-matching conditions are discussed in section 6.2. The following section 6.3 presents the experimental results on several configurations investigated during the development of the high-power continuous-wave green fibre laser. It starts with preliminary set-up in a ring resonator geometry (section 6.3.1), followed by a linear configuration based on a robustly single-mode Yb-doped fibre and a Brewster-angled LBO crystal oriented for non-critical phase matching. Performance of the latter, including wavelength tuning flexibility, has been thoroughly investigated and discussed in section 6.3.2. The next section (6.3.3) presents a procedure using a 'bulk' solid-state laser to aid the alignment of the internally-frequency-doubled fibre laser, which was used to optimise the design of all lasers with a linear resonator configuration described in this chapter. Section 6.3.4a describes the experiment on power scaling of an internally-frequency-doubled laser based on a slightly multi-mode Yb-doped fibre. Coupling light into the enhancement resonator, aided by modal interference is also demonstrated. Another experimental set-up based on a different LBO crystal orientation (critical phase matching in room temperature) with a narrow linewidth and improved beam quality has been discussed in section 6.3.4b.

6.2. Design considerations

Two different LBO crystals, both configured for efficient SHG to ~540 nm but designed for different phase matching techniques were used in the experiments on internal frequency doubling in high-power CW fibre lasers. Careful design of the enhancement cavity was necessary prior to alignment of the experimental set-up. This section briefly reviews the most important design considerations.

a) Brewster-angled 15mm long LBO crystal cut and oriented for type I (ooe) non-critical phase matching (as illustrated in fig. 6.1):

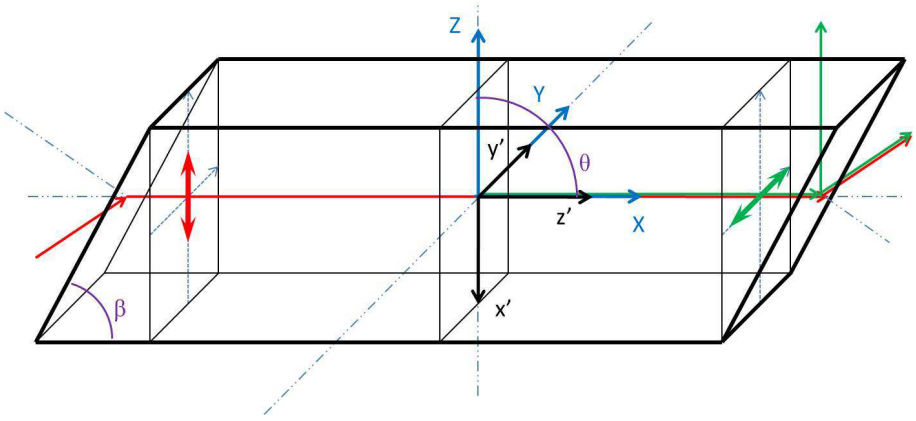

Figure 6.1: Principal crystal axes orientation in type I non-critically phase matched Brewster-cut LBO. (XYZ – principal crystal axes, x'y'z' – laboratory coordinate system)

Fig. 6.1 illustrates the crystal's geometry and principal axes orientation with respect to the laboratory coordinate system. The principal crystal axes coordinate system XYZ is rotated around y' axis by $\theta = 90^{\circ}$ with respect to the laboratory coordinate system (z' – propagation direction). The front surface of the crystal (i.e. the surface the fundamental light is incident on) is tilted at an angle $\beta = \tan^{-1}(n_{\omega}^{Z}) = \theta_B$ (Brewster angle at the fundamental wavelength). The light at the fundamental wavelength (in red) is polarised along the Z axis, while the second harmonic output (in green) has the orthogonal polarisation (along Y axis). The phase matching temperature (4.32) for generating second harmonic output at 540 nm is $T_{pm} \approx 394.8$ K (121.6 $^{\circ}$C). Refractive indices at fundamental wavelength for this

temperature calculated from Sellmeier's relation are $n_\omega^Y \approx 1.5893$ and $n_\omega^Z = n_{2\omega}^Y \approx 1.6048$ in Y and Z directions respectively. The nonlinear coefficient in this configuration is $d_{eff} \approx 0.847$ pm/V. The phase matching temperature bandwidth, FWHM, (4.35) is $\Delta T_{pm} \approx 3.4$ K. The angular acceptance bandwidth, FWHM, (4.42) is $\Delta\theta_{pm} \approx 21.6$ mrad (~1.2°). The wavelength acceptance bandwidth, FWHM, is $\Delta\lambda_{pm} \approx 0.9$ nm. The walk-off angle for the second harmonic output is $\rho \approx 1.8$ mrad (~0.1°)

b) AR-coated 10 mm long LBO crystal cut for type I (ooe) critical phase matching (as illustrated in fig. 6.2):

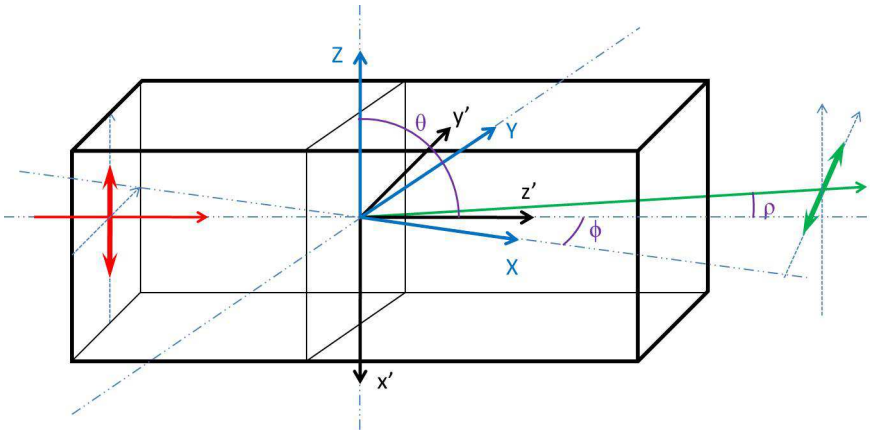

Figure 6.2: Principal crystal axes orientation in type I critically phase matched AR-coated LBO. (XYZ – principal crystal axes, x'y'z' – laboratory coordinate system)

Fig. 6.2 illustrates the geometry and principal axes orientation of the LBO crystal critically phase-matched slightly above room temperature (303.15 K = 30 °C). The coordinate system based on principal crystal axes is rotated by θ = 90° (around y' axis) and by ϕ = 10.2° (around x') with respect to the laboratory coordinate system (z' – direction of propagation). The front surface of the crystal is close to being orthogonal to the propagation direction. The light at the fundamental wavelength (in red) is polarised along the Z axis, while the second harmonic output (in green) has orthogonal polarisation (along Y axis). Refractive indices at fundamental wavelength in the phase-matching temperature calculated from Sellmeier's relation are $n_\omega^Y \approx 1.5892$ and $n_\omega^Z = n_{2\omega}^{Y'} \approx 1.6050$ in Y and Z directions respectively. The

nonlinear coefficient in this configuration is $d_{eff} \approx 0.834$ pm/V. The phase matching temperature bandwidth, FWHM, is $\Delta T_{pm} \approx 6.2$ K. The angular acceptance bandwidth, FWHM, (4.43) is $\Delta\theta_{pm} \approx 10.9$ mrad (~0.6°). The wavelength acceptance bandwidth, FWHM is $\Delta\lambda_{pm} \approx 1.4$ nm. The walk-off angle for the second harmonic output is $\rho \approx 6.2$ mrad (~0.35°). Both crystals in configurations above were used in the experiments described in the next sections of this chapter.

Two different enhancement cavities for the two LBO crystals have been designed and optimised for optimal conditions to yield efficient second harmonic generation. For the Brewster-cut crystal the enhancement cavity was configured as in fig. 5.4. The empty ring resonator geometry was designed to maintain a fundamental resonator mode with a spot size $w_0 \approx 45$ µm between the concave mirrors and a spot size $w_1 \approx 200$ µm in the upper arm (between the plane mirrors). To that end, concave mirrors were chosen with curvature radius *Rc* = 75 mm, and distances between the mirrors were respectively: $|M_1M_2|$ = 102 mm, $|M_2M_3|$ = 101 mm, $|M_4M_1|$ = 116 mm, and $|M_3M_4|$ = 87 mm (taking into account the optical path length through the LBO crystal). The light was incident on the concave mirrors at angle $\theta_A \approx 15.4°$ optimal for astigmatism compensation (5.33). More detailed numerical analysis taking into account the presence of the LBO crystal and the astigmatism effects caused by off-axis incidence on concave mirrors and refraction on LBO crystal's surfaces indicated elliptical beam inside the crystal of spot size $w_{0y} \approx 52$ µm and $w_{0z} \approx 75$ µm, which was close to optimum value ~60 µm (see section 4.4.4).

For the AR-coated LBO crystal the enhancement cavity was configured as in fig. 6.3. The empty ring resonator geometry was designed to maintain a fundamental resonator mode with a larger spot size of $w_0 \approx 76$ µm (so that divergence would not exceed the angular phase-matching bandwidth) between the concave mirrors and a spot size $w_1 \approx 300$ µm in the upper arm (between the plane mirrors). To that end, concave mirrors were chosen with curvature radius *Rc* = 200 mm, and distances between the mirrors were respectively: $|M_1M_2|$ = 270 mm, $|M_2M_3|$ = 260 mm, $|M_4M_1|$ = 260 mm, and $|M_3M_4|$ = 246 mm (taking into account the optical path length through the LBO crystal). The incidence angle was made as small as the geometry of the cavity allowed, (i.e. $\theta_A \approx 4.8°$) in order to minimise the astigmatism

effects. More detailed numerical analysis taking into account the presence of the LBO crystal indicated a circular beam inside the crystal of spot size $w_0 \approx 93$ µm.

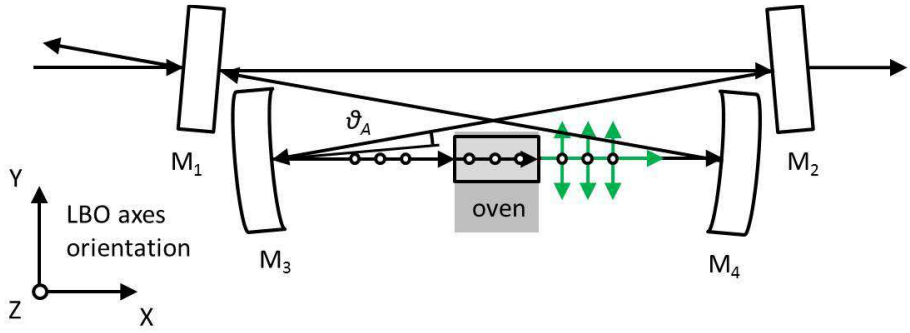

Figure 6.3: Enhancement cavity in "bow-tie" configuration with an AR-coated LBO crystal

Once the cavity is aligned, fine tuning of the waist spot size (both inside the LBO crystal, and the upper arm of the ring resonator) can be performed by changing the distance between the concave mirrors. Figure 6.4 shows the dependence of the waist spot size between the concave mirrors w_0 (green line) and the spot size in the upper arm of the resonator w_1 (red line) on the separation between the concave mirrors d_m in a) empty resonator designed for non-critically phase matched Brewster-angled LBO and b) empty resonator designed for critically phase matched AR-coated LBO.

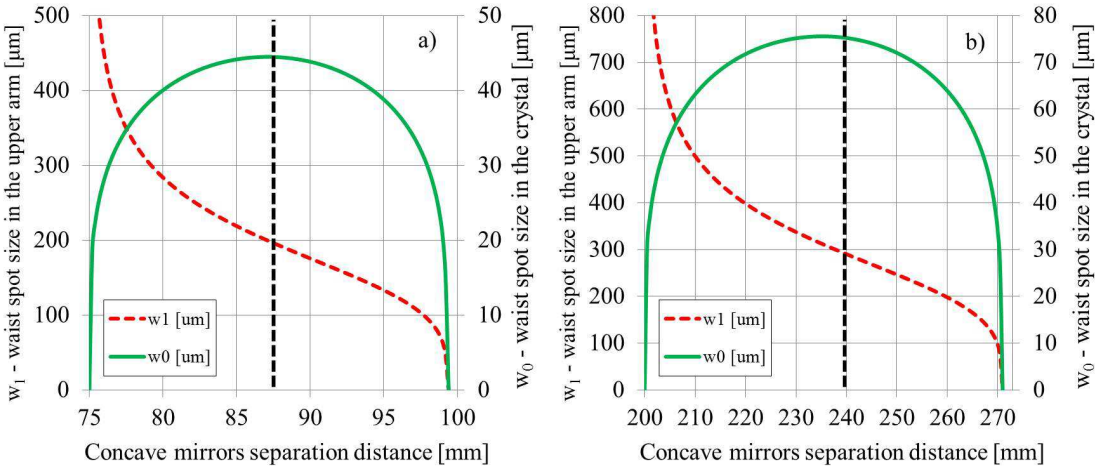

Figure 6.4: Spot size values in empty resonators (without LBO crystals) as a function of concave mirror separation distance a) non-critically phase matched Brewster-cut LBO configuration b) critically phase-matched AR-coated LBO configuration

Resonant enhancement cavity supported a stable fundamental mode for the concave mirrors separation range of 75-99 mm for the Brewster-cut LBO configuration and 200-273 mm for the AR-coated LBO configuration. The black vertical lines mark the optimal mirror separation distances, close to the centre of the stability zone, that were used in the final experimental configurations.

6.3. Experimental results

6.3.1. Initial experiment with a ring cavity

The initial experiment aiming to demonstrate the internal resonantly-enhanced frequency doubling concept described in section 5.2, was based on ring fibre laser resonator architecture, shown in fig. 6.5.

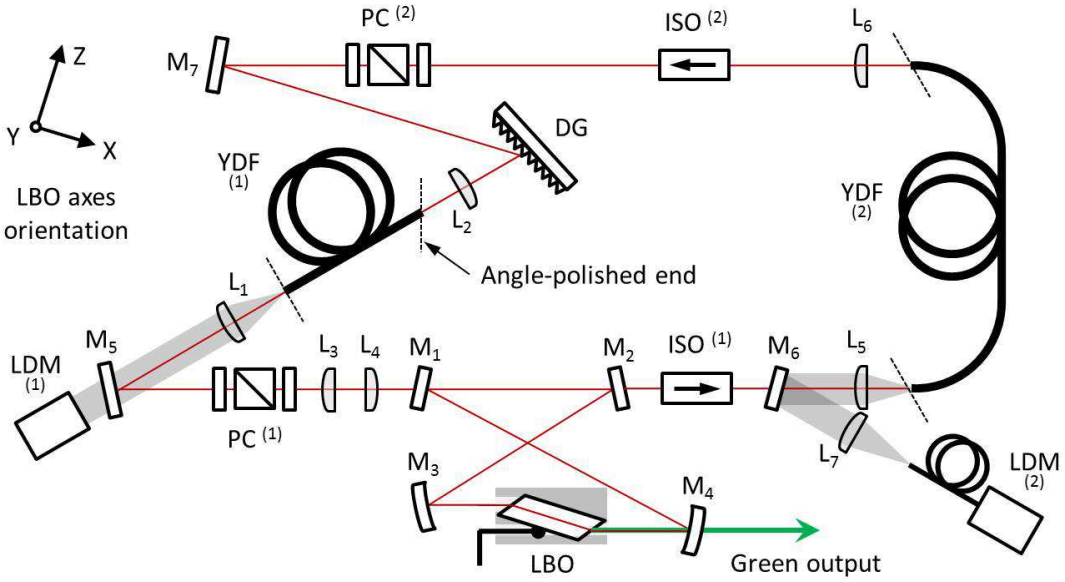

Figure 6.5: Internally-resonantly-enhanced frequency-doubled fibre laser: initial experimental set-up in a ring cavity configuration

A double-clad Yb-doped fibre (YDF $^{(1)}$ – 7 m long section with a single-mode core, 9.6 µm in diameter, and pure silica D-shaped inner cladding, 150 µm in diameter, angle-polished at un-pumped end) acted as the gain element of the laser and was

diode-pumped at 975 nm by a laser diode stack module (LDM $^{(1)}$). The counter-propagating (relative to the pump direction) output beam at $\lambda_\omega \approx 1042$ nm was extracted with a dichroic mirror M_5 and directed onto an input coupler M_1 of the internal resonant enhancement cavity. Prior to incidence on the M_1 mirror surface, the output beam passes through a polarisation control stage PC $^{(1)}$, consisting of two half-wave-plates on either side of a polariser, and a telescope designed to provide good spatial overlap between the incident beam and the fundamental TEM_{00} resonator mode. The internal enhancement resonator was not fully optimised in the initial experiment and comprised two plane-plane mirrors M_1 and M_2 of reflectivities $R_1 = 94\%$ and $R_2 = 92\%$ at the fundamental wavelength respectively, two concave mirrors (125 mm radius of curvature) with high reflectivity ($R_3 = R_4 = R_{HR} > 99.8\%$) at the fundamental wavelength and high transmission at the second harmonic wavelength, and a Brewster-angled LBO crystal configured for type I non-critical phase-matching. The beam transmitted by the enhancement resonator was passing through a Faraday isolator ISO $^{(1)}$ before being coupled to a second 20 m section of a double-clad Yb-doped fibre YDF $^{(2)}$. This fibre was identical to YDF $^{(1)}$, angle-polished at both ends and pumped at 915 nm by a fibre-coupled laser diode module LDM $^{(2)}$. Output from the YDF $^{(2)}$ was propagated through another Faraday isolator ISO $^{(2)}$ and a second polarisation control stage PC $^{(2)}$ comprising a thin-film polariser, half-wave-plate, and a quarter-wave-plate. It was then directed onto a diffraction grating DG. Light reflected from the grating at the appropriate angle (tuned for the operating wavelength λ_ω) was coupled back to the YDF $^{(1)}$ through the angle-polished end. It should be noted that second gain stage formed by YDF $^{(2)}$ was not mandatory for the ring oscillator to operate; it was introduced only for ease of alignment and amplification.

This described set-up delivered maximum second harmonic power of $P_{2\omega} = 215$ mW in the output beam for fundamental power incident on the resonator $P_\omega \approx 8$W (~50% coupled into the internal cavity). This value corresponds to 3.3% conversion efficiency (6.6% with respect to the power coupled to the resonator). Although inefficient and un-optimized for impedance matching or spot size inside LBO crystal, this ring configuration provided a sufficient proof-of-principle, laying down the foundation for further experiments. Due to this scheme's high complexity and time-

consuming alignment requirements, a simpler configuration based on the same principle was proposed, built and developed. This linear oscillator configuration will be discussed in the following section.

6.3.2. Wavelength tuning in a linear cavity configuration

Implementation of the concept of internal resonantly-enhanced frequency doubling in the linear cavity configuration is more straightforward than the ring configuration allowing the removal of the (now redundant) secondary fibre gain stage and isolators (fig. 6.6).

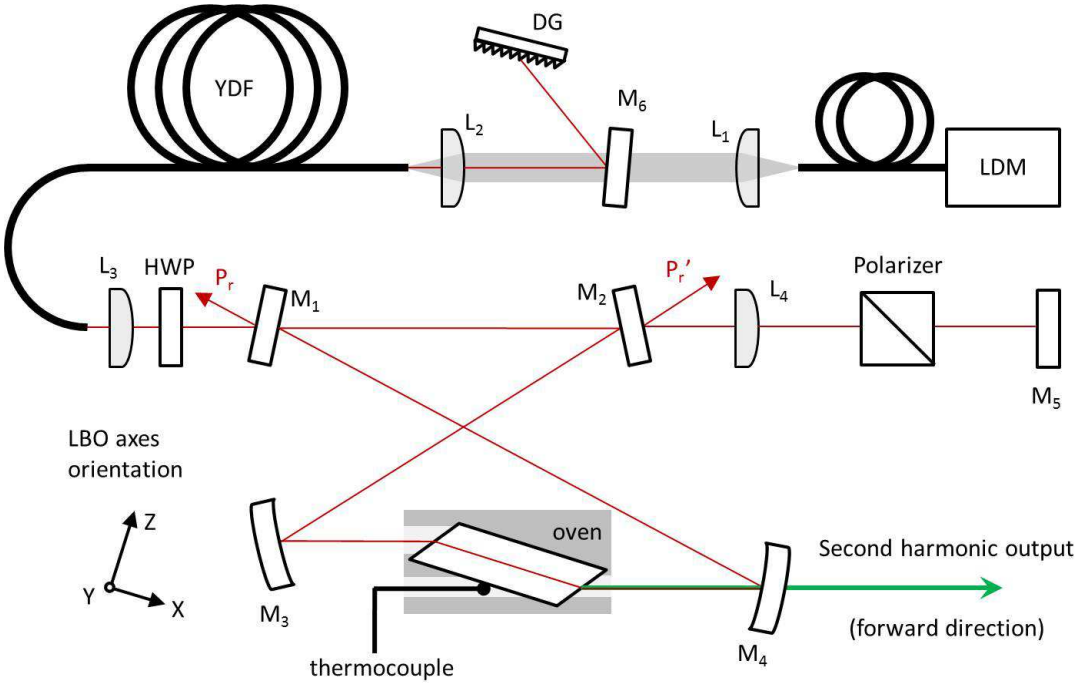

Figure 6.6: Internally-resonantly-enhanced frequency-doubled fibre laser: experimental set-up in a linear cavity configuration

The linear configuration set-up was based on a 20 m long single-mode, double-clad Yb-doped fibre YDF (polarization-maintaining, 7/125 µm), pumped at 975 nm via a fibre-coupled (200 µm core with NA = 0.22) laser diode module LDM (*Jenoptik, JOLD-30-FC-12*) with an aid of a dichroic mirror M_6 (HT@975 nm, HR @1-1.1 µm). Feedback for lasing was provided by an external cavity containing a simple diffraction grating DG (600 lines/mm, blazed at ~1.06 µm) at one end of the fibre and, at the opposite end, by another external feedback arrangement containing the resonant enhancement cavity. The grating was used to tune the fibre laser's operating wavelength close to the gain spectrum maximum (λ_ω = 1093 nm), and to reduce the emission bandwidth to be less than the phase-matching bandwidth for the nonlinear crystal. The reflectivity of the mirrors and geometry of the enhancement cavity was optimised as described in section 6.2. Lens L_4, placed a focal length distance (f_4 = 250 mm) from the resonator mode's waist between the mirrors M_1 and M_2, and the same distance from feedback mirror M_5, was used to ensure good spatial mode-matching to the resonator mode in the reverse direction, i.e. after beam reflection from the feedback mirror surface terminating the external cavity. Unlike in the ring oscillator configuration, second harmonic output is bidirectional, with > 95% of second harmonic power emitted in forward direction. A cube polariser positioned between the feedback mirror M_5 and the lens L_4 was used to enhance the polarisation selection in the cavity, so that the fundamental power incident on the input coupler of the enhancement cavity was linearly-polarised in the XZ plane. The actual arrangement of this experimental set-up is presented in figures 6.7-6.10. Figure 6.7 shows the fibre gain stage with the Yb-doped fibre ends positioned in mounts attached to XYZ positioners, where the mount adjacent to the pumping arrangement was water cooled for management of heat generated by the pump power not coupled into the fibre's cladding. Output from the Yb-doped fibre in the enhancement cavity direction passes through a dichroic mirror designed to reflect any unabsorbed pump power. The geometry of the external cavity arrangement adjacent to the pumped end of the Yb-doped fibre is shown in the figure 6.8. The diffraction grating is positioned on a translation stage to enable fine tuning of the laser's line width via change of the waist spot size on the grating. The beam's waist should be always positioned at the grating's surface to maintain high efficiency of coupling the light back into the fibre's core.

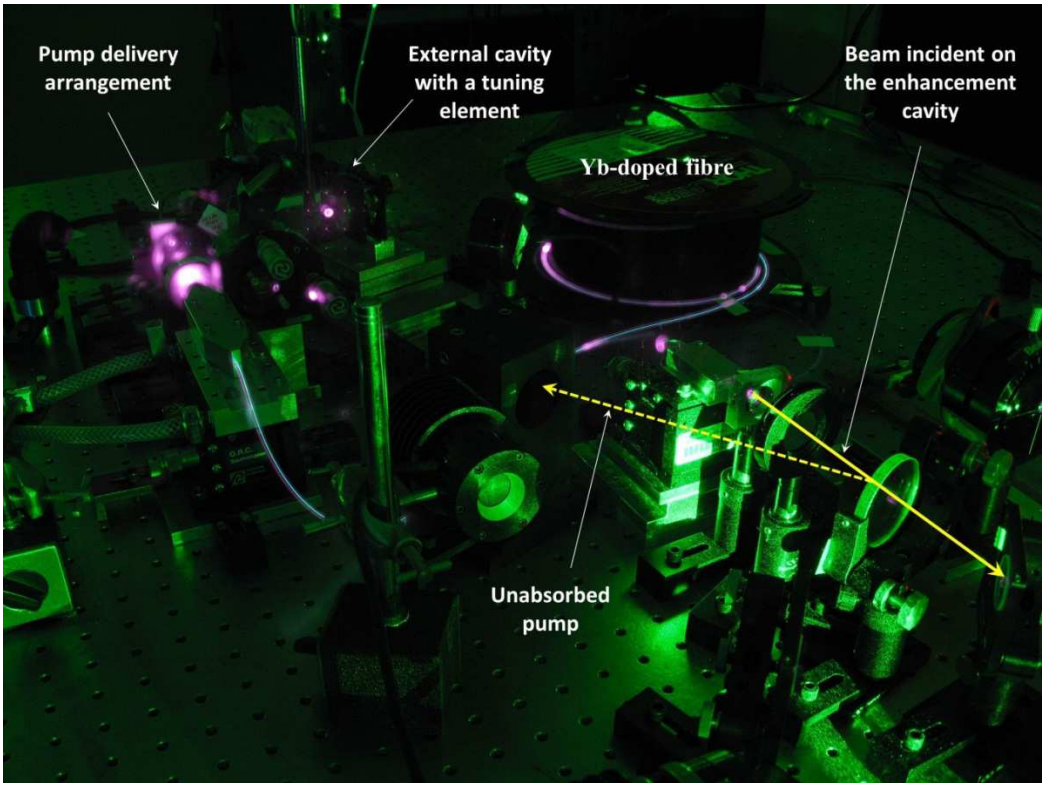

Figure 6.7: Experimental set-up: fibre gain stage arrangement

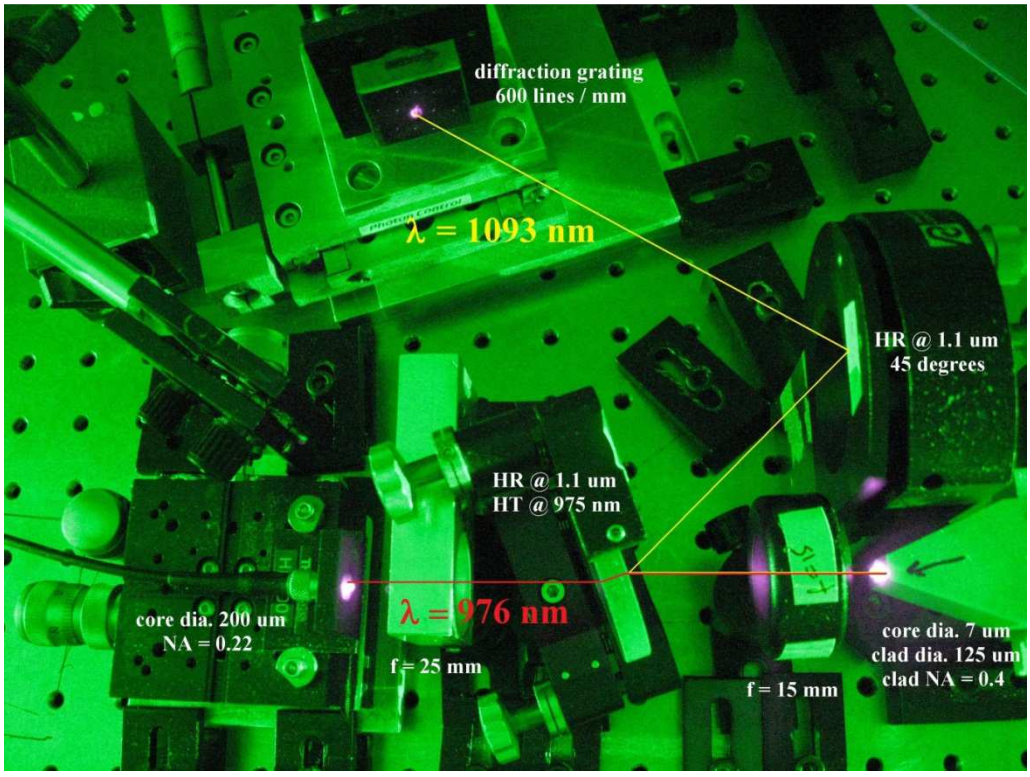

Figure 6.8: Pump delivery and external cavity with the tuning element arrangement

Fine tuning of the laser line width can be performed by changing the distance between the lens L_2 and the active fibre's end, and adjusting the distance from the lens to the grating so the waist position remains at the grating's surface. Changing the distance between the lens and the fibre end affects pump coupling efficiency, so the pump beam divergence and waist position should be adjusted by changing the relative positions of the lens L_1 and the end of pump delivery fibre during the laser line width tuning. Figure 6.9 shows the optimal arrangement of the resonant enhancement cavity with a Brewster-angled LBO crystal. The feedback path was folded with a dichroic mirror with high reflectivity at laser's fundamental wavelength and 45° incidence angle to enable pump beam delivery for the Nd:YVO_4 alignment laser using the mirrors of the resonant enhancement cavity. This "bulk" solid state laser and the final alignment procedure used for optimisation of the internally-frequency-doubled fibre laser will be discussed later, in section 6.3.3. Finally, figure 6.10 shows the whole experimental set-up operating at full pump power delivering ~2.3W of green output.

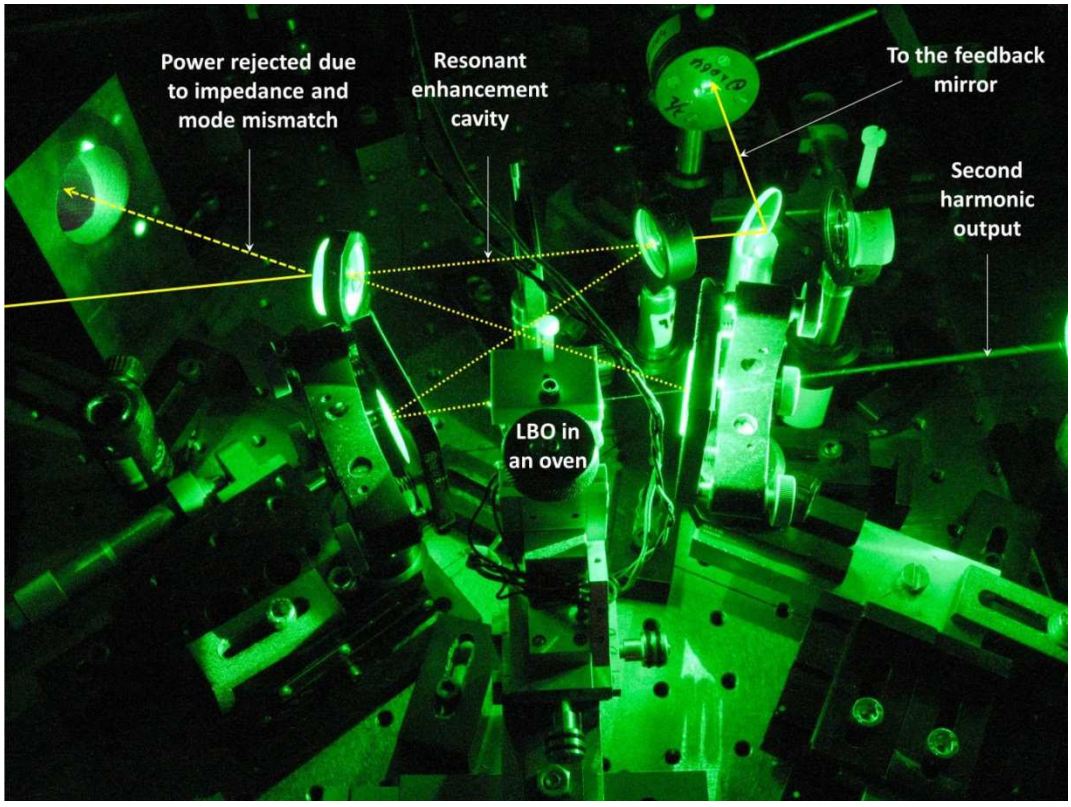

Figure 6.9: Experimental set-up: resonant enhancement cavity

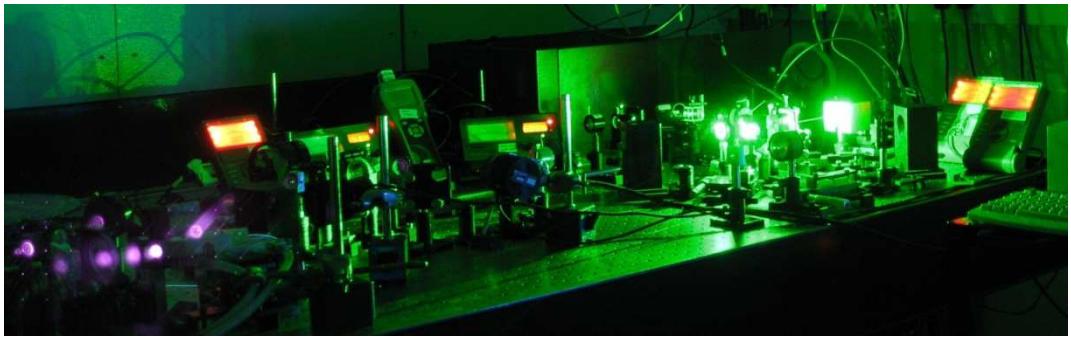

Figure 6.10: Experimental set-up operating at maximum SH output power of ~2.5 W

This experimental arrangement generated ~12.5 W of fundamental power at 1095 nm for the maximum 22.8 W of pump power coupled into the active fibre (fig. 6.11). ~8 W of the total infrared power generated in the active fibre was incident on the input coupler of the enhancement resonator. The rest was either lost in the external cavity arrangement with the diffraction grating or used for diagnostics purposes (small angle wedge and a polariser were placed between the fibre and the enhancement resonator to monitor the polarisation state and power in the beam incident on the input coupler M_1). ~6.6 W of the power incident on the resonator was linearly polarised in the XZ plane, and ~5.8 W was efficiently coupled into the enhancement cavity, which corresponds to 72% coupling efficiency with respect to the total power incident on the input coupler or 88% with respect to the linearly polarised component.

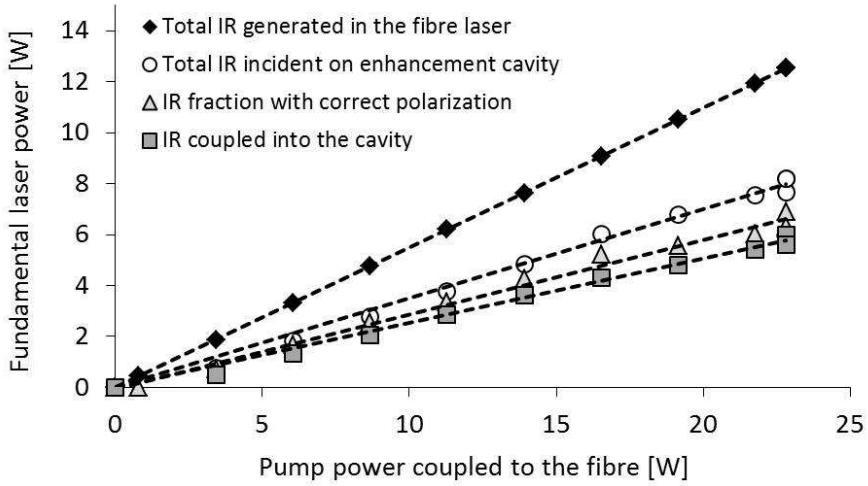

Figure 6.11: Fundamental power in the internally-frequency-doubled fibre laser

The fundamental power circulating in the resonant enhancement cavity was measured by monitoring the power transmitted through the output coupler M_2 and leaking through the feedback mirror M_5. For the maximum fundamental power of ~8 W incident on (or ~5.8 W launched into) the resonant enhancement cavity the power circulating in the resonator was measured to reach ~126 W (fig. 6.12a). The enhancement factor, defined as the ratio of power circulating to the power launched into the enhancement resonator, was measured to decrease from a large number (>50) at low power to ~22 at maximum green output, along with increasing second harmonic conversion efficiency (fig. 6.12b).

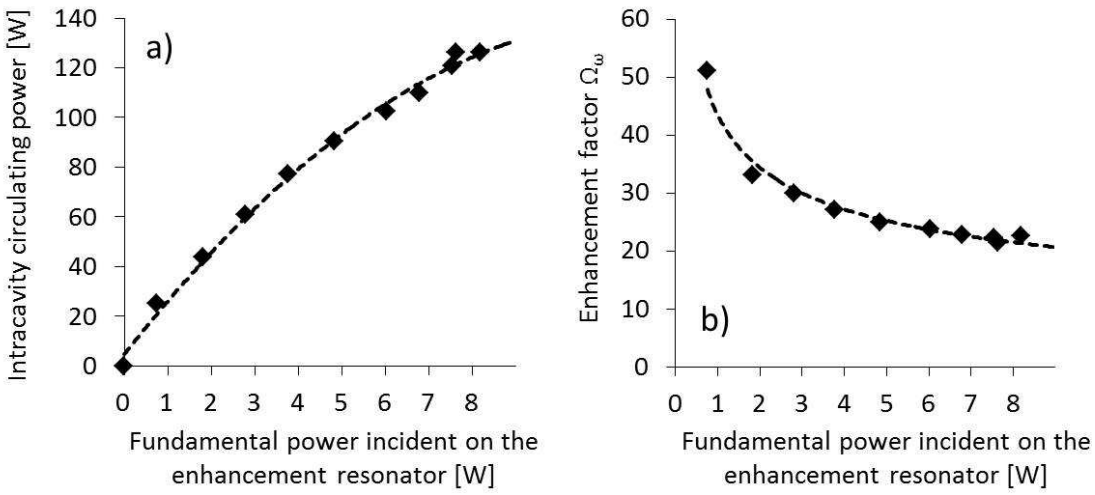

Figure 6.12: a) fundamental power circulating in the enhancement cavity; b) enhancement factor; as functions of the fundamental power incident on the enhancement resonator

The output beam carried ~77% of the total power generated inside the LBO crystal (suffering 19.4% and ~4% Fresnel reflections from the crystal and concave mirror surfaces respectively). Generated green power plotted against circulating fundamental power (fig. 6.13a) fits a quadratic function, and hence the conversion efficiency is a linear function of circulating power (6.13b), according to (4.28). The parameter ϵ characteristic for nonlinear interaction (4.27) has a meaning of a proportionality constant between the SHG conversion efficiency and circulating fundamental power. It was calculated from the fit to the experimental data (6.13a and 6.13b) to be $\epsilon \approx 1.5 \times 10^{-4}\ W^{-1}$ (i.e. the conversion efficiency increases by 1.5% per each 100W of circulating fundamental power), which is in a good agreement with the

theoretical value $\epsilon \approx 1.6 \times 10^{-4}\ W^{-1}$ obtained from (4.27) for this resonator geometry. The maximum generated green power of ~3.2 W (i.e. ~2.4 W in the output beam) was obtained after removing the diagnostic components (small angle wedge and the polariser) from the experimental set-up. This result corresponds to a conversion efficiency of ~2.2% for ~141 W of circulating fundamental power. The second harmonic output power in this configuration was only limited by the available pump power.

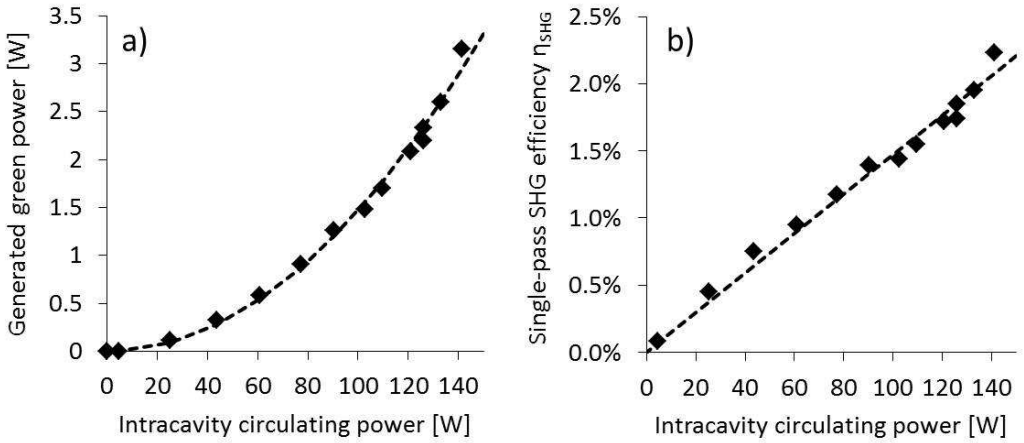

Figure 6.13: a) Green power generated in the LBO crystal; b) single-pass SHG conversion efficiency; as functions of the fundamental power circulating in the resonant enhancement cavity

The green output beam had a nearly Gaussian profile (fig. 6.14b) and the beam quality (M^2 parameter) was measured to be $M_x^2 \approx 1.25$ and $M_y^2 \approx 1.26$ in two orthogonal planes respectively (fig. 6.14a). A small fraction of power incident on the input coupler that was not perfectly spatially matched to the fundamental mode of the enhancement resonator can excite higher order modes supported by the enhancement cavity. Those higher order modes yield lower second harmonic conversion efficiency hence the fraction of light circulating in the enhancement cavity that is not in the fundamental spatial mode of the resonator, can still provide sufficient feedback to the fibre (after a double-pass through the enhancement cavity). The second harmonic output follows the intensity distribution of the spatial mode content of the enhancement resonator which results in the output beam that is not truly diffraction-limited.

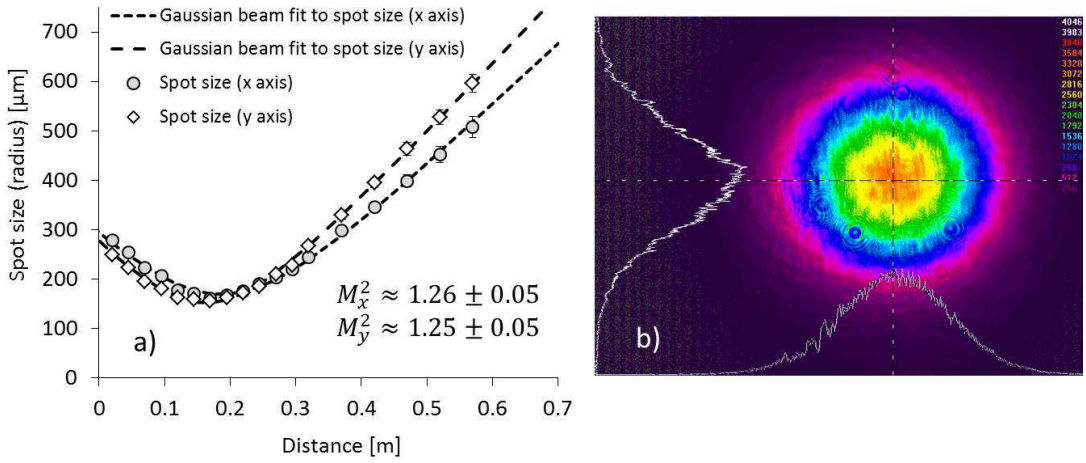

Figure 6.14: a) Measured spot size values of the green output with a Gaussian beam fit b) CCD image of the output green beam after appropriate attenuation

Wavelength tuning of the internally-frequency-doubled fibre laser was studied by changing the diffraction grating orientation (i.e. rotating the grating in the XZ plane) and adjusting the temperature of the oven. The experimental set-up was optimized to yield maximum output power of ~2.3 W at 546 nm. Maximum second harmonic efficiency was obtained when the oven temperature (measured close to the surface of the crystal with an aid of a thermocouple) was ~118.7 °C. Then, the grating orientation was changed and the oven temperature adjusted to maintain the phase-matching condition. The laser could be tuned over a wavelength range from 539 nm to 558 nm with a >1W output power level. The temperature was changed from 135 °C to 95 °C over the laser's tuning range to maintain phase matching (fig. 6.15).

The oven temperature corresponding to the phase matching condition was on average ~12 °C higher than the phase matching temperature calculated from (4.32) and the Sellmeier's relation. This indicates the temperature in the centre of the crystal being lower than the oven surfaces, due to non-ideal thermal contact between the crystal and the oven as well as significant thermal gradient across the crystal's cross section that can induce non-uniform second harmonic conversion efficiency, and hence affect output beam quality.

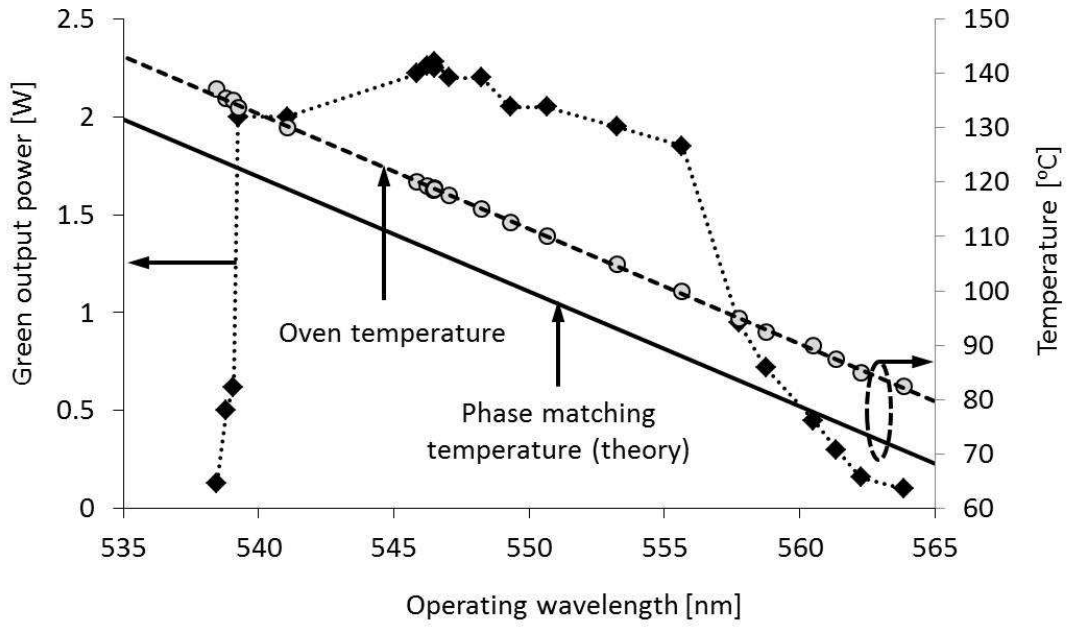

Figure 6.15: Tuning curve of the laser and oven temperature at phase matching condition

6.3.3. Alignment procedure

Efficient generation of the second harmonic output is highly dependent on the resonant enhancement cavity alignment with respect to the main cavity of the fibre laser. To achieve good performance of the internally-frequency-doubled laser two parameters have to be carefully adjusted: optimal waist spot size in the nonlinear crystal, and spatial mode matching between the beam incident on the input coupler and the fundamental resonator mode. It is clear that changing the concave mirrors separation is not sufficient, as it affects both the spot size inside the crystal and spatial mode matching for a fixed incident beam (fig. 6.4) rendering power measurements (of either the SHG or rejected power off the input coupler) an unreliable diagnostic tool for optimization. Another factor to consider is that the angular position of the concave mirrors has to stay fixed to maintain fundamental mode operation of the resonator. Hence, a more sophisticated alignment procedure had to be developed to independently access both crucial parameters. We put forward here a method that entails operating the internal SHG resonator as the cavity of a diode-pumped bulk-solid-state laser as illustrated in fig. 6.16.

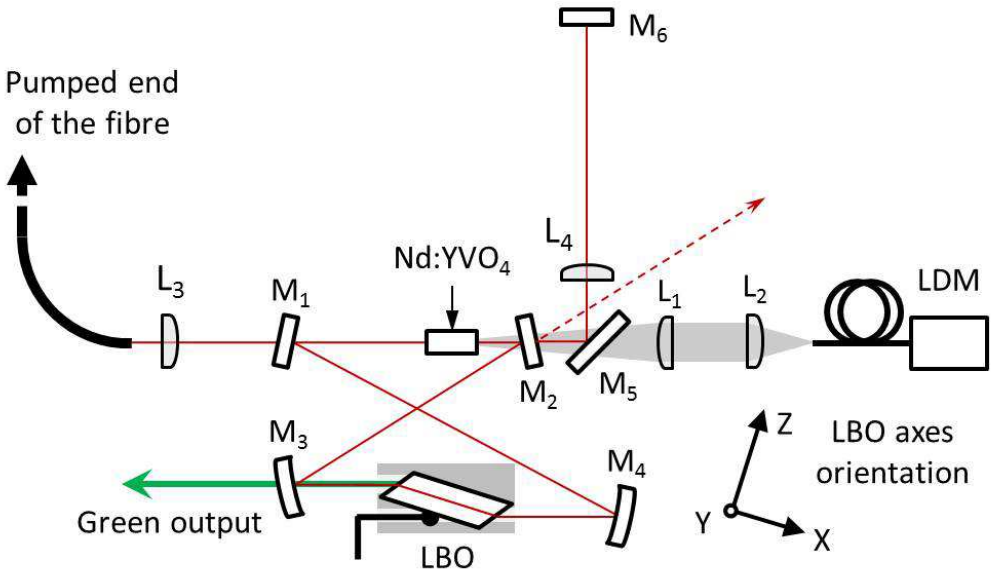

Figure 6.16: “bulk” solid-state laser configuration used for alignment of the internally-frequency-doubled fibre laser

The alignment procedure is as follows: The fibre laser cavity is constructed so that feedback for lasing is provided by the external cavity terminated with a diffraction grating at one (pumped) end of the fibre and, at the other side of the fibre, by the Fresnel reflection from a perpendicularly-cleaved fibre facet (as in fig. 6.6). The output beam from this simple laser configuration, after passing through the collimating lens L_3 can be used for preliminary alignment of the enhancement cavity. This can be done by placing the mirrors M_1, M_2 and M_3 and the LBO crystal in their calculated positions and directing the beam along the calculated path of the resonator mode. The cavity is then formed with an input coupler placed in its calculated position and the resonator mode image can be observed by monitoring the leakage through the output coupler M_2. The angular position of the resonator mode with respect to the incident beam can be changed by adjusting the angular positions of concave mirrors M_3 and M_4 until predominantly fundamental mode of the resonator is excited and circular second harmonic output is generated (providing that the oven temperature is set to maintain phase matching condition), i.e. when the resonator mode between the plane mirrors is collinear with the incident beam. A “bulk” solid-state laser crystal (e.g. Nd:YVO_4) in a water-cooled mount is then positioned in the beam between the plane mirrors of the enhancement resonator. The pump source for

fibre laser can be turned off, and the laser crystal can be pumped with an external source. In our experiments pump light at 808 nm was delivered by a fibre coupled laser diode stack module (LDM) through a telescopic lens configuration (L_1 + L_2) and a dichroic mirror M_5 as illustrated in fig. 6.16. Pump delivery arrangement should be adjusted until lasing in the ring resonator is achieved, and further optimised for maximum output power from the ring laser, corresponding to best overlap between pumped section of the crystal and the resonator mode. This “bulk” solid state produces bidirectional output at fundamental wavelength leaking through mirrors M_1 and M_2 as well as bidirectional output at second harmonic wavelength leaking through the concave mirrors M_3 and M_4. In this configuration concave mirrors separation can be changed until the optimal spot size in the nonlinear crystal, corresponding to maximum second harmonic output power, is achieved. It should be noted that the telescopic lens configuration focusing the pump beam into the laser crystal should be adjusted accordingly to maintain good overlap between the resonator mode and the inverted section of the crystal. Once the optimal concave mirrors separation is found, the feedback path folded with a dichroic mirror M_5 and terminated with a broadband reflector M_6 can be aligned, as illustrated in fig. 6.11. A lens L_4 positioned a focal length distance from the waist between the plane mirrors of the enhancement resonator enables good spatial mode matching in reverse direction between the beam and incident on the plane mirror M_2 and the fundamental mode of the resonator. The feedback path can be precisely aligned by maximising second harmonic output in the reverse direction (through mirror M_3). The laser output (at 1064.2 nm) transmitted by the mirror M_1 can be efficiently coupled to the Yb-doped fibre by changing the distance between the enhancement resonator and the collimating lens L_3 and adjusting the position of the fibre end with respect to L_3 while monitoring the transmitted power at the other end of the fibre. Finally, the source pumping the Yb-doped fibre can be turned on. As the distance between the enhancement resonator and the lens L_3 is already optimised, gentle adjustment of the fibre end position and angular orientation of the concave mirrors should yield perfectly collinear propagation of the beam incident on the input coupler and the resonator mode between the plane mirrors of the enhancement cavity. The laser can be then tuned to the desired fundamental wavelength by changing the grating orientation (rotation in XZ plane) and adjusting the oven temperature accordingly to yield efficient second harmonic generation.

This alignment procedure was successfully applied during the optimisation of all fibre laser configurations described in this chapter. It is helpful to use a laser crystal naturally emitting at wavelength close to the desired fundamental wavelength of the fibre laser. The optimal nonlinear crystal orientation and phase matching temperature can be then found during the alignment procedure. For that reason in experiments involving high-power fibre lasers operating at fundamental wavelength of ~1080 nm that are described in the following sections of this chapter, the Nd:YVO_4 crystal naturally lasing ~1064.2 nm (fig. 6.17a) and pumped with a laser diode stack emitting ~808 nm was replaced with Nd:$YAlO_3$ lasing at ~1079.4 nm (fig. 6.17b) and pumped with a pigtailed diode stack emitting ~802 nm.

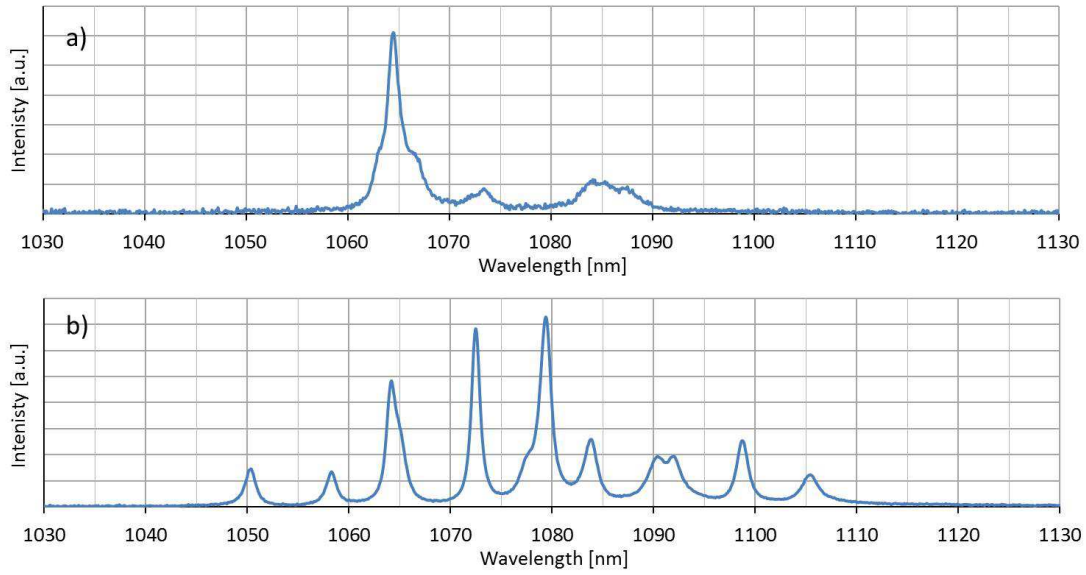

Figure 6.17: Fluorescence spectra of the laser crystals used for alignment of the internally-frequency-doubled fibre laser measured with an optical spectrum analyser: a) fluorescence spectrum of the Nd:YVO_4 crystal b) fluorescence spectrum of the Nd:$YAlO_3$ crystal

6.3.4. Power scaling of internally-resonantly-enhanced frequency doubled CW fibre lasers

a) Non-critically phase matched, Brewster-angled LBO crystal configuration

In the next step towards further power scaling of the proposed internally-frequency-doubled fibre laser architecture, more powerful diode pump source emitting at ~976 nm (*Lumics, LU0976C150-B*) was employed and the 7/125 µm single-mode fibre was replaced by a 10 m, slightly multimode large-mode-area (LMA) Yb-doped fibre section (*Nufern, PLMA-YDF-25/345*). The rationale behind this step was to investigate the mechanism of modal interference on coupling the light into the enhancement resonator, and enhance the power scalability by increasing the mode field area (as discussed in section 4.3.5). The modal interference approach and simulation of the modes supported by this fibre have been discussed in section 5.8. The pump light delivery arrangement has been changed to account for a bigger size of the fibre's inner cladding (collimating lens L_1 from figure 6.6 of focal length f_1 = 25 mm was replaced with a f_1 = 8 mm lens), and the distance between the fibre facet and the diffraction grating adjusted to account for a different mode field diameter. The actual pump delivery and external cavity with the tuning element arrangement is presented in figure 6.18.

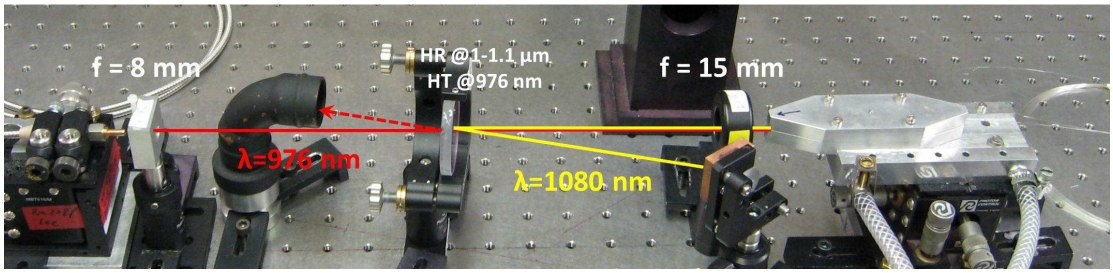

Figure 6.18: Experimental set-up: pump delivery and external cavity with tuning element arrangement

In the external cavity at the other end of the fibre, collimating lens L_3 from figure 6.6 was replaced by a telescopic lens configuration (11 mm and 200 mm focal lengths, the latter acting as a mode matching lens) and the distance between the enhancement cavity and the fibre facet was adjusted to mode-match the beam incident on the input coupler M_1 to the fundamental mode of the resonator, using the alignment procedure described in section 6.3.3. Figure 6.19 presents (almost complete) actual arrangement of the external cavity containing the enhancement resonator. The last element – a polarising beam splitter was later added in the feedback path (between the feedback mirror M_5 and lens L_4). AR-coated wedges were used to attenuate both the second harmonic output beam transmitted through the concave mirror M_4 and the rejected beam, reflected off the input coupler M_1 to aid diagnostics. A half-wave plate positioned before the enhancement resonator was used to rotate the plane of linear polarisation to match fast birefringence axis of the Yb-doped fibre.

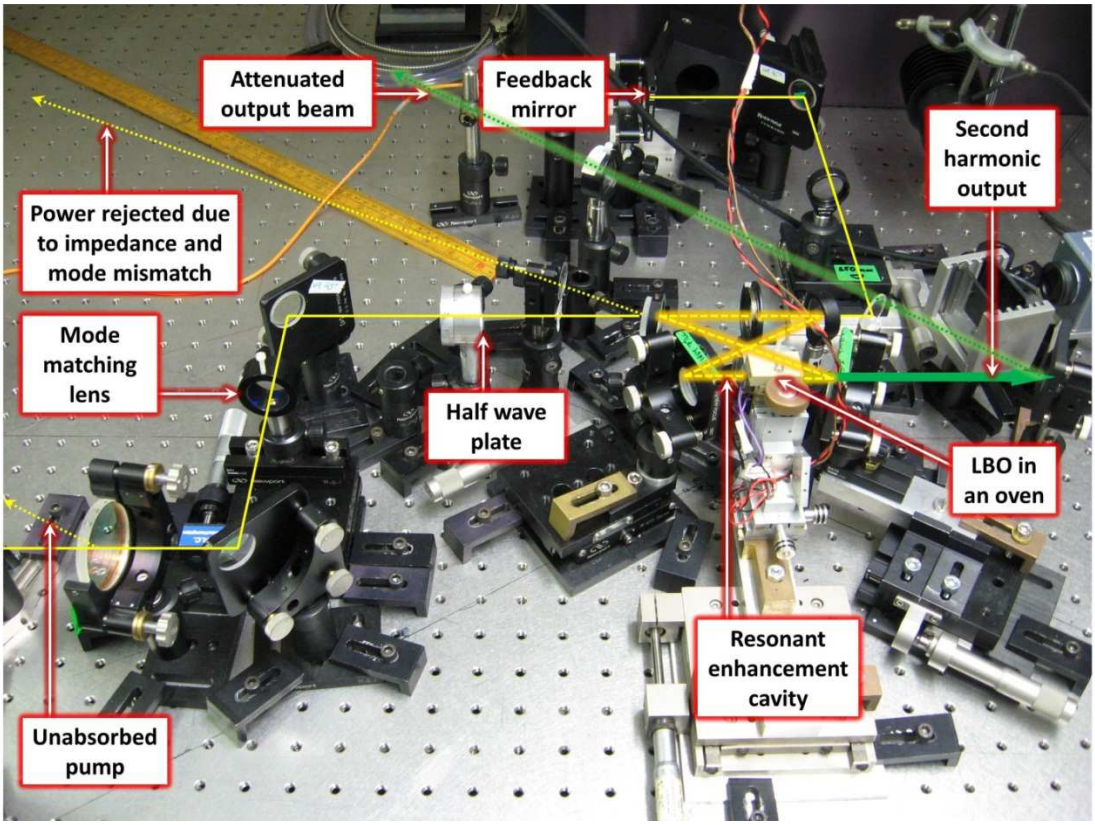

Figure 6.19: Experimental set-up: external cavity with the enhancement resonator arrangement

This experimental arrangement generated ~64 W of fundamental power at ~1080 nm for the ~91.0 W of pump power absorbed in the active fibre (fig. 6.20). ~32 W was efficiently coupled into the enhancement cavity, which corresponds to ~50% coupling efficiency with respect to the total power incident on the input coupler.

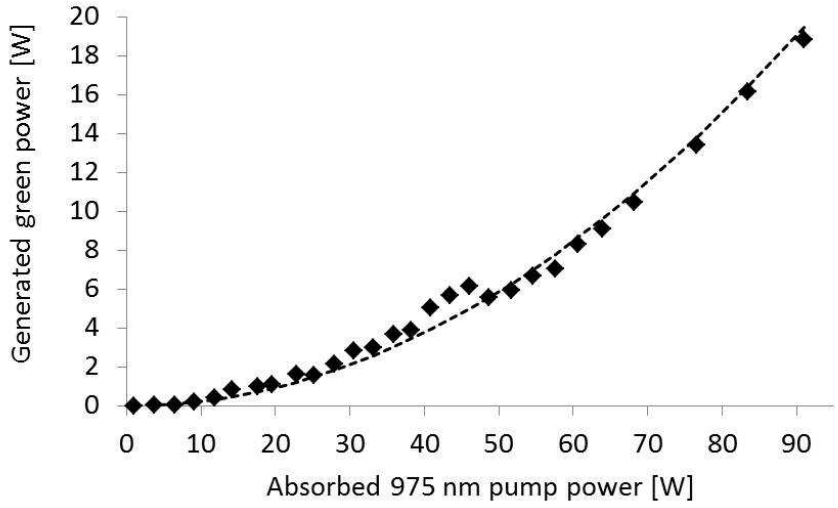

Figure 6.20: Generated second harmonic output power versus absorbed 975 nm pump power

The fundamental power circulating in the resonant enhancement cavity was measured to reach ~440 W for the maximum power incident on the input coupler. The enhancement factor was measured to decrease from a large number (>50) in a low power regime to ~14 at maximum green output, along with increasing second harmonic conversion efficiency. The output beam carried ~15.1 W (~77% of the total second harmonic power generated due to Fresnel reflections from the crystal and concave mirror surfaces). Generated green power was a linear function of the power circulating in the enhancement resonator with the proportionality constant $\epsilon \approx 1.0 \times 10^{-4}$ W^{-1}. This is less than the theoretical value $\epsilon \approx 1.6 \times 10^{-4}$ W^{-1} obtained from (4.27) for this resonator geometry. Second harmonic generation efficiency can be reduced due to non-uniform temperature distribution in the LBO crystal at higher laser power levels leading to imperfect phase-matching. Maximum second harmonic efficiency was obtained when the oven temperature (measured close to the surface of the crystal with an aid of a thermocouple) was ~128.7 $^{\circ}$C. This is ~7 $^{\circ}$C higher than the theoretical phase matching temperature, indicating that the centre of the LBO

crystal was ~7 °C cooler than the surrounding oven (non-uniform temperature distribution). At the same time, the centre of the LBO crystal at the maximum circulating power was ~5 °C hotter than for lower circulating power levels, indicating that fraction of the optical power was being absorbed by the LBO housing. Figure 6.21 shows two typical output spectra measured with an optical spectrum analyser: a spectrum spanning a wavelength range of ~2.4 nm obtained for a certain spot size on the diffraction grating (fig. 6.21a) and another spectrum spanning a wavelength range of ~0.6 nm obtained for a bigger spot size on the diffraction grating (6.21b) after moving the grating closer to the fibre end and adjusting the arrangement of lenses. These emission spectra consist of a number of discrete lines some of them with widths < 0.05nm (limited by the resolution of the spectrum analyser). Each of these lines will consist of groups of one or more axial modes separated by a frequency interval corresponding to at least one free spectral range of the enhancement cavity (i.e., ~ 750 MHz) (see fig.5.2). The spacing ~0.5 nm between individual lines is defined by spacing between wavelengths for which all groups of modes add up in phase, and fits well to the theory described in section 5.8. Individual lines lying between the main peaks separated by ~0.5 nm correspond to wavelengths where two individual groups of modes add up in phase.

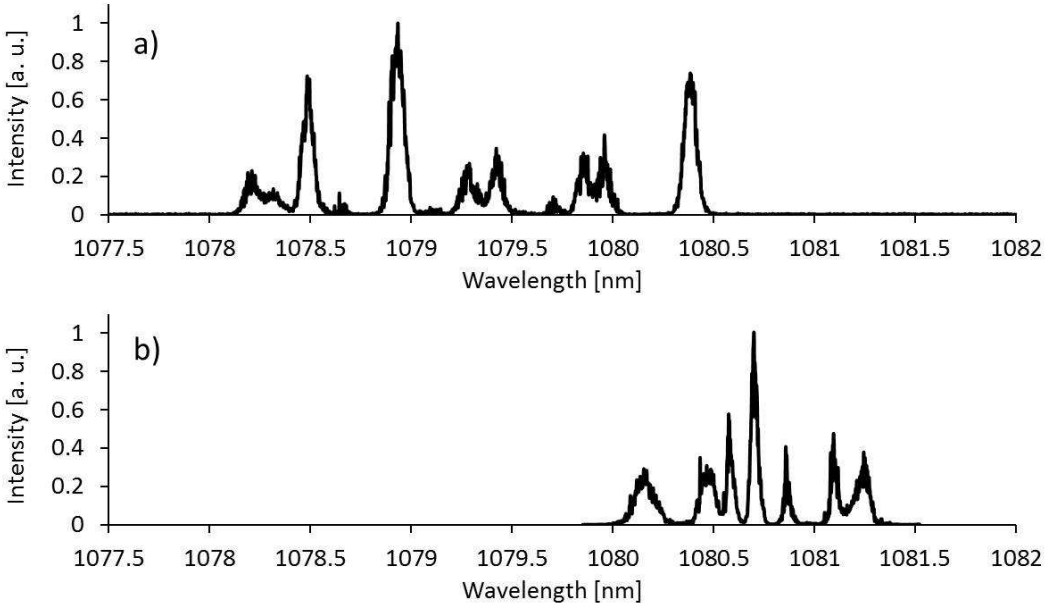

Figure 6.21: Fundamental power spectrum measured for a) smaller spot size; b) bigger spot size on the diffraction grating.

The axial mode content of the emission spectrum is also influenced by many other factors, including spatial hole burning and cavity length, and hence will be sensitive to small changes in cavity length that result from mechanical vibrations and temperature fluctuations. However, regardless of these perturbations to cavity length, there are always a large number of axial modes that are simultaneously resonant in the enhancement cavity, and this guarantees very stable green out-put. The power stability over the time scale range from 10ns to 100 s was measured to be < 0.7% rms (see fig. 6.22). This is much better than we typically obtain for a free-running Yb fibre laser and is attributed to the large number of lasing modes and temporal filtering action provided by the enhancement cavity.

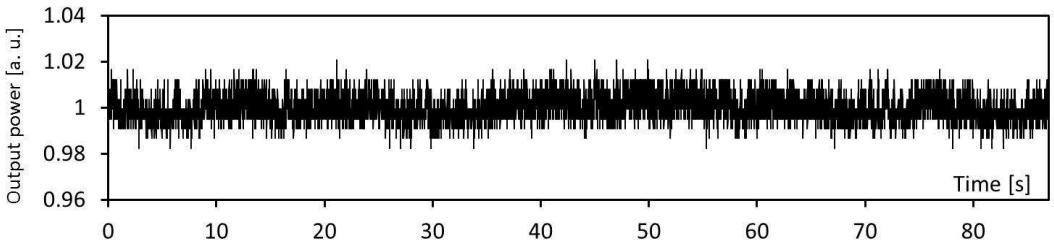

Figure 6.22: Second harmonic output power stability

The output power was mainly limited by the amount of feedback returning to the fibre. In this experiment the amount of light returning to the fibre after double-pass through the enhancement resonator was estimated to be very small - decreasing from ~8% of the total fundamental power incident on the input coupler at low power levels (with negligible SHG conversion efficiency) to ~2% at the maximum output power (corresponding to ~4.5% SHG efficiency). Launching more pump power into the active fibre resulted in further decrease of feedback efficiency and triggered parasitic lasing between the diffraction grating and other objects (e.g. LBO crystal) providing small amounts of feedback arising from scattering. As there was no longer polarisation selection in the cavity formed by this mechanism, the intracavity power was randomly polarised and a significant fraction of light was reflected from the surfaces of the LBO crystal and absorbed by the metal oven causing it to overheat and drift away from phase-matching condition.

b) Critically-phase-matched, AR-coated LBO crystal configuration

The next step in development of the internally-frequency-doubled fibre laser aimed for improvement of its overall performance including the beam quality, laser line width, and changing the range of operating temperatures, to make the design more suitable for a commercial product. The new set-up employed a new design of the resonant enhancement cavity with a 10 mm long, AR-coated LBO crystal oriented for type I critical phase matching slightly above room temperature (as described in section 6.2). Actual arrangement of the enhancement cavity is presented in fig. 6.23.

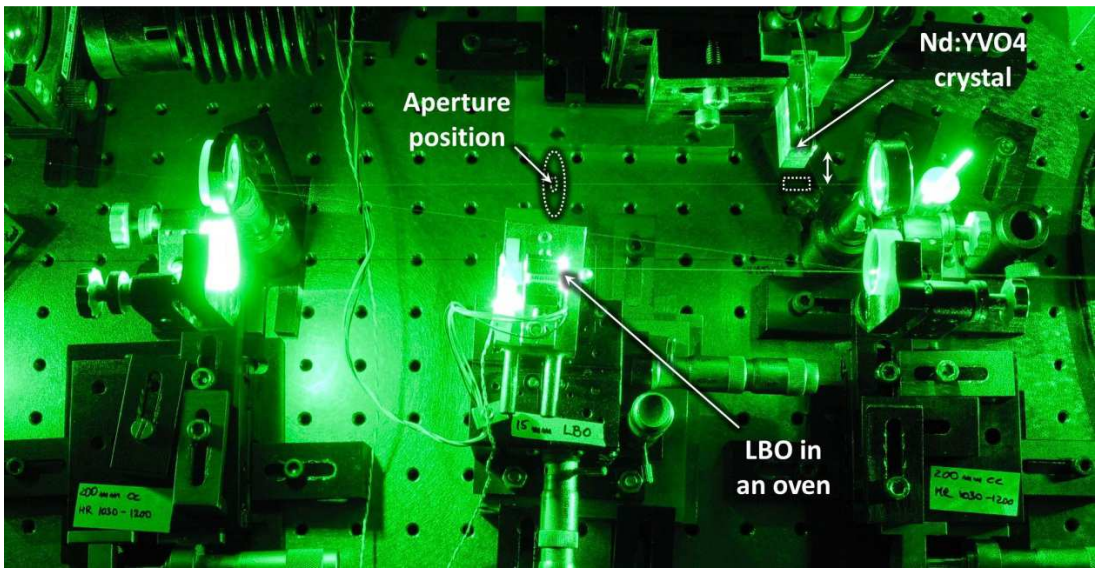

Figure 6.23: Experimental set-up: resonant enhancement cavity

An aperture, 800 µm in diameter, was placed at the waist position between plane mirrors of the resonant enhancement cavity to introduce loss for higher order resonator modes and hence enforce single-spatial-mode operation. A "bulk" solid state laser crystal (Nd:YVO_4, later replaced with Nd:$YAlO_3$) could be positioned near the output coupler (fig. 6.16) to perform the alignment procedure described in section 6.3.3. This procedure was used to find an optimal distance (550 mm) between the waist in the resonant enhancement cavity and the lens L_3 (focal length f_3 = 18.4 mm), collimating the output from the Yb-doped fibre (same fibre as in the previous experimental set-up). A thin film polariser, oriented at Brewster angle with respect to the incident beam, was positioned between the feedback mirror and the enhancement

cavity for linear polarisation selection. The actual arrangement of the external cavity with the enhancement resonator is presented in figure 6.24.

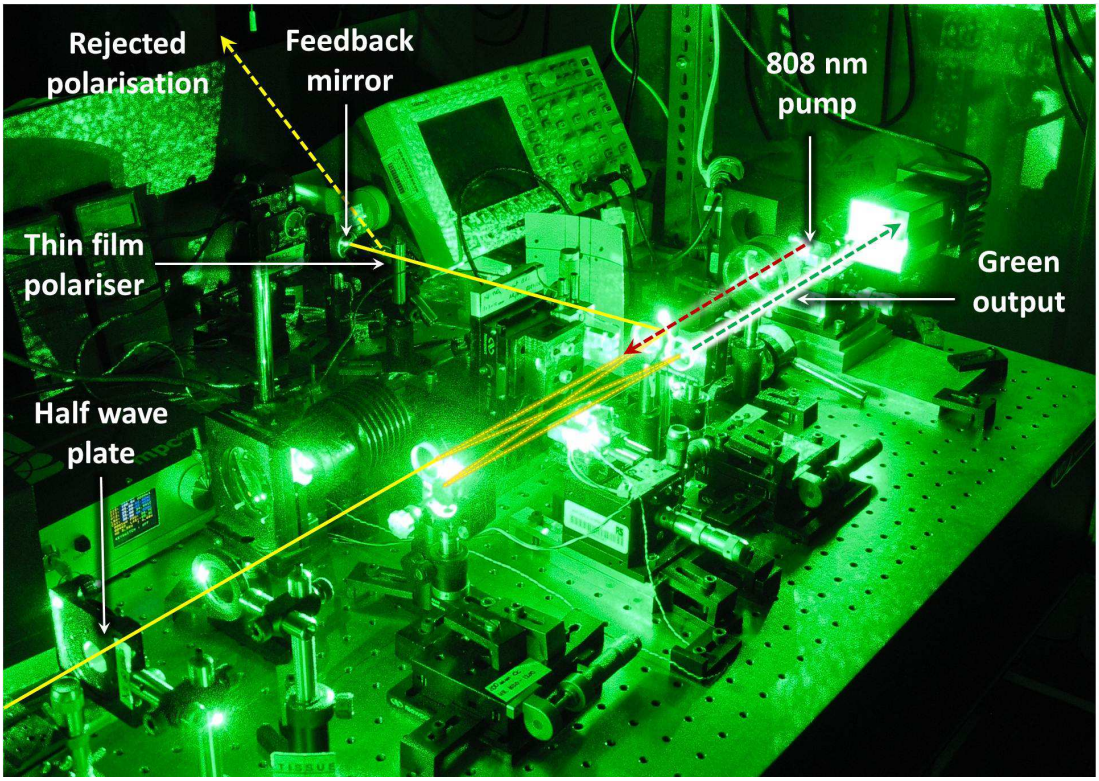

Figure 6.24: Experimental set-up: external cavity with the enhancement resonator

This experimental arrangement generated ~14.6 W of second harmonic power at 540 nm for the maximum ~104 W of pump power coupled into the active fibre (fig. 6.25a). For the maximum ~62 W of the total infrared power generated in the active fibre was incident on the input coupler of the enhancement resonator and ~34 W was efficiently coupled into the enhancement cavity, which corresponds to 55% coupling efficiency. The fundamental power circulating in the resonant enhancement cavity was measured to be ~410 W for the maximum fundamental power incident on the resonant enhancement cavity (fig. 6.25b) The enhancement factor was measured to decrease from a large number (>50) in a low power regime to ~12 at maximum green output, along with increasing second harmonic conversion efficiency. The proportionality constant between the SHG conversion efficiency and circulating fundamental power ϵ was found the fit to the experimental data (6.26a) to be $\epsilon \approx 7.2 \times 10^{-5}\ W^{-1}$ (i.e. the conversion efficiency increases by 0.7% per each 100W

of circulating fundamental power), which stays in a good agreement with the theoretical value $\epsilon \approx 7 \times 10^{-5}$ W^{-1} obtained from (4.27) for this resonator geometry.

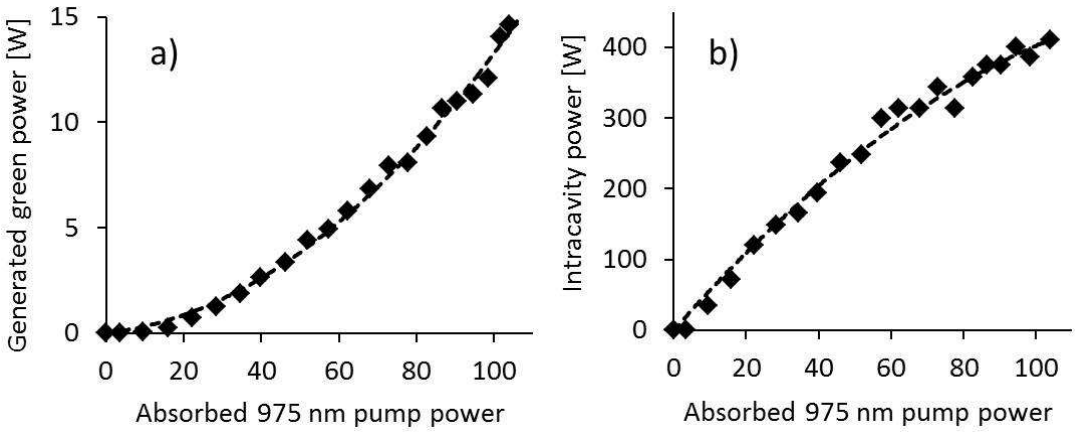

Figure 6.25: a) Generated second harmonic output power versus absorbed 975 nm pump power; b) Circulating resonantly-enhanced fundamental power versus absorbed pump power

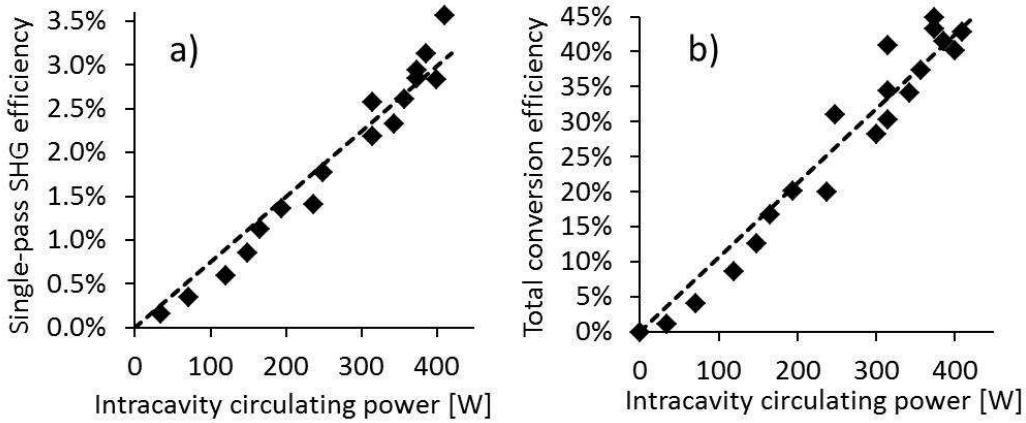

Figure 6.26: SHG conversion efficiency versus intracavity infrared power circulating in the internal ring enhancement cavity; a) single-pass conversion defined as a ratio of green power generated to the circulating infrared power b) total conversion efficiency

The second harmonic output beam quality (M^2 parameter) was measured to be $M_x^2 \approx 1.03$ and $M_y^2 \approx 1.04$ in two orthogonal planes respectively (fig. 6.27a). The green output beam had a Gaussian profile in two orthogonal planes, but the beam remained slightly non-circular due to residual astigmatism effects arising from non-normal incidence on the concave mirrors of the enhancement resonator (fig. 6.28).

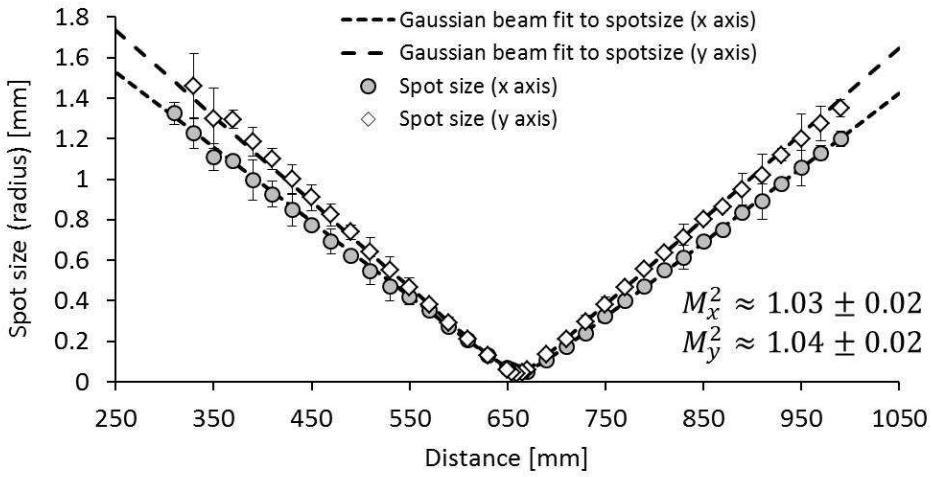

Figure 6.27: Beam size measurements compared to a Gaussian beam fit in x and y planes

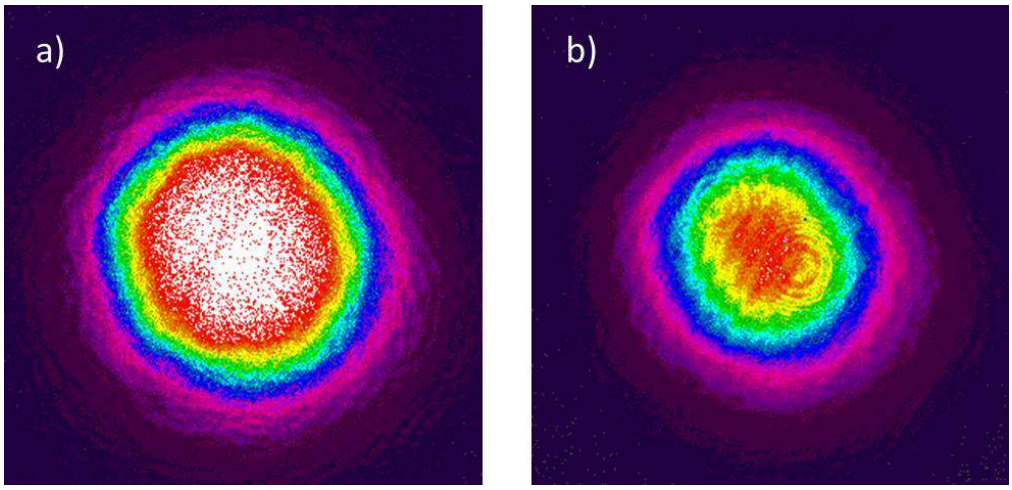

Figure 6.28: Beam profiles at ~10W output power a) CCD image of the output beam attenuated by multiple reflections b) CCD image of the output beam after multiple reflections and passing through several neutral density filters.

The spot size on the diffraction grating was adjusted to narrow the laser's emission bandwidth to ~0.4 nm. The optical spectra of both the second harmonic output beam, and the beam incident on the input coupler of the enhancement resonator were measured using two different optical spectrum analysers (with resolutions 0.05 nm and 0.01 nm respectively). It was found that the envelope of the second harmonic spectrum follows the shape of the fundamental laser line (fig. 6.29). Both spectra will consist of groups of one or more axial modes separated by a frequency interval

corresponding to at least one free spectral range of the enhancement cavity (i.e., ~280 MHz for the fundamental spectrum and ~140 MHz for the second harmonic output) according to (5.10).

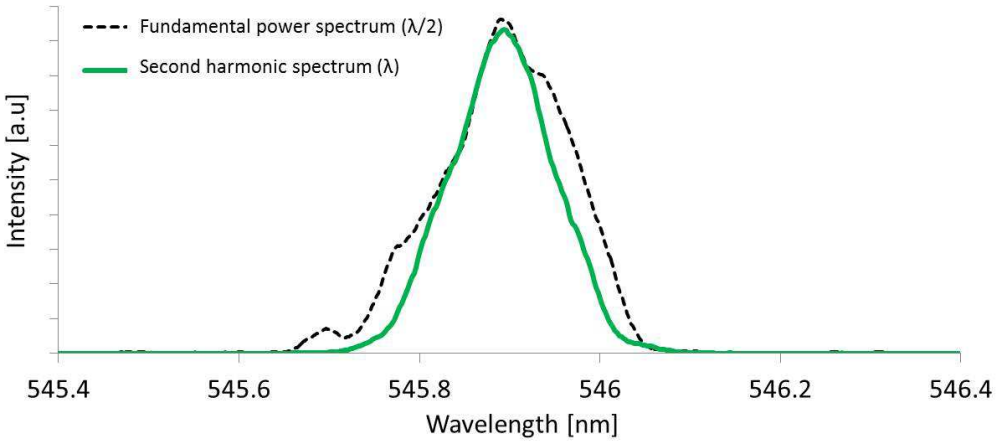

Figure 6.29: Optical spectrum of the green second harmonic output compared to the spectrum of the fundamental intracavity power of the fibre laser (plotted vs. half wavelength); intensities not to scale

The second harmonic output power was again mainly limited by the amount of feedback returning to the fibre, as only ~4% of the maximum total fundamental power incident on the input coupler M_1 was leaking through the output coupler in the forward direction to reflect from the feedback mirror. Over 60% of this feedback signal incident on the output coupler M_2 was later lost via reflection off the M_2 surface due to impedance mismatch. Performance of the laser strongly depends on the round-trip loss of the enhancement resonator, according to (5.8) and (5.13). Due to high intensity circulating in the resonant enhancement cavity, even small loss introduces significant leakage of fundamental power from the system, hence reducing the amount of power that can be converted to second harmonic output or fed back to the fibre (the latter is particularly important to maintain lasing on resonant frequencies of the enhancement resonator). Small losses in the enhancement resonator can also significantly reduce the second harmonic efficiency. The fraction of fundamental power returning to the fibre after a double pass through the enhancement resonator was comparable to the power leaking through a single concave mirror of the resonant enhancement resonator. Additional losses resulted

from the reflections off the AR-coatings on the LBO's and absorption inside the crystal. The transmission loss during a single pass through the LBO crystal was measured using the Findlay–Clay method [6.1]. Lasing threshold of a "bulk" Nd:$YAlO_3$ solid state laser with a short plano-concave linear cavity was measured for measured for several output couplers of a different reflectivity, with and without the LBO crystal in the laser cavity. Single-pass transmission loss calculated from these measurements was ~0.2%, which is in good agreement with reflection losses of ~0.1% per AR-coating, measured with a calibrated photo-detector. The residual round-trip loss (arising from the scattering on the mirrors surfaces, loss on the transmission through the aperture, and astigmatism effects) that could not be directly measured was estimated to fall within 1.0-2.5% range.

In order to facilitate further power scaling in this fibre laser configuration it is particularly important to minimise the round-trip loss as this will enhance both the resonant enhancement factor (hence increasing second harmonic efficiency) and the transmission through the cavity in both directions (hence providing more feedback to the laser, which in turn allows use of more pump power before reaching the parasitic lasing regime). The performance of the laser can be improved by using HR coatings of better quality on the concave mirrors, AR coatings of better quality on the LBO crystal of higher purity (and hence smaller absorption). There is certainly a trade-off between the enhancement factor and the feedback to the fibre in this laser cavity configuration. Using an output coupler (M_2) with a higher reflectivity enables reaching higher conversion efficiency for a given pump power level but decreases amount of light that is fed back to the fibre; using a lower output coupler reflectivity enables more pump power to be employed (before reaching parasitic lasing) at the expense of the second harmonic efficiency. Therefore the actual reflectivity of the output coupler should be carefully chosen for the given level of pump power available.

Another approach can be based on modified laser resonator architectures with higher feedback efficiency in the external cavity with the resonant enhancement cavity. The main loss in the feedback path was arising from the impedance mismatch on launching the fundamental power to the enhancement resonator in the reverse direction. Using fibre laser resonator architectures where the feedback path does not

involve a second pass through the enhancement cavity could vastly improve the feedback efficiency and enable the use of more pump power before reaching parasitic lasing. One example of such a laser architecture overcoming the feedback efficiency limitation could be based on a true ring resonator, as described in the beginning of section 5.3. The signal leaking through the output coupler of the enhancement resonator, pumped by a beam exiting one end of the fibre should be reflected from (or transmitted by) a spectrum-selective element (e.g. a diffraction grating) and launched into the opposite end of the fibre. Although initial alignment of the ring resonator can be challenging, it should allow for lowest round-trip loss of the main fibre laser resonator, and hence superior performance of all described resonator arrangements.

Although the amount of signal power leaking from the enhancement resonator is an important parameter that should be carefully optimised, it is not the ultimate factor limiting power scaling of the second harmonic output. The output coupler reflectivity can be chosen arbitrarily high to provide enough feedback (signal power) to lock the laser on the resonant frequencies of the enhancement cavity, while enabling sufficient intracavity power enhancement and efficient frequency doubling for the maximum pump power available. Hence, other effects will be limiting the second harmonic output power when more pump power is available. Those include thermal damage to the LBO crystal, nonlinear effects and damage to the coatings of the mirrors forming the enhancement resonator and nonlinear effects in the fibre's core such as stimulated Brillouin scattering or stimulated Raman scattering, but they should not be affecting the laser's performance for fundamental power level of several hundreds of watts generated in the fibre or multiple kilowatts circulating in the enhancement cavity. In the experiments on power scaling described in this chapter the output coupler reflectivity was chosen to be close to optimum for the maximum power of the pump source. When more pump power is available, and the feedback path arrangement design is optimised it should be possible to scale the output second harmonic power much further, possibly into multi-hundred watt regime and beyond.

6.4. Conclusions

This chapter described the development and power scaling of the internally-frequency-doubled continuous-wave Yb-doped fibre laser. Three main laser configurations have been constructed and thoroughly investigated. The most important parameters of those systems are compared in table 6.1.

Experiment / Parameter	Laser #1 NCPM (SM fibre)	Laser #2 NCPM (MM fibre)	Laser #3 CPM (MM fibre)
Max. pump power at 975 nm absorbed	~ 23 W	~ 91 W	~ 104 W
Max. IR power generated in the active fibre	~ 12 W	~ 64 W	~ 62 W
Max. IR coupled into the enhancement cavity	~ 7 W	~ 32 W	~ 34 W
Max. IR circulating in the cavity	~ 141 W	~ 440 W	~ 410 W
Max. green power generated inside LBO	~ 3.2 W	**~ 19 W**	~ 15 W
Max. green output	~ 2.5 W	**~ 15 W**	~ 13 W
Phase matching temperature	90 - 135 °C	~129 °C	**20-30 °C**
Output wavelength	**539–558 nm**	~ 540 nm	~540 nm
Output spectrum line width	~ 1.3 nm	~ 1.3 nm	**~ 0.15 nm**
$\epsilon = d\eta_{SHG}/dP_{\omega}$ (proportionality constant)	**15% kW^{-1}**	10% kW^{-1}	7% kW^{-1}
Beam quality (M^2 parameter)	~ 1.25	~ 1.25	**< 1.05**
Max. SHG efficiency (circulating IR to green)	~ 2.2 %	**~ 4.3 %**	~ 3.5 %
Max. SHG efficiency (launched IR to green)	~ 45 %	**~ 59 %**	~ 43 %
Max. SHG efficiency (pump to green)	~ 14 %	**~ 21 %**	~ 14 %
Enhancement factor at max. output power	~ 22	~14	~12
Average mode-matching quality	**~ 86 %**	~ 55 %	~ 50 %

Table 6.1: Comparison of the most important parameters in three investigated laser configurations

‘Laser #1’ configuration, pumped with a ~30 W pump source at 975 nm was based on a robustly single-mode Yb-doped fibre and Brewster-angled LBO crystal oriented for type I non-critical phase matching. Relatively broad wavelength tuning flexibility of ~20 nm in the green spectral region was demonstrated with this experimental set-up. Highest mode-matching quality (~86% of incident light coupled into the enhancement resonator) and SHG efficiency increment rate ($\epsilon = 15\%$ kW^{-1}) were also obtained in this laser geometry.

‘Laser #2’ configuration, pumped with a ~150 W pump source at 975 nm was based on a slightly multimode Yb-doped fibre and a Brewster-cut LBO crystal oriented for type I non-critical phase matching. This was the most powerful of all three geometries investigated (~19 W of green power generated / ~15 W in the output beam) with the best SHG conversion efficiency - with respect to fundamental power circulating in the enhancement resonator, launched into the enhancement resonator, and absorbed pump power at 975 nm (~4.3 %, ~59%, and ~21% respectively).

‘Laser #3’ configuration, pumped with a ~150 W pump source at 975 nm was based on a slightly multimode Yb-doped fibre and an AR-coated LBO crystal oriented for type I critical phase matching. This refined design was more suitable for industrial applications thanks to phase matching condition obtainable room temperature (20-30 $^{\circ}$C) on the expense of slightly reduced maximum output power and conversion efficiency. It also yielded the narrowest laser line width (~0.15 nm) and the best beam quality (M^2 parameter of <1.05).

The power scaling limitations have been identified as arising from low feedback efficiency from the external cavity arrangement. We concluded that it is always possible to increase the feedback efficiency on the expense of SHG conversion efficiency by increasing the transmission of the enhancement resonator’s output coupler. Overall, no other limitations have been observed in the investigated power regime (up to ~100 W pump power absorbed), hence we conclude that further power scaling of this novel laser architecture using more powerful pump sources should yield green output in power regimes not accessible to existing visible laser sources.

References

[6.1] D. Findlay and R.A. Clay, "The measurement of internal losses in 4-level lasers," Phys. Lett., 20, 277 (1966)

Chapter 7
Conclusions and future prospects

7.1 Summary of thesis

The work presented in thesis has explored a range of novel fibre-based coherent light source architectures and strategies for power scaling these sources. In *Part I: Spectrum-controllable fibre based ASE sources*, modelling, development and characterisation of a versatile ASE source using a power-efficient means for spectrum control was descibed. *Part II: Efficient intracavity frequency doubling scheme for continuous-wave fibre lasers* introduced a novel concept for efficient frequency doubling in high power continuous-wave fibre lasers. It also described ways to implement this concept in devices based on both robustly single-mode and multi-mode fibres. Finally, experimental results on wavelength tuning of a continuous-wave Yb-doped fibre laser over ~19 nm in the green spectral region and scaling the generated second harmonic power up to ~19 W have been presented.

7.1.1. Spectrally-controllable fibre-based ASE sources

In the first part of this thesis we have studied several different configurations of a fibre-based ASE seed source. Experimental set-ups of increasing complexity have been constructed and characterized to explore the capabilities and limitations of these devices. To gain an understanding of the basic physical mechanisms present in ASE sources a simplified theoretical model was developed which has proved useful in predicting system performance in the low power (unsaturated gain) regime. We also looked into the influence of various parameters (pump power, fibre architecture, fibre length, doping levels, external cavity loss, spectral reflectivity, fibre facet quality,

etc.) on the system performance. Novel concepts for wavelength selection and narrowing the linewidth in the external cavity have been applied, and the advantages of these approaches over the conventional methods of wavelength selection applied to the source output have been discussed.

This series of experiments have culminated in a versatile seed source with polarized output and a reasonable degree of spectral control. In its final configuration, the source was capable of producing either a broad spectrum from 1-1.1 μm with a FWHM of 15-40 nm and output power > 1W, or single/multiple narrow lines with a FWHM ranging from several nanometres to < 0.05 nm and output power spectral densities of up to 100 mW/nm. The output power was temporally stable with fluctuations at the level < 0.3-0.8% of the total output power (depending on the spectral content). Very high spectral stability (including linewidth fluctuations and central peak position) was obtained, which was limited mostly by the mechanical stability of the external cavity. The output beam was nearly diffraction limited with $M^2 \approx 1.1$. These performance parameters make the final device a very reliable light source that can outperform various laser sources opening up the prospect of many applications. However, the main drawback, observed when it was operating in narrowband regime, was the low broad (spectral) background which can account for a significant portion of the total output power. This would become an issue when launched into an amplifier chain because the background light will be amplified along with the signal, ultimately reducing effective output power in the narrow line.

7.1.2. Efficient intracavity frequency doubling schemes for continuous-wave fibre lasers

In the second part of this thesis we proposed and discussed a strategy for power scaling of laser sources emitting in the visible spectral region. After reviewing the principles and challenges of scaling output power in bulk solid-state lasers we concluded that fibre laser architecture is the most promising route for generating high

power visible output via nonlinear frequency conversion. Unfortunately conventional approaches for frequency doubling in fibre lasers are either inefficient or very complicated. Although the highest output power from a CW visible fibre laser source with a good beam quality was obtained using technique of external resonantly-enhanced second harmonic generation, this approach has the drawback of being very complicated. Moreover, nonlinear loss due to SBS makes scaling single-frequency power at the fundamental wavelength very challenging. In this thesis we introduced a novel approach for efficient nonlinear frequency doubling in CW fibre lasers based on the internal enhancement resonator incorporated in the main cavity of the fibre laser. This concept can be used in both travelling-wave (ring) and standing-wave (linear) laser resonator architectures. It overcomes the limitations of the external resonantly-enhanced SHG exploiting the raw power-scaling potential of a cladding-pumped fibre lasers with a large number of lasing longitudinal modes.

To gain a better understanding of the basic physical mechanisms and dynamics of this novel laser architecture a laser resonator incorporating a single-mode Yb-doped fibre and an intracavity free-space ring enhancement resonator with three partially transmitting mirrors, one of them acting as an output coupler, was constructed. We discussed the fundamental considerations for the enhancement cavity design, the impact of mode-matching between the output from the fibre and the fundamental mode of the enhancement resonator, as well as the impact of optical feedback level on the overall laser's performance. Experimental results led to the conclusion that the output power is strongly dependent on the mode-matching factor, but efficient operation can be obtained even with very low feedback from the external cavity arrangement (<0.5%). The best mode matching obtained between the output from a single-mode fibre and the fundamental mode of the enhancement resonator was measured to be ~96%. We also studied temporal characteristics of the novel resonator architecture and demonstrated the potential for using it in long-pulsed mode of operation. The optical self-locking was very tolerant to vibrations. The output power stability under cavity length changes greater than 18 µm in amplitude and 4.4 mm/s in rate of change was measured to be < 1.3%, while the longitudinal modes required to maintain the optical lock formed very quickly (i.e. < 5 µs). Another fibre laser configuration incorporating a multi-mode Yb-doped fibre and an intracavity enhancement resonator with three partially transmitting mirrors was used

to investigate the use of modal interference to allow efficient coupling of the output from the multi-mode fibre core to the fundamental mode of the enhancement resonator. This experiment confirmed that laser oscillation was locked to frequencies at which the spatial modes in the fibre core added up to form a diffraction-limited beam relatively well mode-matched to the fundamental mode of the enhancement resonator. The mode matching factor was measured to be ~81%.

Finally, we applied the novel resonator design to frequency doubling of a CW fibre laser. The initial experiment involved a travelling-wave (ring) laser resonator based on two sections of a single-mode Yb-doped fibre and a free space resonator with two partially transmitting mirrors and an LBO crystal oriented for type I (ooe) NCPM SHG. This fibre laser delivered 215 mW of CW green output at 521 nm for ~8 W incident on (and ~4 W coupled into) the enhancement resonator. Although inefficient and not optimized for impedance matching, this set-up laid down the foundations for further experiments and proved the concept to be viable in a ring resonator configuration.

In the next steps three different laser configurations employing a linear resonator were built and characterised. The first laser source, based on single-mode Yb-doped fibre aimed for maximising the conversion efficiency at moderate power levels. The highest mode-matching efficiency with ~86% of incident power launched into the enhancement resonator and highest SHG efficiency of ~15% kW^{-1} were obtained for this geometry. We also performed tuning of this laser over relatively broad range between 539 and 558 nm above 1 W output power level.

The second laser source, based on a multi-mode Yb-doped fibre was targeted at maximising the output power and the total (pump to second harmonic) conversion efficiency, as well as demonstrating efficient coupling to the enhancement resonator aided by modal interference. Using this laser ~19 W of second harmonic power was generated in the LBO crystal, which corresponded to ~21% pump to second harmonic conversion ratio. Efficient coupling between the multimode fibre output and fundamental mode of the resonator was successfully demonstrated.

The third laser configuration aimed for improved beam parameters (including a narrower linewidth spectrum and better beam quality) as well as room temperature operation. Changing the LBO crystal and its orientation for type I (ooe) CPM SHG allowed efficient generation of green output in the 20-30 $^{\circ}$C temperature range, while optimisation of the beam size on the diffraction grating allowed for reducing the emission bandwidth from 1.3 nm to 0.15 nm. Positioning an aperture inside the enhancement resonator allowed for selecting only the fundamental mode of the ring enhancement cavity and improved the beam quality to $M^2 < 1.05$ from ~1.25 obtained with a resonator without an aperture.

Power scaling limitations have been attributed mainly to the low feedback efficiency from the external cavity arrangement. The level of feedback decreased for higher output powers due to increasing second harmonic conversion efficiency. We concluded that it is always possible to re-design the set-up, so that the feedback efficiency is optimised for a given level of available pump power. As no other limitations have been observed over the power range investigated, we predict that with further power scaling of this laser architecture it should be possible to reach power levels not currently accessible via other solid-state and fibre laser technologies.

7.2 Future prospects

Power scaling strategies for spectrally-controllable fibre based ASE sources and internally-frequency-doubled CW fibre lasers have been proposed and discussed in this thesis. Although several experimental configurations have been demonstrated, these sources merely scratched the surface of their potential for scaling to very high power levels. In this section we propose future research directions for further power scaling of the spectrally-controllable fibre-based ASE sources in a multi-stage amplifier configuration, further development of the green fibre laser, and extension of the internal resonant enhancement technique to other nonlinear processes and laser pumping configurations.

7.2.1 Multi-stage high power ASE amplifier

Our experiments on spectrum-controllable fibre-based ASE sources concluded with a versatile source, using a simple arrangement for spectral shaping in the external cavity. We propose further development of the seed source as well as its power scaling to very high power levels using a multi-stage chain of power amplifiers. In our opinion further development of the seed ASE source should take at least two directions: broadening the emission bandwidth and extending the spectrum control flexibility. An all-fibre configuration would be a natural step in the development of the high power ASE source architecture. Fig. 7.1 shows one possible configuration for a broadband ASE source emitting in the ~1 µm spectral region.

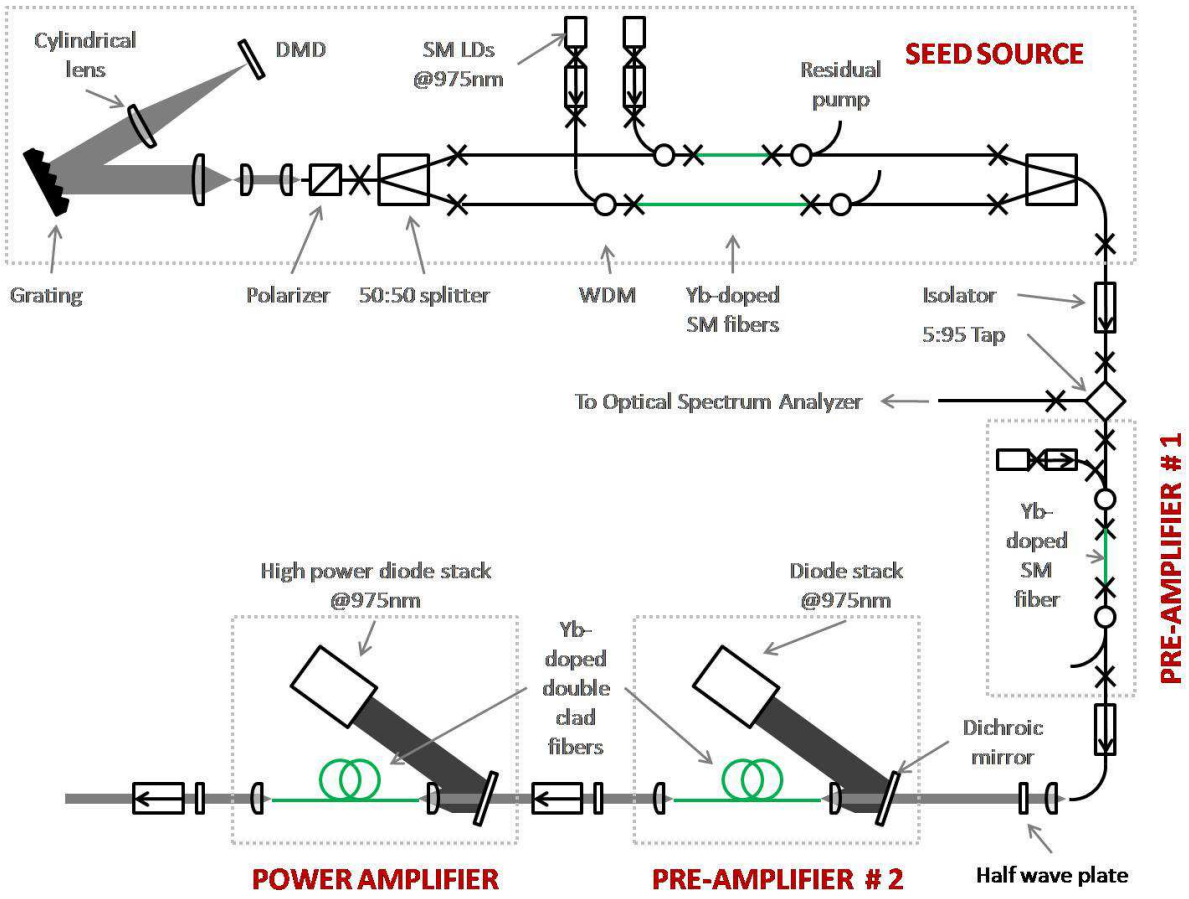

Fig. 7.1: Example of a high-power spectrum-controllable ASE source in a multi-stage amplifier configuration (possible research direction)

The emission bandwidth can be effectively broadened by using a number of parallel Yb-doped fibre sections of different length, sharing the same external cavity with means of spectrum control and combined to a common output. Shorter fibres would exhibit the highest gain at shorter wavelengths, while the gain maximum in longer fibres would be shifted towards longer wavelengths due to stronger reabsorption effect at shorter wavelengths. These active fibres can be core-pumped, allowing for effective output with a very broad spectrum from a number of gain stages with relatively short device lengths. The common output fibre can be spliced to the pre-amplifier input, while the other common end will incorporate a polarizer and be terminated with an external cavity for spectrum shaping purposes. The external feedback arrangement will be similar in principle to the one described in section 3.6, but with the spherical lens - HR mirror arrangement replaced with a cylindrical lens - Digital Micromirror Device (DMD) configuration. Such commercially available DMD array (e.g. containing 1024 x 768 independently controlled micro-mirrors of size 10 x 10 μm each) can be used for two-dimensional spectral shaping of the seed ASE source; by switching vertical columns of mirrors chosen spectral components can be blocked or selected for feedback, while switching some number of the mirrors in a single column allows to determine the amount of power from single spectral component to be fed back into the fibre. This should provide a great degree of flexibility in spectrum tailoring within the ASE emission spectrum. The seed source with multiple active fibres of different lengths and independent pumping diodes provide a route to access a broader ASE spectrum with more tuning flexibility provided by variable pump power ratios between individual parallel gain stages. The output from the ASE seed source, after passing through an isolator and a tap, can be launched to the core-pumped pre-amplifier. The pre-amplifier ASE output can be then amplified by the following cladding-pumped gain stages, each terminated with high-power Faraday isolators. The best approach would be to use amplifiers using parallel gain fibres of different length, to extend the spectrum of the amplified signal. Single stage amplifiers as illustrated in fig. 7.1 can be only used to yield relatively narrowband output. Active stabilization of the spectral characteristics of the source may be implemented by monitoring the output spectrum with a digital spectrometer in a feedback loop. High power broadband ASE sources using such architecture can be used for a wide range of applications including material processing and low-coherence interferometry.

7.2.2 Internal resonant power enhancement in continuous-wave fibre lasers

Further development of the internally-frequency-doubled laser architectures described in chapter 6 should facilitate power scaling to much higher power levels. Initial steps towards higher output power would involve minimising round-trip loss of the enhancement resonator, and further optimisation of the level of feedback from the external cavity arrangement. Another approach to power scaling of this fibre laser system would be to employ a travelling-wave (ring) resonator configuration, wherein the leakage through the output coupler of the enhancement resonator is coupled into the end of the fibre gain stage, opposite to the end emitting the high power beam incident on the input coupler of the enhancement cavity. Although initial alignment of the travelling-wave resonator can be challenging, it should provide the lowest round-trip loss and hence superior performance among all studied resonator geometries. We are convinced that careful optimisation of this architecture should allow power scaling of the visible output into the multi-hundred-watts level and beyond.

The concept of intracavity power enhancement via use of an internal resonator is by no means restricted to second harmonic generation and can be also extended to a wide range of applications. Two examples are sum-frequency generation (SFG) and difference-frequency generation (DFG) using two fibre lasers operating at different fundamental wavelengths and sharing a common external cavity arrangement comprising a feedback path and enhancement resonator with a nonlinear crystal oriented for phase matching of a desired nonlinear process. Efficient sum-frequency generation with continuous wave fibre lasers is particularly important as it offers a potential route to high power output across the visible and near-IR spectral regions. If we consider tuning ranges of Nd-, Yb-, Er-, Bi-, and Tm-doped fibre lasers, we can conclude that high power output at virtually any wavelength from 440 nm - 1200 nm range can be achieved by SHG and SFG with fibre lasers using any two of above dopants. Similarly, cascaded (two-stage) SHG and SFG processes offer route to any

wavelength in the 220 nm – 600 nm spectral region. The same reasoning applies to the DFG process. High power output at any wavelength longer than 1500 nm (provided this wavelength lies within transmission range of the optical materials used in the laser) can be realised by frequency mixing between fibre lasers with different active ion dopants.

A fibre-based optical parametric oscillator can be also based on the resonant enhancement cavity incorporated in a main resonator of the fibre laser. Such an architecture using a periodically-poled nonlinear crystal in the enhancement resonator can provide a relatively simple route to high power output in the mid-IR spectral region.

Other interesting applications for this concept involve novel hybrid fibre-bulk laser sources, optical pumping, optical cooling and many more. Unfortunately, due to limited time of the PhD project, the proposed approach to intracavity power enhancement in continuous-wave fibre lasers merely scratched the surface of its potential. We believe that this technique can become a platform technology for extending the range of operating wavelengths of high power laser sources to the visible and mid-IR spectral regions. In our opinion many more applications will emerge after these novel laser architectures, generating high power output at various wavelengths not accessible to conventional laser sources, are demonstrated.

Appendix A

Etalon theory

The transmission function of a well-adjusted etalon is given by [A.1]:

$$\mathrm{T}(\lambda) = \frac{1}{1 + \phi \sin^2(\delta/2)} \tag{A.1}$$

where $\delta = \left(\frac{2\pi}{\lambda}\right) 2 n_e d_e \cos\theta_e$ is a phase difference between reflections, d_e - mirrors spacing, n_e - refractive index between mirrors, θ_e - incident angle, and ϕ is a finesse coefficient with a maximum value of $\phi_{max} = \frac{4R_e}{(1-R_e)^2}$ for ideal plane-plane mirrors of reflectivity R_e. (A.1) consists of narrow peaks of FWHM $\delta\lambda$ and reaching unity, separated by the free spectral range (FSR):

$$\mathrm{FSR} = \frac{\lambda_0^2}{2 n_e d_e \cos\theta_e + \lambda_0} \tag{A.2}$$

where λ_0 is the central wavelength of the nearest peak. The peak width $\delta\lambda$ is connected with the FSR by the cavity finesse:

$$F = \frac{\mathrm{FSR}}{\delta\lambda} = \frac{\pi}{2 \sin^{-1}\left(1/\sqrt{\phi}\right)} \approx \frac{\pi}{2}\sqrt{\phi} \tag{A.3}$$

where the last approximation is valid for $R_e > 0.5$. Using (A.1), (A.2), (A.3) and putting $n_e \approx 1$ (air), $\theta_e \approx 0$, and assuming $2d \gg \lambda_0$, the expression for minimal peak width becomes:

$$\delta\lambda \geq \frac{\lambda_0^2}{2\pi d_e} \frac{(1 - R_e)}{\sqrt{R_e}} \tag{A.4}$$

References

[A.1] G. Hernandez, “Fabry-Pérot Interferometers”, Cambridge University Press, Cambridge, 1986

List of publications

[1] R. Cieslak, J. K. Sahu, W. A. Clarkson, "Efficient intracavity frequency doubling of an Yb-doped fiber laser using an internal resonant enhancement cavity", CLEO/QELS 2010, San Jose, 16-21 May 2010, paper CMW4

[2] R. Cieslak, J. K. Sahu, W. A. Clarkson, "Wavelength-tunable internally-frequency-doubled Yb-doped fiber laser", 4th EPS-QEOD Europhoton Conference, Hamburg, Aug 29-3 Sep 2010, paper ThA4

[3] R. Cieslak, W. A. Clarkson, "Power-scalable internal frequency doubling scheme for continuous-wave fiber lasers", SPIE Photonics West 2011: LASE San Francisco 22-27 Jan 2011, paper 7914-118 (Postdeadline paper)

[4] R. Cieslak, W.A. Clarkson, "Internal resonantly-enhanced frequency doubling of continuous-wave fiber lasers", Optics letters, vol.36, no.10, pp. 1896-1898, 2011

[5] R. Cieslak, W. A. Clarkson, "Internally-frequency-doubled Yb fiber laser with 15 W CW green output", CLEO/EQEC-Europe 2011, Munich, 22-26 May 2011, paper CJ3.2

[6] W. A. Clarkson, R. Cieslak, "Novel resonantly-enhanced nonlinear frequency conversion scheme for cladding-pumped fiber lasers", Physics of Lasers: International Laser Physics Workshop, Saravejo, 11-15 Jul 2011 (Invited paper)

[7] R. Cieslak, W. A. Clarkson, "Efficient nonlinear frequency conversion scheme for cladding-pumped fiber lasers", SPIE Photonics West, San Francisco, 21-26 Jan 2012, paper 8237-51 (Invited paper)

[8] Patent application no. PCT/GB2011/000742, Patent Title: “Optical Fibre Lasers” Inventors: W. A. Clarkson and R. Cieslak, publication number WO/2012/101391, published on 02.08.2012